

The University of Nottingham

UNITED KINGDOM · CHINA · MALAYSIA

Manufacture and Characterisation of Porous Phosphate, Borate and Silicate Glass Microspheres for Biomedical Applications

By

Md Towhidul Islam

(BSc., MS)

Thesis submitted to the University of Nottingham for the degree of Doctor of Philosophy

August 2019

I dedicate this thesis to my beloved three ladies; my mother, mother-in-law and my wife

Contents

ABSTRACT vii

ACKNOWLEDGMENTS x

LIST OF PUBLICATIONS xi

ABBREVIATIONS xiii

LIST OF FIGURES xv

LIST OF TABLES xxvii

CHAPTER 1: INTRODUCTION 1

1.1 Overview 1

1.2 Aims and Objectives 3

1.3 Thesis Outline 4

CHAPTER 2: LITERATURE REVIEW 6

2.1 Silicate-based glasses 6

2.2 Borate-based glasses 8

2.3 Phosphate-based glasses 11

2.4 Ceramics 14

2.5 Glass-ceramic materials 15

2.6 Crystallisation kinetics 15

2.7 Mechanism of apatite formation 16

2.8 Effect Mg on bioactivity and biocompatibility of glass 23

2.9 Effect of titanium on glass forming ability and biocompatibility 24

2.10 Test protocols for in vitro bioactivity experiment 25

2.11 Biomedical applications of calcium phosphate 30

2.11.1 Dental applications 31

2.11.2 Bone repair 32

2.11.3 Bioactive coatings 33

2.11.4 Drug and Gene delivery 34

2.11.5 Soft Tissue Engineering 35
2.12 Manufacture of microspheres (solid and porous) 35
2.12.1 Phosphate-based glass microspheres 37
2.12.2 Borate-based glass microspheres 38
2.12.3 Silicate-based glass microspheres 40
2.13 Morphology of porous glass microspheres 42
CHAPTER 3: MATERIALS AND METHODOLOGY 43
3.1 Glass Preparation 43
3.1.1 Phosphate based glasses 43
3.1.2 Borate glasses 44
3.1.3 Silicate glasses 45
3.2 Preparation of microspheres 46
3.2.1 Solid glass microspheres 46
3.2.2 Porous glass microspheres 47
3.3 Characterisation methods 48
3.3.1 Compositional analysis 48
3.3.1.1 Composition analysis via EDX 48
3.3.1.2 Composition analysis via ICP-MS 48
3.3.2 SEM analysis 49
3.3.3 X-ray diffraction analysis 49
3.3.4 Density measurement 49
3.3.5 Thermal analysis 51
3.3.6 Activation energy of crystallisation 51
3.3.7 Fourier transform infrared (FTIR) spectroscopic analysis 52
3.3.8 Micro Raman spectroscopic analysis 52
3.3.9 Nuclear magnetic resonance (NMR) spectroscopic analysis 53
3.3.10 Degradation studies 53
3.3.10.1 Phosphate bulk glass disc dissolution study 53
3.3.10.2 Microspheres degradation studies 54
3.3.10.2.1 Phosphate solution for conversion reaction 56
3.3.11 Ion release analysis via ICP-MS 56

3.3.12 Simulated body fluid (SBF) studies 57
3.3.13 Porosity 58
3.3.14 BET surface area analysis 58
3.3.15 Viscosity measurement 58
CHAPTER 4: STRUCTURAL, CRYSTALLISATION BEHAVIOUR, DEGRADATION, ION RELEASE AND IN VITRO BIOACTIVITY STUDIES OF NEAR INVERT PHOSPHATE BASED GLASSES 60
4.1 Introduction 60
4.2 Results 60
4.2.1 Compositional analysis 60
4.2.2 X-ray diffraction analysis 61
4.2.3 Density 62
4.2.4 Oxygen density and molar volume 63
4.2.5 Thermal properties 64
4.2.6 Crystallisation behaviour 66
4.2.7 FTIR and Raman spectroscopy 70
4.2.8 NMR spectroscopy 75
4.2.9 Degradation studies 76
4.2.10 Ion release profiles 80
4.2.11 *In vitro* bioactivity studies 83
4.3 Discussion 89
4.3.1 Density of glasses 89
4.3.2 Thermal properties 90
4.3.3 Structure of glasses 93
4.3.4 Degradation 95
4.3.5 *In vitro* bioactivity 96
4.4 Summary 97
CHAPTER 5: MANUFACTURE AND CHARACTERISATION OF SOLID AND POROUS PHOSPHATE GLASS MICROSPHERES FOR BIOMEDICAL APPLICATIONS 98

5.1 Introduction 98
5.2 Results 98
5.2.1 Composition of PBG glasses 98
5.2.2 Surface morphology via SEM 99
5.2.3 X-ray diffraction (XRD) analysis 102
5.2.4 Compositional analysis via EDX 102
5.2.5 Thermal properties 103
5.2.6 Density, Porosity and Surface area 105
5.2.7 Degradation studies 107
5.2.8 Ion release profiles 112
5.2.9 *In Vitro* SBF study 114
5.3 Discussion 118
5.4 Summary 123
CHAPTER 6: MANUFACTURE AND CHARACTERISATION OF SOLID AND POROUS BORATE GLASS MICROSPHERES FOR BIOMEDICAL APPLICATIONS 124
6.1 Introduction 124
6.2 Results 124
6.2.1 Compositional analysis of starting borate glasses via ICP-MS 124
6.2.2 Manufacture of borate glass microspheres 125
6.2.3 Post processing porous microspheres 126
6.2.4 X-ray diffraction analysis 134
6.2.5 Thermal Analysis 135
6.2.6 Density, tap density and porosity measurement 137
6.2.7 Conversion of borate glasses into HA in dil. K_2HPO_4 138
6.2.7.1 Degradation studies in dil. K_2HPO_4 138
6.2.7.2 pH Measurement 139
6.2.7.3 XRD 140
6.2.7.4 SEM 142
6.2.7.5 Ion release studies in dil. K_2HPO_4 solution 154
6.2.7.6 Compositional analysis 157

6.2.7.7 Conversion reaction at different concentration and different type of phosphate solution 158
6.2.8 *In vitro* bioactivity studies 162
6.2.8.1 XRD for bioactivity study 162
6.2.8.2 SEM for bioactivity study 164
6.2.8.3 Ion release studies in SBF 167
6.2.8.4 pH Measurements of SBF 170
6.2.8.5 Compositional analysis via ICP-MS for bioactivity study 170
6.3 Discussion 172
6.4 Summary 178
CHAPTER 7: MANUFACTURE AND CHARACTERISATION OF SOLID AND POROUS SILICATE GLASS MICROSPHERES FOR BIOMEDICAL APPLICATIONS 180
7.1 Introduction 180
7.2 Results 181
7.2.1 Preparation of solid bio-silicate glass microspheres (SGMS) 181
7.2.2 Preparation of porous bio-silicate glass microspheres 181
7.2.2.1 Initial Trials using the 'Conventional Method' 181
7.2.2.2 Revised particle preparation process named as 'Granular Method' 184
7.2.3 Compositional analysis 193
7.2.4 X-ray diffraction analysis 194
7.2.5 Thermal Analysis 195
7.2.6 Density, tap density and porosity measurements 197
7.2.7 Degradation studies 198
7.2.8 pH Measurement 199
7.2.9 *In vitro* bioactivity studies 200
7.2.9.1 XRD 200
7.2.9.2 SEM for *in vitro* bioactivity study 201
7.2.9.3 pH Measurements of SBF 204
7.2.9.4 Compositional analysis after *in vitro* bioactivity study 204
7.2.10 Improvement of sphericity 205

7.2.11 Optimisation of the Initial 'Conventional Method' 206
7.2.11.1 Compositional analysis of starting bulk glasses 207
7.2.11.2 Thermal analysis 208
7.2.11.3 Viscosity measurement 209
7.2.11.4 Flame length measurement 218
7.2.11.5 Trials of spheroidisation 218
7.2.11.5.1 Trials for borax content 45S5 glass 219
7.2.11.5.2 Trials for V_2O_5 content 45S5 glass 221
7.2.11.5.3 Trials for 45S5 glass alone 224
7.2.11.5.4 Further trials for 45S5 glass alone 225
7.2.11.5.4.1 XRD of porous 45S5 glass microsphere 228
7.2.11.5.4.2 Compositional analysis of porous 45S5 glass microsphere 229
7.3 Discussion 231
7.4 Summary 240
CHAPTER 8: CONCLUSIONS AND FUTURE WORK 241
8.1 Conclusions 241
8.2 Suggestions for future work 244
REFERENCES 247

ABSTRACT

There is a growing trend to develop bioactive materials with enhanced properties for use in biomedical applications especially for bone repair. Ideally, these materials would stimulate a beneficial tissue response, enhance new tissue formation. Microspheres are emerging as potential advanced materials and have been a significant focus of attention due to their advantageous properties over other particle geometries. For example, particles with spherical morphology can provide the advantage of uniformity in size and shape and are easier to deliver to the target tissue site due to their enhanced flow properties. Furthermore, microspheres can be implemented in defect areas more compactly if bimodal distribution of particle sizes are employed.

Initially, the focus of this project was on phosphate-based glasses (PBG's) and novel formulation development (and their characterisation). The second part of this work involved manufacture of both solid and more uniquely porous microspheres from all three glass families (i.e. phosphate, borate and silicate).

A series of PBG's were prepared and their physico-chemical and structural characteristics investigated. Varying formulations in the glass system of $40P_2O_5$-(24-x)MgO-(16+x)CaO-(20-y)Na_2O-yTiO_2 (where $0 \leq x \leq 22$ and y=0 or 1) were prepared via melt-quenching. The structure of the glasses was confirmed by X-ray diffraction (XRD), Fourier transform infrared (FTIR), micro Raman and solid-state nuclear magnetic resonance (NMR) spectroscopies. The thermal properties and the activation energy of crystallisation (E_c) were measured using thermal analysis and the Kissinger equation, respectively. For the bulk glass materials characterisation, the glass forming ability of the formulations investigated was seen to decrease with reducing MgO content down to 8 mol% and the glass stability region also decreased from 106 °C to 90 °C with decreasing MgO content. The activation energy of crystallisation (E_c) values also decreased from 248 (for 24 mol% MgO glass) to 229 kJ/mol (for the 8 mol% MgO content) with the replacement of MgO by CaO for glasses with no TiO_2. The formulations containing less than 8 mol% MgO without TiO_2 showed a strong tendency towards crystallisation. However, addition of 1 mol% TiO_2 in place

of Na_2O for these glasses with less than 8 mol% MgO content, inhibited their crystallisation tendency. Glasses containing 8 mol% MgO with 1 mol% TiO_2 revealed a 12 °C higher glass transition temperature, a 14 °C increase in glass stability against crystallisation and a 38 kJ/mol increase in E_c in comparison to their non TiO_2 containing counterpart. NMR spectroscopy revealed that all of the formulations contained almost equal percentages of Q^1 and Q^2 species. However, FTIR and Raman spectroscopies showed that the local structure of the glasses had been altered with addition of 1 mol% TiO_2, which acted as a network modifier, impeding crystallisation by increasing the cross-linking between phosphate chains and consequently leading to increased E_c as well as their glass forming ability. Degradation studies of phosphate based glass discs were performed in phosphate buffered saline (PBS) at 37 °C, where the 8 mol% MgO glass showed the highest mass loss of around 3.4% after 28 days of immersion. Cation and anion release studies were conducted via ion chromatography and inductively coupled plasma mass spectroscopy (ICP-MS), respectively, using ultra-pure (Milli-Q) water at 37 °C as the degradation medium. The largest release of Ca, Na and P ions was observed with the 8 mol% MgO glass. *In vitro* CaP formation studies were conducted using glass discs immersed in simulated body fluid (SBF) at 37 °C for up to 28 days. The amorphous phase and chemical composition of deposited calcium phosphate layers on the glass discs were confirmed via X-ray Diffraction (XRD) and energy-dispersive X-ray spectroscopy (EDX) analysis, respectively. CaP layers with Ca/P ratio 0.8 to 1.1 were found to be deposited on the lower MgO content (8 to 2 mol%) glass surface after 28 days of SBF study.

The microsphere development studies showed successful manufacture of both solid and highly porous phosphate, borate and bio-silicate glass microspheres with porosity levels up to 78% with a surface area of 0.4345 m^2/g and high levels of interconnectivity. Thermal, degradation, ion release and *in vitro* bioactivity study of microspheres were also conducted. Dissolution studies showed that the higher mass loss was observed for porous glass microspheres (PGMS) in comparison to their respective solid glass microspheres (SGMS) due to the higher surface area for PGMS. Other than phosphate glass microspheres, both solid and porous glass microspheres of borate and silicate glasses showed bioactivity in simulated body fluid. PGMS of

borate and silicate formed hydroxyapatite at earlier time point compared to their respective SGMS. Moreover, porous borate glass microspheres were fully converted into HA porous microspheres in phosphate solutions. However, only amorphous calcium phosphate (a precursor to HA) was found deposited on the surface of porous phosphate glass microspheres after 28 days of immersion in SBF.

ACKNOWLEDGMENTS

I would like to extend my utmost gratitude to my supervisors Dr Ifty Ahmed, Dr Andrew Parsons and Dr Nusrat Sharmin for their unconditional support, kindness and invaluable guidance throughout my PhD project.

Thank you to my friends and colleagues in Advanced Materials Research Group for the constant support and endless discussions; Dr Zakir Hossain, Dr Reda Felfel, Dr Uresha Patel, Dr Sumaya Kabir, Dr Fernando Barrera Betanzos, Dr Chenkai Zhu, Dr Menghao Chen, Caitriona McCarron, Ana Braz De Sousa, Ellena Cartlidge, Farah Nigar, Abul Ararat, Sabrin Abdus Samad, Dr Gabriel Choong, Dr Bryan Stuart, Dr Laura Macrì Pellizzeri, Nigel De Melo, Jesus Molinar Diaz, Benjamin Milborne, Lauren Murrell, Henry Forbes and Saira Bano are only to name a few.

I would like to acknowledge all the technical staff of the ITRC, Wolfson Building and nMRC for their guidance and technical assistance. I would especially like to name, Dr Nigel Neate, Dr Hannah Constantin, Tom Buss, Jason Greaves, Max Mason, Rory Screaton, Julie Thompson, John Kirk, Martin Roe and Elisabeth Steer. I would like to thank Dr Graham A. Rance for the help and support with Raman spectroscopy analyses. I would also like to thank Dr Jeremy J. Titman, Department of Chemistry for his kind help with the NMR analysis.

I am also grateful to the Dean of Engineering Research Scholarship for International Excellence provided by the Faculty of Engineering, University of Nottingham for funding my studentship.

Huge thanks also go to Anik, Sabrin, Shaquie, Mahabub, Mesbah, Kaafi vai, Sanchita apu, Adil vai, Sumaya, Touseef vai, Meem apu, Sakib vai, Faisal vai, Moyna vabi, Rabiul vai for their unconditional love, time and support during my PhD.

A very special thanks to my beloved wife Farah Nigar for her unconditional love, patience and understanding. I am grateful for her positivity and limitless smiles.

Finally, I will always be hugely indebted to my family and family-in-law, especially my mother and mother-in-law, father and father-in-law, my brothers and sisters, my beloved son Ahil and daughter Anaya.

LIST OF PUBLICATIONS

Journal articles

1. Abul Arafat, Sabrin Abdus Samad, **Md Towhidul Islam**, Andrew L. Lewis, Emma Barney and Ifty Ahmed, Effect of Y_2O_3 addition on the glass transition and crystallisation kinetics studies of phosphate based glasses. International Journal of Applied Glass Science, 2019 (***under review***).

2. **Md Towhidul Islam,** Nusrat Sharmin, Graham A. Rance, Jeremy J. Titman, Andrew J. Parsons, Kazi M. Zakir Hossain and Ifty Ahmed, The effect of MgO/TiO_2 on structural and crystallisation behaviour of near invert phosphate-based glasses. Journal of Biomedical Materials Research: Part B, 2019 *https://doi.org/10.1002/jbm.b.34421.*

3. **Md Towhidul Islam**, Kazi M. Zakir Hossain, Nusrat Sharmin, Andrew J. Parsons, Ifty Ahmed, Effect of magnesium content on bioactivity of near invert phosphate-based glasses. International Journal of Applied Glass Science. 2017;1–12.

4. **Md Towhidul Islam,** Reda M Felfel, Ensanya A Abou Neel, David M Grant, Ifty Ahmed and Kazi M Zakir Hossain, Bioactive calcium phosphate–based glasses and ceramics and their biomedical applications: A review. Journal of Tissue Engineering, 2017, 8: p. 1 –16.

.

Conferences

1. Laura Macri-Pellizzeri, Kazi M. Zakir Hossain, Nigel De Melo, **Md Towhidul Islam**, Caitriona McCarron, David Grant, Brigitte Scammell, Ifty Ahmed, Virginie Sottile. Biological characterization of phosphate-based glass microspheres for stem cell culture and differentiation. TERMIS – 26^{th} – 30^{th} June 2017. Davos, Switzerland (***Poster***).

2. **Md Towhidul Islam,** Kazi M. Zakir Hossain, Nusrat Sharmin, Uresha Patel, Andrew J. Parsons & Ifty Ahmed, The effect of Mgo/TiO_2 on crystallisation behaviour of phosphate based glasses. UKSB, June 20th – 21st 2017, Loughborough University, Loughborough (***Poster***).

3. Laura Macri-Pellizzeri, Kazi M. Zakir Hossain, **Md Towhidul Islam**, Caitriona McCarron, Nigel De Melo, David Grant, Brigitte Scammell, Ifty Ahmed, Virginie Sottile, Tailoring the stem cell environment through controlled ion release from degradable calcium phosphate-based glass microspheres. UKSB, June 20th – 21st 2017, Loughborough University, Loughborough (***Poster***).

4. Nusrat Sharmin, Chris Rudd, **Md Towhidul Islam**, Ifty Ahmed and Andrew Parsons, Effect of boron oxide addition on the cytocompatibility and fibre drawing ability of novel phosphate based glasses with 40 mol% P_2O_5 Content. UKSB, June 20th – 21st 2017, Loughborough University, Loughborough (***Poster***).

5. **Md Towhidul Islam**, Kazi M. Zakir Hossain, Nusrat Sharmin, Andrew J. Parsons and Ifty Ahmed, In vitro bioactivity and degradation studies of novel phosphate based glasses for biomedical applications, Society of Glass Technology Centenary Conference, 4–8 September 2016, The University of Sheffield, Sheffield, UK (***Poster***).

ABBREVIATIONS

ACP	Amorphous Calcium Phosphate
A-W	Apatite-Wollastonite
BET	Brunauer Emmet and Teller
BG	Bulk glass
BGs	Bioglasses
BO	Bridging oxygen
c.a.	Circa
3D	Three dimensional
DCPA	Dicalcium phosphate anhydrous
DCPD	Dicalcium phosphate dihydrate
DMEM	Dulbecco's Modified Eagle's Medium
DSC	Differential scanning calorimetry
EDX	Energy dispersive x-rays
FTIR	Fourier transform infrared
HA	Hydroxyapatite
HCA	Hydroxycarbonate apatite
HSM	Hot stage microscopy
HTV	High temperature viscometer
ICPMS	Inductively coupled plasma mass spectroscopy
IUPAC	International Union of Pure and Applied Chemistry
m-SBF	Modified-SBF
NBO	Non- bridging oxygen
NMR	Nuclear magnetic resonance
OCP	Octacalcium phosphate
PBG	Phosphate based glass
PBS	Phosphate buffered saline
PGMS	Porous glass microspheres
r-SBF	Revised-SBF
SBF	Simulated body fluid

SEM	Scanning electron microscope
SGMS	Solid glass microspheres
SSF	Simulated synovial fluid
T_c	Crystallisation temperature
T_g	Glass transition temperature
T_m	Melting temperature
TRIS	Tris(hydroxymethyl)aminomethane
VFT	Vogel–Fulcher–Tammann
XRD	X-Ray Diffraction
α-TCP	α-tricalcium phosphate
β-TCP	β-tricalcium phosphate
η	Viscosity
ρ	Density

LIST OF FIGURES

Figure 2.1: *Structure of silicate tetrahedra..... 6*

Figure 2.2: *Effect of alkali oxide concentration on the relative theoretical concentration of Q^n species in alkali silicate glasses. Modified from James E. Shelby [83].* *..... 7*

Figure 2.3: *Boroxol ring structures in vitreous boric oxide and alkali borate glasses [83].* *..... 9*

Figure 2.4: *Different structural units present in alkali borate glasses [85]. 10*

Figure 2.5*: The structure of PO_4^{3-} tetrahedron. 11*

Figure 2.6: *The four types of Q^n species found in condensed phosphates, where n is the number of bridging oxygens present within a particular phosphate tetrahedron.* *..... 12*

Figure 2.7: *Graphical representation of the relationship between the proportion of Q^0, Q^1, Q^2, Q^3 species in phosphate glass and the metal oxide concentration. Beyond 0.75 M_2O, orthophosphates only exist and the excess metal cations exist as unreacted metal oxide. Modified from M. Becke-Goehring [116]..... 13*

Figure 2.8: *Compositional diagram representing the bone-bonding properties of bioactive glasses [151,152]..... 17*

Figure 2.9: *Schematic illustration of the reaction mechanism of HCA formation on the surface of silicate based bioglass according to Hench and co-workers [13,154]..... 18*

Figure 2.10*: Schematic illustration of the mechanisms of conversion of a 45B5 borate (3B) glass and 45S5 silicate (0B) glass to HA in a dilute phosphate solution [28]..... 19*

Figure 2.11: *SEM images showing the reaction products for silicate (a) and borate 20*

Figure 2.12: *Schematic of ion adsorption on (a) positively charged, and (b)negatively charged Ti metal in SBF medium [165]..... 22*

Figure 2.13: *Examples of biomedical applications of CaP based materials [251]**.** 31*

Figure 2.14: *Examples of additive manufactured implants based on CaP; (a) 3D scaffolds of DCPA/monetite (scale bar: 5 mm) [256], (b) implant made of DCPA for*

treatment of cranial bone defects (Craniomosaic) [248]. DCPA is dicalcium phosphate. 33

Figure 2.15: *CaP nanoparticles for drug and gene delivery applications; (a) CaP nanorods paste containing DNA encoding from BMP-7 and VEGF-A for repairing bone defect [262], (b) multi-shell design of CaP nanoparticles loaded with antigen and TLR ligand [263]..... 34*

Figure 2.16: *(a) SEM images of 15CaO·10.63Li_2O·74.37B_2O_3 (wt%) glass microsphere (b) cross section of hollow HA microsphere formed by reacting glass microsphere in 40*

Figure 3.1: *Device set-up for the extraction of degradation media during the studies. Modified from Fernando Barrera-Betanzos [294]. 55*

Figure 4.1: *X-ray diffraction patterns for glasses in the system 40P_2O_5-(24-x)MgO-(16+x)CaO-(20-y)Na_2O- yTiO_2 (where 0≤x≤22 and y=0 or 1). Represents alpha-calcium pyrophosphate (α- $Ca_2P_2O_7$) (ICDD No. 00-009-0345). 62*

Figure 4.2: *Density of different glass formulations measured using the Archimedes method at room temperature. 63*

Figure 4.3: *Variation of molar volume (M.V) and oxygen density (O.D) as a function of CaO content: a) with no TiO_2 and b) with 1 mol% TiO_2 present..... 64*

Figure 4.4: *DSC curves of the glass compositions with reduced MgO content (from 24 to 2 mol%). 65*

Figure 4.5: *Images of 2 mol% MgO containing glass after casting to room temperature with a) no TiO_2 and b) 1 mol% TiO_2 content present. 67*

Figure 4.6: *Variation of the crystallisation peak as a function of different particle sizes (45-100, 125-200 and 350-500 µm) at 20 $^oC\ min^{-1}$ heating rate for M24T0 glass..... 67*

Figure 4.7: *Variation of the crystallisation peak as a function of different heating rates (10, 15 and 20 $^oC\ min^{-1}$) for M24T0 glass (particle size 45-100 µm). 68*

Figure 4.8: *The Plot of ln (β/T_C^2) vs $1/T_C$ for M24T0 glass (n=3). 69*

Figure 4.9: *a) FTIR spectra and b) mean Raman spectra (N=5) for the glasses in the system of $40P_2O_5$-(24-x)MgO-(16+x)CaO-(20-y)Na_2O-yTiO_2 (where 0≤x≤22 and y=0 or 1). Spectra were averaged from those collected at five different, random locations on the top surface of the glass, with minimal spectral variation indicating a high degree of homogeneity. 71*

Figure 4.10: *a) (i) Optical image, (ii) Raman spectroscopic map overlaid on optical image and (ii) Raman spectroscopic map, including intensity scale bar and b) the mean Raman spectrum extracted from all spectra collected within the mapped area for M8T1 glass..... 74*

Figure 4.11: *^{31}P NMR spectra for glasses in the system $40P_2O_5$-(24-x)MgO-(16+x)CaO-(20-y)Na_2O-yTiO_2 (where 0≤x≤22 and y=0 or 1)..... 75*

Figure 4.12: a) *Mass loss (%) and* ***b)*** *pH change as a function of immersion time (day) of the glass compositions investigated in PBS at 37 °C over 28-day duration. 77*

Figure 4.13: a) *Mass loss (%) and* ***b)*** *pH change as a function of immersion time (day) of the glass compositions investigated in Milli-Q water at 37 °C over 28 day duration. 79*

Figure 4.14: *Concentration of* ***a)*** *[Na],* ***b)*** *[Mg],* ***c)*** *[Ca],* ***d)*** *[P] and* ***e)*** *[Ti] measured via ICP-MS for the glass formulations investigated in ultra-pure-water during 28 days of immersion period. (Error bars are also included in the data above). The Inset on each graph shows the release rates of each element for the glass formulations investigated. 82*

Figure 4.15: *X-ray diffraction pattern for the glass formulations investigated with reduced MgO content after immersion in SBF for 28 days. 83*

Figure 4.16: *SEM images of the surface of the 6 glasses before (Day-0) and after immersion in SBF (day 7, 14 and 28). Scale bars of inset SEM images represent 5 µm. 84*

Figure 4.17: *SEM images of the surface of M24T0, M8T0 and M2T1 glasses before (Day-0) and after immersion in SBF (day-28). Scale bars of inset SEM images represent 5 µm. 85*

Figure 4.18: a-f) *EDX spectra of the six different glass formulations after 28 days of immersion in SBF, g) Ca/P ratio (atomic %) and h) Mg/P ratio (atomic %) of the glasses before and after 28 days of immersion in simulated body fluid obtained via energy dispersive X-ray spectroscopy analysis. 86*

Figure 4.19: *Ca/P atomic ratio of the glasses obtained over 28 days of immersion in SBF. 87*

Figure 4.20: *pH change for the six glasses as a function of immersion time (days) in SBF at 37 ^{o}C, over a period of 28 days**.** 88*

Figure 5.1: *SEM images of prepared A) SGMS B) PGMS (washed) of i) M24T0, ii) M8T0 and iii) M2T1 glass formulations investigated. 100*

Figure 5.2: *Cross-section of prepared porous microspheres of A) M24T0, B) M8T0 and C) M2T1 phosphate glass formulations investigated. 101*

Figure 5.3: *X-ray diffraction pattern for A) SGMS and B) PGMS (washed) of three PBG glass formulations investigated. ★ represents for calcium carbonate ($CaCO_3$) peaks. 102*

Figure 5.4: *Chemical composition for three different morphologies such as BG, SGMS and PGMS of M24T0, M8T0 and M2T1 glass formulations. 103*

Figure 5.5: *DSC curves for the glass particles, solid and porous glass microspheres of three different phosphate glasses. 104*

Figure 5.6: *Pore diameter against Log differential pore volume of porous M24T0, M8T0 and M2T1 glass microspheres. 107*

Figure 5.7: *A) Mass loss (%) and B) pH change as a function of immersion time (day) of the solid (represented as solid symbols) and porous (represented as porous symbols) glass microspheres investigated in mili-Q water at 37 ^{o}C over 28 day duration. 108*

Figure 5.8: *SEM images of degraded SGMS of A) M24T0, B) M8T0 and C) M2T1 glass formulations investigated after 28 days of immersion in milli-Q water. The inset SEM images show the changes in surface morphology at higher magnification (Scale bars of inset SEM images represent 50 and 5 µm). 110*

Figure 5.9: *SEM images of degraded PGMS of A) M24T0, B) M8T0 and C) M2T1 glass formulations investigated after 28 days of immersion in milli-Q water. The inset SEM images show the changes in surface morphology at higher magnification (Scale bars of inset SEM images represent 50 and 5 µm). 111*

Figure 5.10: *Concentration of A) [Na], B) [Ca], C) [Mg], D) [P] and E) [Ti] measured via ICP-MS for SGMS and PGMS of phosphate glasses investigated in ultra-pure-water during 28 days of immersion period. (Error bars are also included in the data above). The Inset on each graph shows the release rates of each element for the glass formulations investigated. 113*

Figure 5.11: *X-ray diffraction pattern A) solid and B) porous microspheres for the glass formulations investigated after 28 days of immersion in SBF. 114*

Figure 5.12: *SEM images of SGMS of A) M24T0, B) M8T0 and C) M2T1 glasses after 28 days of immersion in SBF. Highly degraded microspheres shown in red circle... 115*

Figure 5.13: *SEM images of PGMS of A) M24T0, B) M8T0 and C) M2T1 glasses after 28 days of immersion in SBF. 116*

Figure 5.14: *pH change as a function of immersion time (day) of the glass microspheres investigated in SBF at 37 °C over 28 day duration. 117*

Figure 5.15: *XRD spectra of crushed starting porous glass microspheres. ★ represents for calcium carbonate ($CaCO_3$) peaks and ✚ represents for alpha-calcium pyrophosphate (α-$Ca_2P_2O_7$) peaks. 121*

Figure 6.1: *SEM images for SGMS of A) 45B5, B) B53P4 and C) 1393B borate glass formulations investigated. 125*

Figure 6.2: *SEM images of unwashed PGMS of A) 45B5, B) B53P4 and C) 1393B obtained via flame spheroidisation. 127*

Figure 6.3: *SEM images from A-G displaying the effect of acid washing of the PGMS of 45B5 in different concentration of acetic acid for various time point. 129*

Figure 6.4: *SEM images displaying the effect of acid washing for the PGMS of A) 1393B and B) B53P4 in 0.1 M acetic acid for 2 mins. 130*

Figure 6.5: *SEM images from A-D displaying the effect of washing of the PGMS of 1393B in different media for 1 min. Microspheres degraded by acid wash shown in red circle. 132*

Figure 6.6: *Cross-section of PGMS for three different borate glass formulations investigated. (Scale bar represents 200 μm) 133*

Figure 6.7: *X-ray diffraction pattern for A) BG, B) SGMS and C) washed PGMS of three borate glass formulations investigated. ★ represents for calcium carbonate ($CaCO_3$) peaks and ✚ represents for sodium calcium phosphate ($Na_3Ca_6(PO4)_5$) peaks. 135*

Figure 6.8: *DSC curves of the BG, SGMS and PGMS of three different borate glasses. 136*

Figure 6.9: *Weight loss versus time in day during the conversion reaction of SGMS (represented as solid symbols) and PGMS (represented as open symbols) of three different borate glass in 0.02 M K_2HPO_4 solution at 37 ^oC..... 139*

Figure 6.10: *pH change as a function of immersion time (day) of the SGMS (represented as solid symbols) and PGMS (represented as open symbols) investigated in 0.02 M K_2HPO_4 solution at 37 °C over 21 day duration. 140*

Figure 6.11: *X-ray diffraction pattern for both i) SGMS and ii) PGMS of three borate glass formulations A) 45B5, B) B53P4 and C) 1393B during the conversion reaction of microspheres in 0.02 M K_2HPO_4 solution at 37 $^{\circ}C$ at various time point. XRD spectra for HA shown in each Figure for comparison. 141*

Figure 6.12: *SEM images of SGMS of three borate glass formulations A) 45B5, B) B53P4 and C) 1393B after conversion reaction of microspheres in 0.02 M K_2HPO_4 solution at 37 ^oC at day-21. ..... 143*

Figure 6.13: *SEM images of PGMS of three borate glass formulations A) 45B5, B) B53P4 and C) 1393B after conversion reaction of microspheres in 0.02 M K_2HPO_4 solution at 37 ^oC at day-21. ..... 144*

Figure 6.14: *Cross-section for SGMS of 45B5 borate glass at A) Day-0 (starting microspheres), B) Day-10 and C) Day-21 during the conversion reaction of microspheres in 0.02 M K_2HPO_4 solution at 37 ^oC and i and ii represent the EDX spectra for outer (shell) and inner (core) point of microspheres, respectively. 146*

Figure 6.15: *Cross-section for PGMS of 45B5 borate glass at A) Day-0 (starting microspheres), B) Day-10 and C) Day-21 during the conversion reaction of microspheres in 0.02 M K_2HPO_4 solution at 37 ^oC and i and ii represent the EDX spectra for outer (shell) and inner (core) point of microspheres, respectively. 147*

Figure 6.16: *Cross-section for SGMS of B53P4 borate glass at A) Day-0 (starting microspheres), B) Day-10 and C) Day-21 during the conversion reaction of microspheres in 0.02 M K_2HPO_4 solution at 37 ^oC and i and ii represent the EDX spectra for outer (shell) and inner (core) point of microspheres, respectively. 149*

Figure 6.17: *Cross-section for PGMS of B53P4 borate glass at A) Day-0 (starting microspheres), B) Day-10 and C) Day-21 during the conversion reaction of microspheres in 0.02 M K_2HPO_4 solution at 37 ^oC and i and ii represent the EDX spectra for outer (shell) and inner (core) point of microspheres, respectively. 150*

Figure 6.18: *Cross-section for SGMS of 1393B borate glass at A) Day-0 (before conversion), B) Day-10 and C) Day-21 during the conversion reaction of microspheres in 0.02 M K_2HPO_4 solution at 37 ^oC and i and ii represent the EDX spectra for outer (shell) and inner (core) point of microspheres, respectively. 152*

Figure 6.19: *Cross-section for PGMS of 1393B borate glass at A) Day-0 (before conversion), B) Day-10 and C) Day-21 during the conversion reaction of microspheres in 0.02 M K_2HPO_4 solution at 37 ^oC and i and ii represent the EDX spectra for outer (shell) and inner (core) point of microspheres, respectively. 153*

Figure 6.20: *Concentration of A) [B], B) [P], C) [Ca], D) [Na], E) [K] and F) [Mg] measured by ICP-MS for SGMS and PGMS of borate glasses investigated in dil. K_2HPO_4*

during 21 days of immersion period. (Error bars are also included in the data above) 155

Figure 6.21: *X-ray diffraction pattern for both SGMS and PGMS of A) B53P4 at day-1 and B) 1393B at day-28 during the conversion reaction of microspheres in 0.2 M K_2HPO_4 solution at 37 ^oC. XRD spectra for HA shown in each Figure for comparison. ★ represents for calcium carbonate ($CaCO_3$) peaks. 159*

Figure 6.22: *Weight loss versus time in day during the conversion reaction for PGMS of 1393B at two different concentrations (0.02 and 0.2 M) of Na_2HPO_4 solution at 37 ^oC. 160*

Figure 6.23: *X-ray diffraction pattern for PGMS of 1393B at day-28 during the conversion reaction of microspheres in 0.02 and 0.2 M Na_2HPO_4 solution at 37 ^oC. XRD spectra for HA shown for comparison. ★ represents for calcium carbonate ($CaCO_3$) peaks. 161*

Figure 6.24: *SEM images for PGMS of 1393B glass formulations after conversion reaction of microspheres in A) 0.02 M Na_2HPO_4 and B) 0.2 M Na_2HPO_4 solution at 37 ^oC at day-28. ..... 162*

Figure 6.25: *X-ray diffraction patterns for both i) SGMS and ii) PGMS of three borate glass formulations A) 45B5, B)B53P4 and C) 1393B during the immersion of microspheres in SBF at 37 °C at various time point. XRD spectra for HA shown in each Figure for comparison. 163*

Figure 6.26: *SEM images for SGMS of three borate glass formulations A) 45B5, B) B53P4 and C) 1393B after immersion in SBF at 37 ^oC at day-21..... 165*

Figure 6.27: *SEM images for PGMS of three borate glass formulations A) 45B5, B) B53P4 and C) 1393B after immersion in SBF at 37 ^oC at day-21..... 166*

Figure 6.28: *Concentration of A) [B], B) [P], C) [Ca], D) [Na], E) [K] and F) [Mg] measured by ICP-MS for SGMS and PGMS of borate glasses investigated in SBF during 21 days of immersion period. (Error bars are also included in the data above)..... 168*

Figure 6.29: *pH change as a function of immersion time (day) for the SGMS (represented as solid symbols) and PGMS (represented as open symbols) of three different borate glasses investigated in SBF at 37 ^{o}C over 21 days duration. 170*

Figure 7.1: *SEM images for SGMS of A) 45S5, B) S53P4 and C) 1393 bio-silicate glass formulations investigated. 181*

Figure 7.2: *Initial attempts to prepare porous A) 45S5, B) S53P4 and C) 1393 bio-silicate glass microspheres using $CaCO_3$ porogen via conventional method. 182*

Figure 7.3: *Trials exploring A) particles: $SrCO_3$ (1:3), B) particles: $SrCO_3$ (1:3) + Motor oil, C) particles: $SrCO_3$ (1:5), D) particles: $SrCO_3$ (1:5) + Motor oil and E) particles: $SrCO_3$ + $CaCO_3$ (1:5) to improve the yield and porosity for 1393 bio-silicate glass microspheres. 183*

Figure 7.4*: Schematic diagram of developed granular* ***Method 1*** *to prepare porous bio-silicate microspheres..... 184*

Figure 7.5: *Schematic diagram of developed granular* ***Method 2*** *to prepare porous bio-silicate microspheres..... 185*

Figure 7.6: *Initial trial to prepare porous 1393 bio-silicate glass microspheres using granular* ***method 1*** *via flame spheroidisation process. 186*

Figure 7.7: *Initial trial to prepare porous 1393 bio-silicate glass microspheres using granular* ***method 2*** *via flame spheroidisation process. 187*

Figure 7.8: *Further trial to confirm the reproducibility and to improve the yield and porosity of porous 1393 bio-silicate glass microspheres using granular* ***method 2*** *via flame spheroidisation process..... 188*

Figure 7.9: *SEM images for unwashed S53P4 bio-silicate glass microspheres..... 188*

Figure 7.10: *SEM images from A-C displaying the effect of acid washing of the PGMS of S53P4 in different concentration of acetic acid for various time point A) 1M 10 sec, B) 0.5 M 30 secs and C) 0.1 M 1 min. 190*

Figure 7.11: *Porous S53P4 bio-silicate glass microspheres using glass particles and porogen ratio of A) 1:1, B) 1:0.75 and C) 1:0.5 prepared via flame spheroidisation process..... 191*

Figure 7.12: *SEM images of porous 45S5 bio-silicate glass microspheres using granular* ***method 2*** *via flame spheroidisation process. 192*

Figure 7.13: *Cross-section of porous A) 45S5, B) S53P4 and C) 1393 bio-silicate glass microspheres. 193*

Figure 7.14: *X-ray diffraction pattern for A) BG, B) SGMS and C) PGMS (prepared via granular method) of three bio-silicate glass formulations investigated. ★ represents for nagelschmidtite ($7CaO\text{-}P_2O_5\text{-}2SiO_2$) peaks. 195*

Figure 7.15: *DSC curves for BG (represented as solid line), SGMS (represented as large broken line) and PGMS (represented as small broken line) of three different bio-silicate glasses, presented with three different colours such as blue for 45S5, green for S53P4 and red for 1393..... 196*

Figure 7.16: *Weight loss versus time in day during the degradation study of SGMS (represented as solid symbol) and PGMS (represented as open symbols) of three different bio-silicate glass in Milli-Q water at 37 ^oC..... 199*

Figure 7.17: *pH change as a function of immersion time (day) of the SGMS (represented as solid symbol) and PGMS (represented as open symbol) of three different bio-silicate glass in Milli-Q water at 37 ^oC..... 200*

Figure 7.18: *X-ray diffraction pattern for both i) SGMS and ii) PGMS of three bio-silicate glass formulations A) 45S5, B) S53P4 and C) 1393 during the immersion of microspheres in SBF at 37 ^oC at various time points. XRD spectra for HA shown in each Figure for comparison. 201*

Figure 7.19: *SEM images for SGMS of three bio-silicate glass formulations A) 45S5, B) S53P4 and C) 1393 after immersion in SBF at 37 ^oC at day-14. ..... 202*

Figure 7.20: *SEM images for PGMS of three bio-silicate glass formulations A) 45S5, B) S53P4 and C) 1393 after immersion in SBF at 37 ^oC at day-14. ..... 203*

Figure 7.21: *pH change as a function of immersion time (day) for the SGMS and PGMS of three different bio-silicate glasses investigated in SBF at 37 ^{o}C over 14 days duration. 204*

Figure 7.22: *A) SEM images and B) cross-sections of porous 1393 bio-silicate glass microspheres for smaller starting granular size range of 100-150 µm. 206*

Figure 7.23: *DSC curves for six different glass formulations investigated at 20 ^{o}C min^{-1} heating rate. 208*

Figure 7.24: *An example of snapshot images for sphere, hemisphere and flow based on height and width ratio and contact angle of material obtained by the software of Hot Stage Microscopy (HSM). 210*

Figure 7.25: *Percentage of sintering as a function of temperature for six different glass formulations investigated via Hot Stage Microscopy (HSM). 211*

Figure 7.26: *Temperature difference among flow, hemisphere and sphere point for six different glass formulations investigated via Hot Stage Microscopy (HSM). 212*

Figure 7.27: *Individual viscosity fitting curves for the six different glass formulations investigated using a fixed point viscosity method via Hot Stage Microscopy (HSM). 213*

Figure 7.28: *Combined fixed point viscosity curves for all six different glass formulations investigated via Hot Stage Microscopy (HSM). 213*

Figure 7.29: *Viscosity fitting curves for six different glass formulations investigated via high temperature viscometer. 215*

Figure 7.30: *Viscosity curves for six different glass formulations investigated via high temperature viscometer. 215*

Figure 7.31*: Published viscosity curves for P40 glass [346]. 217*

Figure 7.32: *Published viscosity curves for 45S5 and 1393 glass [347]. 217*

Figure 7.33: *Flame lengths for A) 2:2, B) 2.5:2.5 and C) 3:3 gas flow rate ratio. 218*

Figure 7.34: *SEM images of A) unwashed B) washed and C) cross-sections of 45S5 +* ***2 mol % borax*** *microspheres. 220*

Figure 7.35: *SEM images of A) unwashed B) washed and C) cross-sections of 45S5 +* ***5 mol % Borax*** *microspheres. 221*

Figure 7.36: *SEM images of A) unwashed B) washed and C) cross-sections of 45S5 +* ***2 mol % V_2O_5*** *microspheres. 222*

Figure 7.37: *SEM images of A) unwashed B) washed and C) cross-sections of 45S5 +* ***5 mol % V_2O_5*** *microspheres. 223*

Figure 7.38: *SEM images of A) unwashed B) washed and C) cross-sections of 45S5 microspheres using 3:3 gas flow rate ratio for 63-125 µm starting glass particles. 225*

Figure 7.39: *SEM images of A) washed and B) cross-sections of porous 45S5 microspheres using 3:3 gas flow rate ratio for 63-71 µm starting glass particles. . 226*

Figure 7.40: *SEM images for porous 45S5 microspheres (washed) using A) 3.5:3.5, B) 4:4 and C) 4.5:4.5 gas flow rate ratio for 63-125 µm starting glass particles. 227*

Figure 7.41: *Cross-sections for 45S5 PGMS using A) 3.5:3.5, B) 4:4 and C) 4.5:4.5 gas flow rate ratio for 63-125 µm starting glass particles. 228*

Figure 7.42: *X-ray diffraction pattern for porous 45S5 glass microspheres for different starting particle size (i.e. 63-71 µm and 63-125 µm) and different gas flow rate ratios (i.e. 3:3, 3.5:3.5, 4:4 and 4.5:4.5). 229*

Figure 7.43: *Schematic diagram of proposed model including all of the parameters influencing to prepare porous bio-silicate microspheres. 236*

Figure 8.1: *SEM images of porous microspheres trialled with the A) Apatite-Wollastonite (AW), B) Recycle glass, C) Magnetite and D) TiO_2. ..... 246*

LIST OF TABLES

Table 2.1: *Parameters and test protocols that have been used to investigate the bioactivity of various biomaterials. 26*

Table 2.2: *Ionic concentration in human blood plasma in comprasion with various 28*

Table 3.1: *Glass codes, compositions and melting temperatures used in the glass system $40P_2O_5$-(24-x)MgO-(16+x)CaO-(20-y)Na_2O-yTiO_2 (where $0 \leq x \leq 22$ and y=0 or 1). 44*

Table 3.2: *Compositions of three different borate glasses investigated. 45*

Table 3.3: *Compositions of three different bio-silicate glasses. 46*

Table 4.1: *Expected and obtained chemical compositions from EDX analysis of the different phosphate glass formulations investigated. 61*

Table 4.2: *Glass transition (T_g), onset of crystallisation (T_x), glass stability (ΔT), crystallisation peak (T_c) and melting temperature (T_m) for six different glass formulations, using a 10 $^oC\ min^{-1}$ heating rate. 66*

Table 4.3: *Crystallisation peak temperature at different heating rates, activation energy of crystallisation and JMA exponent for the glasses. 69*

Table 4.4: *Proposed assignment of IR and Raman bands in the vibrational spectra of phosphate glasses in the series of $40P_2O_5$-(24-x)MgO-(16+x)CaO-(20-y)Na_2O-yTiO_2 (where $0 \leq x \leq 22$ and y=0 or 1). Bands are quoted in units of cm^{-1}. BO = bridging oxygen; NBO = non-bridging oxygen. 73*

Table 4.5: *NMR peak positions and relative proportions of Q^1 and Q^2 species in the various glasses. 76*

Table 5.1: *Composition (in mol%) of selected three different phosphate glass formulations for microspheres preparation. 99*

Table 5.2: *Glass transition (T_g), onset crystallisation (T_x), crystallisation (T_c) and melting temperature (T_m) for BG, SGMS and PGMS of three different glass formulation investigated, using a 20 $^oC\ min^{-1}$ heating rate. 105*

Table 5.3: *Density, porosity and surface area of solid and porous microspheres of three different phosphate based glasses investigated. 106*

Table 5.4: *Ca/P (atomic ratio) of SGMS and PGMS for three glasses before and after 28 days of immersion in SBF. 117*

Table 6.1: *Expected and obtained chemical compositions from ICP-MS analysis of three different borate glass formulations investigated. 125*

Table 6.2: *Compositional analysis of SGMS and PGMS of borate glasses via ICP-MS 134*

Table 6.3: *Glass transition (T_g), onset of crystallisation (T_x), glass stability (ΔT), crystallisation peak (T_c) and melting temperature (T_m) for BG, SGMS and PGMS of different borate glass formulations, using a 20 $^oC\ min^{-1}$ heating rate..... 137*

Table 6.4: *Density, tap density and porosity of SGMS and PGMS of three different borate glasses investigated..... 138*

Table 6.5: *Compositional analysis for SGMS and PGMS of borate glasses after conversion in dil. K_2HPO_4 at day 21. ..... 158*

Table 6.6: *Compositional analysis for SGMS and PGMS of borate glasses after immersion in SBF at day 21. ..... 171*

Table 7.1: *Expected and actual chemical compositions obtained via EDX analysis for bulk glass (BG), SGMS and PGMS of three different bio-silicate glass formulations investigated. 194*

Table 7.2: *Glass transition (T_g), onset of crystallisation (T_x), glass stability (ΔT), crystallisation peak (T_c) and melting temperature (T_m) for BG, SGMS and PGMS of different bio-silicate glass formulations, using a 20 $^oC\ min^{-1}$ heating rate..... 197*

Table 7.3: *Density, tap density and porosity of SGMS and PGMS of three different bio-silicate glasses investigated. 198*

Table 7.4: *Compositional analysis for SGMS and PGMS of three bio-silicate glasses after immersion in SBF at day 14. ..... 205*

Table 7.5: *Compositional analysis for six different types of glass formulations via EDX analysis. 207*

Table 7.6: *Glass transition (T_g), onset of crystallisation (T_x), glass stability (ΔT), crystallisation peak (T_c) and melting temperature (T_m) for six different glass formulations, using a 20 $^oC\ min^{-1}$ heating rate. 209*

Table 7.7: *Rate of viscosity change between two points (i.e. flow and sphere or flow and hemisphere) for six different types of glass formulations investigated. 214*

Table 7.8: *Rate of viscosity change between two points (i.e. flow and sphere or flow and hemisphere) for different types of glass formulations investigated. 216*

Table 7.9: *Chemical compositions for starting 45S5 bulk glass and 45S5 PGMS for different starting particle size (i.e. 63-71 µm and 63-125 µm) and different gas flow rate ratios (i.e. 3:3, 3.5:3.5, 4:4 and 4.5:4.5) obtained via EDX analysis. 230*

Table 7.10: *Parameters involved to prepare porous bio-silicate glass microspheres. 237*

CHAPTER 1

INTRODUCTION

1.1 Overview

There is a high need for smart off-the shelf materials that are capable of conforming to the shape of tissues being replaced, modulating cellular function and promoting tissue regeneration. These materials could potentially provide morphological [1-3] or biochemical cues [4,5] that guide cellular interaction which is essential for tissue regeneration. Examples of these smart materials include bioactive glasses and ceramics that undergo specific surface reactions when incubated in simulated body fluid (SBF) [6] or implanted in animal or human body [7] leading to the formation of hydroxyapatite (HA) layer that forms a strong bond with the host tissues. They are osteoconductive and have osteogenic ion release properties, therefore have attracted much interest for bone tissue engineering [8]. They can be also used for soft tissue regeneration [9] and drug delivery applications [10].

Silicate-based bioactive glass, 45S5 with a composition of 45% SiO_2, 24.5% Na_2O, 24.5% CaO, and 6% P_2O_5 (by weight) referred to as Bioglass, was first developed by Prof. Larry Hench [11] for bone repair applications [12,13]. Later other types of silicate-based glasses and glass-ceramics were developed which also had the ability to bond to bone tissue and enhance bone formation [12-21].

Some borate glasses have also been explored very recently for potential biomedical applications such as for rheumatoid arthritis treatments, controlled drug release delivery, wound healing, bone repair application [22-26]. Borate-based glasses have also been shown to undergo more rapid degradation and conversion to hydroxyapatite in comparison to silicate-based glasses [23,27-31]. The excess release of boron can be toxic, [32], however, numerous *in vivo* studies have shown that these glasses were able to regrow bone with no toxicity [33-35].

Phosphate-based glasses (PBGs) have attracted a lot of interest in the field of biomaterials and tissue engineering due to their controllable degradation profiles and chemical similarity with the inorganic component of natural bone [36-38]. PBGs with

various modifying oxides such as CuO (Cu for angiogenesis and antimicrobial activity) [39], ZnO (Zn for osteogenesis, anti-inflammatory and antimicrobial activity) [40], Ag_2O (Ag for antimicrobial activity) [41], Fe_2O_3 (Fe for osteogenesis) [42], TiO_2 (Ti for increasing glass stability) [43], SrO (Sr for osteogenesis and inhibiting osteoclast) [44], have been extensively investigated to provide added fuctionality for biomedical and tissue engineering applications [45]. For example, the addition of CaO has been reported to improve the bioactivity of these glasses and to enhance haemostatic activity [46-49].

Bioactive glasses are amorphous and can be prepared either by melt-quench or sol-gel process [50]. The sol-gel technology allows for incorporation of biomolecules, proteins or drugs that can be delivered *in-situ* [51,52]. Generally, these glasses can be tailored to release metallic ions that have antimicrobial [53,54] or angiogenic potentials [55,56]. They can also be prepared as solid or nano-/micro-/macro-porous scaffolds [57] with highly ordered, controlled pore size and pores interconnectivity [58]. The porous configuration is necessary for cell migration, angiogenesis and tissue infiltration; this further enhances the bond to the host tissues [59]. Functionalisation of the scaffold with amino or carboxylic groups [60] or loading anti-osteoporotic drugs (e.g. ipriflavone) [61] could also be achieved to further improve bone regeneration.

Microspheres have some key advantages for use in biomedical applications over other particle geometries; for example, delivery of the microspheres to the specific target site, can be improved significantly, especially via injection procedures, due to their spherical sizes and shapes and if bimodal size distributions are employed. The microspheres also retain a larger surface area which can allow for sufficient increases in degradation rate and increases in therapeutic ion release. Moreover, in some cases they can also be engineered to be porous or hollow to allow for encapsulation of other biomedically relevant entities [62-65].

Microspheres have been explored for various biomedical applications such as cancer radiotherapy and thermotherapy, drug and protein delivery, and bone filler materials [66-70]. For example, Yttrium doped microspheres have been used as internal brachytherapeutic tools to combat hepatic malignancies in the field of oncology [71-73]. Prof Day's research group has investigated the production of glass microspheres with

particle size ranges of 20–30 µm containing 89Y isotopes that convert into 90Y by neutron bombardment for treatment of liver tumours through intra-arterial radiotherapy [74-76].

Porous microspheres can be fabricated with either external or internal porosity, or even a combination of both, as well as with or without interconnectivity for cell attachment and spreading over the available surface area [77]. Microspheres containing tailored porosity exhibit greater surface area, lower mass density, superior cell attachment, cell proliferation, drug absorption and drug release kinetics compared to solid glass microspheres [63]. In addition, these microspheres can be fabricated as stand-alone products or assembled into three-dimensional (3D) porous scaffolds [63,65,78]. Specific applications have been designated for porous microspheres based on the composition of these materials as well as the pore structures (e.g. level of porosity, pore size, surface area, interconnectivity, etc.). Microspheres can be prepared [79] using different techniques such as flame spheroidisation [80], laser [81] and thermally induced phase separation and/or oil-in water processing [82].

1.2 Aims and Objectives

The main aim of this project was to develop novel phosphate-based glass (PBG) formulations which could release therapeutic ions in a controlled manner, particularly for repair and regeneration of bone for the prevention of fragility fractures. This project also aimed to investigate manufacture of both solid and porous PBG's microspheres for bone tissue repair applications. After successful manufacture of PBG's microspheres, three bio-silicate glasses (i.e. 45S5, S53P4 and 1393) and three different types of borate glasses (i.e. 45B5, B53P4 and 1393B which were derived from 45S5, S53P4 and 1393 silicate glasses, respectively by fully replacing the SiO_2 with B_2O_3) were also investigated for manufacture of microspheres (both solid and porous) suitable for use in biomedical applications, with a particular focus on minimally invasive injectable prophylactic, bone treatment options.

The work included the following specific objectives:

- Characterisation of the PBG compositions developed in terms of structural and crystallisation behaviour, thermal, density, degradation, ion release and *in vitro* bioactivity studies.

- Selection of appropriate PBG compositions based on degradation, ion release and *in vitro* bioactivity studies for manufacture of solid and porous glass microspheres.

- Characterisation of PBG glass microspheres (both solid and porous) in terms of thermal, density, porosity, surface area, degradation, ion release and *in vitro* bioactivity studies.

- Manufacture and characterisation of three different borate glass microspheres (both solid and porous) (i.e. 45B5, B53P4, 1393B).

- Production and characterisation of microspheres (both solid and porous) from the three different bio-silicate glasses (i.e. 45S5, S53P4, 1393)

1.3 Thesis Outline

The outcomes of the aims and objectives have been divided into several chapters as outlined below:

Chapter 2: reviews the literature relating to common group of biomaterials such as bioactive glasses (i.e. phosphate, borate and silicate glasses), ceramics and glass ceramics used for different biomedical applications (i.e. dental applications, bone repair, bioactive coatings, drug and gene delivery, soft tissue engineering). Reviews the details mechanism of apatite formation on bioactive materials for *in vitro* study. The literature on solid and porous glass microspheres was also considered.

Chapter 3: Presents the materials and methods used throughout this thesis.

Chapter 4: Discuss the effect of MgO/TiO_2 on the structural and crystallisation behaviour of near invert phosphate based glasses ($40P_2O_5$-(24-x)MgO-(16+x)CaO-

(20-y)Na_2O-yTiO_2 (where 0≤x≤22 and y=0 or 1)). Degradation, ion release and *in vitro* bioactivity studies were also discussed.

Chapter 5: Select optimum PBG compositions based on degradation, ion release and *in vitro* bioactivity studies described in Chapter 4 to prepare solid and porous glass microspheres. A comparative studies between solid and porous glass microspheres on physical, thermal, degradation, ion release and *in vitro* bioactivity of optimised three PBG formulations in $40P_2O_5$-(24-x)MgO-(16+x)CaO-(20-y)Na_2O-yTiO_2 (where 0≤x≤22 and y=0 or 1) system was discussed.

Chapter 6: Prepare both solid and porous glass microspheres of three different types of borate glasses (i.e. 45B5, B53P4 and 1393B) which were derived from 45S5, S53P4 and 1393 silicate glasses, respectively by fully replacing the SiO_2 with B_2O_3 and comprehensively characterise the conversion of these three borate glasses to HA. In addition, a comparative analysis between solid and porous glass microspheres on physical, thermal, conversion of borate glass into HA in phosphate solution, ion release and *in vitro* bioactivity were also discussed.

Chapter 7: Prepare both solid and porous glass microspheres of three bio-silicate glasses (i.e. 45S5, S53P4 and 1393) via our flame spheroidisation process. Moreover, a comparative analysis between solid and porous glass microspheres on thermal, degradation and *in vitro* bioactivity were also discussed.

Chapter 8: Summarises the findings of all the work in this thesis and puts forward areas of future work.

CHAPTER 2

LITERATURE REVIEW

2.1 Silicate-based glasses

Vitreous silica is composed of a three dimensional network of SiO_4 tetrahedral units (**Figure 2.1**), where all four oxygens are shared. This SiO_4 tetrahedral unit is connected with four others via bridging oxygen bonds to form a continuous, 3-dimensional network giving the stoichiometry of $SiO_{4/2}$ or SiO_2, which is charge balanced (assuming a charge of 2- on the oxygen as silicon has a charge of 4+). Pure vitreous silica (or fused quartz) is thermally and chemically stable.

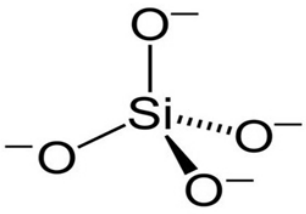


Figure 2.1: *Structure of silicate tetrahedra.*

Silicate glasses are mainly based on SiO_2 (the glass network former); other modifying oxides are also included as Na_2O, CaO and P_2O_5 to adjust the properties of the produced glass. These oxides are usually included in specific molar ratios to produce a biologically active glass. Moreover, the addition of modifying oxide (i.e. alkali or alkaline earth oxides) to silica helps to reduce the viscosity of the melt and the glass transformation temperatures. However, the densities and thermal expansion coefficients of the glasses increases with increasing amount of modifying oxides. The additions of modifier oxides depolymerise the silicate structure by breaking the Si-O-Si linkage and forming Si-O- terminations. The oxygen in Si-O-Si linkage is known as bridging oxygen (BO) and the oxygen in Si-O- is known as non- bridging oxygen (NBO). The increase in non-bridging oxygens and decrease in bridging oxygens is directly proportional to the amount of modifier oxides added. A common way to describe the SiO_4 tetrahedral is using the Q^n terminology, where n represents the number of bridging oxygens per tetrahedron and varies from 0 to 4 for silicate based glasses. A tetrahedron with fully connected with four bridging oxygens is termed as Q^4 species,

whereas a tetrahedron with no bridging oxygen is termed as Q^0 species and Q^3, Q^2 and Q^1 species contain 3, 2 and 1 bridging oxygen, respectively [83-85]. The effect of modifier concentration on silicate structure is presented in **Figure 2.2**[83].

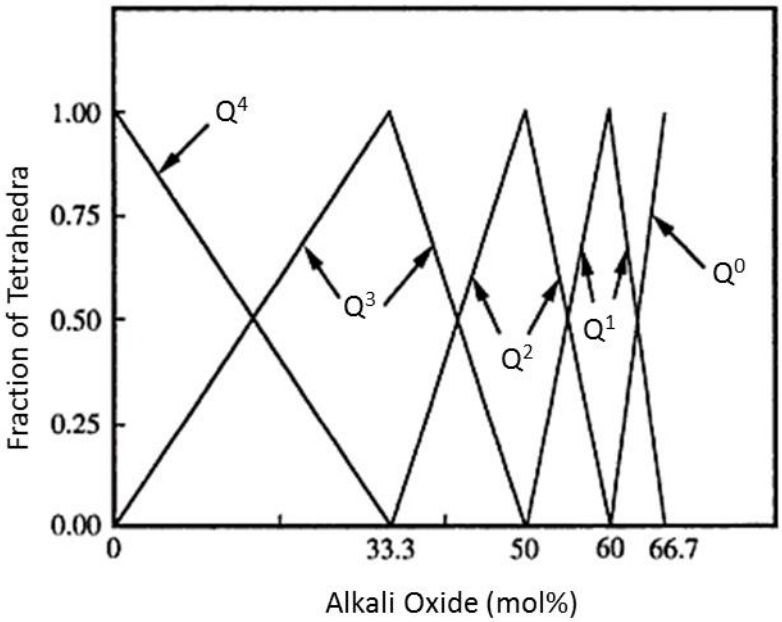


Figure 2.2: *Effect of alkali oxide concentration on the relative theoretical concentration of Q^n species in alkali silicate glasses. Modified from James E. Shelby* [83].

To improve the bioactivity of silicate glasses, three important compositional features, including (i) SiO_2 content <60mol%, (ii) high Na_2O and CaO content, (iii) high CaO/P_2O_5 ratio [59], must be fulfilled. During the glass preparation, a spontaneous crystallisation is undesirable as it reduces the rate of HA formation on its surface [86]. The rate of HA layer formation is highly dependent on the glass' degradation. Accordingly, the presence of Na_2O and other alkali or alkaline earth metals increases the rate of HA layer formation. The presence of high silica content or multivalent ions e.g. boron and aluminium reduces the rate of glass breakdown and hence the apatite layer formation rate [87]. Due to their texture (pore size/volume and high surface area), sol-gel produced glasses showed higher bioactivity than the melt-quenched counterparts [50]. Furthermore, using the sol-gel technique, the silica content can be increased from 60 mol% in melt-quenched to 85 mol% in sol-gel without reducing the bioactivity [88].

A family of silicate-based glasses have been used for dental and orthopaedic applications [89] since 1960s under the commercial name of 45S5 Bioglass®. This

formulation has been used as a benchmark for measuring the properties of new silicate glass compositions. When doped with boron, 45S5 Bioglass™ showed angiogenic potential caused by their ionic dissolution products [56,90]. Boron [91,92] and silver [53] also induced antibacterial action to bioactive silicate glasses.

Silicate-based glasses, however, require high melting temperature during their manufacture, and the addition of various metal oxides to reduce the melting temperature could adversely affect the glass bioactivity. The compositional range and form of this glass is also limited. The degradation of this glass often takes 1-2 years to totally degrade [50] and the long term effect of silica is still questionable [93]. Fabrication of fibrous scaffold from this glass is also difficult. The search for new bioactive materials that could overcome the limitations of silicate-based glasses has led to the emergence of borate and phosphate-based glasses as alternatives. These glasses can be easily formed without significant crystallisation during their preparation.

2.2 Borate-based glasses

Borate glasses are based on a B_2O_3 network. B_2O_3 is one of the most important glass forming oxides and has been used in various kinds of glass systems in order to achieve the desired physical and chemical properties [28,94,95]. Boron oxide can occur in both triangular and tetrahedral coordination [83,85]. For example, in the compound $Na_2O{\cdot}4B_2O_3$ there are two boron atoms in tetrahedral coordination, six boron atoms in triangular coordination, and all oxygen atoms are bridging [96]. However, the vitreous boric oxide can occur only in triangular coordination where three boron-oxygen triangles are joined to form boroxol rings in hexagonal arrangement of six B-O bonds (**Figure 2.3**).

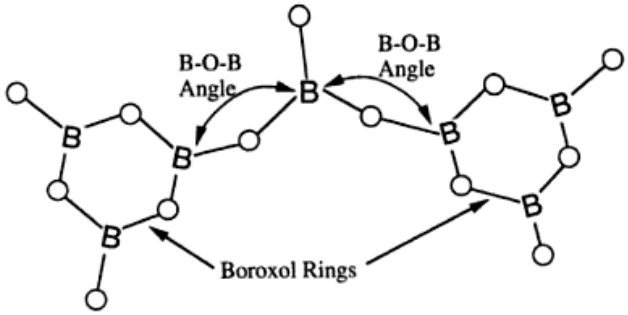


Figure 2.3: *Boroxol ring structures in vitreous boric oxide and alkali borate glasses* [83].

The structure of boric oxide changes from triangular to tetrahedral coordination, with no NBO formation by the addition of alkali oxides [83,85]. Therefore, the primary building blocks in all borate glasses are [$BO_{3/2}$] unit where B has 6 electrons in its outermost orbit and can accept 2 more electrons in the form of a dative bond. Moreover, alkali borate glasses contain a number of other intermediate structural groups along with the boroxol rings found for vitreous boric oxide, which is presented in **Figure 2.4**. The relative concentrations of these groups are functions of the overall glass composition [83,85].

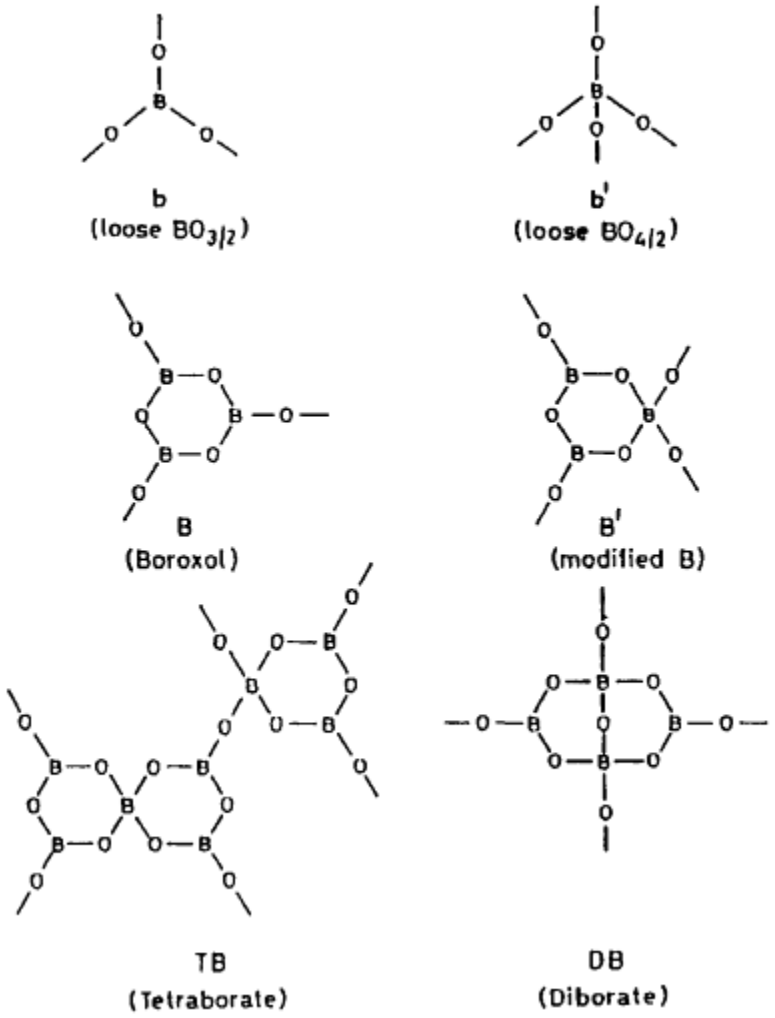


Figure 2.4: *Different structural units present in alkali borate glasses [85].*

However, the conversion of boron from triangular to tetrahedral coordination only occurs until the network reaches the critical concentration of tetrahedrally coordinated boron. Further addition of alkali oxides beyond this point would cause the formation of NBOs, which results in a reversal in property /composition trend. This behaviour of borate glasses is termed as 'borate anomaly' [83,85].

Using borate (BO_3^{3-}) in the glass network provides faster degrading glasses with rapid and complete conversion into HA than silicate-based glasses [8]. Controlling the boron content tailors the degradation rate of these glasses [97]. Boron has also beneficial action on bone remodelling and repair [98]. Furthermore, the presence of boron may reduce the possibility of bacterial infection through its antimicrobial action [92]. An

example of borate-based glasses is D-AlK-B (double alkali borate) glass, based on $Na_2O–K_2O–MgO–CaO–SiO_2–P_2O_5–B_2O_3$ system [99].

These glasses supported *in vitro* human mesenchymal stem cells proliferation [25] and *in vivo* tissue formation [100]; they could also be used as drug delivery vehicles [101]. However, the main concern with these glasses is their potential toxicity [8]. The degradation products of certain concentration produced an inhibitory effect on the growth of goat bone marrow stromal cells. Adjusting the pH of the glass extract and reducing the concentration of boron to be less than 2.96 mM were observed to stimulate the cell proliferation. Adjusting the boron content to get a reasonable cellular response may jeopardise the bioactivity of these glasses [99]. The toxicity could also be reduced by dynamic culture conditions [102].

2.3 Phosphate-based glasses

This class of glasses is based mainly on P_2O_5 (the glass network former), Na_2O and CaO. Other modifying oxides e.g. CuO [54], ZnO [103], Ag_2O [104], Fe_2O_3 [105], TiO_2 [106], SrO [107] can also be included to induce a specific property, function or different biological response [108-110]. Unlike silicate glasses, the phosphate tetrahedral has one terminal oxygen; this reduces the network connectivity and hence the rigidity but increases the compositional range of the produced glasses [111].

The structure of PBGs is composed of PO_4^{3-} tetrahedral units which are the main building block as shown in **Figure 2.5**.

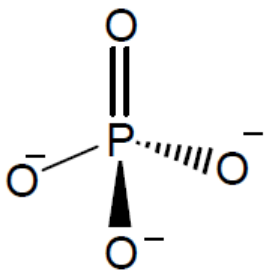


Figure 2.5: *The structure of PO_4^{3-} tetrahedron.*

The tetrahedra can be described in terms of Q^n terminology, where *n* represents the number of bridging oxygens (BOs) per PO_4^{3-} tetrahedron as shown in **Figure 2.6**. The networks of phosphate glasses can be classified by the oxygen to phosphorus ratio (O/P), which sets the number of tetrahedral linkages, through bridging oxygens, between neighbouring PO_4^{3-} tetrahedral [112]. In vitreous P_2O_5 each tetrahedral unit is connected with three others via bridging oxygen and the fourth oxygen of each tetrahedral unit is double bonded and referred to as a terminal oxygen [113]. When the oxygen of phosphate units bonds with network modifier (i.e. Na, Ca) referred to as a non-bridging oxygen (NBO). Phosphate tetrahedra with three bridging oxygens (BOs) are referred to as Q^3 species where the fraction O/P = 2.5. Addition of modifying oxides, such as CaO, disrupts the phosphate network and increases the O/P ratio. As the O/P ratio increases from 2.5 to 4 the phosphate structural group goes from Q^3 to Q^0, where Q^0 represents isolated PO_4^{3-} units with four NBOs [114]. PBGs with smaller phosphate units can crystallise easily as compared to glasses with longer phosphate chains as the entangled chains of the long chain phosphate glasses increase the viscosity of melt and impede crystallisation [115].

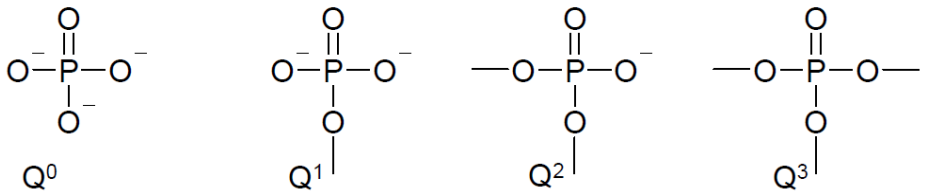


Figure 2.6: *The four types of Q^n species found in condensed phosphates, where n is the number of bridging oxygens present within a particular phosphate tetrahedron.*

The percentages of Q species of any glass depends on the amount of metal oxide (MeO) added as shown in **Figure 2.7** [116]. As the ratio MeO/P_2O_5 increases from 0 to 3 (0,1,2,3) the phosphate structural groups passes from Q^3 to Q^0 [117], respectively.

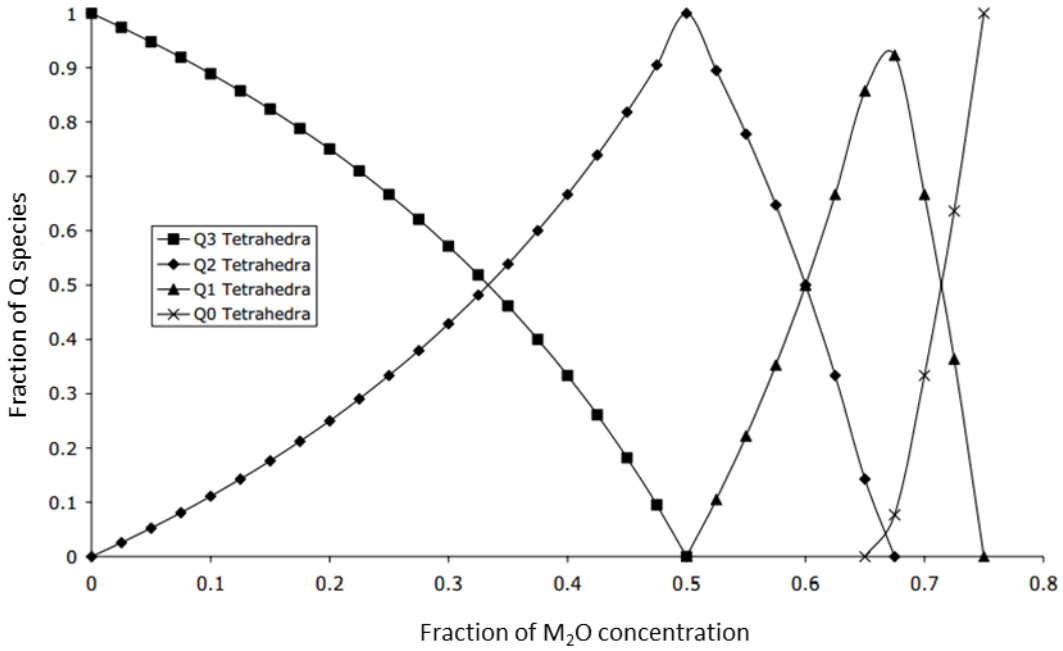


Figure 2.7: *Graphical representation of the relationship between the proportion of Q^0, Q^1, Q^2, Q^3 species in phosphate glass and the metal oxide concentration. Beyond 0.75 M_2O, orthophosphates only exist and the excess metal cations exist as unreacted metal oxide. Modified from M. Becke-Goehring* [116].

Unlike vitreous silica, P_2O_5 is chemically unstable; addition of metal oxides improves its stability [118]. The degradation of these glasses varies from hours to years according to the composition and intended applications.

These glasses can be prepared in different forms including discs [119-121], microtubes [122], microspheres [80,123] and fibres [105,110,124]. Fibres can be used as cell transportation and expansion device [123], nerve conduit [125] or as a scaffold for muscle regeneration [9]. Fibres with antibacterial properties (e.g. copper-containing) can be produced as wound dressing meshes for the treatment of leg ulcers and severe burns [54]. The phosphate glass fibres has an intriguing ability to form microtubes; therefore, they can be incorporated within various polymers to help in diffusion of nutrients and ingrowth of vascularisation when used as scaffolds for soft and hard tissue regeneration [126].

Phosphate glass microspheres were also prepared [79] for radiotherapy [127] applications. The morphology of microspheres provide a stable surface for cells to attach and proliferate [80] and prevent tissue damage and haemorrhage when used for radiotherapy [127]. The spherical morphology would provide large interstitial spaces that can be consistent and quantifiable for cells growth and proliferation than randomly shaped particles when packed into a perfusion bioreactors [80].

2.4 Ceramics

Another class of bioactive materials include CaP-based ceramics (i.e. crystalline materials) e.g. HA, β-tricalcium phosphate (β-TCP) and biphasic calcium phosphate (a mixture of HA and β-TCP).

HA can be produced as solid or porous materials. The porous configuration with pores <10 µm in diameter is essential for circulation of body fluids and those >100 µm are essential for colonisation of target cells [59]. HA is normally sintered above 1000 °C in a granular or block form; after sintering it cannot be reshaped (if they are present in block form) to fit the defect and it is non-degradable. β-TCP, however, is degradable. The degradation of biphasic calcium phosphate is highly dependent on the ratio of its components; the higher the β-TCP content; the faster the degradation. Generally the degradation of CaP ceramics varies according to their type, porosity, surface area (granular vs blocks), and degree of crystallinity (high crystallinity means low degradation) [128].

Injectable CaP ceramics are also available. They can be easily delivered through a minimally invasive method into the defect as aqueous-based paste. They then set, fill the defect and support tissue regeneration over time [129]. This allows for their use as drug delivery vehicle [130] or treating a defect in challenging areas e.g. craniofacial complex [128] or vertebroplasty [131]. Examples of CaP ceramics that are commercially available include Norian® (Synthes Craniomaxillofacial, USA), BoneSource® (Stryker Leibinger, Germany), and Mimix® (Walter Lorenz Surgical, USA) [128].

2.5 Glass-ceramic materials

Glass-ceramics are partially crystallised glasses that produced by heating the parent glass above its crystallisation temperature [132]. Unlike spontaneous surface crystallisation, which is undesirable during glass manufacturing, the crystallisation process is controlled. As a result, the produced glass-ceramics contain one or more crystalline phases embedded in a residual glassy phase [133]. The bioactivity of glass-ceramics is highly dependent on proportion and type of crystals formed during crystallisation process [134]. Controlled crystallisation yields dense, strong materials with unusual combinations of properties when compared with their parent glasses [135]. It is also possible to design glass-ceramics with nano- or micro-structure according to the end application [133].

A common example of glass-ceramics is apatite/wollastonite (A-W) that has improved mechanical properties than their parent glass [136]. Due to their micro-nanostructure and improved mechanical properties, these glass-ceramics could be promising matrices for bone regeneration [137] e.g. intramedullary plug in total hip replacement [138]. Surface functionalisation of glass-ceramics with lysine improved their cytocompatibility [139].

Regardless of the most obvious advantages of these bioactive glasses and ceramics, their brittle nature remains a big challenge particularly with the production of porous scaffolds. The expected reduction in strength associated with the degradation of the scaffold is also another challenge that require careful consideration during scaffolds' designing.

2.6 Crystallisation kinetics

Crystallisation kinetics is an important topic for glass formation and glass-ceramic synthesis [140]. The glass forming ability of a composition can be assessed by its reluctance to undergo crystallisation [140]. The crystallisation process is usually described by the activation energy of crystallisation (E_c) and the Johnson-Mehl-Avrami (JMA) exponent (n). The E_c gives an indication of the temperature

dependence of the crystallisation process, whereas n gives an idea on the crystal growth dimensionality [141]. The activation energy of crystallisation can be calculated using the Kissinger equation [142], amongst others. The JMA exponent can be calculated using the Augis and Bennett equation [143]. It is also worth noting that the crystallisation parameters can often be influenced by the size of glass particles [144,145]. The resistance of a glass against crystallisation can also be quantified in terms of the glass stability, which is the temperature difference between the glass transition (T_g) and the onset of crystallisation (T_x) [146].

2.7 Mechanism of apatite formation

Glass composition, surface charge, types of the medium (supersaturated solutions) and test conditions are the most influencing factors that affect the nucleation of apatite onto bioactive materials [147]. The mechanisms of bioactivity for various bioactive materials (such as, silicate, borate glasses and some metal) have been described in detail elsewhere [28,97,147-150]. Among them, the mechanism of hydroxycarbonate apatite (HCA) layer formation on the surface of silicate based glass (especially, 45S5 bioglass) implant has been most widely investigated. As the bioactivity of glasses mainly depends on the compositions of bioactive materials, a bone-bonding compositional diagram of silicate glass system (SiO_2-CaO-Na_2O-P_2O_5) has been proposed by Hench [151,152] (as presented in **Figure 2.8**). The diagram suggested that the glasses with composition fall within the region A are bioactive and hence can induce bonding with the bone, whereas compositions in region B are nearly bioinert. Compositions in region C are highly resorbable (10-30 days) and those fall within the region D do not form glass. Therefore, selection of proper compositions which in turn regulates the surface activity of the glass materials are important to understand the mechanism of apatite formation when tested *in vitro* to evaluate the *in vivo* bone-bonding capacity of bioactive materials. For example, a comparative study between *in vivo* bone ingrowth and *in vitro* apatite formation in SBF were investigated using Na_2O–CaO–SiO_2 glass system which reported that the induction period for apatite formation on the glass surface in SBF increased with increasing SiO_2

content (from 50 to 70 mol%) which was well correlated with the results obtained from the *in vivo* bone ingrowth study [153].

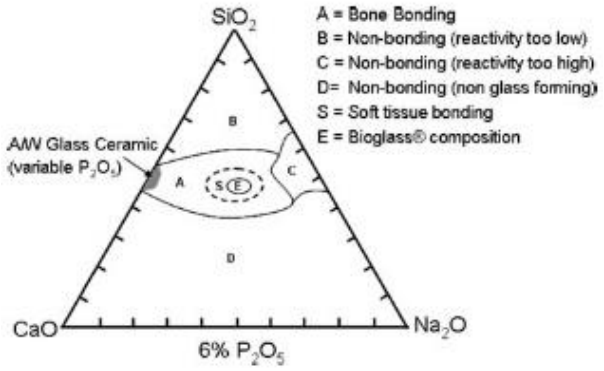


Figure 2.8: *Compositional diagram representing the bone-bonding properties of bioactive glasses [151,152].*

Apatite formation on the surface of bioactive glasses occurs through a sequence of chemical reactions when immersed in SBF. A schematic illustration of the reaction sequence leading to HCA formation according to Hench and co-workers [13,154] has been described in the **Figure 2.9** [155]. First two stages involve the ion exchange reactions between the modifier ions of glass network (like, Ca^{2+} and Na^{+}) and H^{+} ions from the medium (SBF) which promote the hydrolysis of silica groups and followed by formation of silanol (Si-OH) groups on the glass surface. At stage 3, condensation and polymerisation of SiO_2-rich layer take place on the surface, whereas stage 4 imply migration of Ca^{2+} and PO_4^{3-} ions from the glass network and also from SBF medium to the SiO_2-rich layer leading to the formation of amorphous calcium phosphate (ACP) layer. At the final stage, uptake of additional ions from medium such as OH^{-}, CO_3^{2-} and Na^{+} into the ACP layer promotes the conversion of ACP into HCA via crystallisation.

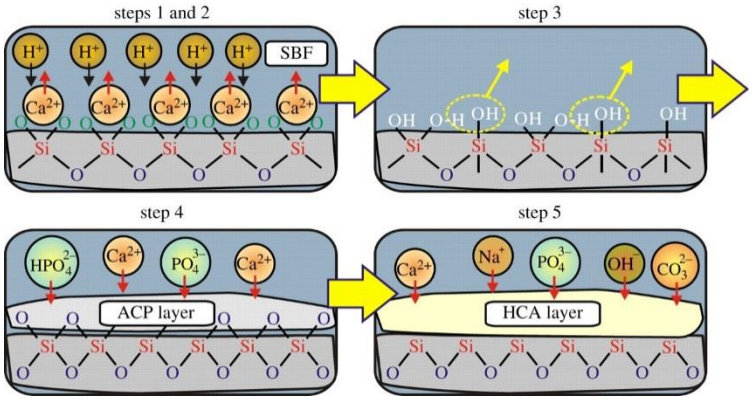


Figure 2.9: *Schematic illustration of the reaction mechanism of HCA formation on the surface of silicate based bioglass according to Hench and co-workers* [13,154].

The release of calcium ions in combination with phosphorous ions was reported to help in deposition of apatite layer on the glass surface according to the mechanism mentioned above [46,47] . For example, large amount of Ca^{2+} ion released from CaO-SiO_2-TiO_2 glass was found to form apatite layer on its surface within a day of immersion in SBF which was suggested to be due to increase of ionic activity during the apatite nucleation process [156] .

Borate based bioactive glasses (e.g. 46.1B_2O_3-24.4Na_2O-26.9CaO in mol%) follow the same mechanism of HA layer formation as described for silicate based glasses except for the formation of SiO_2-rich layer [28,149]. The faster dissolution rate of the borate glass when compared to the silicate glass (due to their lower chemical durability) are considered as the main reason behind the fast deposition rate of HA-like material on surfaces of borate glasses [28,97]. The conversion mechanisms of borate glass into HA in phosphate solution are illustrated in

Figure 2.10 [28]. When borate glasses are immersed in a dilute phosphate solution, dissolution of Na^+ and BO_3^{3-} ions from the glass structure into the solution occurs first. Then, PO_4^{3-} ions from the medium are assumed to react with Ca^{2+} ions leading to nucleation and growth of HA. The process is supposed to be continued until the glass is completely converted to HA.

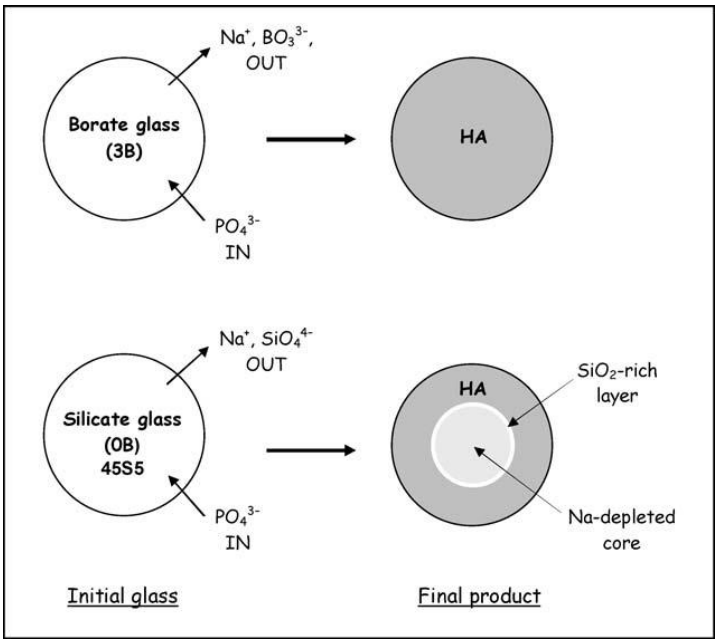


Figure 2.10: *Schematic illustration of the mechanisms of conversion of a 45B5 borate (3B) glass and 45S5 silicate (0B) glass to HA in a dilute phosphate solution* [28].

A comparative study on bioactivity of a borate (45B5) and silicate (45S5) glasses was carried out by Liang *et al.* [157], where borate glass was found to react faster (more than 5 times) than silicate glasses in a solution of 0.25 M K_2HPO_4 (pH=9). HA layer was seen to form on borate glass within 24 h, whereas HA layer was not visible on silicate glass even after 7 days of immersion in the same medium. In addition, the conversion of borate glass into HA layer was reported to be completed within 4 days (in 20 mM K_2HPO_4 solution), whilst silicate glass (45S5) was seen to convert to HA partially (~50%) after 70 days of test period [28]. For example, HA reaction product formed on the surface of silicate (SiO_2-46.1, CaO-26.9, Na_2O-24.4, P_2O_5-2.6 in mol%) and borate (B_2O_3-46.1, CaO-26.9, Na_2O-24.4, P_2O_5-2.6 in mol%) glasses after immersion in dilute K_2HPO_4 solution (20 mM) had a layered structure (as presented in **Figure 2.11 a-b**).

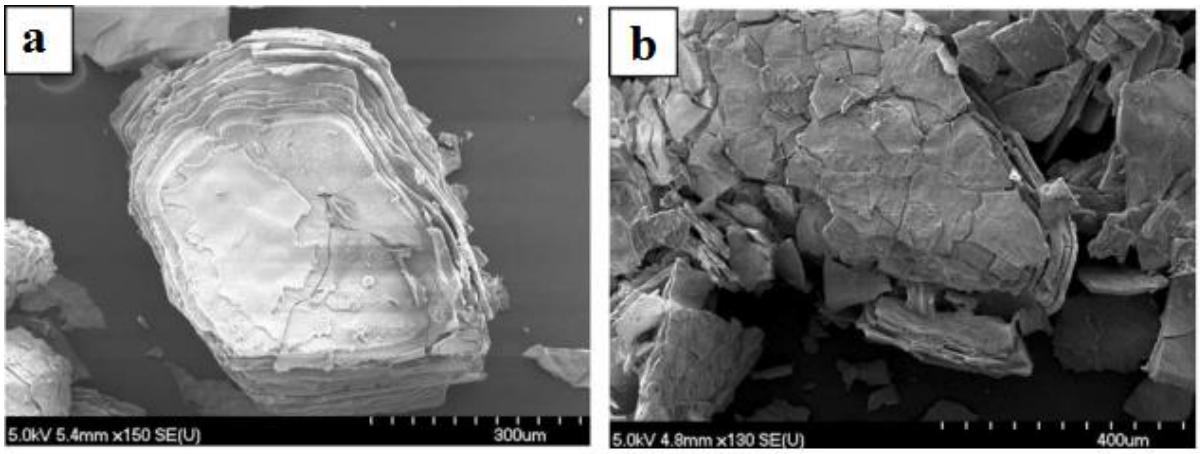


Figure 2.11: *SEM images showing the reaction products for silicate (a) and borate glass (b) glasses after immersion in dilute K_2HPO_4 solution (20 mM)* [28].

Bioceramics such as, wollastonite and pseudowollastonite have been revealed faster apatite formation in SBF compared to other bioglasses and glass-ceramics [158-161]. The mechanism of apatite formation on wollastonite in SBF was suggested to be due to the negative surface charge of the functional group (=Si–O-) on the ceramic surface rather than the dissolution of calcium ions into SBF [162]. Various types of sintered bioceramics such as, HA, α-tricalcium phosphate (α-TCP) were seen to form apatite layer on their surface after 24 h when immersed in SBF [163]. The effect of pH (6.5 and 7.4) and the concentration of HCO_3^- ions (4.2 and 27 mM) in modified SBF (m-SBF) were also reported to have influence on the bioactivity response of bioceramics (e.g. commercial HA Captal®) [164]. No mineralisation was detected on the HA surface when tested in m-SBF at the pH of 6.5. However, HCA layer was seen to form on the HA surface in m-SBF at pH 7.4 and a thicker HCA layer was observed on the HA substrate that immersed in m-SBF containing higher HCO_3^- ions.

In case of metal substrate (for example, bioinert titanium, Ti) the surface charge and the pH of the medium play the vital role in the apatite formation [148,165,166]. It has been previously reported that Ti and its alloys were found to form apatite when treated with basic (NaOH) [166,167] or acidic (H_2SO_4/HCl) solution [148]. Ti and its alloys display a certain level of positive and negative zeta potential when exposed to a strong acidic or basic solution, followed by a subsequent heat-treatment. A schematic illustration

of apatite formation mechanism on the positively and negatively charged Ti metal is described in **Figure 2.12** [165]. When the positively charged Ti substrate is immersed into SBF, the negatively charged phosphate ions from the medium are assumed to first accumulate on its surface leading to creation of negatively charged surface. As a result, positively charged calcium ions (from medium) are migrated to the negatively charged surface in order to form a CaP layer prior to crystallisation into apatite layer, as shown in **Figure 2.12 a**. On the other hand, the Ti surface is expected to form a sodium titanate layer after alkali (in NaOH) and heat treatments. Afterwards, the sodium titanate exchanges Na^+ ions with the H_3O^+ ions (from SBF) to form Ti-OH on the surface which leads to an increase in pH due to the consumption of H_3O^+ ions from medium and releasing Na^+ ions to the medium. Consequently, Ti metal that carrying a negative charge would initially attract calcium cations followed by phosphate anions to form CaP layer, as shown in **Figure 2.12 b**. Therefore, Ti-OH on the surface seems to induce apatite nucleation [168,169]. For example, the bone like apatite layer was reported to form on the NaOH (5M) and heat (600 ^oC for 1 hr) treated Ti metal after immersion in SBF for 10 days. Likewise, alkali treated titanium based alloys such as Ti-6Al-4V, Ti-6Al-2Nb-Ta and Ti-15Mo-SZr-3Al were also reported to promote bone-like apatite deposition on their surfaces in SBF following the same mechanism, see **Figure 2.12** [170,171]. Apatite formation on the surface of titanium has also been enhanced after acid treatment [172,173] as well as by producing a negative surface charge via the light-illuminationin of SBF with mercury lamp [174]. Ti substrates without any treatment possess no surface charge, therefore when exposed to SBF they can only form a CaP layer on their surface which does not bond to the bone [175].

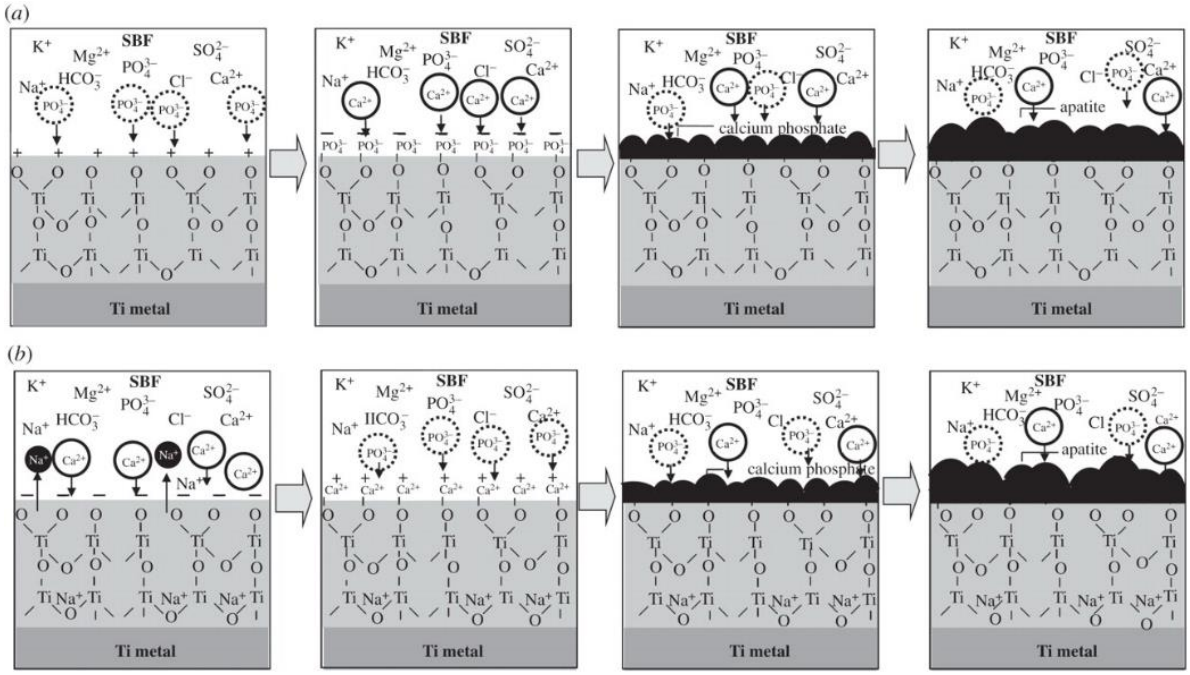


Figure 2.12: *Schematic of ion adsorption on (a) positively charged, and (b)negatively charged Ti metal in SBF medium* [165].

Phosphate based glasses (PBGs) have attracted huge interest in the field of biomaterials and tissue engineering due to their chemical similarity with the inorganic component of the natural bone and controllable degradation profile [36,37]. However, very few literatures have examined the bioactivity of PBGs [176-179]. The presence of TiO_2 in phosphate glasses are reported to induce CaP nucleation and improve their bioactivity [180,181]. Ti doped PBGs were investigated for bioactivity and an intermediate hydrated titania layer (0.5-2µm Ti-OH layer/gel) was observed to form in SBF which played an important role in the formation of apatite [178]. Another bioactivity study on $xCaO\text{-}(90\text{-}x)P_2O_5\text{-}10TiO_2$ glasses was suggested that the formulations containing 35 and 40 mol% of P_2O_5 did not support any apatite layer deposition even after 30 days of immersion in SBF. On the other hand, apatite layer was found to form on the phosphate invert glasses, containing 30 mol% of P_2O_5, after 20 days of immersion in SBF [182]. This was suggested to be due to the release of relatively small amount of phosphate ions from lower P_2O_5 containing glasses which promoted the apatite nucleation [176].

Apatite formation also depends on the basicity of the gel layer formed on the glasses and the amount of the functional groups present for HA nucleation in the layer [182]. The basicity of the gel layer can be enhanced via the addition of Na_2O [176]. The high amount of Na_2O and CaO as well as the relatively higher ratio of CaO/P_2O_5 would provide highly reactive surface of bioactive glasses in physiological environment which would eventually facilitate apatite formation [183]. Hydrated gel layers such as Si-OH, Ti-OH, Ta-OH, Zr-OH, Nb-OH, -COOH and PO_4H_2 groups are proved to provide nucleation sites for HA in SBF [66].

Apart from apatite formation, several other possible phases of calcium orthophosphates such as ACP, brushite $CaHPO_4{\cdot}2H_2O$ (DCPD), monetite $CaHPO_4$(DCPA) or octacalcium phosphate (OCP) can be formed in SBF depends on the experimental conditions of formation and state of ageing [184]. These calcium orthophosphates except ACP are more stable than HA in acidic conditions [185] and at the later stages, all of the phases would be converted into HA in various pathways [186].

2.8 Effect Mg on bioactivity and biocompatibility of glass

It has been reported in a number of studies that magnesium is essential for cells and with the interaction of phosphate ions can act as a cofactor for many enzymes [187,188]. Magnesium can also help to enhance bone formation [189,190] and to adhere osteoblastic cells on the surface of implants [189,191]. The rate of hydroxyapatite formation on the surface of SiO_2-based glasses in SBF has been reported to be increased with MgO addition [192,193]. Oliveira *et al.* studied the effect of MgO on $31SiO_2$-$11P_2O_5$-(58-x)CaO-xMgO glass system and reported that the early stage of mineralisation increased with the addition of MgO due to increasing Q^0 species in this glass system [194]. They showed that high magnesium oxide content (17.25 wt%) in MgO-$3CaO.P_2O_5$-SiO_2 glasses helped to form a Ca–P-rich layer in SBF [195]. Salinas *et al*. developed glasses in the $3CaO$-P_2O_5–$CaO.SiO_2$-$CaO.MgO.2SiO_2$ system and reported that relatively high MgO containing (13 mol%) glasses showed *in vitro* bioactivity in SBF at day 7 [196].

Kasuga *et al.* investigated the bioactivity of $CaO–P_2O_5–SiO_2–MgO$, Al_2O_3 in pseudo-extracellular fluid (PECF) and reported that the hydroxyapatite forming ability of this glass and glass ceramic system decreased with increasing MgO content and the formulation with more than 8 wt% MgO content did not form any apatite layer at all [197]. Ebisawa *et al*. studied *in vitro* evaluation of $CaO.SiO_2$ based glasses and reported that the apatite forming ability in P_2O_s-free $CaO.SiO_2$ glasses increased with increasing Na_2O and P_2O_5 but decreased with the addition of MgO, B_2O_3, CaF_2 and Fe_2O_3 [198]. They also reported that the release of sodium and phosphorous ions increased the pH and degree of supersaturation of the solution, respectively which promoted apatite formation. On the other hand, the release of calcium ions decreased with the addition of MgO, B_2O_3, CaF_2 and Fe_2O_3, revealing a negative effect on apatite formation [198]. Rajkumar *et al.* investigated the effect of MgO on hydroxyapatite formation in a $45P_2O_5$-30CaO-(25-x)Na_2O-xMgO glass system and reported that 2.5 mol% MgO containing phosphate glasses showed comparatively higher hydroxyapatite forming ability after 21 days of immersion in SBF due to the compact glass network resulting in a controlled release of ionic species, i.e., PO_4^{3-} [177]. Vallet-Regi *et al*. considered the effect of increasing magnesium content on *in vitro* bioactivity of CaO-MgO-SiO_2-P_2O_5 glass system and reported that magnesium delayed the transformation of ACP to more stable apatite phases [199]. ACP can act as an intermediate product for *in vitro* and *in vivo* apatite formation [200] and has been widely investigated in orthopaedics and dentistry due to its biological and osteoconductive responses [200].

2.9 Effect of titanium on glass forming ability and biocompatibility

The chemical durability and glass-forming ability of phosphate-based glasses has been reported to be significantly improved with the addition of TiO_2 [201,202]. Furthermore, Ti containing PBGs have shown improved biocompatibility [43,203-206] and were further investigated for their bioactive properties [176,178]. Titanium can be present in the glass as Ti^{4+} or Ti^{3+}, with the oxidation state of Ti in the glass dependent on the melting conditions (oxidizing or reducing) and the total amount of titanium

present in the glass [207]. Ti^{4+} has also been reported to act as a glass former, whilst Ti^{3+} serves as a glass modifier [207]. In addition, titanium containing glasses have shown good cell viability, attachment and proliferation [43,203-206]. Abou Neel *et* al. studied the effect of TiO_2 on the cytocompatibility of P50Ca30$Na_2$0Ti0 glasses and reported that the addition of 5 to 15 mol% TiO_2 in place of Na_2O was effective in increasing cell viability [43]. It has also been reported that TiO_2 in phosphate glasses could help to induce calcium phosphate surface nucleation and thus improve the bioactivity of glasses [178]. This behaviour is in contrast to what is seen in silicate glasses where TiO_2 can act as a nucleating agent and favours devitrification at a local level [208-211]. Danewalia *et al.* studied the incorporation of TiO_2 (at 1.25, 2.50, 3.75 and 5.00 wt%) on the structural, magnetic and bioactive properties of a base formulation $45SiO_2$–25CaO– $10Na_2O$–$5P_2O_5$–$10MnO_2$–$5Fe_2O_3$ glass ceramic [210]. They reported that the local glass structure became more ordered with increasing TiO_2 content from 1.25 to 5 wt% [210].

2.10 Test protocols for in vitro bioactivity experiment

In vivo bioactivity of a material can be predicted from its ability to form apatite in SBF and/or other similar types of supersaturated medium [6]. A vast number of work have been focused so far on the effect of composition and morphology of glass and ceramic materials on their *in vitro* dissolution rate and apatite forming ability. Various protocols with respect to the types of medium (e.g. SBF, PBS, TRIS, K_2HPO_4, DMEM), morphology of materials (powder, pellets, discs), surface area to volume ratio and the test condition (static, dynamic) have been considered for the *in vitro* bioactivity experiment (summarised in the **Table 2.1**).

Table 2.1: *Parameters and test protocols that have been used to investigate the bioactivity of various biomaterials.*

Materials	Medium	Geometry	Surface area or mass/vol	Condition	Length of study	Comments	Ref
Silicate glass (45S5)	SBF	Block (1×1.5×0.2 cm)	S/V= 0.05cm^{-1}	Static	14 days	HA formed (2 days)	212
Glass-ceramics (A-W)	SBF	Block (22×40×2 mm)	200ml	-	30 days	HA formed (7 days)	21
Silicate glass (45S5/S53P 4/S68)	SBF/TRIS/ Na-PBS	Block (20×15×1. 5 mm)	20ml S/V=0.4 cm^{-1}	Solution was replenishe d after 7 days	14 days	CaP layer formed on 45S5/S53P4 (24 hrs) and S68 (7 days)	213
Borate glass 15Na_2O– 15CaO– xB_2O 3–(70-x)P_2O_5	SBF	Particles (106-180µm)	500 mg in 50 ml	-	30 days	HA formation increased with increasing B_2O_3 content	214
Silicate glass (37CaO– 58SiO_2– 5P_2O_5)	SBF	Powder (<20 mm particles)	600 mg in 1 L	Stirring (100 rpm)	30 days	HCA formed (24 hrs)	215
Silicate glass (46S6)	SBF	Disc (13 mm diameter × 5 mm thick)	30 mL	Agitation	30 days	HA formed (1 day)	216
Bioceramics (A-W; BG; HA; HA/TCP; α-TCP; β -TCP)	SBF	cube (5×5×5 mm)	200 ml	-	-	OCP formed (1 day) on all bioceramics except on β -TCP	163
calcium aluminate (CA), glass ionomer cement (GIC), CA/GIC hybride	PBS	Block (22×15×4 mm)	50 ml	PBS was changed once a week	28 days	HA formed on CA (24 hrs) and CA/GIC hybride (7 days) GIC did not show any bioactivity in PBS.	217
Silicate glass 41.7SiO_2-(44.14-X) CaO-XMgO-3.13ZnO-5.2Na_2O-K_2O-4.7P_2O_5	SBF and Tris-Buffer	Powder (<45 µm)	75 mg in 50 ml	Agitated using mechanica l shaker	30 days	HA formed on non-magnesium containing glasses by 7 days in both SBF and Tris-Buffer whereas HA formed on Mg containing glasses after 1 month in	218

						SBF but not in Tris-buffer.	
Bioceramics (HA)	SBF	Particles (< 5 mm)	50 mg in 120mL	-	120 hrs	HA formed (12 hrs)	[219]
Glass-ceramics (A-W)	SBF	Block (22 x 40 x 2 mm)	200 mL	-	60 days	HA formed (7 days)	[220]
Glass-ceramic (Ceravital)	SBF	Block (15 x 10 x 1 mm)	35 mL	-	20 days	HCA formed (1 day)	[221]
Borate glass (45B5)	K_2HPO_4 (0.25 M)	Disc (15 mm diameter and 3 mm thick)	-	-	14 days	HA formed (1 day)	[157]
Borate glass (36 to 61 mol % B_2O_3)	SBF/ K_2HPO_4 (0.25 M)	Powder (25−75 µm)	1.5 mg/mL ratio	Gentle agitation	7 days	HCA formed (6 hrs)	[222]
Borate glass	K_2HPO_4 (0.2 M)	Disc (5 mm diameter x 5 mm thick)	100 mL	Static	7 days	HA formed (6 days)	[223]
Silicate glass (58S)	DMEM	Particles (20-40 µm)	75 mg in 50 ml	Solution was changed at 6 h, 24 h, and 2 days	3 days	HCA formed (3 days)	[224]
Titanium alloy (Ti6Al4V)	DMEM	Block (10x10x1 mm)	40 ml	-	360 hrs	HA formed (360 hrs)	[225]
ISO/23317: 2014(E)	SBF	**Disc** (10 mm diameter × 2 mm thick). **Block** (10× 10× 2mm)	Vs=Sa/10 ml ratio	Static	30 days	Apatite formation	[226]
Unified method (TC04)	SBF	**Particles** (45-90 µm)	75 mg in 50 ml	Agitation (120 rpm)	28 days	Apatite formation	[227]

The effect of different solutions on dissolution of bioactive materials has been studied [228-232]. In the early 1980s, TRIS buffer was used to evaluate the apatite forming ability of glass and glass-ceramic materials [233,234]. Later, in 1990, Kokubo *et al*. [21] developed the simulated solution which reproduced *in vivo* surface structure changes of glass ceramics A-W more precisely than TRIS. The pH of simulated solutions is maintained by using TRIS of HEPES buffers. However, these buffers were

seen unable to maintain the neutral pH of SBF during *in vitro* test [231]. SBF is a supersaturated solution containing similar ionic concentrations of inorganic parts of human blood plasma (presented in the **Table 2.2**) [235]. However, it has higher Cl^- ions and lower HCO_3^- ion concentration than those of the blood plasma. In 2001, Helebrant *et al.* [212] investigated the apatite formation on 45S5 bioglass using a series of SBF solutions with increasing HCO_3^- ion concentration up to the value close to blood plasma and suggested that the SBF with increased amount of HCO_3^- ions is more appropriate for *in vitro* bioactivity testing of biomaterials. Oyane *et al.* [236] also prepared the revised SBF (r-SBF) and modified SBF (m-SBF) which contained the ion concentrations equal or close to those in blood plasma (except for HCO_3^- ion concentrations in m-SBF) [237]. In terms of stability, r-SBF and m-SBF were seen to remain stable, no change in ion concentrations and pH value, up to 2 and 8 weeks, respectively when stored in sealed containers at 36.5 °C.

Table 2.2: *Ionic concentration in human blood plasma in comprasion with various deveolped SBF medium [235].*

Ion		**Ion concentration (10^{-3} mol) in**		
	Human blood plasma (pH 7.2 to 7.4)	**SBF (pH 7.4)**	**Revised-SBF (r-SBF)**	**Modified-SBF (m-SBF)**
Na^+	142.0	142.0	142.0	142.0
K^+	5.0	5.0	5.0	5.0
Mg^{2+}	1.5	1.5	1.5	1.5
Ca^{2+}	2.5	2.5	2.5	2.5
Cl^-	103.0	147.8	103.0	103.0
HCO_3^-	27.0	4.2	27.0	10
HPO_4^{2-}	1.0	1.0	1.0	1.0
SO_4^{2-}	0.5	0.5	0.5	0.5

In addition to SBF, cell culture medium (Dulbecco's Modified Eagle's Medium, DMEM) were also used for bioactivity testing and it has been found that the non-buffered DMEM solution containing an organic phase was not suitable for bioactivity test [238]. DMEM contains lower concentration of Ca^{2+} ions but higher concentration of HCO_3^- ions compared to blood plasma which leads to formation of $CaCO_3$ instead of apatite [238]. However, recently Popa *et al.* [239] studied the *in vitro* bioactivity of bioglass films (SiO_2 38.5, CaO 36.1, P_2O_5 5.6, MgO 15.2, ZnO 4, and CaF_2 0.6 in mol%) in different medium (namely SBF, DMEM, DMEM supplemented with 10% fetal bovine serum) and found that bioactivity test in DMEM supplemented with proteins under homeostatic conditions was more appropriate than that in SBF. They also suggested an unique bioactivity testing protocol utilising specific surface area to medium volume ratio (Sa/V=0.5 cm^2/mL) for the materials with different shapes and dimensions including bulk objects, thin films, powder and scaffolds [239].

Phosphate buffered saline (PBS) medium were also used in *in vitro* studies for bioactive glass (45S5) containing polymer (poly-L-lactic acid, PLLA and , polylactic-co-glycolic acid, PLGA) composites [240,241]. It was found that the formation of apatite on the glass surface was faster in PBS than SBF or TRIS [230]. Fagerlund *et al.* [230] investigated the dissolution of bioactive glasses (45S5, S53P4, 13-93) in PBS and reported that pH of the solution increased when alkaline and alkaline earth ions dissipated from the glasses. The release of silica ions and CaP precipitation also increased at higher pH. They also found that the CaP layer formed quickly due to the higher concentration of phosphorus ions in PBS [230]. *In vitro* bioactivity of glasses especially for borate glasses have been evaluated in aqueous K_2HPO_4 medium [101,157,222,242,243]. This medium was used to save the experimental time through the reaction of available HPO_4^{2-} and OH^- ions in K_2HPO_4 solution with glasses [157].

Apart from the use of various medium, other factors such as geometry of the test specimen, surface area to volume ratio, test conditions are also key to justify the test protocol. Therefore, an ISO standard (ISO/23317:2014(E): Implants for surgery — *In vitro* evaluation for apatite-forming ability of implant materials) has been proposed to conduct the *in vitro* bioactivity test [226]. The ISO standard suggested to use acellular

and protein free SBF solution buffered with TRIS. The standard also suggested the dimension and shape of test specimen only for bulk compact inorganic materials (solid disc and rectangular block) with a defined sample surface area to SBF volume ratio (V_{SBF}=100* S_a; where, V_{SBF} is the volume of SBF and S_a is the surface area of glass). However, this ratio is not defined for the materials in other forms of biomaterials such as powder and porous scaffolds. Moreover, the ISO standard stated the static testing condition, whereas some literatures conducted dynamic condition to mimic the *in vivo* environment [244-247].

Recently, the members of the Technical Committee 4 (TC04) of the International Commission on Glass (ICG) have proposed a unified method (modified version of ISO standard) for testing the bioactivity of glass particles (45-90 µm), particularly those of high surface area [227]. The modified method suggested to use of fixed mass per solution volume ratio (75 mg in 50 mL) with agitation (120 rpm).

2.11 Biomedical applications of calcium phosphate

Earlier in the section 2.7, it has been mentioned that during the initial stage of the *in vitro* bioactivity study, the ACP layer formed onto the surface of bioactive materials followed by crystallisation into apatite (HA), which is nucleated by the interaction of ions and pH of the medium [248]. However, some biomaterials can be limited to release of the desirable ions (due to their compositions) and also may be unable to produce favourable pH environment for ACP layer to be crystallised into apatite at the late stages of the *in vitro* study [249]. Therefore, the biomedical applications of both ACP and apatite will be discussed in this section.

Similar to apatite (i.e. HA), ACPs have excellent biological, osteoconductivity, and no cytotoxicity responses, therefore they have been introduced to orthopaedics and dentistry [200]. ACPs have been investigated for a range of biomedical applications in different forms; powders, granules, composites, self-setting cements or coatings [250]. Examples of biomedical applications of CaP based materials can be seen in **Figure 2.13**.

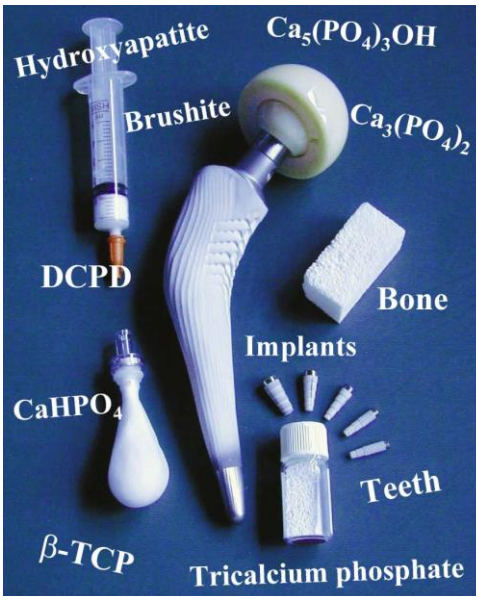


Figure 2.13: *Examples of biomedical applications of CaP based materials* [251]**.**

2.11.1 Dental applications

Due to good osteoconductivity and tuneable degradation rate of ACPs, they have been added to mouthwashes, chewing gums, toothpastes and also to ionomer cements as a filler for carious lesions [252]. Complexes of casein phosphopeptides (CPP) and ACP have been used as abrasive pastes for treatment of tooth sensitivity after root canal repair, scaling or bleaching procedures. Clinical trial revealed an increase in the content of inorganic phosphate and calcium in supra gingival plaque after three days use of mouthwash containing CPP-ACP complexes [253]. This product is commercially known as GC Tooth Mousse [254]. CPP-ACP complexes can be also incorporated into food, drinks and confectionary for potential prevention of the dental caries due to their natural origin (milk derivative). ACP has also been explored as a filler for bioactive polymer composites to be used for tooth repair [200]. Tooth repair can be stimulated through the released ions (calcium and phosphate) form the breakdown of ACP particles. Effect of ACP addition to orthodontic adhesives has been also evaluated and demonstrated satisfactory bracket bonding strength in clinical trials [200]. Toothpastes containing CaP can be used to reduce tooth sensitivity, to promote remineralisation of the demineralised enamel and for whitening and polishing purposes. Toothpastes containing HA have been showed a significant

positive effect on sensitivity and whitening of tooth and it was found that the whitening effect increased as the amount of HA within the toothpaste increased [252]. Both ACP and HA have been added to toothpaste and are available commercially. Examples of HA-containing toothpastes are Sensitive Reminx (Pharma Jenistec Co., Ltd., Korea), Triple Denta (TripleLife Co., Ltd., Korea), Kalident—calcuim hydroxyapatite (Kalichem Italia S.r.l.), DIO (DIO Co., Ltd., Korea), Coolin Bubble (Canavena Co., Ltd., Korea), YP Dental (You Co., Ltd. Japan). There are also toothpastes containing ACP such as Enamelon, Arm and Hammer's Enamel Care, Premier Dental's Enamel Pro [252]. In addition, a fine Bioglass 45S5 particulate, named NovaMin® (NovaMin Technology, FL, owned by GlaxoSmithKline, UK since 2010), has been used in certain toothpastes [255].

2.11.2 Bone repair

Human bone contains 70% of CaP minerals, hence CaP based materials have been considered as the best choice for repairing the damaged bone post trauma [248]. CaP has been thoroughly studied in various forms for repairing hard tissue because of their excellent biocompatibility, composition similarity with the bone mineral, inexpensive and easy to produce [248]. It has been reported that the rate of new bone formation was well correlated with the rate of ACP resorption. Moreover, ACP revealed significantly better osteoconductivity response compared to tricalcium phosphate *in vivo* study. Therefore, ACP has been incorporated within biodegradable polymers (e.g. PLLA, PLGA) for manufacturing porous scaffolds for bone and cartilage tissue engineering. It was also found that ACP particles within the polymer composites transferred after a short period of immersion in PBS into bone-like apatite which would potentially facilitate the formation of new bone *in vivo* and clinical trials [200]. Recently, CaP powder was manufactured into 3D porous scaffolds with aid of additive manufacturing techniques (robocasting), see **Figure 2.14**.

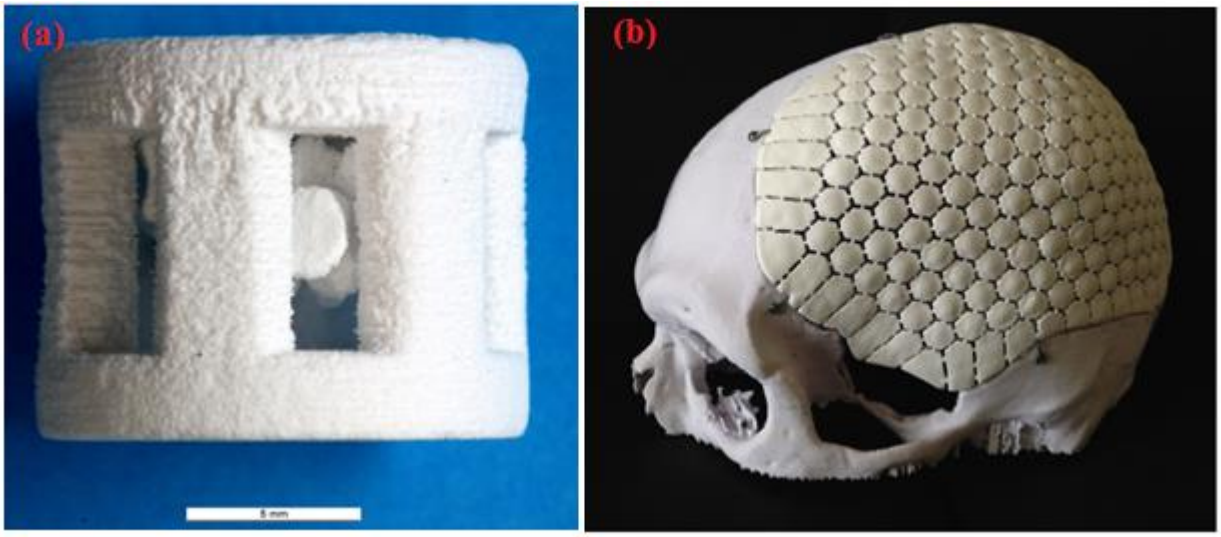


Figure 2.14: *Examples of additive manufactured implants based on CaP; (a) 3D scaffolds of DCPA/monetite (scale bar: 5 mm) [256], (b) implant made of DCPA for treatment of cranial bone defects (Craniomosaic) [248]. DCPA is dicalcium phosphate.*

2.11.3 Bioactive coatings

Metallic implants are still commonly used for load bearing applications such as hip-joint replacement, bone fixation devices (i.e. nails, plates and screws) and tooth sockets [250]. The lack of the bioactivity and poor bonding with the host bone of the metals had been a challenge for their clinical uses [257]. Therefore, coating with bioactive materials such as ACP, HA or other CaPs have been conducted to overcome the bioactivity and biocompatibility complications. HA coating of metallic implants was found to enhance their rate of clinical success to be more than 98% [258]. Numerous coating methods have been utilised e.g. thermal spray, plasma spraying, electrophoretic and biomimetic deposition [259]. The presence of ACP was reported in plasma sprayed HA coating, however the quantity could not be well controlled [250].

Since magnesium alloys are biodegradable metals, non-toxic and have similar mechanical properties of the cortical bone, they have been considered as attractive candidate for load bearing biomedical applications [260]. The main complication associated with use of magnesium implant is the fast degradation in physiological environment. Thus, CaP coatings have been applied to magnesium alloys to enhance their bioactivity, biocompatibility and control their degradation rates. A significant

reduction in degradation rates of magnesium alloys was obtained after surface coating with CaP materials [261].

2.11.4 Drug and Gene delivery

CaP-based nanoparticles have been explored for targeted drug and gene delivery due to their unique characteristics; similarity to inorganic component of bone, excellent adsorption capability to many biomolecules and proteins and biodegradability in moderate acidic medium (similar to the pH inside lysosome). CaP nanoparticles, with size less than 200 nm, can enter into the cells via endocytosis mechanism and may end up in lysosomes [248]. Consequently, CaP can break down at acidic conditions into phosphate and calcium ions. Phosphate ions are not harmful and amount of calcium ions can be tolerated by using moderate quantities of the nanoparticles [248]. Dissolution of CaP nanoparticles after cellular uptake made them a promising competitor to conventional nanoparticles (silica, gold and polymers). CaP nanoparticles loaded with vascular endothelial growth factor (VEGF) and bone morphogenetic proteins (BMPs) were produced in a water-based paste for bone repair purposes through direct injection into the defect (see **Figure 2.15a**) [248]. CaP nanoparticles can be used to deliver most of drugs and molecules and they can be loaded with several drugs and biomolecules by produced them with multi-shells (see **Figure 2.15b**).

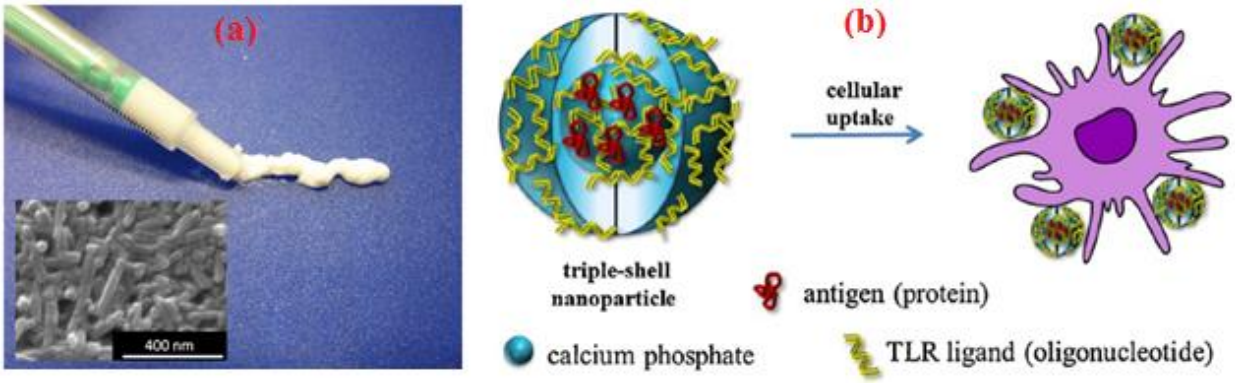


Figure 2.15: *CaP nanoparticles for drug and gene delivery applications; (a) CaP nanorods paste containing DNA encoding from BMP-7 and VEGF-A for repairing bone defect [262], (b) multi-shell design of CaP nanoparticles loaded with antigen and TLR ligand [263].*

2.11.5 Soft Tissue Engineering

Due to their ease of preparation into fibres, CaP glass fibres (in particular, phosphate based) were studied for their potential use in muscle and nerve regeneration. A 3D fibrous contruct, having the composition of $(P_2O_5)_{62.9}(Al_2O_3)_{21.9}ZnO_{15.2,}$ supported the proliferation and differentiation of human masseter muscle-derived cell cultures [9]. CaP glass fibres, based on $(P_2O_5)_{50}(CaO)_{30}(Na_2O)_{20-x}(Fe_2O_3)_x$ composition where x = 1-5, supported high level of attachment of immortal muscle precursor cell line [105]. Phosphate glass fibres containing 5-22.5 wt % Fe_2O_3 have been used as reinforcing agents in the development of bioabsorbable composites designed for orthopedic applications. A cortical plug method was used to test the biocompatibility of these glasses; the results showed that no inflammation was observed over periods of up to five weeks [264]. Due to the intriguing ability of phosphate glass fibres to form capillary-like channels during their degradation [122], they were used for in *in situ* formation of continuous aligned channels of 30-40 µm in diameter within 3D dense collagen scaffolds to allow for proper diffusion of nutrients and waste products through the constructs [126]. These constructs therefore maintained an excellent viability of human oral fibroblasts that formed a 3D network [126].

2.12 Manufacture of microspheres (solid and porous)

It is clearly observed that the bioactive glasses have huge potential in the field of bio-medical applications. It is very important to fabricate these glasses into practical morphologies for clinical applications. Particularly, glass particles with spherical morphology provide the advantage of uniformity in size and shape, easier to delivery to the target tissue, as well as having increased surface area in comparison to irregular particles, which could increase degradation rate and allow release of more therapeutic ions [265]. Spherical morphologies also provide enhanced versatility in filling the shape of the defect compared to bulk scaffolds which tend to have pre-set shapes [266]. Addition of porosity could further increase the surface area which allow for efficient cell attachment, encapsulation and proliferation, along with intrusion and extrusion of oxygen and nutrient by-products [63]. Moreover, porous spherical

morphologies have the capacity to enable the penetration of blood vessels, leading to an increase in cell viability throughout the entire construct. Porosity can be defined as the ratio of void spaces/ pore volume and the bulk volume/ total volume occupied by the solid and is generally expressed as a percentage. The International Union of Pure and Applied Chemistry (IUPAC) defines pore sizes based on the internal pore width:[267] such as micropores (<2 nm), mesopores (2 – 5 nm) and macropores (>50 nm). Calcium carbonate ($CaCO_3$) has previously been used as pore forming agent in ceramics used in filtration applications [268]. $CaCO_3$ decomposes at around 800 °C and produces CO_2 gas. The release of CO_2 during the process produce smaller rounded pores, and formulations with higher $CaCO_3$ content produce a larger amount of closed pores.

Material selection for the manufacture of microsphere can be application specific. For example, polymer-based porous microspheres have been explored extensively for the use of controlled drug delivery vehicles and delivery of biological components (i.e. proteins, cells and growth factors) [63,266]. Whilst, ceramic and glass microspheres have been explored for use in hard tissue regeneration, dental and orthopaedic applications and radionuclide applications [68,269-271]. The aim of this study was investigation into the manufacture of phosphate, borate and silicate-based microspheres (both solid and porous) and so the subsequent sections will cover glasses for microsphere manufacture however, in depth reviews of polymer and ceramic microspheres can be found by the following authors [63,266,272].

Microspheres can be prepared by various processing techniques such as sol-gel, flame spheroidisation, tube furnace method etc [62]. The flame spheroidisation technique is a relatively fast and inexpensive process which can easily be scaled-up for commercialisation purposes. However, for manufacture of larger microspheres the tube furnace process usually yields better results. There are several parameters of the flame spheroidisation technique which can all affect the outcome of the sphere size and shape, for example; i) particle separation before entering the flame is a key criterion to obtain dispersed uniform spheres; ii) residence time in the flame is also an important factor as larger particles will require a longer residence time for the glass to spheroidise, iii) the flame temperature can also influence outcomes of the

microspheres produced and is generally controlled by the type of fuel and ratios used [270]. Several studies have utilised varying gases to create a flame including propane/oxygen, acetylene/ oxygen, petrol/oxygen [69] and natural gas/air flames [22,270,273].

The following sections will focus on the manufacture of microspheres from the three main glass families, phosphate, borate and silicate based glasses.

2.12.1 Phosphate-based glass microspheres

Manufacture of microspheres from phosphate-based glasses has been shown by Lakhkar *et al.* [270], where a flame spheroidisation process was used to fabricate $50P_2O_5{\cdot}40CaO{\cdot}(10\text{-}x)Na_2O{\cdot}xTiO_2$ microspheres in the size range *of* 10-200 µm. They reported that the spheroidisation of particles below 30 µm was difficult due to agglomeration occurring at the feed apparatus. Larger glass particles (above 300 µm) were also difficult to spheroidise due to the shorter residence time for particles in the flame. Structural characterisation in terms of density and thermal properties (i.e. glass transition, T_g) were found to be comparable to both discs and irregular particles of the same composition, suggesting that the flame spheroidisation did not affect the atomic structure of the glass but rather the morphology. The spherical morphology increased the degradation and ion release rates due to the increase of surface area. This study also showed the positive biocompatibility results of the microspheres as MG63 cell attachment and proliferation was observed by 7 days of culture. Therefore, titanium doped PBG microspheres were suggested to be used as potential micro carriers to act as cell expansion platforms due to their stable surface.

Guedes *et al.* [123] studied dissolution, ion release, and E12.5-13.5 CD-1 mouse embryo primary fibroblast activity on $50P_2O_5{\cdot}40CaO{\cdot}(7\text{-}x)Na_2O{\cdot}xTiO_2$ glass microspheres (63-106 µm). Cells cultured on 5 mol% TiO_2 containing PBG microspheres appeared to form bridges between adjacent microspheres after 7 days. Whereas, 3 mol% TiO_2 containing PBG microspheres showed an unstable surface for cell growth. Lakhkar *et al.* [274] also found the enhanced proliferation of human mesenchymal stem cells and MG63 osteoblastic cells on 5 mol% TiO_2 containing ($50P_2O_5{\cdot}40CaO{\cdot}5NaO{\cdot}5TiO_2$) glass

microspheres (50 – 100µm) when compared to commercially available silica glass microspheres (Polysciences Inc., USA). Another study by Sene *et al.* [68] reported that higher content of P_2O_5 in glass showed resistance to crystallisation during spheroidisation and exhibited advantageous chemical durability and cell viability which makes the spheres promising for use in radiotherapy applications.

Hossain *et al.* [265] recently prepared highly porous and fully interconnected calcium phosphate-based glass ($40P_2O_5{\cdot}16CaO{\cdot}24MgO{\cdot}20Na_2O$ in mol %) microspheres via flame spheroidisation process. They reported that stem cells not only attach and proliferate but more importantly migrate to within the core of the porous microspheres, highlighting applications for bone tissue engineering and regenerative medicine [265]. More recently, *in vivo* study has been carried out on ($40P_2O_5{\cdot}16CaO{\cdot}24MgO{\cdot}(20 - x)Na_2O{\cdot}xTiO$ (x = 0, 2.5 mol %) porous glass microspheres by McLaren *et al.* [275]. They reported that both formulations (P40 and P40Ti2.5) showed biocompatibility. However, the faster degrading P40 formulation produced poor trabecular-like interconnection, which may negatively affect tissue functionality. Whereas, the slow degrading P40Ti2.5 microspheres, which were still remain within the host tissue at the end of study (at 13 weeks), promoted dense interconnected tissue but also delayed tissue maturation and remodelling [275].

Therefore, the development of new formulation with suitable degradation profile could enhance tissue regenerative response to the material.

2.12.2 Borate-based glass microspheres

There are very few literature studies on the development of porous microspheres of borate-based materials. For examples, porous, amorphous dysprosium lithium-borate glass microspheres (of the composition 30% Dy_2O_3, 8.8% Li_2O and 61.2% B_2O_3 (by weight)) with pore size ~30 nm have been prepared via chemical reaction between solid dysprosium lithium-borate glass microspheres and 0.25 M phosphate solution at 37 ^oC [276]. Three-dimensional (3D) flower-like magnesium borate ($Mg_3B_2O_6$) porous microspheres (0.6–1.0 µm) have been synthesised via poly(vinyl pyrrolidone) (PVP) assisted method. Mesopores and macropores were observed in the 3D flower-like $Mg_3B_2O_6$ microspheres [277]. Another type of dysprosium lithium-borate (of the

composition 10% Dy_2O_3, 11% Li_2O and 79% B_2O_3 (by weight)) microspheres (5-15 µm) have been prepared via flame spheroidisation process by Conzone *et al*. [22,278] for the treatment of rheumatoid arthritis, as well as in radiation synovectomy. The uniform size and shape of these microspheres are ideal for their use in radiation synovectomy. However, the solubility of this particular glass composition was found to be non-uniform. The soluble components (Li and B) of the glass dispersed into the simulated synovial fluid (SSF), whereas the insoluble dysprosium remained in the microspheres and therefore porous dysprosium phosphate-rich reaction product formed. Approximately 80% weight loss of the microspheres after 64 days without changing the size and shape was observed. The non-uniform behaviour of solubility was attributed to the soluble and nonsoluble components in glass rather than an outcome of spheroidisation, since similar results were observed for non-spheroidised particles. [22,278]. Flame spheroidisation has also been used to manufacture hollow hydroxyapatite (HA) microspheres [24,27]. Firstly, solid Li_2O-CaO-B_2O_3 glass microspheres were prepared using this technique followed by immersion of the microspheres in a phosphate buffer solution, resulting in heterogeneous precipitation of calcium phosphate. The reacted microspheres were then subjected to heat treatment at 600°C for 4 hours to convert the amorphous calcium phosphate hollow shells into crystallised HA microspheres [24,27,279]. Post heat treatment increased the strength of microspheres, however an increase in brittleness was also observed [24].

Borate glasses are an ideal material to prepare hollow microspheres due to their low network connectivity and ease of hydrolysis in acids or base [24,273]. Scanning electron microscopy images (SEM) confirmed that these microspheres were consist of multiple porous layers which made up the shell wall of the hollow microspheres. In general it was found that the outer layer of the shells were smooth and less porous than the inner layer as shown in **Figure 2.16 [273].** The smallest pore sizes (outer shell wall pore size of ~10 nm) was found for low concentration of K_2HPO_4 (0.02 M) and high reaction temperatures (60 °C). This reduction in pore size and formation of multiple layers is likely to occur due to densification of the HA shell and separation during the conversion reaction [273,279].

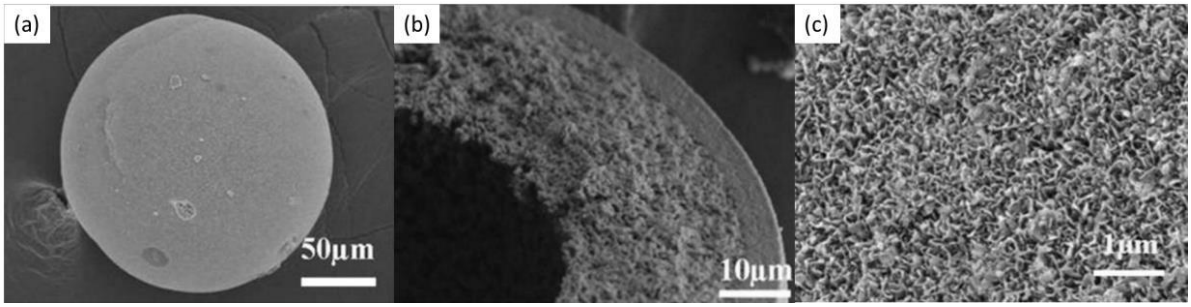


Figure 2.16: *(a) SEM images of 15CaO·10.63Li_2O·74.37B_2O_3 (wt%) glass microsphere (b) cross section of hollow HA microsphere formed by reacting glass microsphere in 0.02M K_2HPO_4 at 37 °C, pH 9 for 48h (c) HA surface at high magnification* [273].

However, highly porous structures of borate glass microspheres with interconnectivity have not been reported in the literature so far and these highly porous microspheres could be considered as candidates for controlled drug delivery, catalysis, chromatographic separation, filtration, and for biomedical applications.

2.12.3 Silicate-based glass microspheres

The most heavily investigated silicate based glass is 45S5 Bioglass® due to its inherent bone bonding ability [280,281]. Bioglass® was first developed by Larry Hench in 1969 [37,280,281]. Fu *et al.* [282] fabricated 45S5 glass microspheres in the size range of 75-150 µm via flame spheroidisation process and immersed in K_2HPO_4 (5g to 500 ml) to investigate the long term conversion to HA. The 45S5 glass-ceramic microspheres converted to a HA like material partially after 10 years and it was concluded that these glass-ceramic 45S5 microspheres would take up to 45 years to convert into HA when immersed in 1.0 M K_2HPO_4.

Martinelli *et al.* [69] also fabricated Yttrium aluminosilicate ($45Y_2O_3$·$20Al_2O_3$·SiO_2 (wt%)) glass ceramic microspheres in the size range of 20-50 µm via flame spheroidisation for use in hepatic cancer treatment [283]. They reported that the spheroidisation of the glass is dependent on where the particle falls in the flame trajectory i.e. they should fall in the hottest area of the flame to increase spheroidisation efficiency.

Until now (as seen above) all the studies on silicate microspheres were based on solid (non-porous) spherical particles. There are very few literature studies on the development of porous microspheres from silicate-based materials phase [65,284,285]. For example, the porous 45S5® microspheres (20 ± 5 µm) with pore size range of ~200-1000 nm were fabricated recently (2019) by Hong *et al.* via electro spray technique combined with phase inversion [284]. However, the process developed was time consuming as it required 24 hrs to prepare homogeneous slurry from BG powders and other precursors [i.e. N-methyl-2-pyrrolidone (NMP) and Polyethersulfone (PES)] followed by sintering the microspheres to remove the polymeric materials [284] (i.e. this was similar to a polymer burn-off method). Moreover, due to the sintering process, the microspheres crystallised and the main crystalline phases such as sodium calcium phosphate silicate (46–0163, isostructural to apatite, $(Na_{0.11}Ca_{0.89})$ $(P_{0.11}Si_{0.89})O_3$), apatite (09–0432, $Ca_5(PO_4)_3(OH)$) and wollastonite (84–0655, $CaSiO_3$) had formed. Calcium sulfate ($CaSO_4$, 37–0184), the product of unexpected reactions between the starting BG powders and PES/NMP solutions, was also formed [284]. Another study (2019) on preparation of porous 45S5 porous glass microspheres via flame synthesis process was done by Kraxner *et al* [285]. Alkaline activation process for 45S5 glass powder had been conducted using 1 M NaOH for 1 h under mechanical stirring at 500 rpm. After alkaline activation, the suspension of glass powders obtained, was subjected to surface dissolution and cast in polystyrene cylindrical moulds, and cured at 75 ^oC for 24 h. The hardened gel was then crushed and sieved to obtain size fraction of 45–75 µm, which were the spheroidised via oxygen-methane torch to obtain porous 45S5 microspheres[285]. However, this process was also time consuming, and the porous microspheres prepared were not fully amorphous as sodium calcium silicate crystalline phase was observed. Moreover, 11 wt% higher SiO_2 content was found for porous 45S5 microspheres compared to the starting glass powder[285].

Porous-wall hollow glass microspheres with size range of 10- 100 µm were prepared from sodium borosilicate glass powder (20- 40 µm) using sulfate blowing agent by controlled gas-air flame. The hollow microspheres were then treated with 4 M HCl to form porous microspheres with pore size range of 10-100 nm by leaching sodium and boron-rich phase [65].

However, highly porous structures having large external pores with interconnectivity from bio-silicate glass microspheres have not been reported in the literature so far. Such highly porous microspheres could enable enhanced degradation and *in vitro* bioactivity and could be considered as candidates for controlled drug delivery, catalysis, chromatographic separation, filtration, and for the biomedical applications highlighted above.

2.13 Morphology of porous glass microspheres

The size and structure of the pores are crucial factors affecting the properties of these porous microspheres. Most porous microsphere applications are based on the porous structure (porosities, pore sizes, surface areas, and so on) [63]. For example, a highly porous structure with well interconnected pores is required not only to achieve sufficient cell seeding density within the scaffolds, but also to facilitate transport of nutrients and oxygen for subsequent cell proliferation and differentiation [286]. The pore size is also important factor to determine the adsorption and release of biomolecules. Moreover, pore size also affects the blood vessel formation and bone growth is affected more by pore size than porosity. Larger pore size induces greater bone formation [275]. Several studies were conducted to define the influence of material pore size on the outcome of new bone formation *in vivo*, with contrasting results. For instance, when comparing ceramic scaffolds with different pore sizes between 50 and 500 µm, larger values were associated with more bone formation [287-289]. However, an opposite trend has been reported recently by Diao *et al*., where they observed that 100 µm pore scaffolds performed better than 250 and 400 µm pore devices [290]. Moreover, Hossain *et al.* reported recently that the pore size range of 30−50 µm was suitable to promote stem cell migration and colonization [265]

CHAPTER 3

MATERIALS AND METHODOLOGY

3.1 Glass Preparation

3.1.1 Phosphate based glasses

Varying formulations in the glass system $40P_2O_5$-(24-x)MgO-(16+x)CaO-(20-y)Na_2O-yTiO_2 (where $0 \leq x \leq 22$ and y=0 or 1) were prepared using sodium dihydrogen phosphate (NaH_2PO_4), calcium hydrogen phosphate ($CaHPO_4$), magnesium hydrogen phosphate trihydrate ($MgHPO_4.3H_2O$), phosphorous pentoxide (P_2O_5) and titanium dioxide (TiO_2) as starting materials (Sigma Aldrich, UK, $\geq 99\%$). The required amounts of precursors were weighed, mixed and transferred to a 100 ml volume Pt/Rh crucible (Birmingham Metal Company, U.K.) which was then placed into a furnace at 350 ^oC for 0.5 hours to remove H_2O. The mixture was then transferred to another furnace pre-heated to between 1150-1200 ^oC for 1.5-2 hours depending on the glass composition, as shown in **Table 3.1**. The resulting molten glass was poured onto a steel plate and left to cool to room temperature. The T_g of the glass obtained via DSC (see the thermal analysis section), using this information, some of the resulting molten glasses were cast into 9 mm diameter rods (using a graphite mould) which was preheated to 10 ^oC above the T_g of the glass formulation. The mould was then held at temperature for an hour after which it was cooled to room temperature to remove any residual stresses present. The glass rods were then cut into discs (9 mm diameter x 3 mm thick) for further analysis.

Table 3.1: *Glass codes, compositions and melting temperatures used in the glass system $40P_2O_5$-(24-x)MgO-(16+x)CaO-(20-y)Na_2O-yTiO_2 (where 0≤x≤22 and y=0 or 1).*

Glass Code (highlighted in bold)	P_2O_5 (mol%)	MgO (mol%)	CaO (mol%)	Na_2O (mol%)	TiO_2 (mol%)	Melt Temp/ Time (°C/h)
P40Mg24Ca16Na20 **(M24T0)**	40	24	16	20	-	1150/1.5
P40Mg16Ca24Na20 **(M16T0)**	40	16	24	20	-	1150/1.5
P40Mg8Ca32Na20 **(M8T0)**	40	8	32	20	-	1150/1.5
P40Mg4Ca36Na20 **(M4T0)**	40	4	36	20	-	1150/1.5
P40Mg2Ca38Na20 **(M2T0)**	40	2	38	20	-	1150/1.5
P40Mg8Ca32Na19Ti-1 **(M8T1)**	40	8	32	19	1	1200/2
P40Mg4Ca36Na19Ti-1 **(M4T1)**	40	4	36	19	1	1200/2
P40Mg2Ca38Na19Ti-1 **(M2T1)**	40	2	38	19	1	1200/2

3.1.2 Borate glasses

Three different types of borate glasses i.e. 45B5, B53P4 and 13-93B, which were derived from the 45S5, S53P4 and 13-93 glass equivalents, by fully replacing the SiO_2 with B_2O_3, were prepared using sodium carbonate (Na_2CO_3), potassium carbonate (K_2CO_3), calcium carbonate ($CaCO_3$), magnesium carbonate (Mg_2CO_3), calcium hydrogen phosphate ($CaHPO_4$), magnesium hydrogen phosphate trihydrate ($MgHPO_4.3H_2O$), phosphorous pentoxide (P_2O_5) and boron oxide (B_2O_3) as starting materials (Sigma Aldrich, UK). The composition of borate glasses is shown in **Table 3.2**. The required amounts of precursors were weighed, mixed and transferred to a

platinum rhodium alloy crucible (Birmingham Metal Company, U.K.) which was then placed into a furnace and followed a controlled program using 10 °C /min ramp for melting (at 350 °C for 0.5 hours to remove H_2O, at 800 °C for 0.5 hours to remove CO_2 and at 1150 °C for 1.5 hours for melting). The resulting molten glass was quenched between two steel plates.

Table 3.2: *Compositions of three different borate glasses investigated.*

Glass Formulation	B_2O_3 (mol%)	P_2O_5 (mol%)	CaO (mol%)	Na_2O (mol%)	MgO (mol%)	K_2O (mol%)
45B5	46.1	2.6	26.9	24.4	0	0
B53P4	53.85	1.72	21.77	22.66	0	0
13-93B	54.6	1.7	22.1	6	7.7	7.9

3.1.3 Silicate glasses

Three different bio-silicate glasses i.e. 45S5, S53P4 and 13-93 were prepared using sodium carbonate (Na_2CO_3), potassium carbonate (K_2CO_3), calcium carbonate ($CaCO_3$), magnesium carbonate (Mg_2CO_3), calcium hydrogen phosphate ($CaHPO_4$), magnesium hydrogen phosphate trihydrate ($MgHPO_4.3H_2O$), phosphorous pentoxide (P_2O_5) and silicon dioxide (SiO_2) as starting materials (Sigma Aldrich, UK). The composition of silicate glasses is shown in **Table 3.3**. The required amounts of precursors were weighed, mixed and transferred to a platinum rhodium alloy crucible (Birmingham Metal Company, U.K.) which was then placed into a furnace and followed a controlled program using 10 °C /min ramp for melting (at 350 °C for 0.5 hours to remove H_2O, at 800 °C for 0.5 hours to remove CO_2 and at 1380 °C for 2 hours for melting). The resulting molten glass was poured onto a steel plate and left to cool to room temperature.

Table 3.3: *Compositions of three different bio-silicate glasses.*

Glass Formulation	SiO_2 (mol%)	P_2O_5 (mol%)	CaO (mol%)	Na_2O (mol%)	MgO (mol%)	K_2O (mol%)
45S5	46.1	2.6	26.9	24.4	0	0
S53P4	53.85	1.72	21.77	22.66	0	0
13-93	54.6	1.7	22.1	6	7.7	7.9

3.2 Preparation of microspheres

3.2.1 Solid glass microspheres

The phosphate, borate and silicate glasses produced from the melt quenching process were then ground using a ball mill (Retsch PM 100) and the particle size range of 63-125 µm and 125-200 µm were achieved via separation using sieves. The particles 125-200 µm were then processed utilising a flame spheroidisation process to prepare solid microspheres. The flame spheroidisation equipment consisted of the following components: (1) thermal flame spray gun, (2) hopper feed and (3) collection trays. The thermal flame spray gun used was a MK74, developed by Metallisation Ltd (UK) which was connected to oxygen and acetylene gas cylinders. The thermal flame spray was positioned in such way that the flame of the gas torch was horizontal. The glass particles were passed through the hopper feed on top of the gun. The collection trays consisted of three rectangular glass trays placed at varying distances in from of the gun. The first tray was placed directly below the flame so as to collect particles that did not pass through the flame. The glass particles that underwent spheroidization due to surface tension forces as the particles passed through the flame, were collected from the 2nd and 3rd glass trays. The solid microspheres from each collection tray were initially visualized using light microscopy. The materials in the 1st collection tray were spheroidised again as it usually contained a mixture of glass microspheres along with a significant proportion of non-spherical particles.

3.2.2 Porous glass microspheres

The glass particles of phosphate and borate with the size range of 63-125 µm were mixed with porogen (calcium carbonate) of specific particle size with 1:3 ratio of glass particles to porogen and then processed via flame spheroidisation as described above (using oxy-acetylene ratio of 2.5:2.5) to prepare porous glass microspheres, as described elsewhere [265]. The microspheres were again collected from 2nd and 3rd collection trays. Porous phosphate glass microspheres were then washed using acetic acid (5 M) for 2 mins followed by washing using deionised water for 5 mins and then dried at 50 °C overnight. However, different washing protocols were used for borate porous glass microspheres. Porous B53P4 and 13-93B borate glass microspheres were washed using deionised water only for 1 min whereas, 45B5 porous glass microspheres were washed using 0.1 M acetic acid, followed by washing using deionised water and industrial methylated spirit (IMS) for quick drying and then dried at 50 °C overnight. The porous glass microspheres of 125-200 µm were then separated using sieves for further studies.

On the other hand, porous silicate glass microspheres were prepared using a modification to the existing (Conventional) method originally developed within our research group. Silicate glass particles of below 45 µm size were mixed thoroughly with porogen of specific particle size with 2:1 glass particles to porogen ratio and ground using a ball mill (Retsch PM 100, 20 small balls approx. 5 min). The materials prepared were then processed via the flame spheroidization process (using oxy-acetylene ratio of 2.5:2.5) highlighted above. The microspheres utilised for characterisation were collected from the 2nd and 3rd collection trays. The washing protocol for porous silicate glass microspheres was also different from that of phosphate and borate porous glass microspheres. 0.1 M acetic acid was used for 1 min for the washing of porous silicate glass microspheres. The newly developed method for the preparation of porous silicate glass microspheres and new washing protocols for porous borate and silicate glass microspheres will be described in further detail in chapters 6 and 7.

3.3 Characterisation methods

3.3.1 Compositional analysis

3.3.1.1 Composition analysis via EDX

Energy dispersive X-ray analysis (EDX, Oxford Instruments INCA, UK) with accelerating voltage of 15 kV and a working distance of 10 mm was used to examine the composition of each of the phosphate and silicate glass formulations. The phosphate glass discs were mounted on double sided carbon tape and coated with carbon using evaporation coater (Edwards coating System E306A). Compositional analysis for glass particles/microspheres were carried by embedding the particles/microspheres in a cold set epoxy resin and polished with SiC paper followed by a diamond cloth and ethanol was used as lubricant. The samples were then cleaned and dried with air spray and coated with a thin carbon layer by vacuum evaporation. Quantitative analysis of the glass formulations was performed using the following standards: Jadeite (sodium), MgO (magnesium), GaP (phosphorous), Wollastonite (calcium) and Ti metal (titanium). EDX analysis was performed on both large area and 5 separate spots on each sample and an average value was taken.

3.3.1.2 Composition analysis via ICP-MS

The borate glass formulations produced were ground into powder to conduct compositional analysis using inductively coupled plasma mass spectroscopy (ICPMS, Thermo-Fisher Scientific iCAP-Q equipped with collision cell technology with energy discrimination) to verify their composition. For analysis, 0.1g of each glass formulation (before and after degradation in dil. K_2HPO_4 and SBF) were digested in 50 ml 37 % HCl until a clear solution was obtained. The solution was then 50 % diluted with Milli-Q water (1:1). The resultant solution was then diluted with 2 % HNO_3 with 1:10 ratio. The final solution was then filtered through a 0.2 µm syringe filter for ICPMS analysis. Moreover, blank samples of pure Milli-Q water were mixed with the same proportion of HCl and 2% HNO_3 using standard calibration solutions. Three replicates were analysed and their averages reported.

3.3.2 SEM analysis

Scanning electron microscopy (SEM- Philips XL30, FEI, USA) with accelerating voltage of 15 kV and a working distance of 10 m, was used to examine the surface morphology of glass discs and microspheres before and after immersion in various degradation media such as PBS, Mili-Q water, SBF and dil. K_2HPO_4. The respective samples were fixed onto aluminium stubs with conductive carbon sticky tabs and sputter coated (Agar Sputter Coater) with platinum prior to examination and viewed with a Philips XL30 scanning electron microscope. Cross-sectional analyses of the microspheres were achieved by embedding the microspheres in a cold set epoxy resin and polished with SiC paper followed by a diamond cloth and then coated.

3.3.3 X-ray diffraction analysis

X-ray diffraction analysis was used to explore the amorphous nature of each glass formulation including the solid and porous glass microspheres produced using a Bruker D8 Advanced diffractometer (BRUKER AXS, Germany). The instrument was operated at room temperature and ambient atmosphere with Ni-filtered CuKα radiation (λ=0.15418 nm), generated at 40 kV and 35 mA. Data were collected from 8^o to 50^o 2θ diffraction angle using a scan step time of 8 sec, step size of 0.04^o and a 5^o glancing angle (only for glass discs analysis) against the incident beam on the specimen surface. XRD analysis was also used to examine any deposits on the surface of the glass discs or microspheres during the 28 days immersion period in SBF, ultra-pure water or dil. K_2HPO_4. Phases were identified using the EVA software (DIFFRACplus suite, Bruker-AXS) and the International Centre for Diffraction Data (ICDD) database (2005).

3.3.4 Density measurement

The density of the glasses was determined in accordance with the standard ASTMD-792 using the Archimedes method. The measurement was carried out at room temperature using industrial methylated spirit (IMS) as the immersion fluid. Bubble

free glass rods (9×20 mm) were used for the experiment, which was repeated three times for each glass formulation. The density of glasses was calculated using **Equation 3.1**:

$$\rho = \frac{A}{A-B} \times \rho_o \qquad \textbf{Equation 3.1}$$

Where A and B are the weight of the glass rods in air and in IMS respectively, and ρ_o is the density of IMS at the given temperature.

The compactness of a glass structure can be measured by the oxygen density of that glass [218,291,292].The oxygen density considers the effect of oxygen and neglects the effect of other components in the glass [218] and was calculated by dividing the mass of oxygen atoms in one mole of glass, m_o using **Equation 3.2**:

$$m_o = M_o \times \left(5x_{P_2O_5} + x_{MgO} + x_{CaO} + 2x_{Na_2O} + 2x_{TiO_2}\right) \qquad \textbf{Equation 3.2}$$

(where, M_o is the atomic weight of oxygen and x is the mole fraction of oxide) by the molar volume of the glass, V_m , which was calculated by dividing the mass of 1 mole of glass by experimental density of the glass, *ρ (as shown in **Equation 3.3**).*

$$V_m = \frac{x_{P_2O_5}M_{P_2O_5} + x_{MgO}M_{MgO} + x_{CaO}M_{CaO} + x_{Na_2O}M_{Na_2O} + x_{TiO_2}M_{TiO_2}}{\rho} \qquad \textbf{Equation 3.3}$$

The density of the glass microspheres was also determined by using a MicromeriticsAccuPyc 1330 helium pycnometer (Norcross,GA, USA). The equipment was calibrated using a standard calibration ball (3.18551 cm^3) with errors of ± 0.03%. Bubble-free glass microspheres, with an average weight of approximately 1 g, were used for the density measurements, and the process was repeated three times.

The bulk or tap density of the microspheres were also carried out using the following **Equation 3.4**.

$$Density\ (\rho) = \frac{Weight\ (W)}{Volume\ (V)} \qquad \textbf{Equation 3.4}$$

3.3.5 Thermal analysis

The thermal properties of various types of glasses and glass microspheres, specifically the glass transition (T_g) (measured at the midpoint), onset of crystallisation (T_x), crystallisation peak (T_c), melting peak (T_m) temperatures and glass stability against crystallisation, were characterised using a simultaneous thermal analysis instrument (SDT, TA Instruments SDT Q600, USA). Approximately 20 mg of glass powder (particle size range between 45-100 µm were used which were obtained by crushing the glass using Ball mill and followed by sieving through stainless still sieves) or microspheres was placed into a platinum (for phosphate and borate) or alumina (for silicate) pan and then heated from room temperature to up to 1300 °C at different heating rates (i.e. 10, 15 and 20 °C min^{-1}) for glass powder and at 20 °C min^{-1} for microspheres under 100 mL min^{-1} of nitrogen gas flow. An empty pan was also analysed in order to determine the baseline which was then subtracted from the thermal traces using TA Universal Analysis 2000 software. Triplicate was used for this measurements.

3.3.6 Activation energy of crystallisation

The activation energy for crystallisation (E_c) associated with the crystallisation peak of the glasses was calculated using the Kissinger **Equation 3.5** [142].

$$ln(\frac{\beta}{{T_c}^2}) = -\frac{E_c}{RT_c} + Constant \qquad \textbf{Equation 3.5}$$

Where β is the heating rate, T_c is the crystallisation peak temperature measured at the different heating rates (i.e. 10, 15 and 20 °C min^{-1}) and R is the gas constant.

The Johnson-Mehl-Avrami (JMA) exponent (n), provides information on the crystal growth dimensionality [141], and can be obtained using the equation proposed by Augis and Bennett [143] (see **Equation 3.6**)

$$n = \frac{2.5\,{T_c}^2}{\Delta T_{FWHM}\frac{E_c}{R}} \qquad \textbf{Equation 3.6}$$

Where n is the JMA exponent, T_c is the crystallisation peak temperature, ΔT_{FWHM} is the full width at half maximum of the crystallisation peak, E_c is the activation energy of crystallisation and R is the gas constant.

3.3.7 Fourier transform infrared (FTIR) spectroscopic analysis

Infrared spectroscopy was performed using a Bruker Tensor-27 spectrometer (Germany). All spectra were analysed using Opus™ software version 5.5. The glass powders (particle size range 45-100 µm) were scanned in absorbance mode in the region of 4000 to 550 cm^{-1} (wave numbers) and the spectra were collected with a resolution of 4 cm^{-1} by averaging 32 scans using a standard pike attenuated total reflectance (ATR) cell (Pike technology, UK).

3.3.8 Micro Raman spectroscopic analysis

Micro Raman spectroscopy was performed using a Horiba JobinYvonLabRAM HR Raman spectrometer equipped with an automated *xyz* stage (Märzhäuser). Spectra were acquired over the range 100-1400 cm^{-1} using a 532 nm laser at 34 mW power, a 100x objective and a 50 µm confocal pinhole. To simultaneously scan a range of Raman shifts, a 600 lines mm^{-1} rotatable diffraction grating along a path length of 800 mm was employed. Spectra were detected using a Synapse CCD detector (1024 pixels) thermoelectrically cooled to −60 °C. Before spectra collection, the instrument was calibrated using the zero-order line and a standard Si (100) reference band at 520.7 cm^{-1}. The spectral resolution in this configuration is better than 1.8 cm^{-1}.

For single point measurements of all glass formulations, spectra were acquired with an acquisition time of 30 seconds and 8 accumulations to improve the signal to noise ratio, from five random locations and averaged to give a mean spectrum. For M8T1 (as a representative of a 1 mol% TiO_2 containing glass), a lateral map of the top surface of the glass was obtained by acquiring spectra at 2 µm steps within a square 40 x 40 µm (a total of 441 spectra). In this configuration, the spatial resolution was ~1 and ~3 µm in the lateral (xy) and axial (z) dimensions, respectively. As each individual

spectrum was collected for 10 seconds, repeated once in order to automatically remove the spikes due to cosmic rays, the whole map required approximately 2.5 hours of acquisition time. The intensity (as height) of the band in the region 845-940 cm^{-1} (a diagnostic vibrational mode the TiO_5 unit) was evaluated within the map using univariate analysis within Labspec 6 software. Optical micrographs of the glasses were obtained using a 100x objective lens.

3.3.9 Nuclear magnetic resonance (NMR) spectroscopic analysis

^{31}P NMR is used to evaluate the structural connectivity of the phosphate glass network [293].

^{31}P MAS NMR spectra were recorded at room temperature on a Varian Chemagnetics Infinityplus spectrometer operating at a Larmor frequency of 121.468 MHz using a 4 mm MAS probe spinning at 12.5 kHz. The ^{31}P π/2 pulse duration was 3.0 µs, the spectral width was 100 kHz and the acquisition time was 10.24 ms. Chemical shifts are quoted relative to 85% H_3PO_4 using $Na_4P_2O_7.10H_2O$ as an external secondary reference. Prior to acquiring quantitative ^{31}P spectra the spin-lattice relaxation time T_1 was determined for each sample by saturation recovery. Saturation was achieved by 100 ^{31}P π/2 pulses spaced by delays of between 5 and 20 ms with recovery delays of up to 1000 s. Quantitative ^{31}P NMR spectra required relaxation delays (5 T_1) of the order of between 60 s and 250 s depending on the sample. The resulting spectra were deconvoluted into a set of Gaussian line shapes which were integrated in order to quantify the proportions of the different Q environments in the sample. First-order MAS sidebands were included in the analysis. Higher-order sidebands contained less than 1 % of the spectral intensity and were neglected.

3.3.10 Degradation studies

3.3.10.1 Phosphate bulk glass disc dissolution study

The mass loss of the glass discs of each formulation were calculated gravimetrically using **Equation 3.7**. The mass of each sample was measured before and after

degrading in both PBS and Milli-Q-water (ultra-pure) media (30 mL) at 37 °C for a period of up to 28 days. The degraded discs were removed from both media at various time points (1, 3, 7, 14, 21, and 28 days) and were placed onto tissue paper to blot dry and weighed immediately. The degradation medium was refreshed at each time point. Three replicates were used for this study.

$$\textit{Mass Loss (\%)} = \frac{M_0 - M_t}{M_0} \qquad \textbf{Equation 3.7}$$

Where M_o is the initial mass and M_t is the mass at test time point t. The pH change of the PBS solution and Milli-Q-water at each time point was also measured using a microprocessor pH meter (Mettler Toledo, Switzerland). The pH electrode was calibrated using standard pH buffer solutions of pH 4.0, pH 7.0 and pH 10.0 (Fisher Scientific, UK).

3.3.10.2 Microspheres degradation studies

Degradation studies of glass microspheres were carried out by means of mass loss measurements in Milli-Q-water (ultra-pure) for phosphate and silicate glass microspheres and in dil. K_2HPO_4 or dil. Na_2HPO_4 for borate microspheres at 37 °C up to 28 days. 1 wt % of mass to volume ratio was used and the medium was refreshed at every time points. At each time points of 1, 3, 7, 10, 14, 21 and day 28, the medium was removed from the vials and collected for ion release studies and then the microspheres were dried at 50 °C overnight and their masses were measured using a 5 decimal point balance (Sartorius CP 225D). The mass loss (%) was calculated according to the **Equation 3.7**. Degradation studies for microspheres were carried out using the device shown in **Figure 3.1** (developed by Fernando Barrera-Betanzos [294], a PhD student in the research group). Briefly, a 5 µm square piece of nylon mesh was stretched across the top of the sample vials by means of a threaded plastic lid in which a hole was made. The top of a 60 ml plastic syringe barrel was then fitted on top of the sample vial. A rubber O-ring was placed inside of the severed syringe barrel to create a seal at the interface between the vial and the syringe barrel. Subsequently, the barrel-fitted sample vial and a 60 ml syringe were locked at the respective ports of a 3-way stopcock as shown in **Figure 3.1**. The discharge port was

blocked as illustrated in Step 1 in **Figure 3.1** and the plunger was pulled to extract the medium through the nylon mesh. Afterwards, the sample port was blocked as shown in Step 2 in **Figure 3.1** and the conditioning media was collected through the discharge port for analysis. The discharge port was then blocked again and deionised water was injected and then extracted again following the procedure described in Step 1 to eliminate residual soluble salts. Finally, the sample vial was either i) refilled with fresh medium as shown in Step 3 in **Figure 3.1**, if the dissolution study was to be continued or ii) evacuated from liquid and dried in an oven at 50 °C until constant weight was achieved.

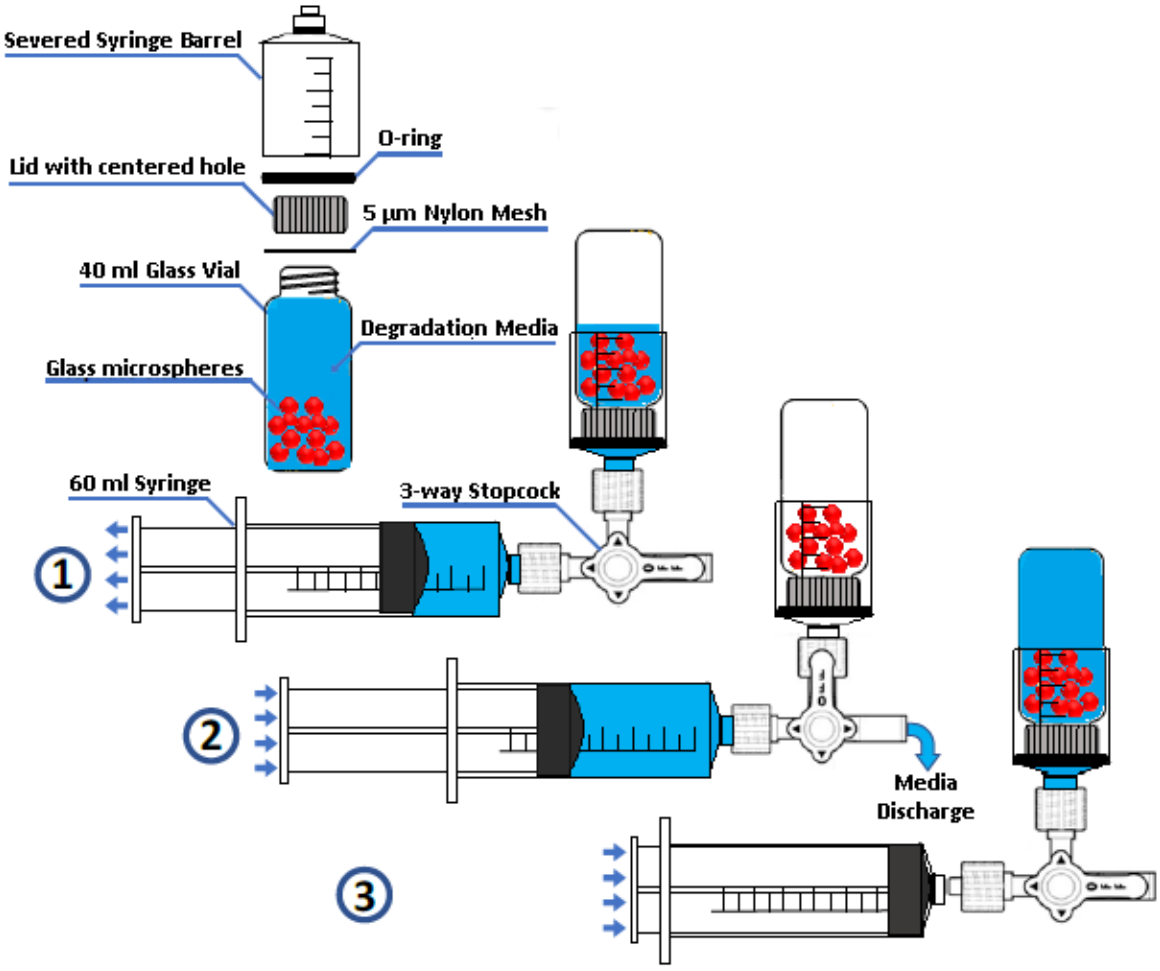


Figure 3.1: *Device set-up for the extraction of degradation media during the studies. Modified from Fernando Barrera-Betanzos* [294].

The pH change of the solution at each time point was also measured using a microprocessor pH meter (Mettler Toledo, Switzerland). Finally, the solutions obtained at each time point were analysed for various ion release profiles such as sodium, potassium, calcium, magnesium, phosphorous, titanium, boron and silicon from their respective glass formulations. The ion release studies were carried out via inductively coupled plasma mass spectrometry (ICPMS, Thermo-Fisher iCAP-Q model).

3.3.10.2.1 Phosphate solution for conversion reaction

The phosphate solution with a 0.02 M concentration used for the conversion of borate glass microspheres into HA was prepared by dissolving K_2HPO_4 (Reagent grade; Fisher Scientific) in deionised water. The pH of the starting solution was adjusted to 7.4, which is approximately equal to that of the human body fluid, by adding a few drops of dilute HCl. The concentration of K_2HPO_4 solution was chosen on the basis of research work has been carried out by Huang *et al.* [28]. 100 cm^3 phosphate solution have been used for 1 g glass particle and it has been reported that the solution contained sufficient PO_4^{3-} ions to react completely with all of the Ca^{2+} ions from the glass to form stoichiometric HA [$Ca_{10}(PO_4)_6(OH)_2$].

3.3.11 Ion release analysis via ICP-MS

Ion release profiles of the glass formulations were determined by immersing glass discs in 30 ml of ultra-pure (Milli-Q) water at 37 ^oC. The dissolution medium at each time point (1, 3, 7, 14, 21, and 28 days) was analysed for sodium, calcium and magnesium, phosphorous and titanium concentration using ICP-MS. Ion release profiles of the glass microspheres were determined by immersing the microspheres in various media such as ultra-pure (Milli-Q) water, SBF and K_2HPO_4 solution with 1 wt% of mass to volume ratio at 37 °C. The ion release profiles of diluted solutions was undertaken by ICP-MS (Thermo-Fisher Scientific iCAP-Q; Thermo Fisher Scientific, Bremen, Germany). The instrument was run employing three operational modes, including (i) a collision-cell (Q cell) using He with kinetic energy discrimination (He-cell) to remove polyatomic interferences, (ii) standard mode (STD) in which the

collision cell is evacuated and (iii) hydrogen mode (H_2-cell) in which H_2 gas is used as the cell gas. Samples were introduced from an autosampler (Cetac ASX-520) incorporating an ASXpress™ rapid uptake module through a perfluoroalkoxy (PFA) Microflow PFA-ST nebuliser (Thermo Fisher Scientific, Bremen, Germany). Internal standards were introduced to the sample stream on a separate line via the ASXpress unit and included Ge (10 µg L-1), Rh (10 µg L-1) and Ir (5 µg L-1) in 2% trace analysis grade (Fisher Scientific, UK) HNO_3. External multi-element calibration standards (Claritas-PPT grade CLMS-2 from SPEX Certiprep Inc., Metuchen, NJ, USA) included Ag, Al, As, Ba, Be, Cd, Ca, Co, Cr, Cs, Cu, Fe, K, Li, Mg, Mn, Mo, Na, Ni, P, Pb, Rb, S, Se, Sr, Ti, Tl, U, V and Zn, in the range 0 – 100 µg L-1 (0, 20, 40, 100 µg L-1). A bespoke external multi-element calibration solution (PlasmaCAL, SCP Science, France) was used to create Ca, Mg, Na and K standards in the range 0-30 mg L-1. Phosphorus, boron and sulphur calibration utilized in-house standard solutions (KH_2PO_4, K_2SO_4 and H_3BO_3). In-sample switching was used to measure B and P in STD mode, Se in H_2-cell mode and all other elements in He-cell mode. Peak dwell times were 10 mS for most elements with 300 scans per sample. Sample processing was undertaken using Qtegra™ software (Thermo-Fisher Scientific) utilizing external cross-calibration between pulse-counting and analogue detector modes when required.

3.3.12 Simulated body fluid (SBF) studies

In vitro study in simulated body fluid (SBF) was carried out for 7, 14, 21 and 28 days to examine the deposition of any calcium phosphate phases on the surface of prepared glass discs or microspheres. The SBF solution was prepared using the standard procedure of BS ISO 23317:2014 [295] . The prepared SBF solution was kept at 5 °C for 48 h prior to use and Bioglass 45S5 was used to confirm the apatite forming ability of the prepared SBF. The glass discs of each formulation were immersed in a specific volume (Vs) of SBF solution, such that Vs=Sa/10, where Sa is the apparent surface area of specimen (mm^2) and 75 mg of microspheres (solid and porous) were immersed in 50 ml SBF solution at 37 °C in a polyethylene vial. At each time point, the discs were removed from SBF solution and rinsed with deionised (DI) water before drying at room temperature and the microspheres were filtered and washed

with deionised water and then dried overnight at 50 °C in an oven. XRD, scanning electron microscopy (SEM) and energy dispersive X-ray (EDX) analysis were carried out on the surface of glass discs and microspheres to explore the structural, morphological and compositional changes, respectively. The changes in pH values of SBF solutions were also measured at each time.

3.3.13 Porosity

The porosity of the microspheres was evaluated via mercury intrusion porosimetry (Micromeritics Autopore IV 9500). A 5 cc powder penetrometer (Micromeritics) with 1 cc intrusion volume was used for all of the compositions. Before running the samples, an empty penetrometer test was also carried out as a blank.

Porosity of microspheres was also theoretically calculated using the following simple **Equation 3.8**.

$$Porosity = (1 - \frac{Bulk\ density}{True\ density}) \times 100 \qquad \textbf{Equation 3.8}$$

3.3.14 BET surface area analysis

Surface area measurements were also carried using a Micromeritics ASAP 2420 system using Krypton (Kr) as an adsorbate. Approximately 0.25 gm of samples were carefully weighed into a sample tube with a sealed frit. The samples were degassed at 250 °C for 15 hrs under vacuum to remove moisture and other adsorbed gases. Kr Isotherms were carried out from 0.07 to 0.25 relative pressure (P/Po) at -196 °C in liquid nitrogen. Specific BET surfaces were calculated from the isotherms using the BET model in the above relative pressure range using Microactive V3.0 software purchased from Micromeritics Instrument Corporation.

3.3.15 Viscosity measurement

Viscosity of the glasses were measured at high temperatures using rotational viscometer (Brookfield DV-III UTRA, USA). The viscosity was measured by measuring

the force required to rotate a spindle in a fluid. The viscosity was determined by measuring the shear stress and the shear rate exerted by the viscous fluid on a rotating cylindrical platinum spindle according to:

$$\eta = \frac{\tau}{\gamma} \qquad \textbf{Equation 3.9}$$

where, η is the viscosity in poise, τ is the shear stress in dynes/cm^2 and γ is the rate of shear in sec^{-1}.

In order to derive a viscosity curve for glasses, the fixed viscosity at glass transition temperature and the viscosity data obtained via rotational method were used and fitted to the Vogel–Fulcher–Tammann (VFT) **Equation 3.10** [296] by a least squares calculations [297]. The equation is:

$$Log(\eta)=A+B/(T-T_o) \qquad \textbf{Equation 3.10}$$

where, T is the temperature in °C, η is the viscosity in Pa s and A, B and T_o are constants.

CHAPTER 4

STRUCTURAL, CRYSTALLISATION BEHAVIOUR, DEGRADATION, ION RELEASE AND *IN VITRO* BIOACTIVITY STUDIES OF NEAR INVERT PHOSPHATE BASED GLASSES

4.1 Introduction

As seen from the literature, there is considerable conflict regarding the role of Mg and apatite formation in phosphate glass systems. The main aim of this chapter was to investigate the effect of MgO content (from 2 to 24 mol%) on *in vitro* calcium phosphate formation, degradation and ion release of a near invert PBG system of $40P_2O_5$-(24-x)MgO-(16+x)CaO-$20Na_2O$. However, reducing the MgO content lower than 8 mol% revealed that the glasses crystallised. As such, a further series of glasses were then evaluated incorporating 1 mol% TiO_2 (in the series $40P_2O_5$-(8-x)MgO-(32+x)CaO-$19Na_2O$-TiO_2), to investigate if the crystallisation could be arrested. Therefore, thermal, physical (i.e. density) and structural analyses were also conducted initially via simultaneous thermal analysis (SDT), the Archimedes method and X-ray diffraction (XRD), Fourier transform infrared (FTIR), Raman and nuclear magnetic resonance (NMR) spectroscopies, respectively.

4.2 Results

4.2.1 Compositional analysis

The relative concentration (mol%) of elements in each formulation were measured using EDX and the values are summarised in **Table 4.1**, where it can be seen that the respective oxide contents were within 1.5 mol% of their expected values.

Table 4.1: *Expected and obtained chemical compositions from EDX analysis of the different phosphate glass formulations investigated.*

Glass code	P_2O_5 (mol%) (Expected / actual)	MgO (mol%) (Expected /actual)	CaO (mol%) (Expected /actual)	Na_2O (mol%) (Expected /actual)	TiO_2 (mol%) (Expected /actual)
M24T0	40 / 39.9 ± 0.1	24 / 23.5 ± 1.7	16 / 16.3 ± 1.6	20 / 20.3 ± 0.6	0 / 0
M16T0	40 / 40.1 ± 0.2	16 / 15.3 ± 2.3	24 / 24.3 ± 2.1	20 / 20.3 ± 0.3	0 / 0
M8T0	40 / 39.9 ± 0.1	8 / 8.3 ± 0.5	32 / 31.4 ± 0.6	20 / 20.5 ± 0.2	0 / 0
M4T0	40 / 40.1 ± 0.2	4 / 3.7 ± 0.3	36 / 36.3 ± 0.4	20 / 19.9 ± 0.3	0 / 0
M2T0	40 / 39.9 ± 0.3	2 / 2.2 ± 0.2	38 / 38.4 ± 0.6	20 / 19.5 ± 0.4	0 / 0
M8T1	40/ 40.1 ± 0.1	8 / 8.4 ±0.5	32 / 31.8 ± 0.7	19 / 19.7 ± 0.3	1 / 0.9 ± 0.1
M4T1	40 / 40.1 ± 0.3	4 / 4.5 ± 0.2	36 / 35.2 ± 0.3	19 / 19.4 ± 0.2	1 / 0.9 ± 0.1
M2T1	40 / 40 ± 0.1	2 / 2.5 ± 0.1	38 / 36.9 ± 0.2	19 / 19.7 ± 0.1	1 / 0.9 ± 0.1

4.2.2 X-ray diffraction analysis

XRD profiles of PBGs investigated are presented in **Figure 4.1**. With the exception of M4T0 and M2T0 formulations, a single broad peak between 20° and 40° (2θ) was observed for all of the glass compositions. The absence of any sharp crystalline peak

confirmed the amorphous nature of these glasses. The amorphous glasses were chosen for further characterisation in this study. The crystalline phase for M4T0 and M2T0 were indexed with alpha-calcium pyrophosphate (α-$Ca_2P_2O_7$) (ICDD No. 00-009-0345). As M2T0 and M4T0 crystallised during manufacture they were not studied further.

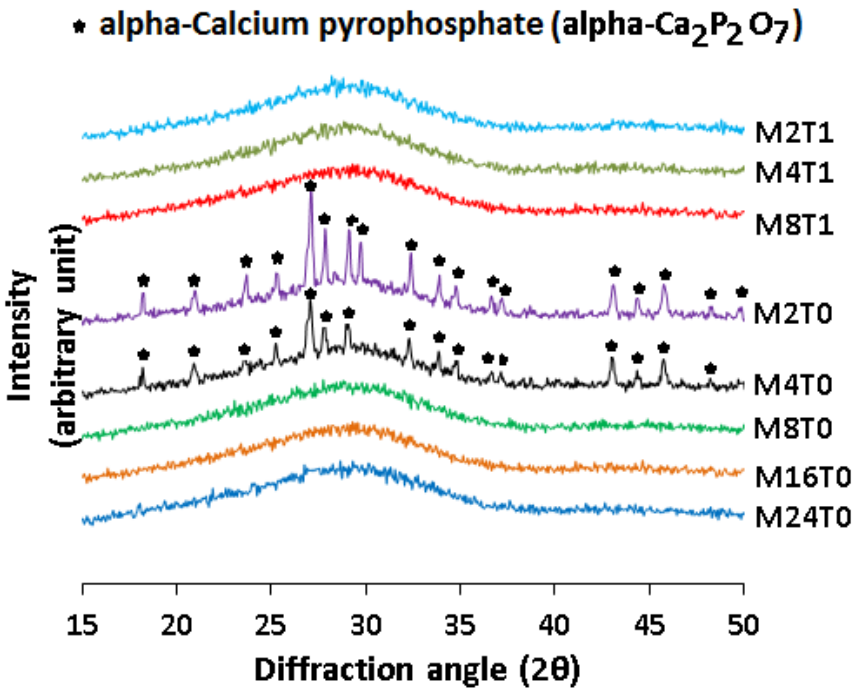


Figure 4.1: *X-ray diffraction patterns for glasses in the system $40P_2O_5$-(24-x)MgO-(16+x)CaO-(20-y)Na_2O- $yTiO_2$ (where 0≤x≤22 and y=0 or 1). ★ Represents alpha-calcium pyrophosphate (α- $Ca_2P_2O_7$) (ICDD No. 00-009-0345).*

4.2.3 Density

Figure 4.2 shows the density of the glasses, which decreased from 2745 to 2725 kgm^{-3} with decreasing MgO content from 24 to 8 mol% for the glasses that did not contain TiO_2. However, 1 mol% titanium contianing glasses had higher density in comparison to M8T0.

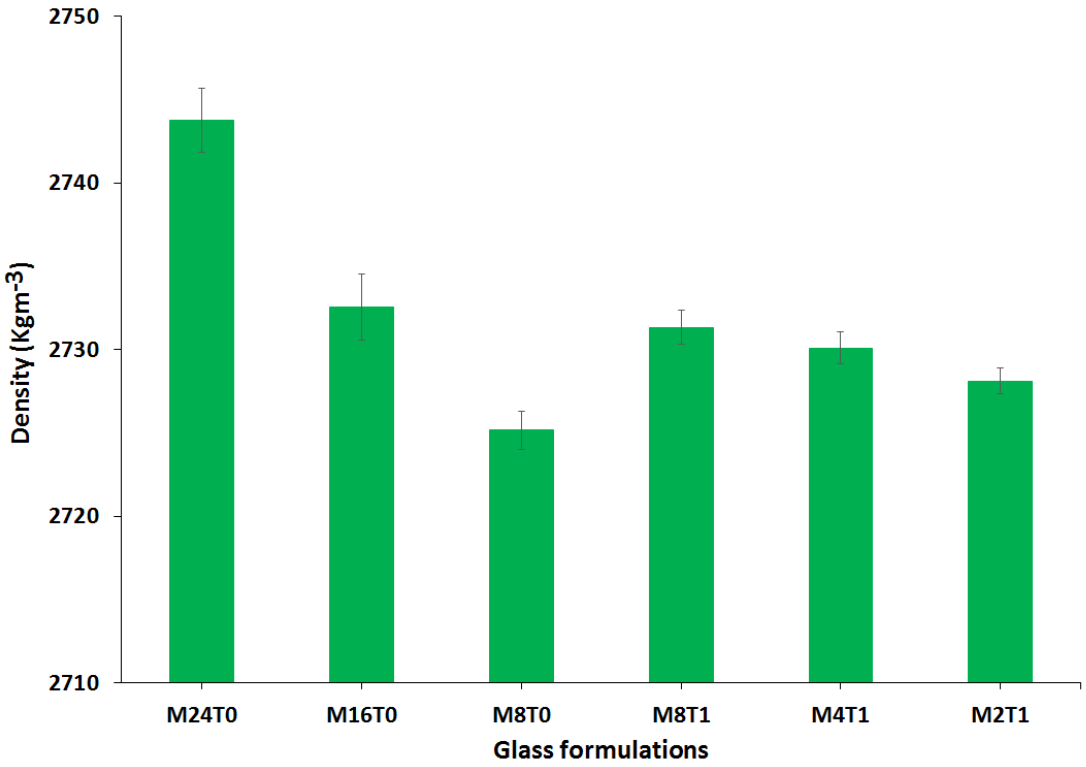


Figure 4.2: *Density of different glass formulations measured using the Archimedes method at room temperature.*

4.2.4 Oxygen density and molar volume

Figures 4.3 a and **b** represent the oxygen density and molar volume of glasses with no TiO_2 and with 1 mol% TiO_2, respectively. **Figure 4.3 a** shows the oxygen density decreased from 1.30 to 1.25 gcm^{-3}, whereas the molar volume increased from 32.05 to 33.21 cm^3mol^{-1}, as the CaO content increased from 16 to 32 mol% (i.e. the MgO content correspondingly decreased from 24 to 8 mol%). For the glasses with 1 mol% TiO_2 (see **Figure 4.3 b**), the oxygen density decreased from 1.26 to 1.24 gcm^{-3}, whereas molar volume increased from 33.1 to 33.5 cm^3mol^{-1}, with increasing CaO content from 32 to 38 mol% (or decreasing MgO content from 8 to 2 mol%).

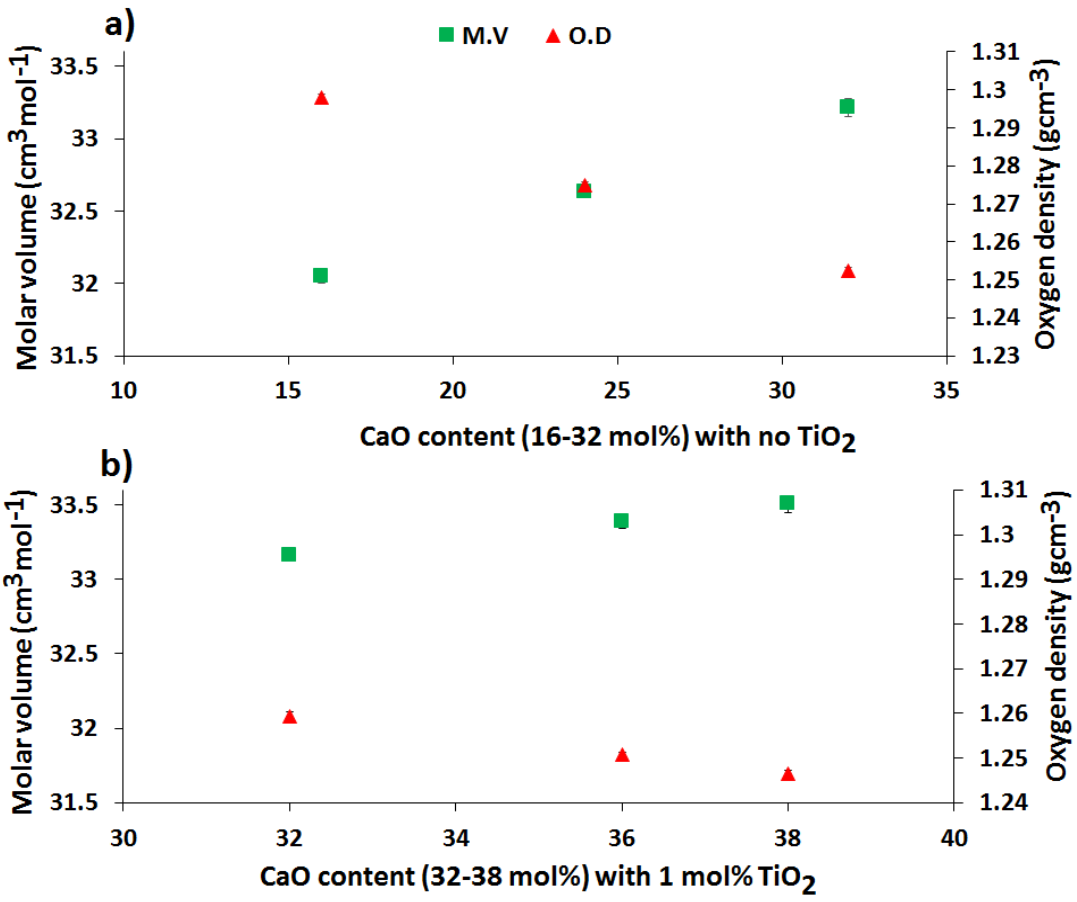


Figure 4.3: *Variation of molar volume (M.V) and oxygen density (O.D) as a function of CaO content: a) with no TiO_2 and b) with 1 mol% TiO_2 present.*

4.2.5 Thermal properties

Figure 4.4 shows the thermal traces of the glasses, where the corresponding glass transition (T_g) (using middle point), onset of crystallisation (T_x) (using tangents), crystallisation peak (T_c) (using peak maximum) and melting (T_m) temperature have been labelled. The T_g, T_x, T_c, initial melting (T_m) temperatures and the stability (ΔT) of the glasses against crystallisation decreased with decreasing MgO content (see **Table 4.2**). The T_g value decreased from 448 ^oC (for M24T0) to 430 ^oC (for M8T0) with decreasing MgO content from 24 to 8 mol%. However, with the addition of 1 mol% of TiO_2, the M8T1 glass had a 12 ^oC higher T_g value than M8T0. For the fixed 1 mol% TiO_2 content glasses, the T_g value decreased from 442 ^oC (for M8T1) to 436 ^oC (for

M2T1) with decreasing MgO content from 8 to 2 mol%. Similarly, the T_c decreased from 571 °C (for M24T0) to 541 °C (for M2T1).

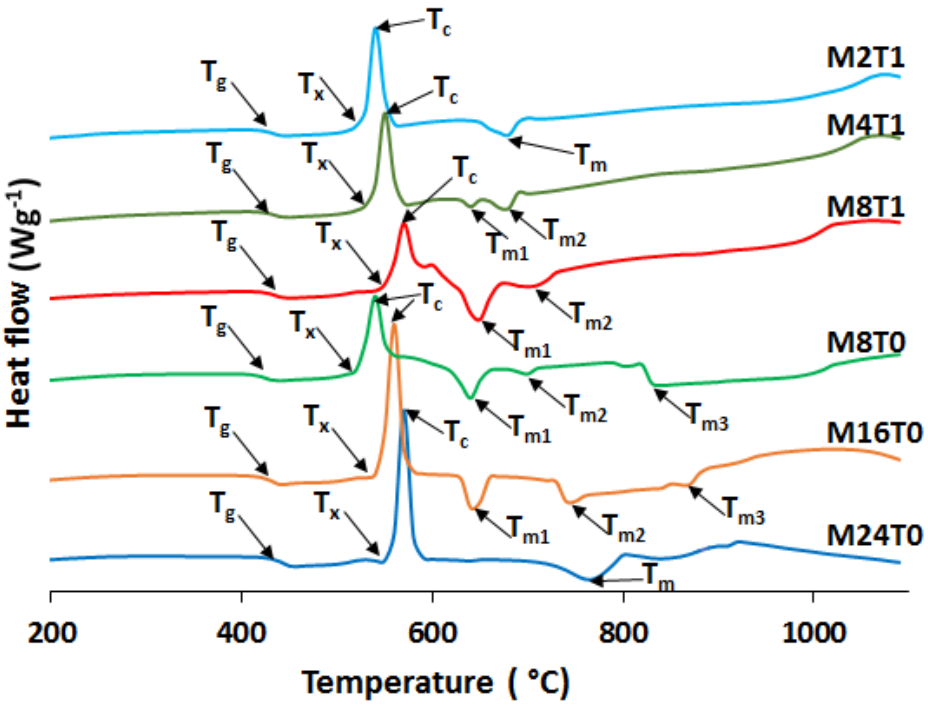


Figure 4.4: *DSC curves of the glass compositions with reduced MgO content (from 24 to 2 mol%).*

In addition, three melting peaks were observed for M16T0 (at 645 °C, 751 °C and 875 °C) and M8T0 (at 638 °C, 696 °C and 869 °C) with two melting peaks observed for M4T1 formulation (at 639 °C and 677 °C).

Table 4.2: *Glass transition (T_g), onset of crystallisation (T_x), glass stability (ΔT), crystallisation peak (T_c) and melting temperature (T_m) for six different glass formulations, using a 10 $^oC\ min^{-1}$ heating rate.*

Glass code	Glass transition T_g (°C)	Onset crystallisation T_x(°C)	Glass stability $\Delta T = (T_x - T_g)$ °C	Crystallisation Temperature T_c (°C)	Melting temperature T_m (°C)
M24T0	448 ± 1	554 ± 1	106	571 ± 1	764 ± 1
M16T0	437 ± 1	540 ± 2	103	560 ± 1	645 ± 1 751 ± 4.5 875 ± 3
M8T0	430 ± 1	520 ± 1	90	539 ± 1	638 ± 1 696 ± 4 869 ± 2
M8T1	442 ± 1	546 ± 2	104	570 ± 1	646 ± 1 710 ± 2
M4T1	440 ± 1	532 ± 1	92	552 ± 1	639 ± 1 677 ± 2
M2T1	436 ± 2	520 ± 3	84	541 ± 1	680 ± 2

4.2.6 Crystallisation behaviour

As stated earlier, PBGs in the glass system $40P_2O_5$-(24-x)MgO-(16+x)CaO-(20-y)Na_2O-yTiO_2 (where 0≤x≤22 and y=0 or 1) with MgO content of 8 mol% and above 8 mol% (without TiO_2 content) were formed successfully, as confirmed by XRD analysis. However, further replacement of MgO with CaO showed a strong tendency towards crystallisation (i.e. M4T0 and M2T0 glasses, see **Figure 4.1**). On the other hand, the addition of 1 mol% TiO_2 in place of Na_2O for glasses with less than 8 mol% MgO (i.e. M4T1, M2T1) reduced the tendency of the glass to crystallise. **Figures 4.5 a** and **b** show 2 mol% MgO containing glasses with and without 1 mol% TiO_2 content, respectively.

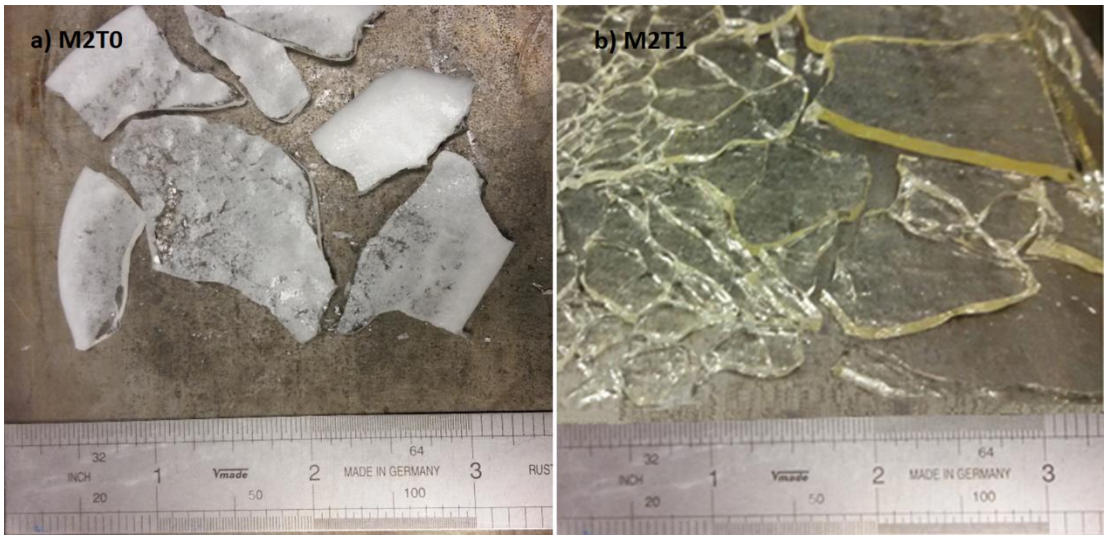


Figure 4.5: *Images of 2 mol% MgO containing glass after casting to room temperature with a) no TiO_2 and b) 1 mol% TiO_2 content present.*

Figure 4.6 shows results for the M24T0 glass as an example of the effect of different particle size on the crystallisation temperature. From **Figure 4.6**, it is clearly observed that the crystallisation peak moved to higher temperature (from 587 °C to 643 °C) and the peak intensity decreased with increasing particle size ranges (from 45-100 µm to 350-500 µm). As the crystallisation temperature varied with glass particle sizes, a fixed particle size range of 45-100 µm was used to calculate the activation energy of cystallisation for all glass formulations investigated.

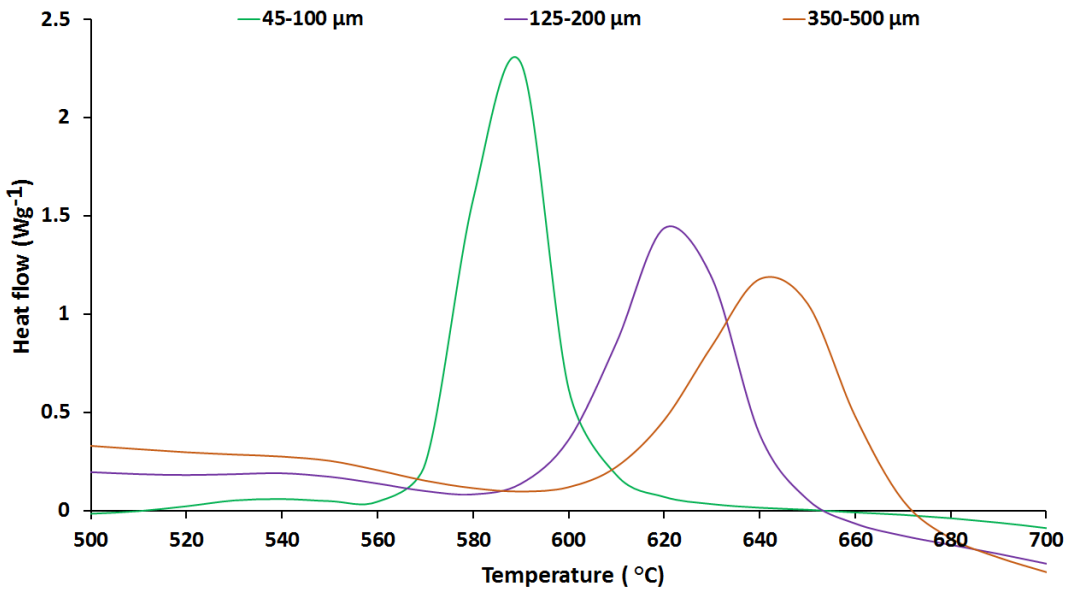


Figure 4.6: *Variation of the crystallisation peak as a function of different particle sizes (45-100, 125-200 and 350-500 µm) at 20 ^{o}C min^{-1} heating rate for M24T0 glass.*

Figure 4.7 shows the results for the M24T0 glass as an example of the effect of different heating rates on the crystallisation temperature. This process was repeated three times for each glass formulation. As can be seen, the crystallisation peak shifted to higher temperature (from 571 to 587 °C) and the peak intensity increased with increasing heating rate (from 10 to 20 °C min^{-1}).

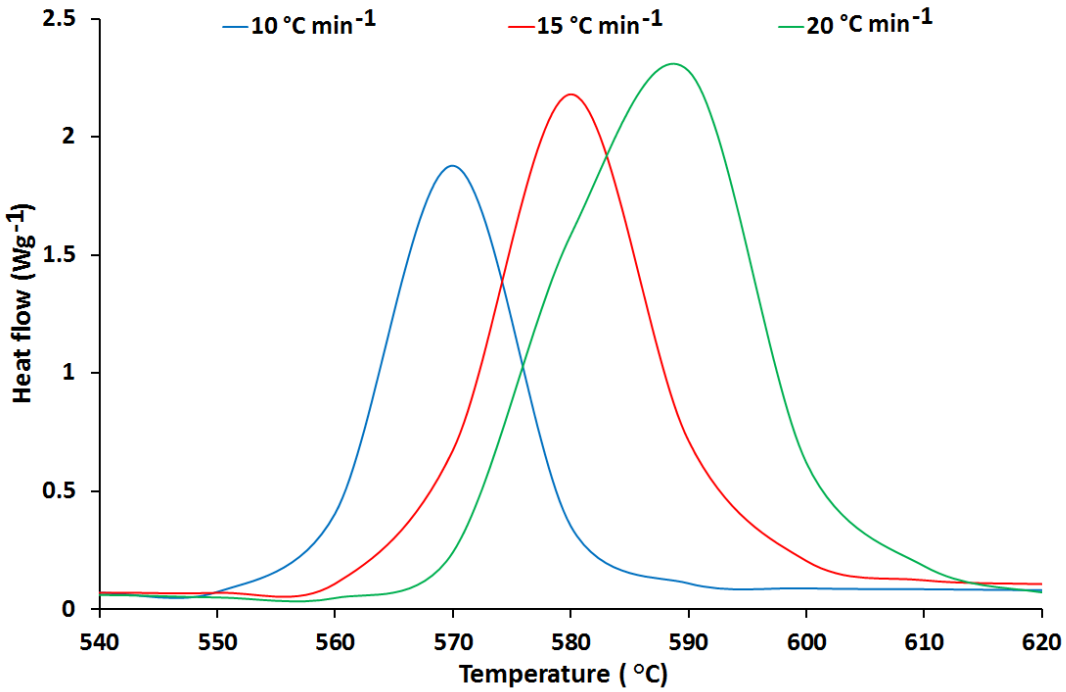


Figure 4.7: *Variation of the crystallisation peak as a function of different heating rates (10, 15 and 20 °C min^{-1}) for M24T0 glass (particle size 45-100 µm).*

In order to calculate the activation energy of crystallisation, ln (β/T_c^2) over $1/T_c$ was plotted for all glass formulations (see **Figure 4.8** for M24T0 as an example) and the slope of these lines corresponds to $-E_c/R$ (where, R is the gas constant).

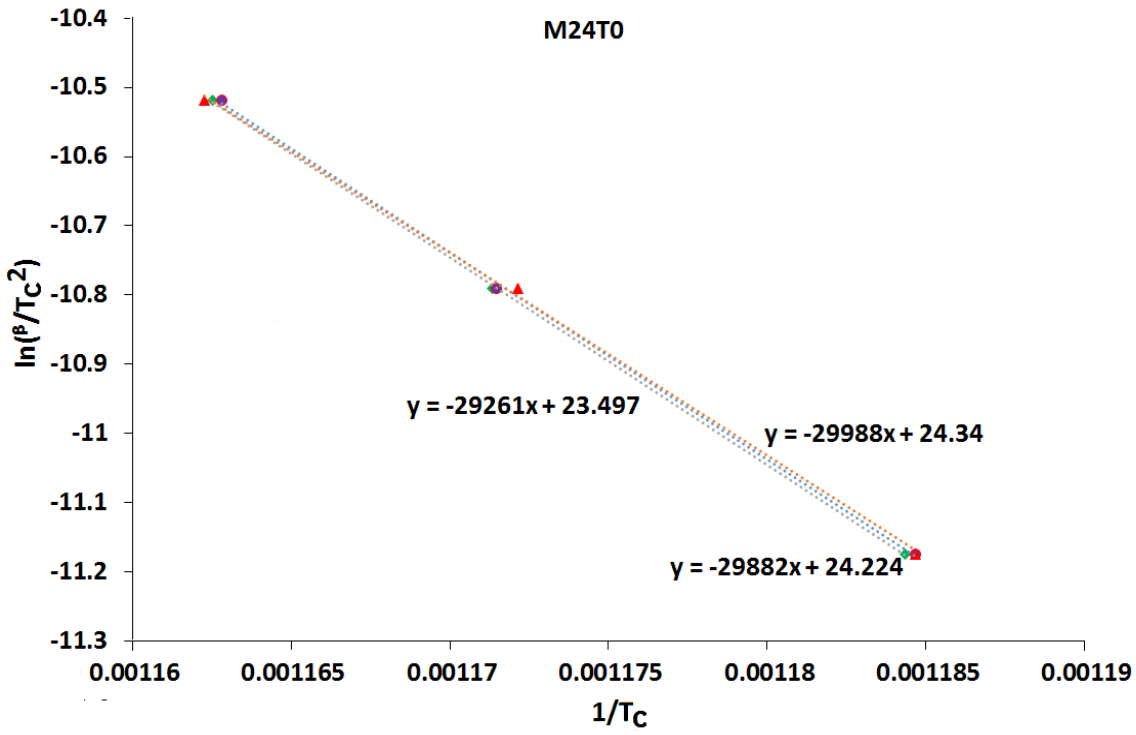


Figure 4.8: *The Plot of ln (β/T_C^2) vs $1/T_C$ for M24T0 glass (n=3).*

Table 4.3 provides values of the crystallisation peak temperatures obtained at the different heating rates, the activation energy of crystallisation (E_c) and the JMA exponent for the glasses. It was found that E_c decreased from 248 to 229 kJmol^{-1} as the content of MgO decreased from 24 to 8 mol% for glasses with no TiO_2. However, the M8T1 glass had an E_c value of 267 kJmol^{-1} which was 38 kJmol^{-1} higher in comparison to M8T0. For the glasses containing 1 mol% TiO_2, the E_c decreased from 267 to 233 kJmol^{-1} as MgO content decreased from 8 to 2 mol%.

Table 4.3: *Crystallisation peak temperature at different heating rates, activation energy of crystallisation and JMA exponent for the glasses.*

Glass	T_{c10}(°C)	T_{c15}(°C)	T_{c20}(°C)	E_c(kJmol^{-1})	JMA, n (± 0.1)
M24T0	571 ± 1	580 ± 1	587 ± 1	248 ± 4	4.8
M16T0	560 ± 1	569 ± 1	576 ± 1	237 ± 3	4.1
M8T0	539 ± 1	549 ± 1	555 ± 1	229 ± 4	2.7
M8T1	570 ± 1	578 ± 1	585 ± 1	267 ± 4	1.8
M4T1	552 ± 1	561 ± 1	568 ± 1	240 ± 4	3.4
M2T1	541 ± 1	550 ± 1	557 ± 1	233 ± 3	3.6

4.2.7 FTIR and Raman spectroscopy

Figures 4.9 a and **b** show the FTIR and Raman spectra collected from the fingerprint region for the glasses investigated. At least five (725, 900, 1000, 1100 and 1250 cm^{-1}) and eight (347, 500, 546, 700, 900, 1040, 1160 and 1260 cm^{-1}) vibrational modes associated with the phosphate network [298-300] were observed in the FTIR and Raman spectra, respectively, the position and proposed assignments of which are presented in **Table 4.4**.

Of note in the IR spectra (**Figure 4.9 a**), the intensity of the peaks at ca. 900 and 1100 cm^{-1}, associated with asymmetric P-O-P stretching vibrations of bridging oxygens in Q^2 and Q^1 tetrahedra, respectively [44,300], were seen to increase with decreasing MgO content (from 24 to 8 mol%) for glasses containing no TiO_2. However, the M8T1 glass showed a lower peak intensity at the same positions relative to M8T0. Moreover, redshifting of bands from 739 to 729 cm^{-1} (ν_s(P-O-P), Q^2), from 899 to 889 cm^{-1} (ν_{as}(P-O-P), Q^2) and from 1119 to 1101 cm^{-1} (ν_{as}(P-O-P), Q^1) was observed with decreasing MgO content for the glasses containing no TiO_2. Interestingly, these same vibrational modes were blueshifted to a higher frequency for M8T1 relative to M8T0.

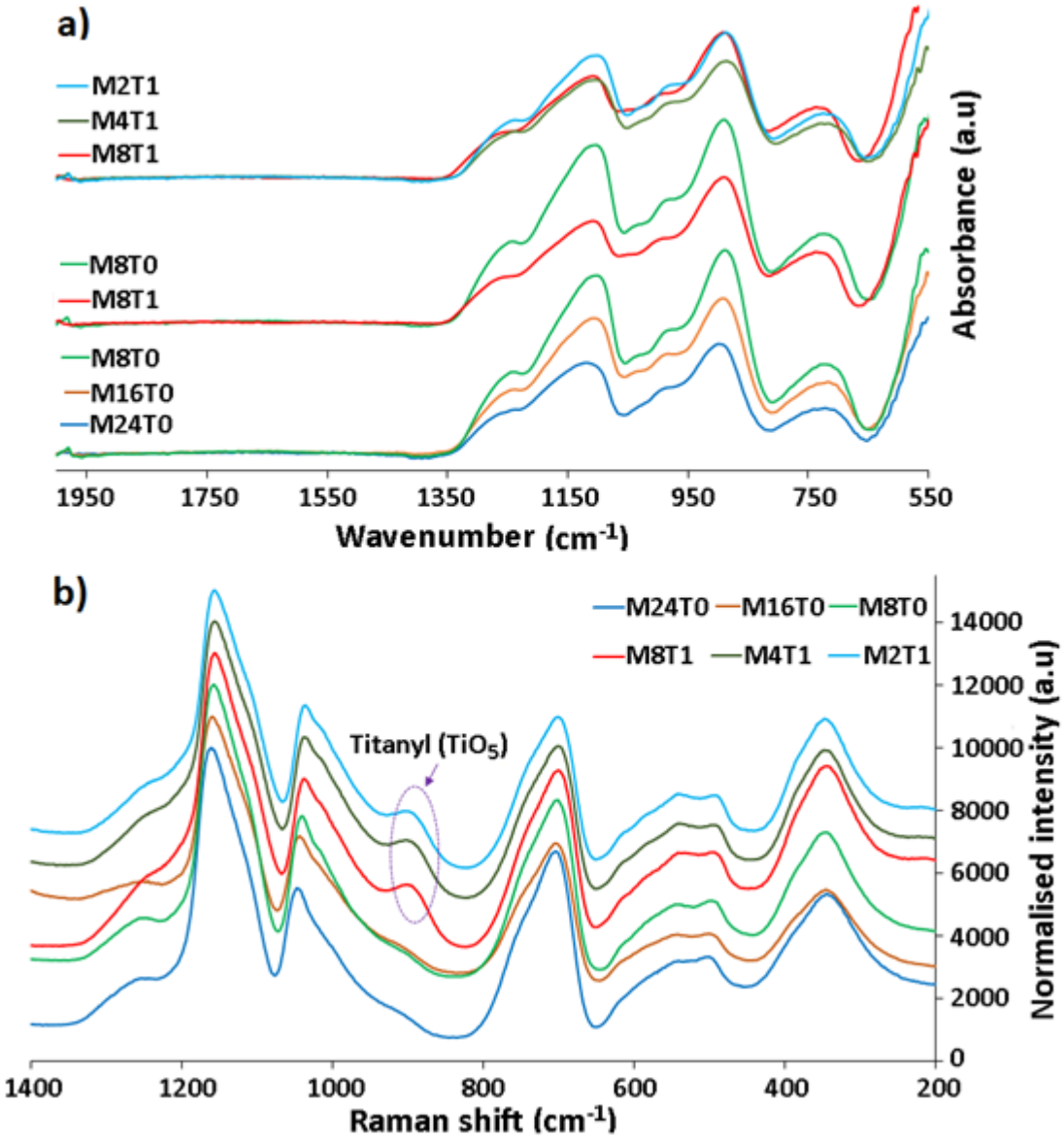


Figure 4.9: *a) FTIR spectra and b) mean Raman spectra (N=5) for the glasses in the system of $40P_2O_5$-(24-x)MgO-(16+x)CaO-(20-y)Na_2O-yTiO_2 (where $0 \leq x \leq 22$ and y=0 or 1). Spectra were averaged from those collected at five different, random locations on the top surface of the glass, with minimal spectral variation indicating a high degree of homogeneity.*

In the Raman spectra (**Figure 4.9 b**), analogous redshifting of bands, such as those associated with the PO_2 symmetric stretching of non-bridging oxygen in Q^1 (from 1046 to 1042 cm^{-1}) and Q^2 (from 1161 to 1158 cm^{-1}) units, respectively,[301] was noted with decreasing MgO content. The position of these bands did not change for the Ti containing glasses. Likewise, the characterstic band at ca. 500 cm^{-1}, assigned to the bending vibrations of P-O bonds [301], redshifted from 503 to 497 cm^{-1} (for M24T0 and M8T0, respectively), remaining at 493 cm^{-1} for the Ti containing glasses. Furthermore, a distinctive band at 899 cm^{-1} was observed in the Raman spectra of the Ti containing glasses, assigned to the TiO_5 (titanyl) unit and a symmetric P-O stretch of phosphate interacting with Ti [302]. No evidence of a vibrational mode at ca. 640 cm^{-1}, diagnostic of the Ti-O stretch in TiO_6 octahedra, was noted.

Table 4.4: *Proposed assignment of IR and Raman bands in the vibrational spectra of phosphate glasses in the series of $40P_2O_5$-(24-x)MgO-(16+x)CaO-(20-y)Na_2O-yTiO_2 (where 0≤x≤22 and y=0 or 1). Bands are quoted in units of cm^{-1}. BO = bridging oxygen; NBO = non-bridging oxygen.*

Glass formulations										Proposed assignment
M24T0		M16T0		M8T0		M8T1		M4T1	M2T1	
IR	Raman	IR	Raman	IR	Raman	IR	Raman	IR	IR	Raman	
-	348	-	348	-	350	-	348	-	-	348	Chains of O-P-O bending motions
-	503, 546	-	501, 546	-	497, 546	-	493, 546	-	-	493, 546	P-O-P bending motions, various modes
739	706	735	704	729	704	737	702	727	725	702	Symmetric P-O-P stretching vibration (BO) in Q^2 species
-	754	-	754	-	754	-	754	-	-	754	Symmetric P-O-P stretching vibration (BO) in Q^1 species
899	-	893	-	889	-	891	-	885	887	-	Asymmetric P-O-P stretching vibration (BO) in Q^2 species
-	-	-	-	-	-	-	899	-	-	899	Ti-O stretching vibration in TiO_5 tetragonal pyramids
987	-	984	-	977	-	979	-	975	972	-	Symmetric P-O-P stretching vibration (BO) in chain-terminating Q^1 species
-	1046	-	1045	-	1042	-	1038	-	-	1037	Symmetric P-O-P stretching vibration (NBO) in Q^1 species
1119	-	1109	-	1101	-	1109	-	1103	1101	-	Asymmetric P-O-P stretching vibration (BO) in chain-terminating Q^1 species
-	1161	-	1160	-	1158	-	1157	-	-	1157	Symmetric P-O-P stretching vibration (NBO) in Q^2 species
1236	1263	1238	1255	1238	1255	1257	1255	1236	1238	1255	Asymmetric P-O-P stretching vibrations (NBO) in Q^2 species

To explore the relative distribution of the TiO_5 component (899 cm^{-1}) within the glass, the top surface of M8T1 (as representative of the Ti containg glasses) was chemically mapped using Raman spectroscopy (**Figure 4.10 a**). The resultant false colour image indicated that the 1 mol% TiO_2 was uniformly distributed throughout the surface of the glasses, with the mean spectrum (**Figure 4.10 b**) extracted from the map (441 spectra) matching well with that previously obtained from random, single point measurements.

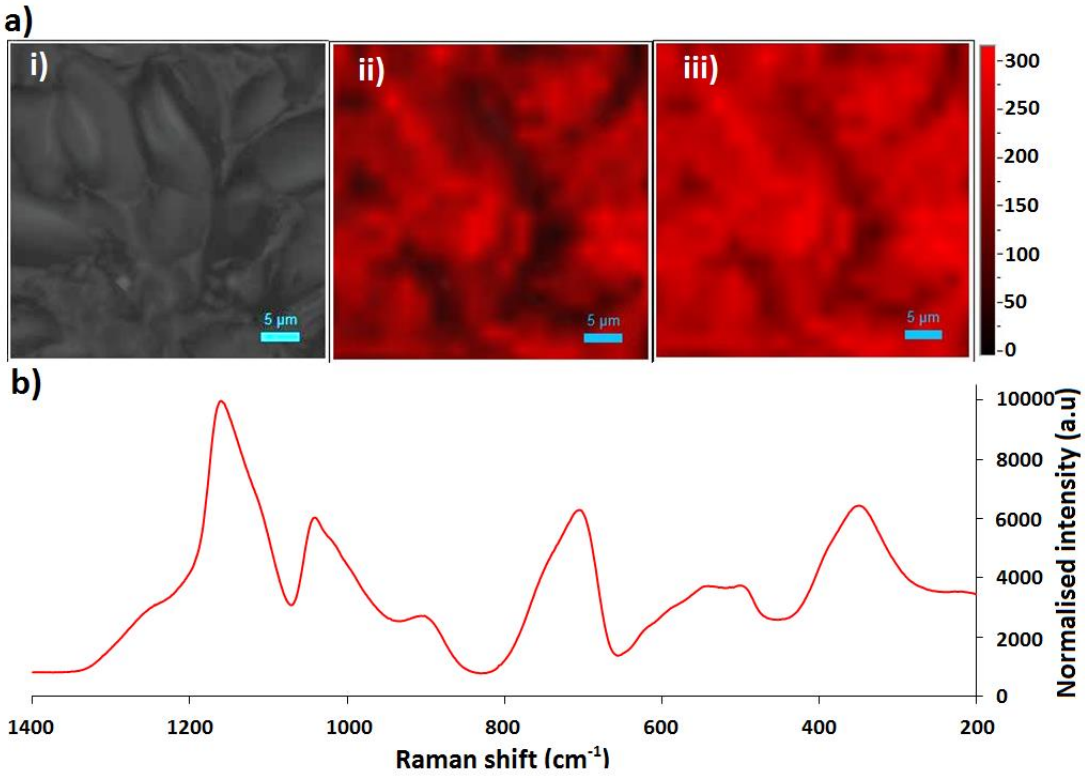


Figure 4.10: *a) (i) Optical image, (ii) Raman spectroscopic map overlaid on optical image and (ii) Raman spectroscopic map, including intensity scale bar and b) the mean Raman spectrum extracted from all spectra collected within the mapped area for M8T1 glass.*

4.2.8 NMR spectroscopy

Figure 4.11 shows ^{31}P MAS NMR spectra of the glasses. Two peaks were observed within the range of - 22.4 to -21.5 and -8.3 to -7.1 ppm. These ranges were assigned to Q^2 and Q^1 species, respectively [112]. The spectra showed that the peaks associated with Q^2 species shifted slightly from -22.44 to -21.75 ppm with substitution of MgO by CaO (from M24T0 to M8T0).

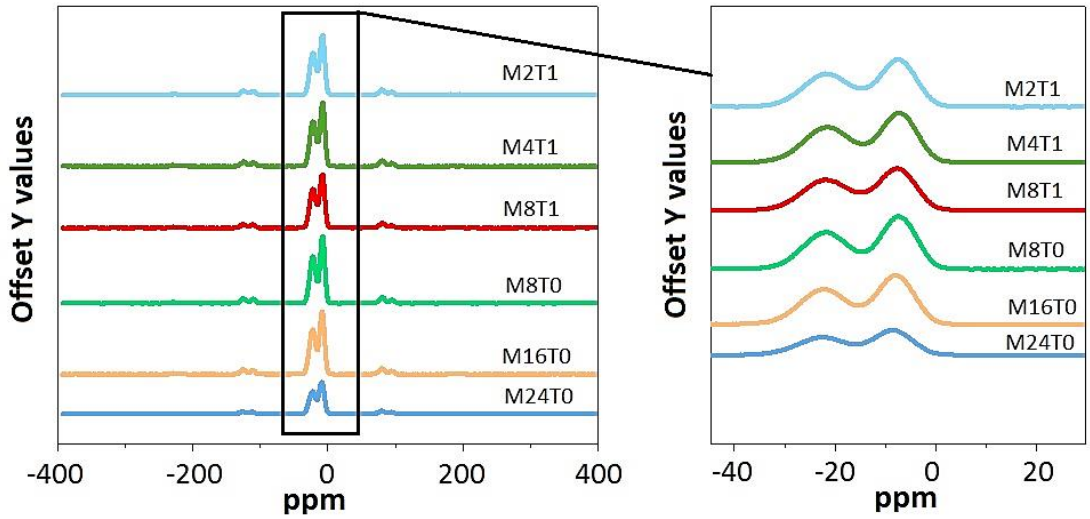


Figure 4.11: *^{31}P NMR spectra for glasses in the system $40P_2O_5$-(24-x)MgO-(16+x)CaO-(20-y)Na_2O-yTiO_2 (where 0≤x≤22 and y=0 or 1).*

Table 4.5 provides peak positions and relative proportions of Q^1 and Q^2 species for the individual glasses. The proportion of Q^2 species for the glasses without Ti was found to be between 50 to 51%. No significant variation in the relative proportions was observed between the M8T0 and M8T1 glasses.

Table 4.5: *NMR peak positions and relative proportions of Q^1 and Q^2 species in the various glasses.*

Glass formulation	$\nu(Q^1)$ / ppm **error=**± 0.2 ppm	$\nu(Q^2)$ / ppm **error=**± 0.2 ppm	Q^1 (%) **error=**± 1 %	Q^2 (%) **error=**± 1 %
M24T0	-8.3	-22.4	50	50
M16T0	-7.8	-22.1	49	51
M8T0	-7.2	-21.8	50	50
M8T1	-7.5	-21.6	48	52
M4T1	-7.1	-21.4	48	52
M2T1	-7.3	-21.5	49	51

4.2.9 Degradation studies

The degradation profiles of the glasses degraded in PBS at 37 °C over a period of 28 days are presented in **Figure 4.12 a.** An increase in mass loss was observed (from 1.9% to 3.4%) with decreasing MgO content (i.e. from 24 to 8 mol%) over the course of the study. However, with the addition of 1 mol% of TiO_2, the M8T1 glass showed 2% mass loss which was a similar mass loss to M24T0 and 41% lower mass loss than M8T0. For the fixed 1 mol% TiO_2 content glasses, mass loss was seen to increase from 2% (for M8T1) to 2.7% (for M2T1) with decreasing MgO content from 8 to 2 mol%. The medium containing the dissolution products maintained a relatively consistent pH value close to 7.5 for all the glass formulations, as can be seen in **Figure 4.12 b**.

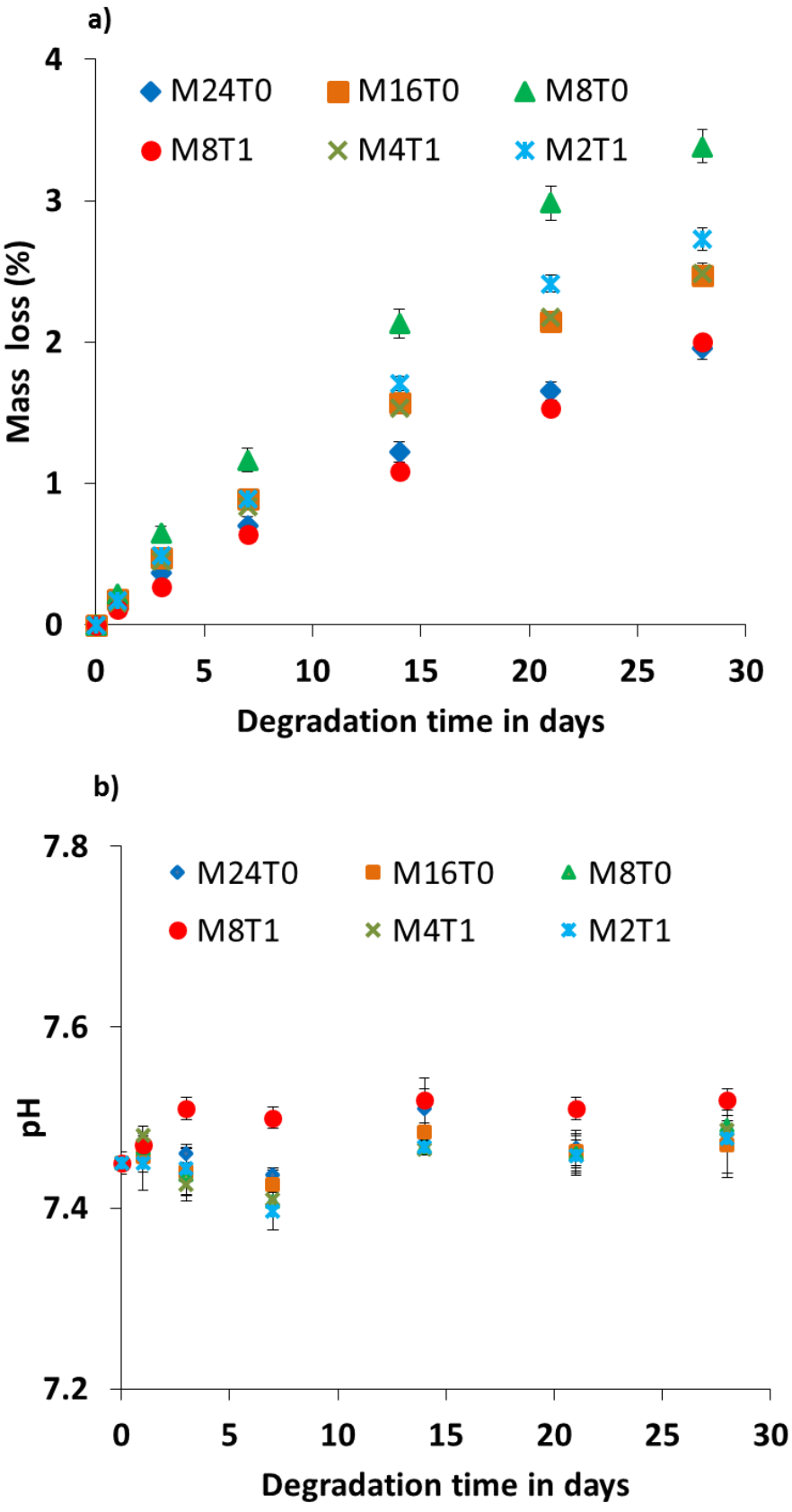


Figure 4.12: ***a)*** *Mass loss (%) and* ***b)*** *pH change as a function of immersion time (day) of the glass compositions investigated in PBS at 37 °C over 28-day duration.*

Figure 4.13 a represents the mass loss (%) of the glasses as a function of immersion time (day) in ultra-pure water (Milli-Q-water) at 37 °C. The degradation profiles of the glasses that were degraded in Milli-Q-water followed a similar trend to the mass loss profiles of the glasses that were observed in PBS. However, approximately 12% (for M16T0 and M4T1) and 20 % (for M24T0 and M8T1) higher mass loss (%) was observed in Milli-Q-water than the mass loss in PBS. On the other hand, similar mass loss was observed for M8T0 (3.4%) and M2T1 (2.7%) in both Milli-Q water and PBS over a period of 28 days. The pH values in Milli-Q-water increased slightly from 7.2 to 7.7 at day-1, then gradually decreased to 7 by day-14 and remained relatively constant for the remainder of the study as can be seen in **Figure 4.13 b**.

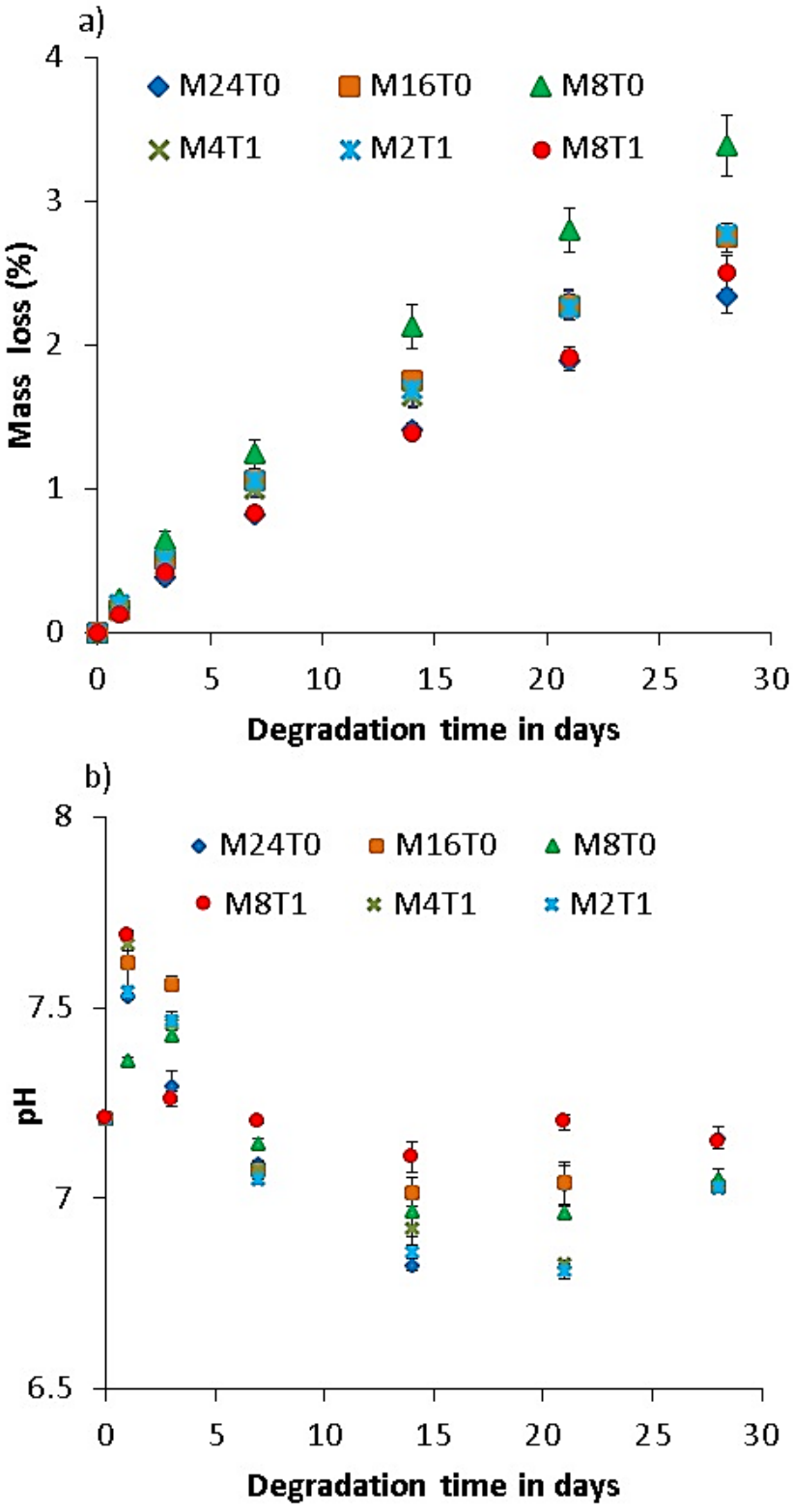


Figure 4.13: ***a)*** *Mass loss (%) and* ***b)*** *pH change as a function of immersion time (day) of the glass compositions investigated in Milli-Q water at 37 °C over 28 day duration.*

4.2.10 Ion release profiles

Concentration of Na, Mg, Ca, P and Ti in ultra-pure water during the 28 days of immersion period for phosphate glasses were investigated via ICP-MS. The cumulative ion release profiles of the glass formulations investigated appeared to follow a linear relationship with time (as can be seen in **Figures 4.14 a-e**). The ion release rates were calculated using an assumed linear relationship and are presented as an inset in **Figure 4.14 a-e**. The highest Na^+ ion release (64.5 ppm with release rate of 2.3 ppm day^{-1}) among all the formulations tested was observed for M8T0 glass and the lowest Na^+ ion release (50.5 ppm with release rate of 1.8 ppm day^{-1}) was observed for M24T0 at day 28 for the glasses containing no Titanium. On the other hand, M8T1 glass showed the lowest Na^+ ion release (45.9 ppm with release rate of 1.6 ppm day^{-1}) among all of the formulations at day 28. From **Figure 4.14 b**, it was seen that the highest Mg^{2+} ion release was observed for M24T0 glass formulation at day 28 with a release value of 22.3 ppm (release rate 0.8 ppm day^{-1}). Meanwhile, M4T1 and M2T1 glasses showed very little Mg^{2+} ion release after 28 days of immersion in ultra-pure water. Similar Mg^{2+} ion release was observed for M8T0 (6.7 ppm with release rate of 0.24 ppm day^{-1}) and M8T1 (5.3 ppm with release rate of 0.19 ppm day^{-1}) at the same time point. The calcium ion release profiles (**Figure 4.14 c**) were opposite to the magnesium ion release profiles (**Figure 4.14 b**). The M2T1 formulation showed the highest Ca^{2+} ion release (70 ppm with release rate of 2.5 ppm day^{-1}) whereas, M24T0 showed the lowest Ca^{2+} ion release (25 ppm with release rate of 0.9 ppm day^{-1}). The Ca^{2+} ion release rates for M4T1 and M2T1 were found to be similar to M8T0 (release rate 2.5 ppm day^{-1}). Whereas, M8T1 glass showed lower Ca^{2+} ion release (62 ppm with release rate of 2.2 ppm day^{-1}) than M8T0. The highest P ion (total) release (172 ppm with release rate of 6.1 ppm day^{-1}) was observed for M8T0 glass whereas the lowest P ion (total) release (120 ppm with release rate of 4.3 ppm day^{-1}) was observed for M8T1 glass at day 28 (**Figure 4.14 d**). The total P ion release for M24T0 (126 ppm with release rate of 4.5 ppm day^{-1}) and M2T1 (130 ppm with release rate of 4.6 ppm day^{-1}) glasses were found to be quite similar value of ion release rate for M8T1. On the other hand, similar P ion (total) release were observed for M16T0 (145 ppm with release rate of 5.2 ppm day^{-1}) and M4T1 (142 ppm with release rate of 5.1 ppm day^{-1}

^{1}). 1 mol% titanium containing glasses showed very small amount of titanium ion release rates (around 0.02 ppm day^{-1}). The titanium ion release for M8T1, M4T1 and M2T1 were found to be 0.5, 0.8 and 0.7 ppm, respectively after 28 days of immersion in ultra-pure water (**Figure 4.14 e**).

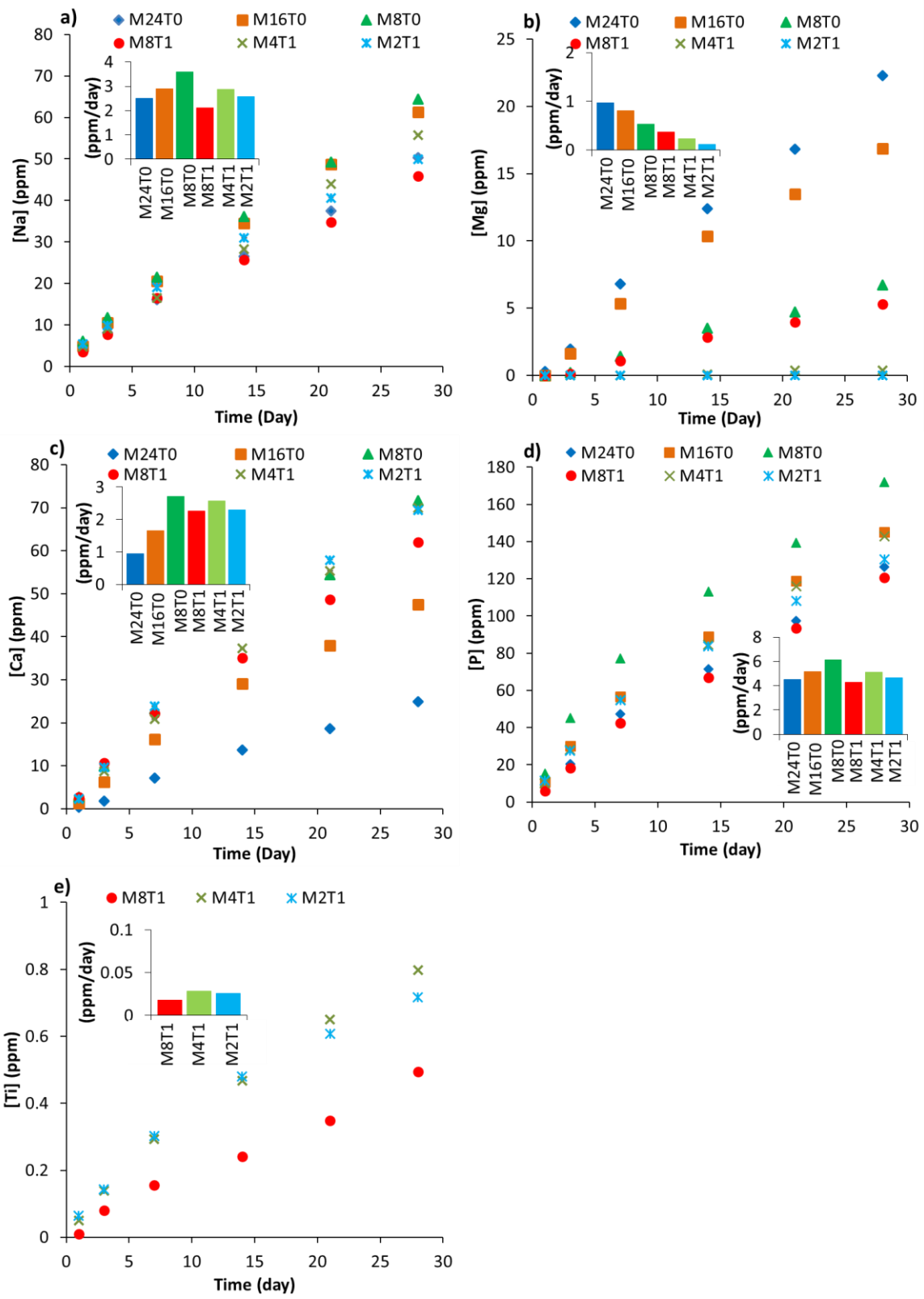


Figure 4.14: *Concentration of **a)** [Na], **b)** [Mg], **c)** [Ca], **d)** [P] and **e)** [Ti] measured via ICP-MS for the glass formulations investigated in ultra-pure-water during 28 days of immersion period. (Error bars are also included in the data above). The Inset on each graph shows the release rates of each element for the glass formulations investigated.*

4.2.11 *In vitro* bioactivity studies

XRD profiles of the glass formulations after immersion in SBF at 37 °C for 28 days are shown in **Figure 4.15**, where an absence of crystalline peaks suggested that no apatite formation occurred during the bioactivity study. However, the apatite forming ability of the prepared SBF solution was confirmed using bioactive 45S5 bioglass, where crystalline apatite peaks can be seen after 7 days of immersion in SBF (as can be seen in the inset **Figure 4.15**).

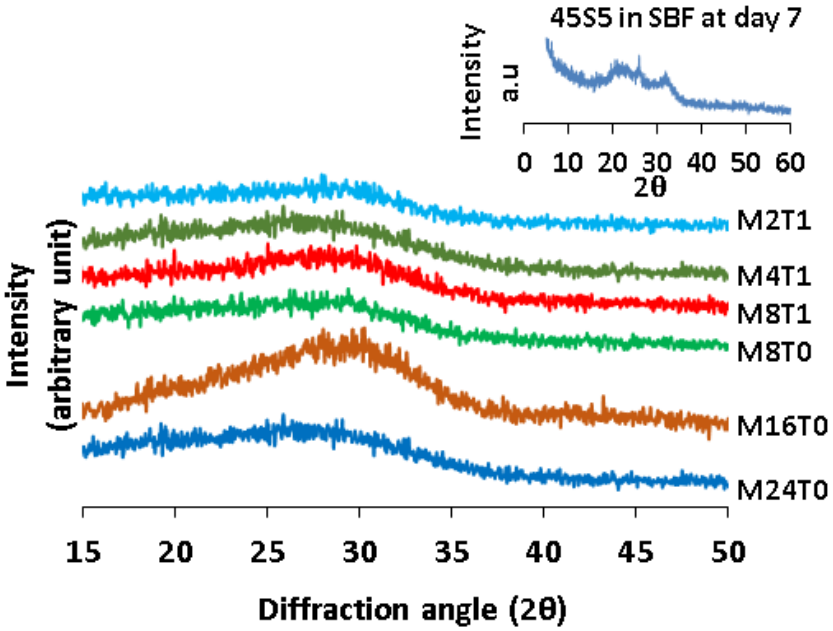


Figure 4.15: *X-ray diffraction pattern for the glass formulations investigated with reduced MgO content after immersion in SBF for 28 days.*

Figure 4.16 shows the SEM images of the surfaces of investigated glass discs before and after immersion (day 7, 14 and 28) in SBF. From the SBF studies, a small amount of precipitation was seen to form on the surface of all the glass discs after 7 and 14 days of immersion in SBF. Higher deposition was observed after 28 days of immersion in SBF. The inset SEM images of **Figure 4.16** shows the changes in surface morphology (at higher magnification) over time.

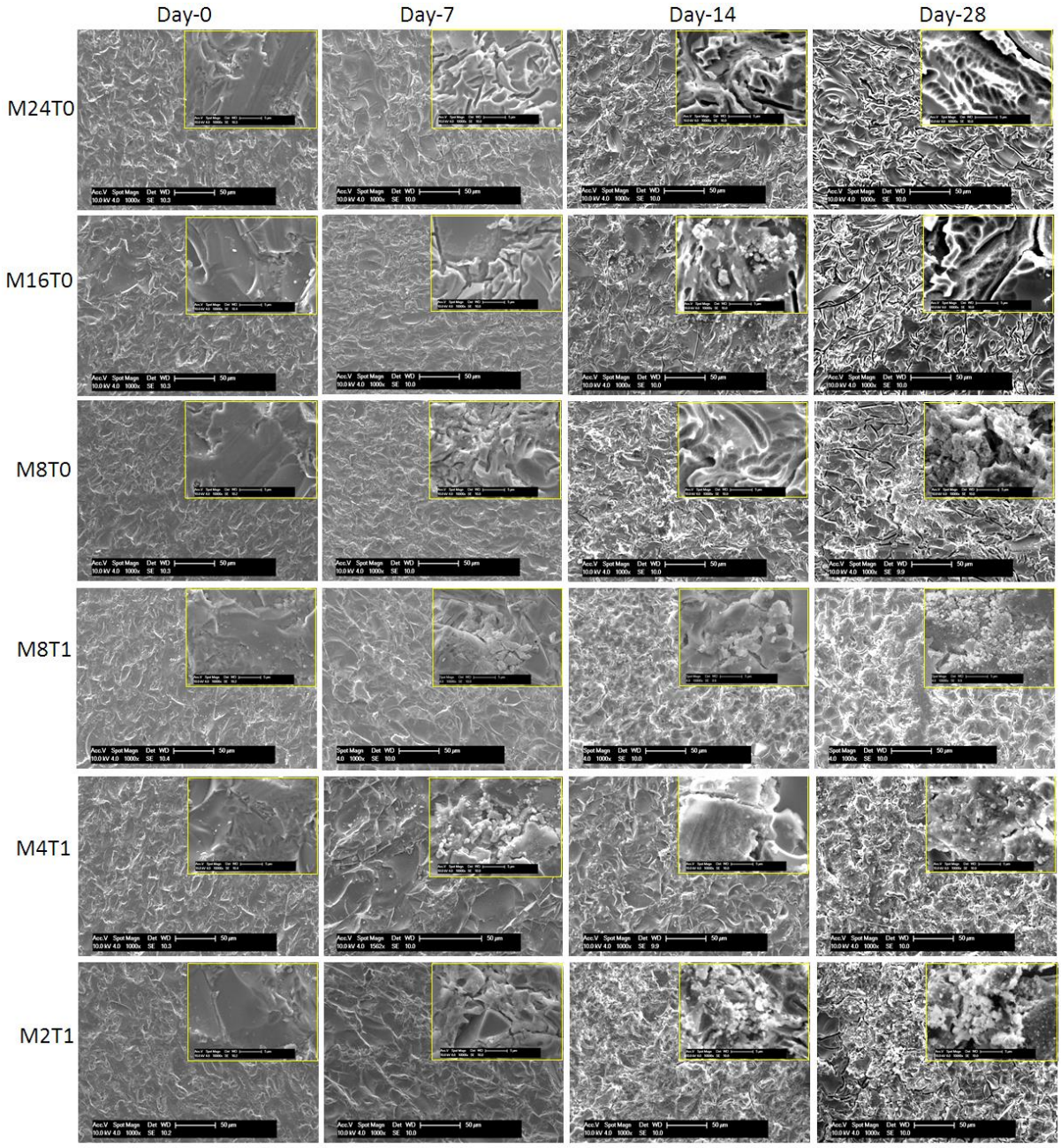


Figure 4.16: *SEM images of the surface of the 6 glasses before (Day-0) and after immersion in SBF (day 7, 14 and 28). Scale bars of inset SEM images represent 5 µm.*

Figure 4.17 shows more in-depth analysis via higher resolution images of the glass surface (M24T0, M8T0, M2T1) before and after 28 days of immersion in SBF.

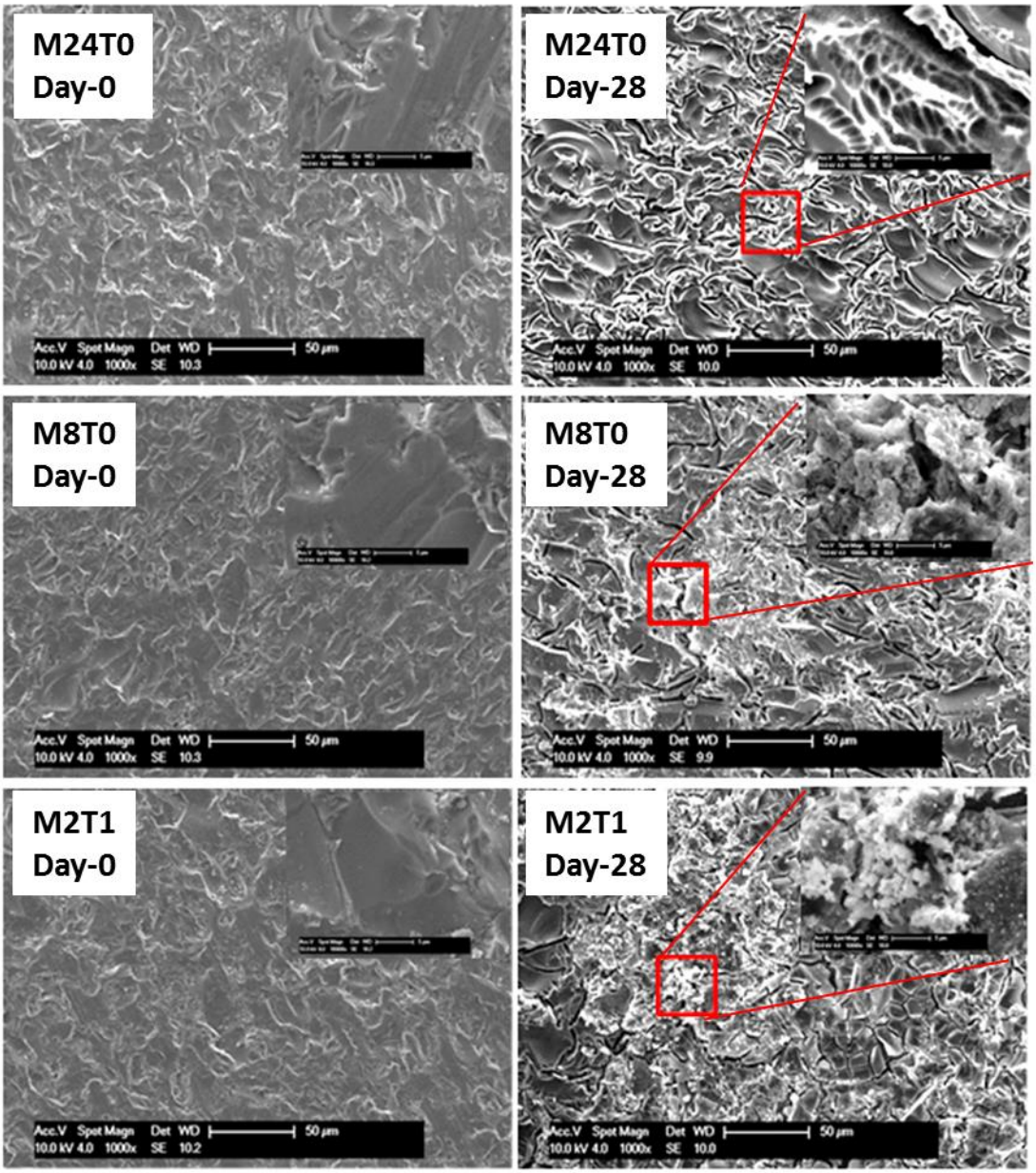


Figure 4.17: *SEM images of the surface of M24T0, M8T0 and M2T1 glasses before (Day-0) and after immersion in SBF (day-28). Scale bars of inset SEM images represent 5 µm.*

After 28 days of immersion in SBF, the chemical compositions of the precipitates on the glass discs were characterised via EDX (presented in **Figures 4.18 a-f**).

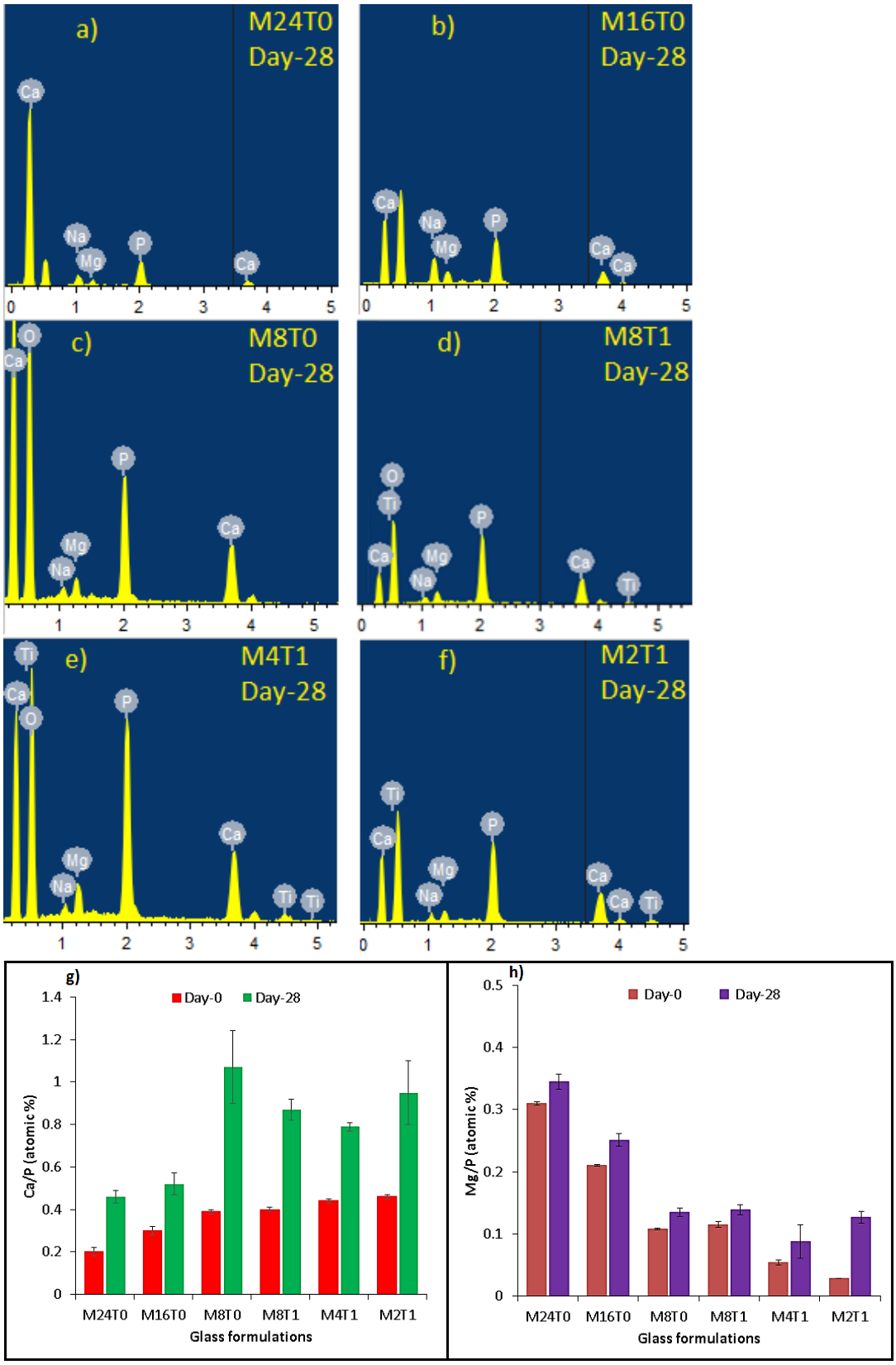


Figure 4.18: ***a-f)*** *EDX spectra of the six different glass formulations after 28 days of immersion in SBF, g) Ca/P ratio (atomic %) and h) Mg/P ratio (atomic %) of the glasses before and after 28 days of immersion in simulated body fluid obtained via energy dispersive X-ray spectroscopy analysis.*

The Ca/P ratio of each glass formulation was also calculated from the EDX values obtained as shown in **Figure 4.18 g**. The Ca/P ratio was seen to increase with immersion time in SBF (see **Figure 4.19**) and the Ca/P ratios were used to predict the potential phases present on the glass surface. Furthermore, the Mg/P ratios of these glasses have been calculated and are presented in **Figure 4.18 h**, where the Mg/P ratio was seen to decrease with the reduced MgO content as expected. However, after the SBF study, the Mg/P ratio of each glass formulation had increased when compared to their initial values (i.e., before SBF study).

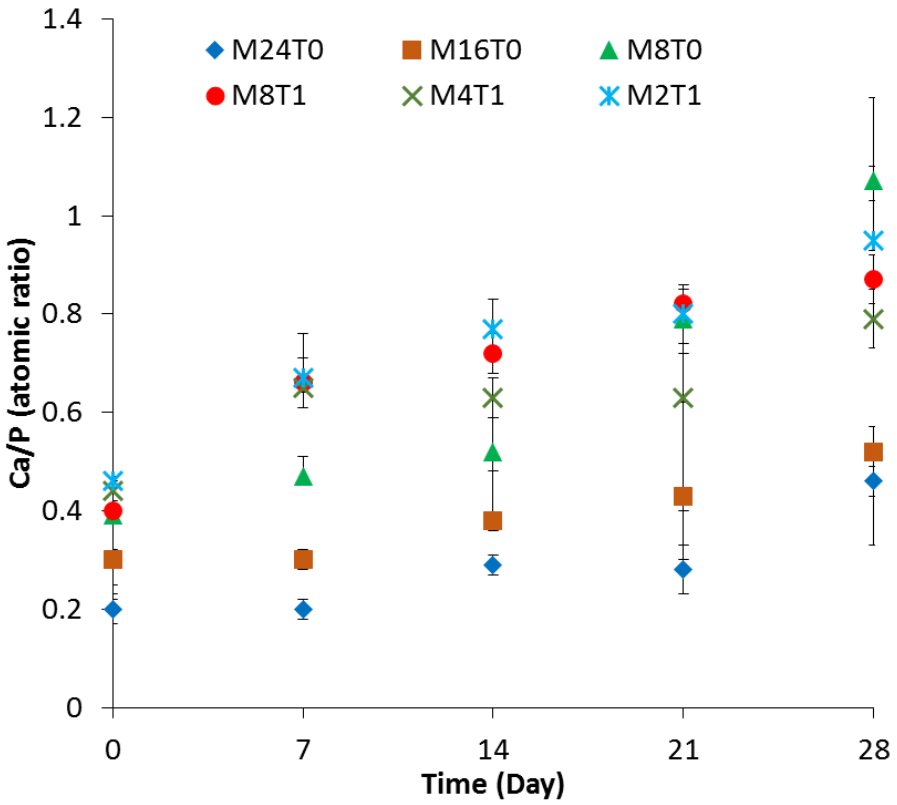


Figure 4.19*: Ca/P atomic ratio of the glasses obtained over 28 days of immersion in SBF.*

Figure 4.20 represents the variation of pH for the six glasses as a function of immersion time (days) in SBF at 37 °C, over a period of 28 days. A relatively neutral pH value (at around 7.3) of the SBF containing the dissolution products was observed for all glass formulations (except M8T1, pH ~7.6) (see **Figure 4.20**).

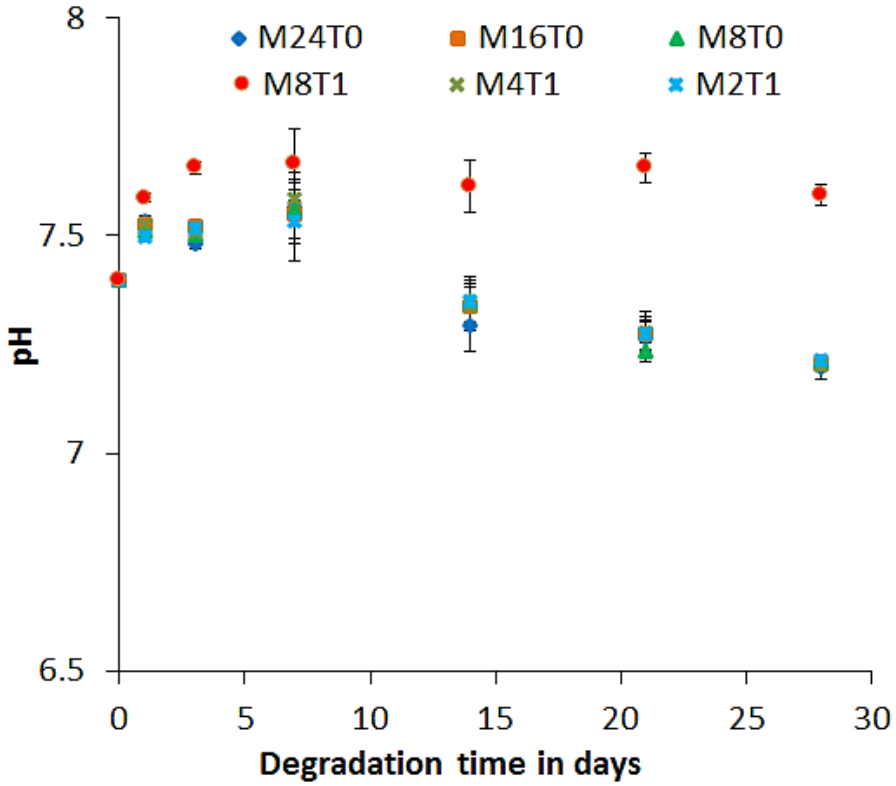


Figure 4.20: *pH change for the six glasses as a function of immersion time (days) in SBF at 37 °C, over a period of 28 days*.

4.3 Discussion

PBGs are composed of P_2O_5 (as network former) and in this study have been modified with other modifying oxides, such as, CaO, Na_2O, MgO, and TiO_2. By varying the glass compositions, degradation and ion release profiles can be tailored accordingly to their specific end application. Reports in the literature show conflicting evidence for the role of Mg on apatite formation [198] suggesting that it can delay the transformation of ACP to more stable apatite phases [199]. However, the glass forming ability strongly depends on glass composition [146]. Several researchers have investigated the crystallisation behaviour of different types of glasses [218,303-305] and report that crystallisation is strongly affected by the glass composition, heating rate and particle size [218,303]. In this current study, the effect of decreasing MgO (and hence increasing CaO) content and the addition of TiO_2 on glass formation ability was investigated for glasses in the system $40P_2O_5$-(24-x)MgO-(16+x)CaO-(20-y)Na_2O-yTiO_2 (where $0 \leq x \leq 22$ and y=0 or 1), including assessment of the physical, thermal, structural and crystallisation properties. In addition, the effect of MgO content (from 2 to 24 mol%) on degradation, ion release, and *in vitro* bioactivity properties in the above glass system with fixed 40 mol% P_2O_5 was also evaluated.

4.3.1 Density of glasses

Density measurements give an indication of the degree of change in the glass structure with the variation of glass composition. The decrease in glass density from 2745 kgm^{-3} (for M24T0) to 2725 kgm^{-3} (for M8T0) (see **Figure 4.2**) with reducing MgO content was attributed to the replacement of the higher density element Mg (1.74 gcm^{-3}) [306] with the lower density element Ca (1.55 gcm^{-3}) [306]. Furthermore, the M8T1 glass showed a higher density than M8T0 which was attributed to the lower density element Na (0.97 gcm^{-3}) [306] being replaced by the higher density element Ti (4.5 gcm^{-3}) [306]. A similar study conducted by Abou Neel *et al.* found that the density increased from 2.58 to 2.68 gcm^{-3} with the addition of 15 mol% TiO_2 into a ternary phosphate glass formulation [43]. They reported that the increase in density was due to the replacement of low density Na with the higher density element Ti [43].

As seen from **Figure 4.3**, the oxygen density decreased, whilst the molar volume increased, with the substitution of MgO by CaO in this glass series. This was attributed to the fact that calcium has a larger ionic radius than magnesium, and as a result has lower polarising power due to its small charge to size ratio and subsequently lower attractive force to non-bridging oxygens (NBO) [218]. A similar finding was suggested by Al-noaman *et al.* who reported that the oxygen density increased from around 1.19 to 1.23 gcm^{-3} with the addition of 20 mol% MgO in place of CaO [218]. The compactness of the glasses in this study decreased with decreasing MgO content for the formulations containing no TiO_2. However, with the addition of 1 mol% TiO_2 the compactness of the structure increased as evidenced when compared to the oxygen density of the glass without TiO_2 (i.e. M8T0).

4.3.2 Thermal properties

The thermal properties of phosphate-based glasses (PBGs) are strongly dependent on their structural features, such as chain length, cross-linking density, bonding strength [307] and composition [308,309]. The decrease in T_g, T_x, T_c and initial melting temperature with decreasing MgO content for glasses that did not contain TiO_2 (see **Table 4.2**) was also attributed to the same reasons as discussed above for the oxygen density, i.e. due to the replacement of Mg-O bonds with Ca-O bonds. This was also suggested to be due to the lower field strength of Ca^{2+} (0.33) as compared to Mg^{2+} (0.45) [176], as Mg^{2+} has a smaller ionic radius (0.65 Å) compared to Ca^{2+} (0.99 Å) [310]. Furthermore, the smaller size of Mg results in a high charge to size ratio and thus exhibits higher electronegativity, which creates higher attractive forces to non-bridging oxygens (NBO) as compared to Ca [218]. Therefore, it was anticipated that Mg developed a stronger cross-linking effect with phosphate chains, compared to Ca [311,312], which also correlated with a high compact structure for higher Mg content glasses as indicated by the oxygen density data.

The addition of 1 mol% TiO_2 was found to have increased T_g, T_x, T_c and initial T_m of M8T1 in comparison to glass code M8T0. This increase in T_g, T_x, T_c and initial T_m was attributed to the replacement of Na-O bonds with Ti-O as Ti^{4+} ions have a higher field strength and greater bond strength than Na^+ [43,313]. A similar effect on T_g values for

replacing Na^+ with Ti^{4+} was also observed in the $50P_2O_5$-30CaO-(20-x)Na_2O-xTiO_2 glass system investigated by Abou Neel *et al.* where the T_g values increased from 383 to 538 °C with addition of up to 15 mol% TiO_2 [43]. They suggested that this increase in T_g with addition of TiO_2 was due to the smaller ionic radius of Ti^{4+} (0.56 Å) compared to Na^+ (0.97 Å), where the size of ions (i.e. ionic radius) introduced into the glass network was a key factor in controlling their chemical durability and thermal stability. As TiO_2 has a smaller ionic radius and higher electrical charge than Na^+ it most likely generated stronger cross-linking between the phosphate chains via creating Ti–O–P links [314-316]. This finding also correlated with the compactness of the glass structure as the oxygen density increased with the addition of TiO_2.

The glass forming tendency of the formulations investigated was seen to decrease with the substitution of MgO with CaO as the glass stability against crystallisation decreased from 106 °C (for M24T0) to 90 °C (for M8T0) (see **Table 4.2**). Formulations containing less than 8 mol% MgO in the series investigated showed a strong tendency towards crystallisation (see **Figure 4.5 a**). The crystalline phase was indexed with alpha-calcium pyrophosphate (α-$Ca_2P_2O_7$) (ICDD No. 00-009-0345) (see **Figure 4.1**). According to Dietzel, MgO can behave as an intermediate oxide [317] and in its intermediate state, can potentially act as a network former as well as a cross-linker between the phosphate chains [311,312,318]. On the other hand, Ca acts only as a network modifier and depolymerises the phosphate chains, which consequently increases the mobility of the phosphate structural groups in the melt [146]. As a result, the components can arrange themselves into an ordered crystalline structure more easily [146]. Therefore, for this glass series, a decrease in MgO content promoted the formation of a calcium phosphate phase which lead to an increase in crystallisation tendency.

It has also been reported that the addition of TiO_2 to PBGs increased the glass stability by the formation of cross-links between the phosphate chains [202,315,316,319]. A number of studies have also suggested that titanium can enter the phosphate glass network as Ti^{4+} ions and thus behave as a glass network former [202,207]. In the present study, 1 mol% of Na_2O was replaced with TiO_2 in those glass formulations with MgO content 8 mol% and less than 8 mol%. A rapid cooling process was also employed (for M4T1

and M2T1) by pouring the molten glass in between two metal plates at room temperature, which resulted in an amorphous glass structure, as evidenced by the XRD traces presented in **Figure 4.1**. Therefore, the crystallisation tendency may have been inhibited by the addition of 1 mol% TiO_2 (see **Figure 4.5 b**).

Crystallisation is generally described by the activation energy for crystallisation (E_c) and the Johnson-Mehl-Avrami (JMA) exponent [304]. As seen from **Figure 4.7**, the crystallisation temperature and peak height increased with increasing heating rate. This could be attributed to the fact that the heat flow to the samples increased with increasing heating rate [218]. A similar result of increasing crystallisation peak intensity was also observed by Al-noaman *et al.* for silicate glasses, which increased from around 1 to 45 mcal/sec with increasing heating rate from 5 to 20 $^oCmin^{-1}$ [218]. This result was also in good agreement with the results found by Clupper and Hench [320] and Bretcanu *et al.* [321]. Massera *et al*. also studied the effect of heating rate on the crystallisation peak intensity for $50P_2O_5$-40CaO-SrO-$10Na_2O$ glasses with particle sizes in the range 300-500 µm [304]. They reported that the crystallisation peak intensity increased from 1.1 to 1.4 Wg^{-1} with increasing heating rate from 5 to 20 $^oCmin^{-1}$ [304]. The changes in the width (broad vs narrow) of the crystallisation peaks are usually indicative of changes in the crystallisation mechanism [303]. The intensity of crystallisation peaks are often used to determine whether crystallisation has occurred at the surface or within the bulk of the materials [145,322]. A broad crystallisation peak can be associated with surface crystallisation whereas a sharp peak is associated with bulk crystallisation [303].

The decrease in E_c with decreasing MgO content for glasses containing no Ti content and the higher E_c for M8T1 (compared to M8T0) was attributed to the effect of field strength as discussed above for oxygen density and thermal analysis. This result also correlated well with the glass stability (ΔT) data (shown in **Table 4.2**). Brauer *et al.* investigated the effect of TiO_2 on crystallisation behaviour in the P_2O_5-CaO-MgO-Na_2O glass system and reported that the activation energy increased from 270 to 360 $kJmol^{-1}$ with increasing TiO_2 content from 0 to 5 mol% due to the formation of higher cross-links between phosphate units [313]. The variation of E_c as a function of glass composition was in good agreement with the change in the crystallisation behaviour

found by SDT analysis. Types of crystal growth must be determined for understanding the nucleation and growth kinetics of the first crystal that forms during heat treatment. During crystallisation of the glasses, the parameter, n, of the JMA model provides some insight into the crystal growth dimensionality [141]. The JMA exponent was calculated by the equation proposed by Augis and Benett [Eq 3.6] and shown in **Table 4.3**. Usually, n~1 is associated with surface crystallisation, n=2 with 2D and n=3 with 3D bulk crystallisation, with n>3 indicative of complex crystallisation behaviour[323].

4.3.3 Structure of glasses

FTIR and Raman spectra for the glasses showed small variations in terms of intensities and positions of peaks as a function of composition. These results were expected as the substitution of MgO by CaO did not change the O/P ratio and hence no variation in Q species was expected. Similarly, no significant change in the relative proportion of Q^1 and Q^2 species was found from the ^{31}P NMR analysis and all of the glass formulations contained an almost equal percentage of Q^1 and Q^2. The small variations observed were within error from the fitting. The redshift in the position of the symmetric and asymmetric P-O-P stretching modes observed in the FTIR spectra was consistent with the replacement of higher field strength Mg^{2+} by lower field strength Ca^{2+} [324], leading to increases in the P-O-P bond angle as a consequence of either longer phosphate chain lengths or the presence of larger cationic size [325]. The same vibrational modes (ν_s(P-O-P) and νa_s(P-O-P)) were blueshifted to a higher frequency for M8T1 relative to M8T0 due to the same reason as the replacement of lower field strength Na^+ ions by higher field strength Ti^{4+} ions [324] . A similar study was done by Abou Neel *et al.* who found that the asymmetric ν_{as}(P-O-P) stretching modes shifted to higher frequency and the peak intensity decreased with increasing SrO content due to the replacement of Na^+ ions by higher field strength of Sr^{2+} ions [44]. Pickup *et al.* also studied the neutron diffraction of $CaO–Na_2O–P_2O_5$ glasses and reported that the phosphorus to bridging oxygen distance (P-O) decreased with increasing the average cation field strength by replacing Na^+ with Ca^{2+} [326]. Koo *et al.* investigated the structural analysis of binary copper phosphate glass, $xCuO.(1- x)P_20_5$ where, x = 0.4, 0.5, and 0.55 and various $[Cu^{2+}]/[Cu_{total}]$ ratios [327]. They reported that the asymmetric

ν_{as}(P-O-P) stretching modes shifted to longer frequency for higher [Cu^{2+}] ratio sample due to the decreasing of P-O-P bond angle as smaller ionic size of Cu $^{2+}$ compared to Cu^{1+} [327]. The increase in the intensity of the asymmetric ν_{as}(P-O-P) stretching modes with reducing MgO for the glasses containing no TiO_2 could be due to the decrease in phosphate-cation bonding interaction as Mg^{2+} has higher field strength than Ca^{2+} [44]. On the other hand, the Ti containing glasses showed broader peaks as compared to M8T0, which may have been due to Ti^{4+} increasing the phosphate-cation bonding interactions compared to Na^{+} [44]. The bands at around 1000 and 1100 cm^{-1} were assigned to symmetric $\nu_s(PO_3)^{2-}$ and asymmetric $\nu_{as}(PO_3)^{2-}$ modes, respectively which are associated with Q^1 species [113,328]. The intensity of the absorption bands for asymmetric stretching modes, $\nu_{as}(PO_3)^{2-}$ of the chain terminating groups of the glasses increased with decreasing MgO content down to 8 mol%, which was an indication for decreasing the cross-links between the glass network and thereby reducing the rigidity of the network [299]. However, the addition of 1 mol% TiO_2 (i.e. M8T1) reduced the intensity (compared to M8T0) of the absorption bands for the asymmetric stretching modes, $\nu_{as}(PO_3)^{2-}$ significantly. Similarly, this could be attributed to the increase in degree of polymerisation or creating more cross-linking between the glass network as Ti can act as a network former or network modifier [299].

From the mean Raman spectra, obtained by averaging point spectra collected from five random locations, a diagnostic peak for Ti containing glasses was observed at 899 cm^{-1}, associated with a Ti-O stretching vibration in TiO_5 (titanyl) units which suggested the role of TiO_2 as a network modifier [302]. Although subtle differences in the intensity of the red colouration were noted in the false colour spectroscopic map, associated with differences in surface topography, TiO_5 was found to be within every pixel of the map, indicating its uniform dispersion throughout the surface of the glass. No evidence for the presence of TiO_6 (titanate) units, which typically are observed at around 640 cm^{-1} in the Raman spectrum, and known to act as a network former [302], were found for the 1 mol% TiO_2 containing glasses investigated. However, titanium can also behave as a network former at low concentrations (upto 3 mol%) in phosphate glasses [329]. Therefore, further investigation is required to confirm the role of titanium in the glass series explored.

4.3.4 Degradation

The effects of exchanging MgO for CaO and Na_2O for TiO_2 and the effect on structure was also reflected in the degradation studies. As might be expected, providing a reduced number of higher strength bonds within the structure of the glasses (by switching Mg to Ca) resulted in a lower resistance to hydrolysis, with the opposite being the case switching Na to Ti [43]. This can be seen in the degradation data in **Figure 4.12 a**, with mass losses increasing from M24T0 to M8T0, and reducing with M8T1 and then increasing again from M8T1 to M2T1. From the ion release studies conducted, magnesium ion release rates were seen to decrease whereas calcium ion release rates increased with the substitution of MgO for CaO, as expected. For the formulation containing no titanium, the highest Na^+ ion release rates (2.3 ppm day^{-1}) were observed for M8T0, whilst M24T0 glass showed the lowest Na^+ ion release rates (1.8 ppm day^{-1}). Overall, the total amount of ions (Na, Ca and Mg, P, Ti) released for the glass formulations investigated after 28 days of immersion in ultra-pure water were found to increase from 250 ppm to 363 ppm with reducing MgO content from 24 to 8 mol%. This could be explained in terms of the more compact glass structure of M24T0 than M8T0 due to higher density of higher Mg-containing glasses (**Figure 4.2**) as well as the Mg intermediate oxide. This result also correlated with NMR and Raman analysis, where no change in network was observed with the replacement of Mg with Ca. However, higher degradation rate was observed for higher calcium containing glasses due to the replacement of stronger bond Mg-O with weaker bond Ca-O (for the glasses with no Ti). On the other hand, M8T1 glass showed the total ion release of 113 ppm which was 30 ppm in lower than for M8T0. This could also be attributed to the same reason of a more compact glass structure of M8T1 than M8T0 as the density increased with the replacement of Na with Ti (**Figure 4.2**) as well as due to the replacement of weaker bond Na-O with the stronger bond Ti-O. Moreover, Ti can create higher cross-linking compared to Na. It was also reported that phosphate glasses with a more compact network structure showed lower solubility due to the difficulty of water molecules to penetrate and hydrate phosphate chains in the glasses [311].

The rate of degradation between day-0 and day-15 was higher for all of the glasses in comparison to the rate of degradation between day-15 and day-28 (see **Figure 4.13 a**). Similar trend was observed from the ion release profiles (especially for P ion release) (see **Figure 4.14**) which correlated well with the decrease in pH observed, where the minimum pH was seen at day-15 for all of the glass formulations investigated (see **Figure 4.13 b)**.

4.3.5 *In vitro* bioactivity

In vitro bioactivity tests conducted in this study suggested that apatite formation was not observed on any of the glass formulations even after 28 days of immersion in SBF (see XRD traces in **Figure 4.15**). However, some precipitate deposits (i.e. amorphous calcium phosphate) were found on the surface of some of the glasses (see **Figure 4.16**). EDX analysis of the deposits on the surface of glass discs (see **Figure 4.18 g**) showed a difference in Ca/P ratio as compared to the bulk glass. The Ca/P ratios for M8T0 (1.07), M8T1 (0.87), M4T1 (0.79) and M2T1 (0.95) fell within the range suggested for precipitated amorphous calcium phosphate (ACP) (0.67 to 1.5) [248,330]. This precipitated ACP phase has been stated to be a precursor phase towards formation of hydroxyapatite [331]. This conversion is mediated by surface charge, pH and the proportion of ions in solution (Ca^{2+}, PO_4^{3-}, OH^-, CO_3^{2-} and Na^+) [13,154]. Since SBF is designed to provide the right ionic and pH conditions for HA crystal deposition it would suggest that the glasses do not provide an optimum surface charge. Surface stability may also be a factor, since the mass loss rates shown in **Figure 4.12 a** and **Figure 4.13 a** (albeit in PBS or in ultra-pure water rather than SBF) are considerable.

The addition of 1 mol% TiO_2 to the phosphate glass network (in the glass series investigated) was shown to increase durability via cross-linking of the phosphate chains, and was sufficient to reduce the crystallisation tendency of the lower Mg containing glasses in the glass system $40P_2O_5$-(24-x)MgO-(16+x)CaO-(20-y)Na_2O-yTiO_2 (where $0 \leq x \leq 22$ and y=0 or 1). Moreover, for the more stable titanium containing glasses that show some evidence of ACP deposition, longer term development of HA may be feasible.

4.4 Summary

The glass forming ability for the composition with the replacement of MgO by CaO in $40P_2O_5$-(24-x)MgO-(16+x)CaO-(20-y)Na_2O-yTiO_2 (where $0 \leq x \leq 22$ and y=0 or 1) glass system was investigated. The substitution of MgO with CaO in the glasses lead to a decrease in glass transition, onset crystallisation, crystallisation, initial melting temperature, density, oxygen density and activation energy of crystallisation due to the replacement of higher field strength Mg^{2+} by lower field strength Ca^{2+}. For similar reasons, an increase in mass loss was observed in both PBS solution and ultra-pure water.

The addition of 1 mol% TiO_2 was sufficient to suppress the crystallisation of lower MgO containing (M4T0, M2T0) glasses and increased the resistance to hydrolysis. No significant change of Q species was observed.

Total amount of ion (Na, Ca and Mg, P, Ti) release for the glasses investigated at day 28 in ultra-pure water, was seen to increase from 250 ppm to 363 ppm with decreasing MgO content from 24 to 8 mol%, which correlated well with mass loss profiles.

During the *in vitro* bioactivity study none of the glasses formed HA. However, the glasses with reduced amounts of MgO (8 mol% and below) indicated the formation of ACP (a precursor to HA) with the Ca/P ratio ranging from 0.79 to 1.07.

CHAPTER 5

MANUFACTURE AND CHARACTERISATION OF SOLID AND POROUS PHOSPHATE GLASS MICROSPHERES FOR BIOMEDICAL APPLICATIONS

5.1 Introduction

Based on degradation, ion release and *in vitro* bioactivity study of phosphate based glasses (PBGs) in the system of $40P_2O_5$-(24-x)MgO-(16+x)CaO-(20-y)Na_2O-yTiO_2 (where 0≤x≤22 and y=0 or 1) mentioned in previous chapter 4, three PBG formulations (M24T0, M8T0 and M2T1) were selected to investigate manufacture of solid and porous glass microspheres. M8T0 and M2T1 glass formulations were selected due to comparatively higher amorphous calcium phosphate (ACP) deposition observed on the surface of these glass discs and M24T0 glass formulation was selected as a control formulation due to the excellent cytocompatibity properties of this formulation[265] and its ease of manufacture (as it requires no P_2O_5 addition).
In this chapter, a comparative studies between solid and porous glass microspheres on physical, thermal, degradation, ion release and *in vitro* bioactivity of three different PBG formulations was conducted.

5.2 Results

5.2.1 Composition of PBG glasses

The composition obtained via EDX of selected three different phosphate glass formulations to prepare microspheres are presented in **Table 5.1**, where it can be seen that the respective oxide contents were within 1.5 mol% of their expected values.

Table 5.1: *Composition (in mol%) of selected three different phosphate glass formulations for microspheres preparation.*

Glass code	P_2O_5 (mol%) (Expected / actual)	MgO (mol%) (Expected /actual)	CaO (mol%) (Expected /actual)	Na_2O (mol%) (Expected /actual)	TiO_2 (mol%) (Expected /actual)
M24T0	40 / 39.9 ± 0.1	24 / 23.5 ± 1.7	16 / 16.3 ± 1.6	20 / 20.3 ± 0.6	0 / 0
M8T0	40 / 39.9 ± 0.1	8 / 8.3 ± 0.5	32 / 31.4 ± 0.6	20 / 20.5 ± 0.2	0 / 0
M2T1	40 / 40 ± 0.1	2 / 2.5 ± 0.1	38 / 36.9 ± 0.2	19 / 19.7 ± 0.1	1 / 0.9 ± 0.1

5.2.2 Surface morphology via SEM

Figures 5.1 A and **B** show the SEM images of solid and porous microspheres prepared from the phosphate based glass formulations investigated. From **Figure 5.1**, it is seen that both solid and porous glass microspheres were successfully prepared via the flame spheroidisation processing route.

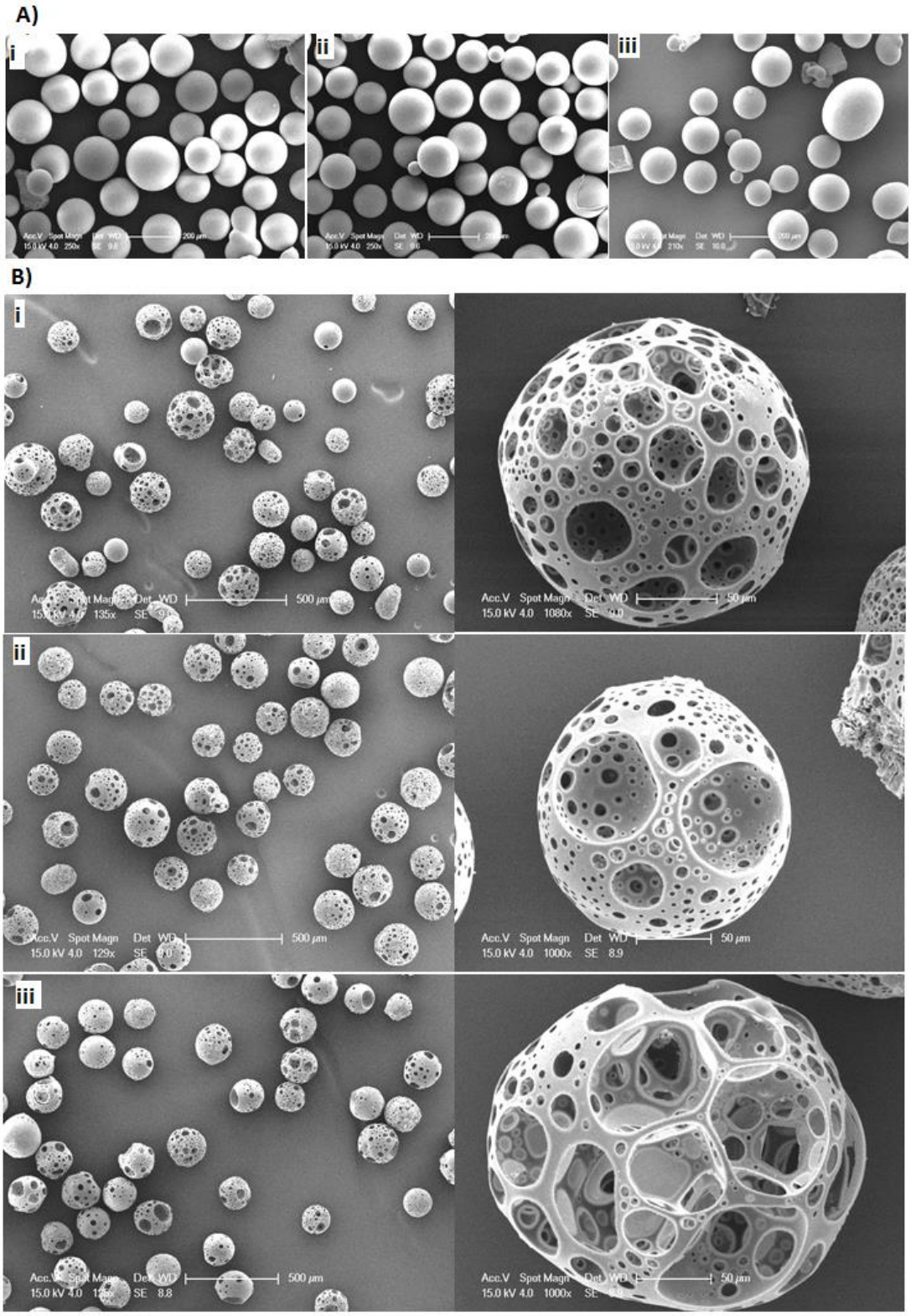


Figure 5.1: *SEM images of prepared A) SGMS B) PGMS (washed) of i) M24T0, ii) M8T0 and iii) M2T1 glass formulations investigated.*

In order to examine the internal structure of the porous phosphate glass microspheres, the cross-section was imaged after embedding the microspheres in a cold setting epoxy resin and ground and polished using SiC paper and a diamond cloth. **Figure 5.2** shows the SEM cross-sections of three different porous phosphate glass microspheres.

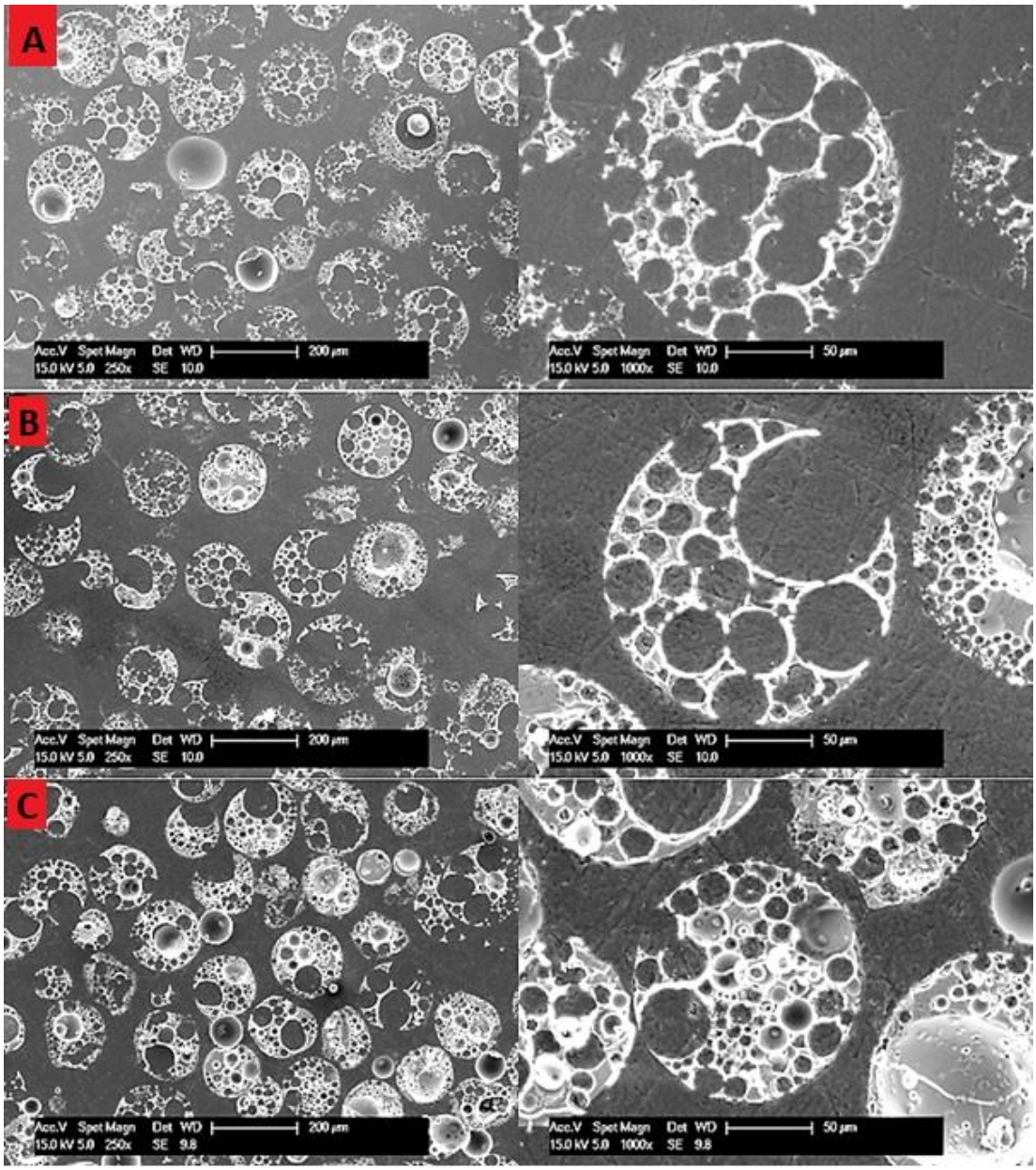


Figure 5.2: *Cross-section of prepared porous microspheres of A) M24T0, B) M8T0 and C) M2T1 phosphate glass formulations investigated.*

5.2.3 X-ray diffraction (XRD) analysis

XRD traces for the solid and porous glass microspheres are presented in **Figures 5.3 A** and **B** respectively, where a single broad peak between 20° and 40° (2θ) was observed for solid glass microspheres of each composition. The absence of any sharp crystalline peaks for SGMS confirmed the amorphous nature of the glass microspheres. However, small peaks were observed for the porous glass microspheres of every composition.

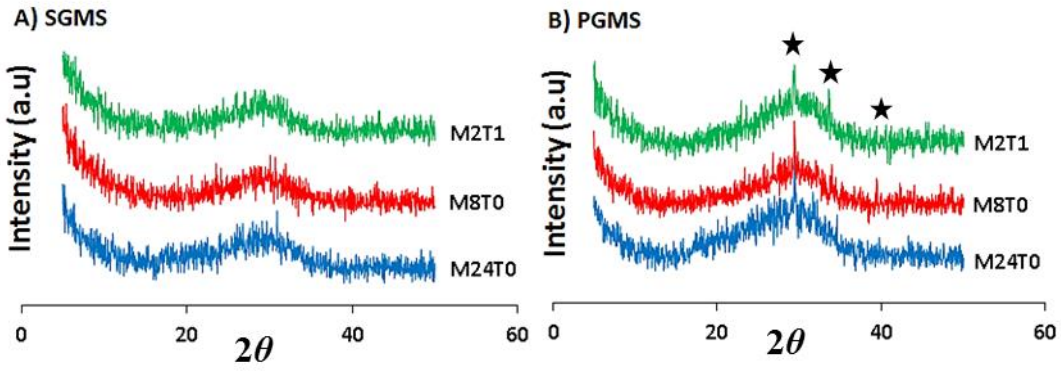


Figure 5.3: *X-ray diffraction pattern for A) SGMS and B) PGMS (washed) of three PBG glass formulations investigated. ★ represents for calcium carbonate ($CaCO_3$) peaks.*

5.2.4 Compositional analysis via EDX

Figure 5.4 represents the chemical compositions obtained from EDX analysis of the starting bulk glass (BG), SGMS and PGMS for M24T0, M8T0 and M2T1 glass formulations. As seen from **Figure 5.4**, no significant variation of chemical composition between BG and SGMS was observed for all three glass formulations. However, in comparison significantly higher CaO content and lower P_2O_5 content was observed for the PGMS. For example, around 5 mol% lower P_2O_5 and 7 mol% higher CaO content was observed for PGMS of M2T1 as compared to the BG and SGMS of the same formulation.

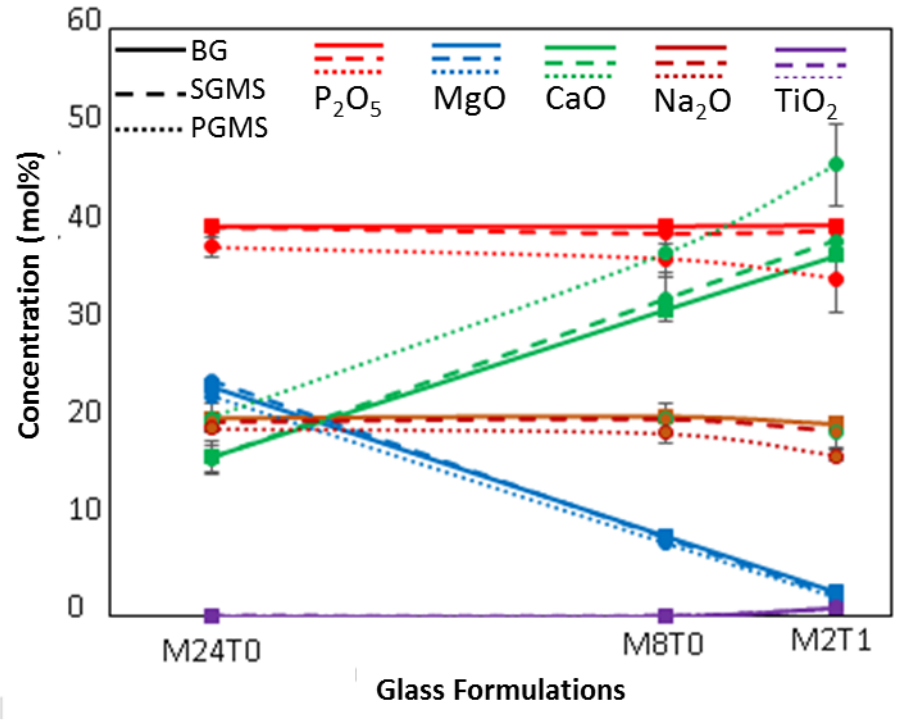


Figure 5.4: *Chemical composition for three different morphologies such as BG, SGMS and PGMS of M24T0, M8T0 and M2T1 glass formulations.*

5.2.5 Thermal properties

Figure 5.5 shows the thermal traces of BG, SGMS and PGMS where the corresponding glass transition (T_g), onset of crystallisation (T_x), crystallisation peak (T_c) and melting (T_m) temperature have been labelled. The thermal data such as T_g, T_x, T_c and T_m for the three different morphologies (i.e. bulk glass, solid and porous glass microspheres) are presented in **Table 5.2**. No significant changes were observed for T_g and initial melting temperature among BG, SGMS and PGMS of the same glass formulation (see **Table 5.2**). However, no melting peak was observed for M2T1 PGMS. On the other hand, SGMS showed higher T_x and T_c than for their respective BG formulation. Whereas, PGMS showed lower in T_x and T_c than for BG. For example, 17 ^oC higher T_x and 22 ^oC higher T_c value were observed for SGMS of M24T0 than for BG. On the other hand, 46 ^oC lower in T_x and 25 ^oC lower in T_c value were observed for PGMS of M24T0 as compared to BG.

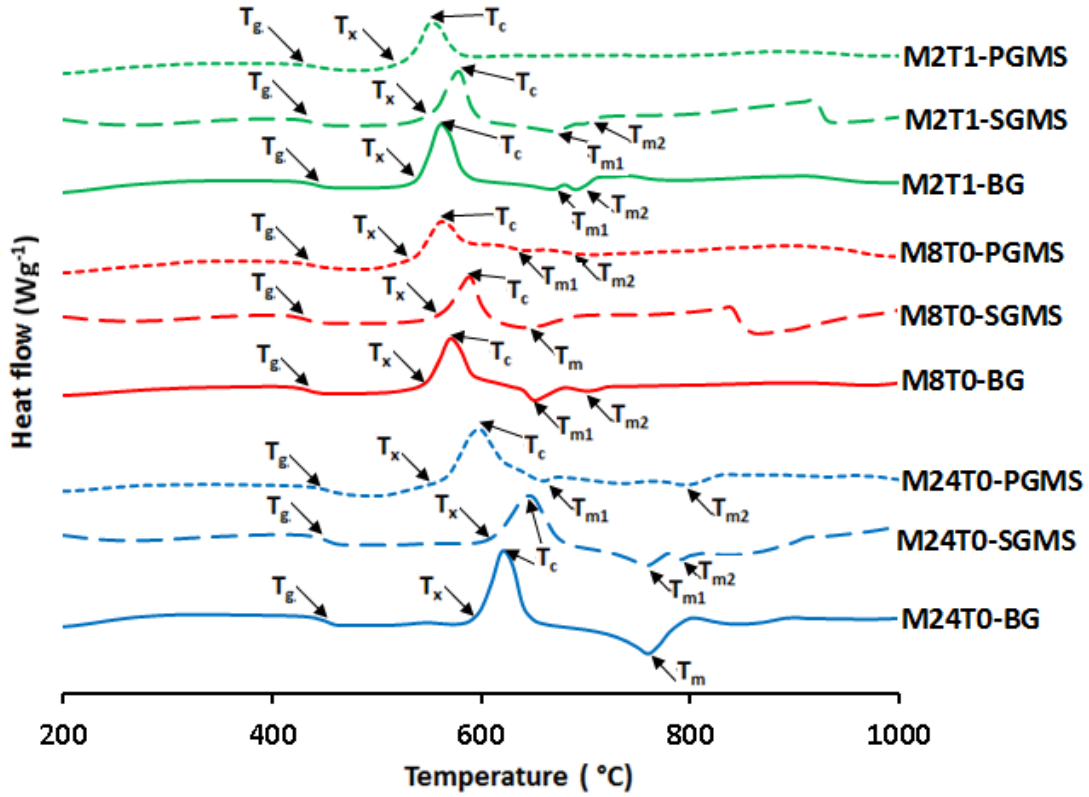


Figure 5.5: *DSC curves for the glass particles, solid and porous glass microspheres of three different phosphate glasses.*

Table 5.2: *Glass transition (T_g), onset crystallisation (T_x), crystallisation (T_c) and melting temperature (T_m) for BG, SGMS and PGMS of three different glass formulation investigated, using a 20 $^oC\ min^{-1}$ heating rate.*

Glass Formulations	Formation	Glass Transition (T_g) (°C)	Onset Crystallisation (T_x) (°C)	Crystallisation (T_c) (°C)	Melting (T_m) (°C)
M24T0	**BG**	450 ± 3	590 ± 3	623 ± 3	765 ± 4
	SGMS	452 ± 3	607 ± 3	645 ± 2	762 ± 5, 845 ± 4
	PGMS	450 ± 2	544 ± 5	598 ± 3	658 ± 5, 735 ± 4
M8T0	**BG**	431 ± 2	545 ± 3	572 ± 3	653 ± 4, 702 ± 5
	SGMS	433 ± 2	561 ± 2	588 ± 2	642 ± 5
	PGMS	436 ± 3	524 ± 4	563 ± 2	644 ± 5 707 ± 4
M2T1	**BG**	440 ± 2	536 ± 3	563 ± 2	667 ± 4 694 ± 5
	SGMS	438 ± 2	552 ± 5	577 ± 3	670 ± 5, 695 ± 4
	PGMS	444 ± 3	510 ± 4	553 ± 3	-

5.2.6 Density, Porosity and Surface area

Table 5.3 shows the density (measured by He pycnometer and tap density), porosity and surface area of solid and porous microspheres for M24T0, M8T0 and M2T1 glass formulations. As seen from **Table 5.3**, the density and tap density reduced significantly, however the theoretical porosity calculated increased 2 fold for the PGMS for all of the glass compositions when compare to SGMS. For example, density and tap density of SGMS were found to be around 2.6 and 1.6 g/cm^3, respectively. Whereas, density and tap density for the porous microspheres was found to be around 2.5 and 0.6 g/cm^3, respectively. In addition, theoretical calculated porosity (Inter-particle packing porosity for SGMS, inter-particle porosity and pores for PGMS) of SGMS and PGMS were found to be ˜35 and ˜75 %, respectively. These theoretically calculated porosities (using **Equation 3.8**) was found to be very similar to the porosity obtained experimentally via Hg porosimetry for PGMS having same composition.

All of the glass formulations within the size range (125-200 µm) were expected to exhibit similar surface area for the SGMS. Surface area for SGMS (M24T0) were found to be 0.0231 m^2/g. Whereas, PGMS of same glass formulation (M24T0) revealed a 94 % increase in surface area than SGMS in the same size range. PGMS of M8T0 and M2T1 glass formulations showed similar surface areas to PGMS of M24T0 and surprisingly all the values were under 1 m^2/g.

Table 5.3: *Density, porosity and surface area of solid and porous microspheres of three different phosphate based glasses investigated.*

Glass formulations	Solid microspheres				Porous microspheres				
	Density (He Pycnometer) (g/cm^3)	Tap density (Tap) (g/cm^3)	Interpar-ticle packing porosity (%)	Surface area (m^2/g)	Density (He Pyc.) (g/cm^3)	Tap density (Tap) (g/cm^3)	Porosity (Hg porosim-etry) (%) Open	Porosity (Calculat-ed) (%)	Surface area (m^2/g)
M24T0	2.650 ± 0.002	1.63 ± 0.02	36 ± 3	0.0231	2.516 ± 0.002	0.59 ± 0.02	76 ± 5	77 ± 2	0.4187
M8T0	2.596 ± 0.004	1.58 ± 0.06	37 ± 3	-	2.475 ± 0.008	0.56 ± 0.03	74 ± 4	77 ± 3	0.3794
M2T0	2.627 ± 0.006	1.69 ± 0.02	35 ± 4	-	2.182 ± 0.02	0.74 ± 0.02	69 ± 5	69 ± 2	0.4345

Figure 5.6 displays the pore diameters of the measured samples against the log differential pore volume. It should be noted that mercury porosimetry determines the largest entrance to a space as pore size and is not the actual "pore size" [332]. M24T0 porous glass microspheres showed multimodal pore size distribution with the first prominent peak showing a modal value of c.a. 55 µm, second peak at c.a. 30 µm, third peak at c.a. 5 µm and the fourth peak at c.a. 2 µm. Moreover, the analysis revealed that the inner pore features were at submicron and nano porosity levels as shown in **Figure 5.6**. A trimodal behaviour was observed for M8T0 and M2T1 porous

glass microspheres with the first two prominent peaks displaying a modal pore diameter of c.a. 45 µm and c.a. 21 µm. The modal pore diameter for the third peak appeared at c.a. 3 µm.

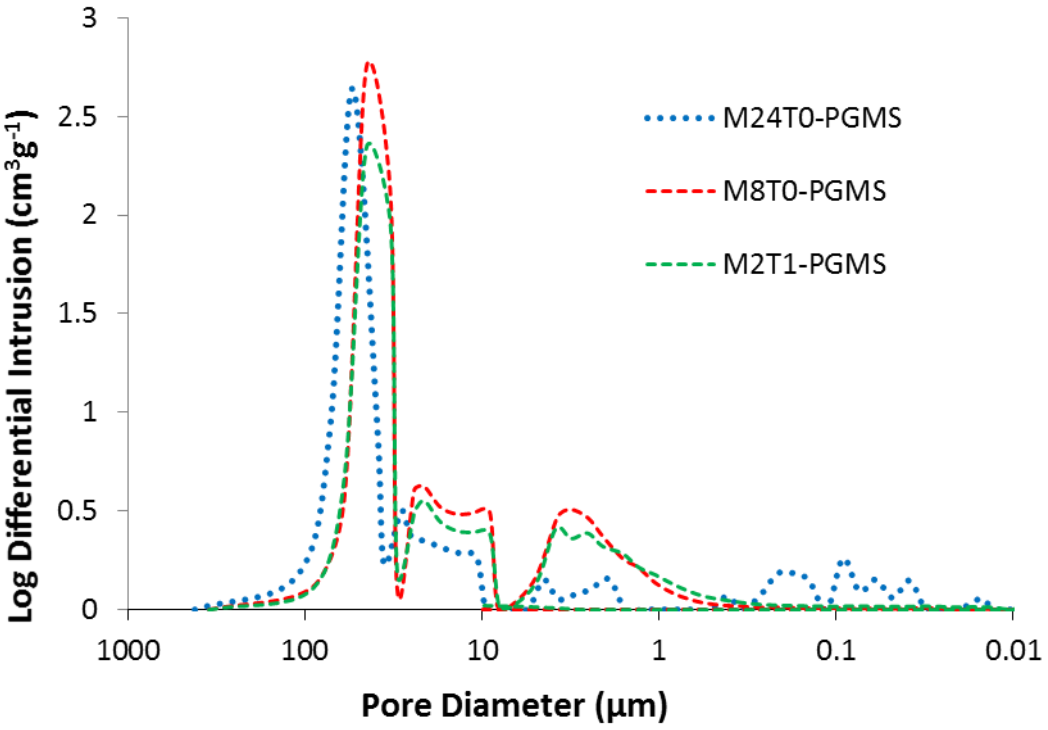


Figure 5.6: *Pore diameter against Log differential pore volume of porous M24T0, M8T0 and M2T1 glass microspheres.*

5.2.7 Degradation studies

The degradation profiles of the glass microspheres that were degraded in Milli-Q water at 37 °C over a period of 28 days are presented in **Figure 5.7 A**. An increase in mass loss was observed with increasing degradation time for all glass formulations (SGMS and PGMS). The porous glass microspheres showed higher mass loss than solid microspheres of the same respective glass composition (as was expected). For example, PGMS of M24T0 showed 141 % higher mass loss at day-28 than for SGMS (see **Figure 5.7 A**). The mass loss % of porous glass microspheres were found to be 20, 13 and 11.4 % for M24T0, M8T0 and M2T1, respectively after 28 days of immersion in milli-Q water. Whereas, solid glass microspheres showed only 8.3 % for both M24T0 and M2T1 and 7.5 % mass loss for M8T0 in milli-Q water at day 28.

The pH for the medium (Milli-Q water) used containing the dissolution products of porous microspheres slightly increased from ~7.5 to ~7.7 at day-1 for all of the glass compositions then gradually decreased to slightly acidic with increasing degradation time, as can be seen in **Figure 5.7 B**. On the other hand, the pH values for the solution containing dissolution products of solid microspheres gradually decreased with increasing degradation time. Moreover, pH values were found to be ~ 6.5 for both solid and porous microspheres after 28 days of immersion in milli-Q water.

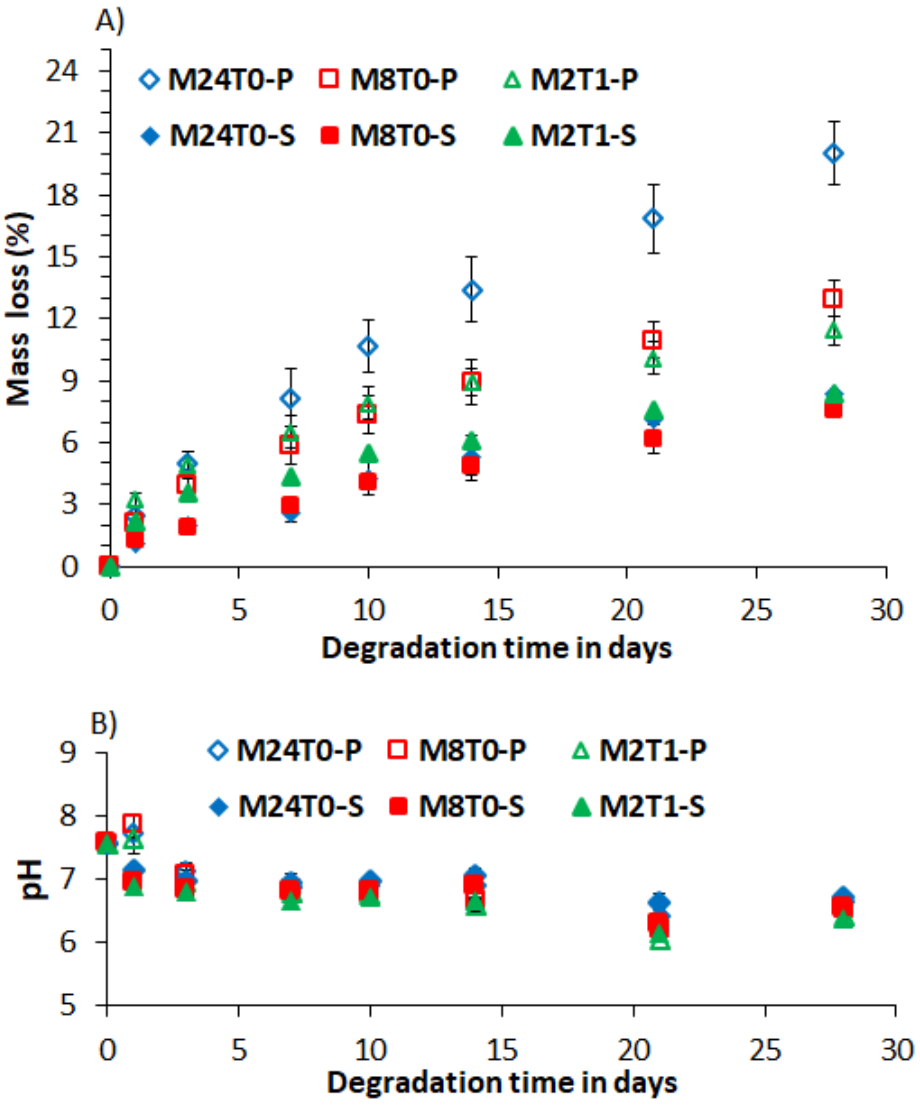


Figure 5.7: *A) Mass loss (%) and B) pH change as a function of immersion time (day) of the solid (represented as solid symbols) and porous (represented as porous symbols) glass microspheres investigated in mili-Q water at 37 °C over 28 day duration.*

Figure 5.8 and **Figure 5.9** are representative SEM images of degraded solid and porous glass microspheres after 28 days of immersion in milli-Q water, respectively. Uniform degradation was not observed for SGMS as some appeared to have been degraded more while others appeared to remain unchanged after 28 days. The M24T0 PGMS degraded more as compared to other PGMS whereas M2T1 PGMS remained relatively stable after 28 days as can be seen from **Figure 5.9**.

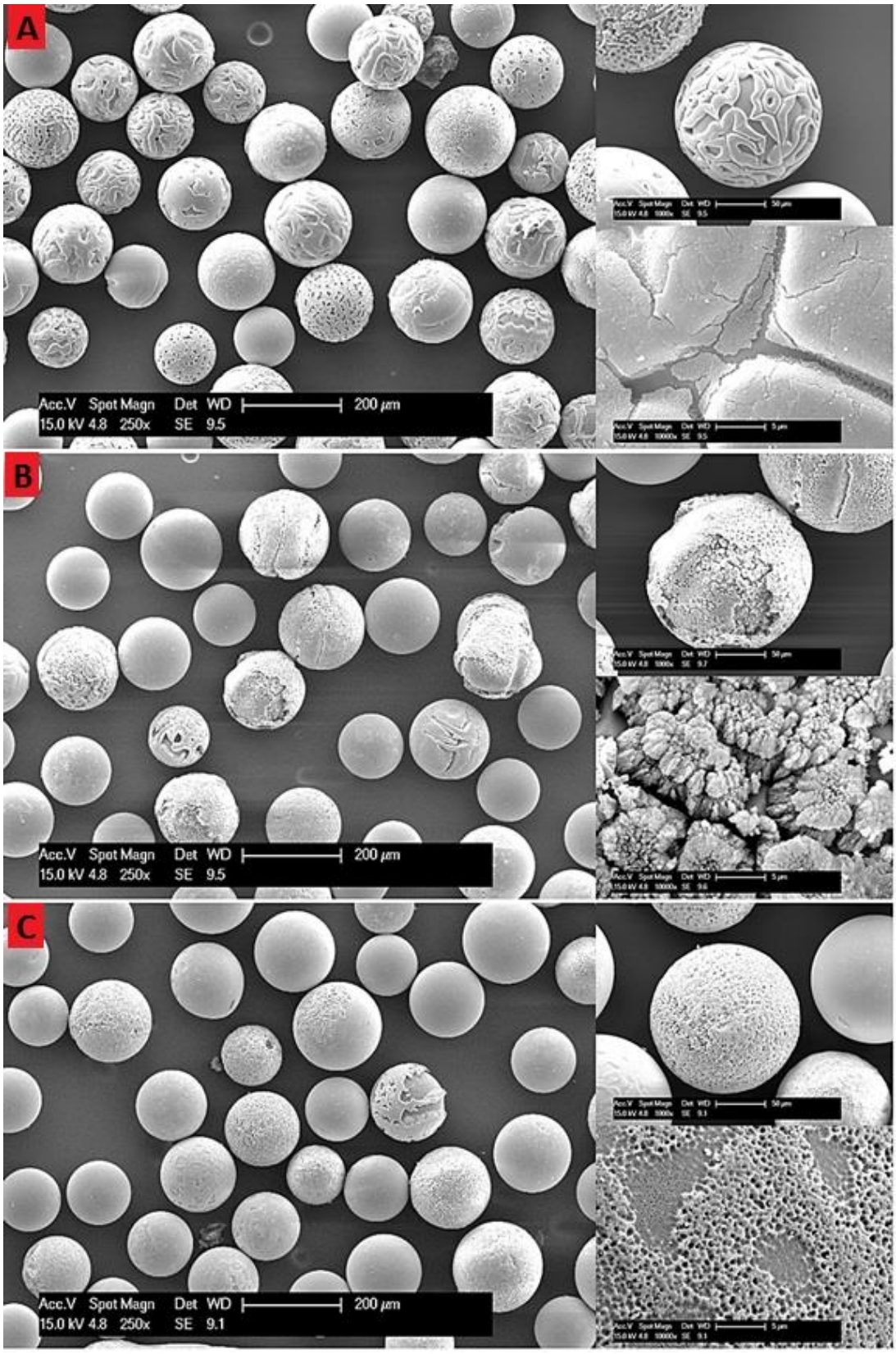


Figure 5.8: *SEM images of degraded SGMS of A) M24T0, B) M8T0 and C) M2T1 glass formulations investigated after 28 days of immersion in milli-Q water. The inset SEM images show the changes in surface morphology at higher magnification (Scale bars of inset SEM images represent 50 and 5 µm).*

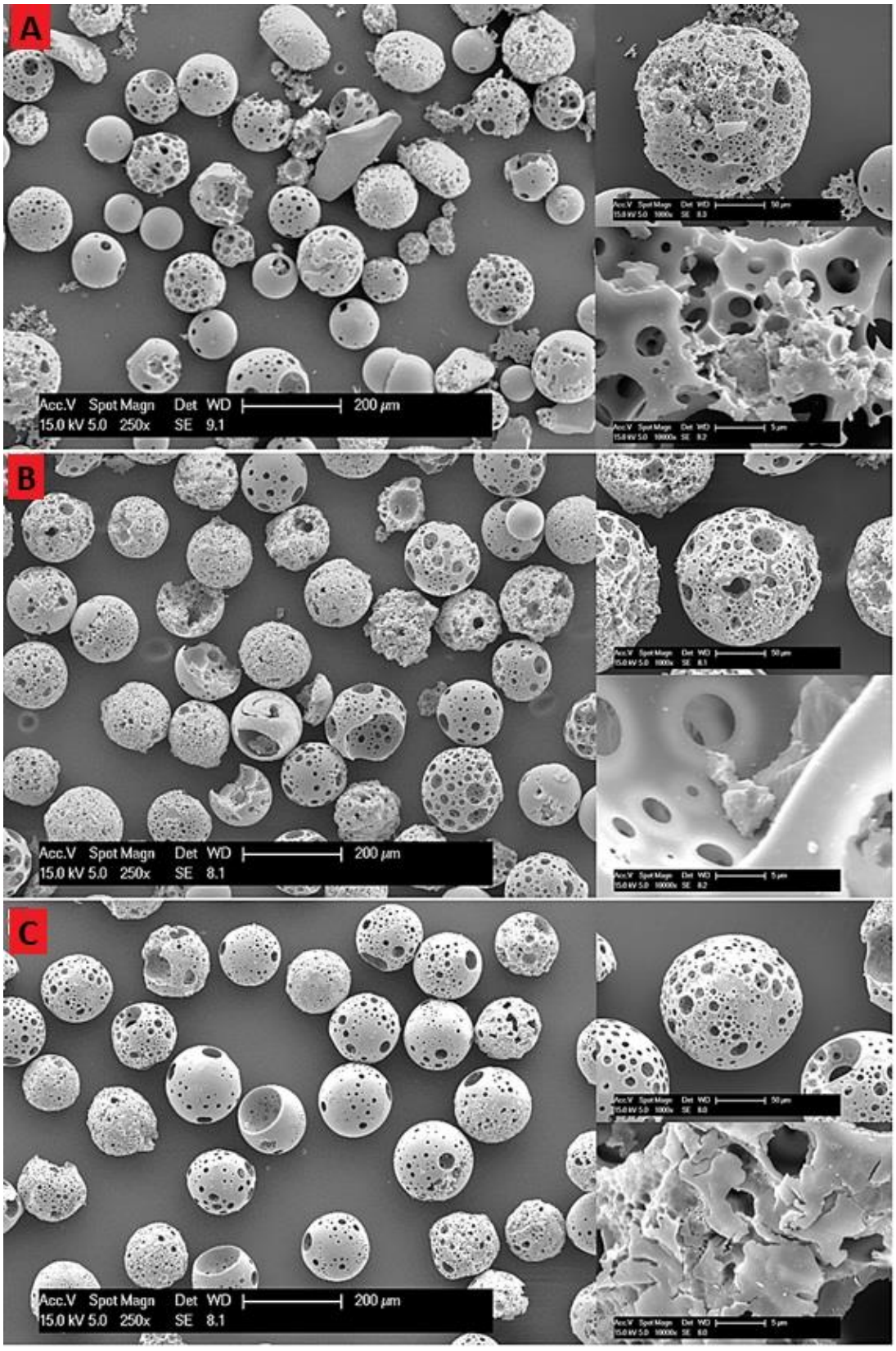


Figure 5.9: *SEM images of degraded PGMS of A) M24T0, B) M8T0 and C) M2T1 glass formulations investigated after 28 days of immersion in milli-Q water. The inset SEM images show the changes in surface morphology at higher magnification (Scale bars of inset SEM images represent 50 and 5 µm).*

5.2.8 Ion release profiles

The concentration of Na, Ca, Mg, P (total) and Ti in ultra-pure water for the glass microspheres were investigated via ICP-MS. The cumulative ion release profiles of all the glass formulations appeared to follow a linear relationship with time (as can be seen in **Figure 5.10 A-E**). The release rates of each element for SGMS and PGMS of PBG formulations investigated are shown in inset of **Figure 5.10 A-E**. All of the ion release rates for porous glass microspheres were higher than their respective solid glass microspheres (as expected) (see the inset of **Figure 5.10 A-E**).

From **Figure 5.10 A**, **C** and **D**, the highest Na^+ (197.1 ppm), Mg^{2+} (98.9 ppm) and P (472.9 ppm) ion release were observed for PGMS of M24T0 whereas the lowest Na^+ (152.9 ppm), Mg^{2+} (18.1 ppm) and P (255.9 ppm) ion release were observed for PGMS of M2T1 at day 28 among the porous glass microspheres. On the other hand, Ca^{2+} ion release was found to be quite similar for all of the PGMS (highest 115 ppm for M8T0 PGMS and lowest 108 ppm for M2T1 PGMS) at day 28 (see **Figure 5.10 B**).

The ion release profiles for SGMS followed similar trends to that of PGMS with significantly lower ion release. For example, 45 % higher Na^+, 33 % higher Ca^{2+}, 41 % higher Mg^{2+} and 53 % higher P ion release were observed for the PGMS of M24T0 as compared to the SGMS (see **Figure 5.10 A-D**).

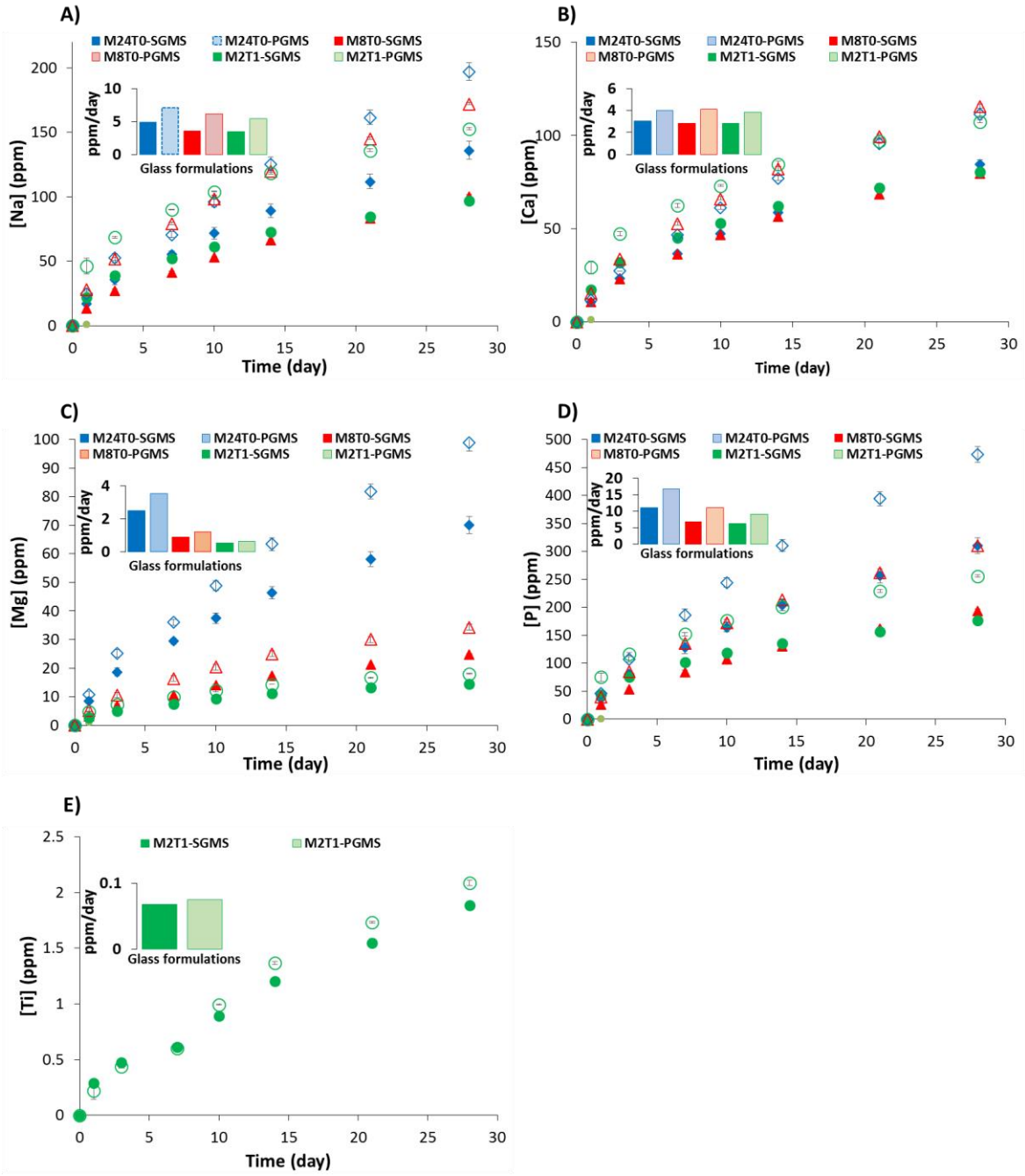


Figure 5.10: *Concentration of A) [Na], B) [Ca], C) [Mg], D) [P] and E) [Ti] measured via ICP-MS for SGMS and PGMS of phosphate glasses investigated in ultra-pure-water during 28 days of immersion period. (Error bars are also included in the data above). The Inset on each graph shows the release rates of each element for the glass formulations investigated.*

5.2.9 *In Vitro* SBF study

XRD traces of solid and porous microspheres for all the glass formulations after 28 days of immersion in SBF are shown in **Figure 5.11 A** and **B**, respectively where an absence of crystalline peaks suggest that no apatite formation occurred during the bioactivity study. However, the apatite forming ability of the prepared SBF solution was confirmed using bioactive 45S5 bioglass, where crystalline apatite peaks were seen after 7 days of immersion in SBF (not shown in **Figure 4.15**).

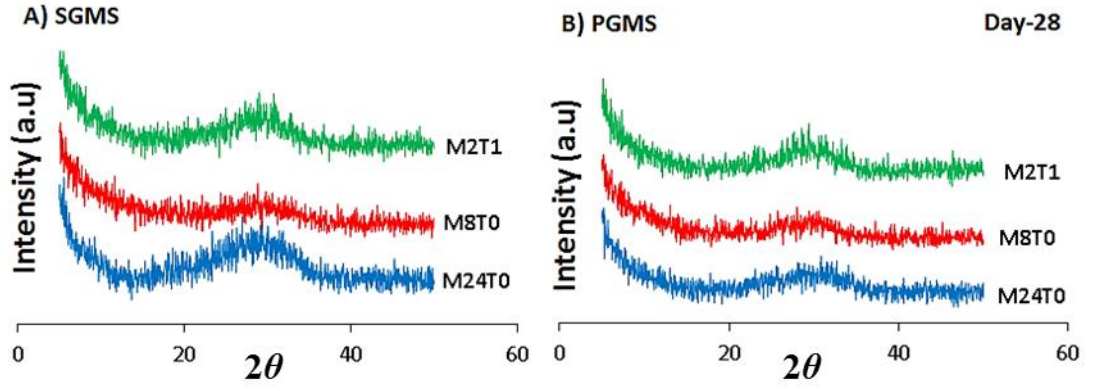


Figure 5.11: *X-ray diffraction pattern A) solid and B) porous microspheres for the glass formulations investigated after 28 days of immersion in SBF.*

SEM images of the SGMS and PGMS for three glass formulations after 28 days of immersion in SBF are shown in **Figure 5.12** and **Figure 5.13** respectively. From **Figure 5.12**, it can be seen that the degradation of SGMS in SBF did not occur uniformly for all of the microspheres. Some of them were highly degraded as shown at higher magnification in **Figure 5.12** and precipitation deposits were clearly observed on the surface of degraded microspheres. On the other hand, some PGMS of M24T0 had agglomerated during the *in vitro* SBF study as seen from **Figure 5.13 A**. Rough surface of the microspheres was clearly observed at higher magnification. Whereas, no agglomeration was observed for PGMS of M8T0 and M2T1 formulation. Only small amount of precipitation depoists were found inside PGMS of M8T0 (see **Figure 5.13 B** at higher magnification).

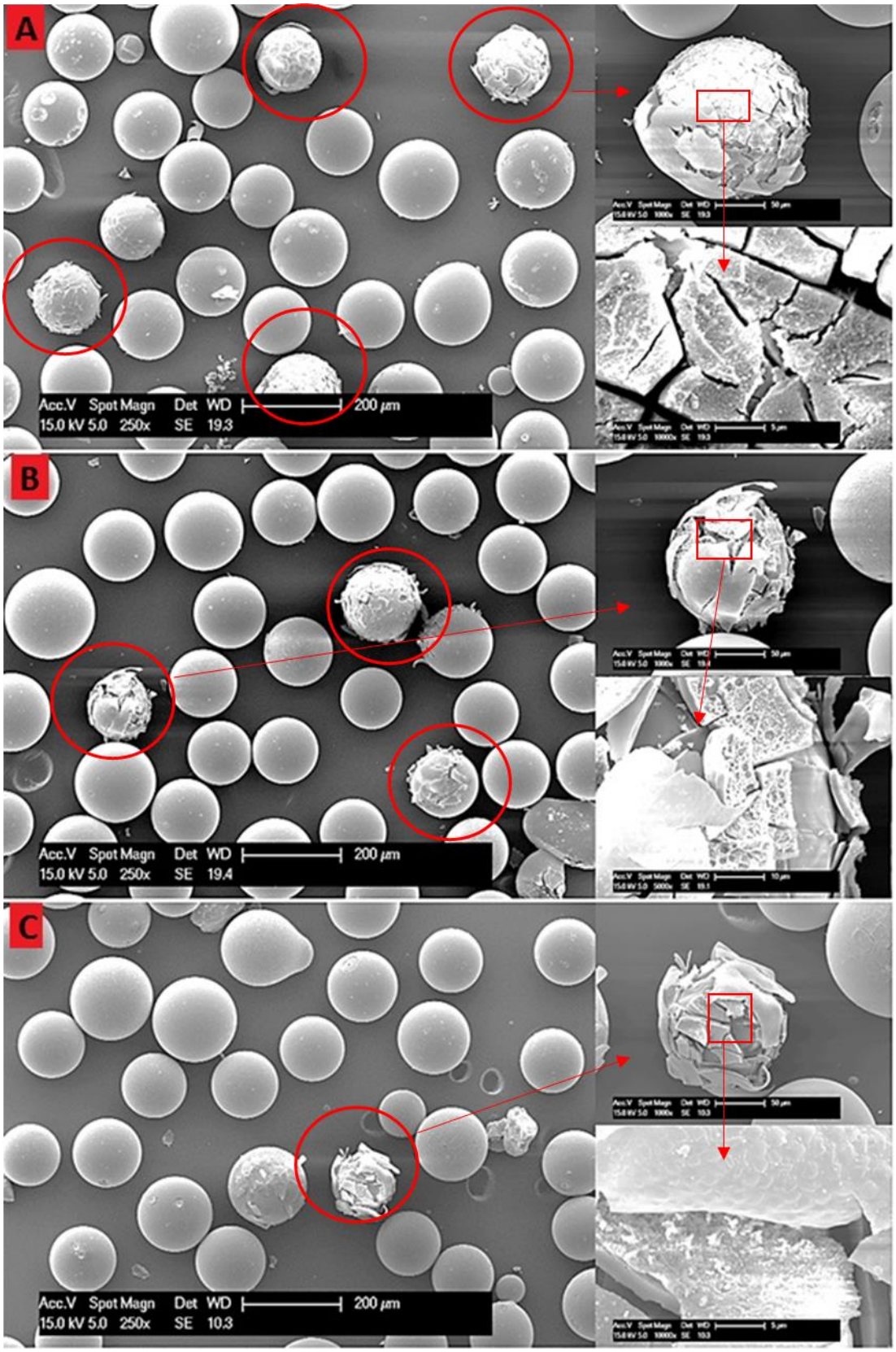


Figure 5.12: *SEM images of SGMS of A) M24T0, B) M8T0 and C) M2T1 glasses after 28 days of immersion in SBF. Highly degraded microspheres shown in red circle.*

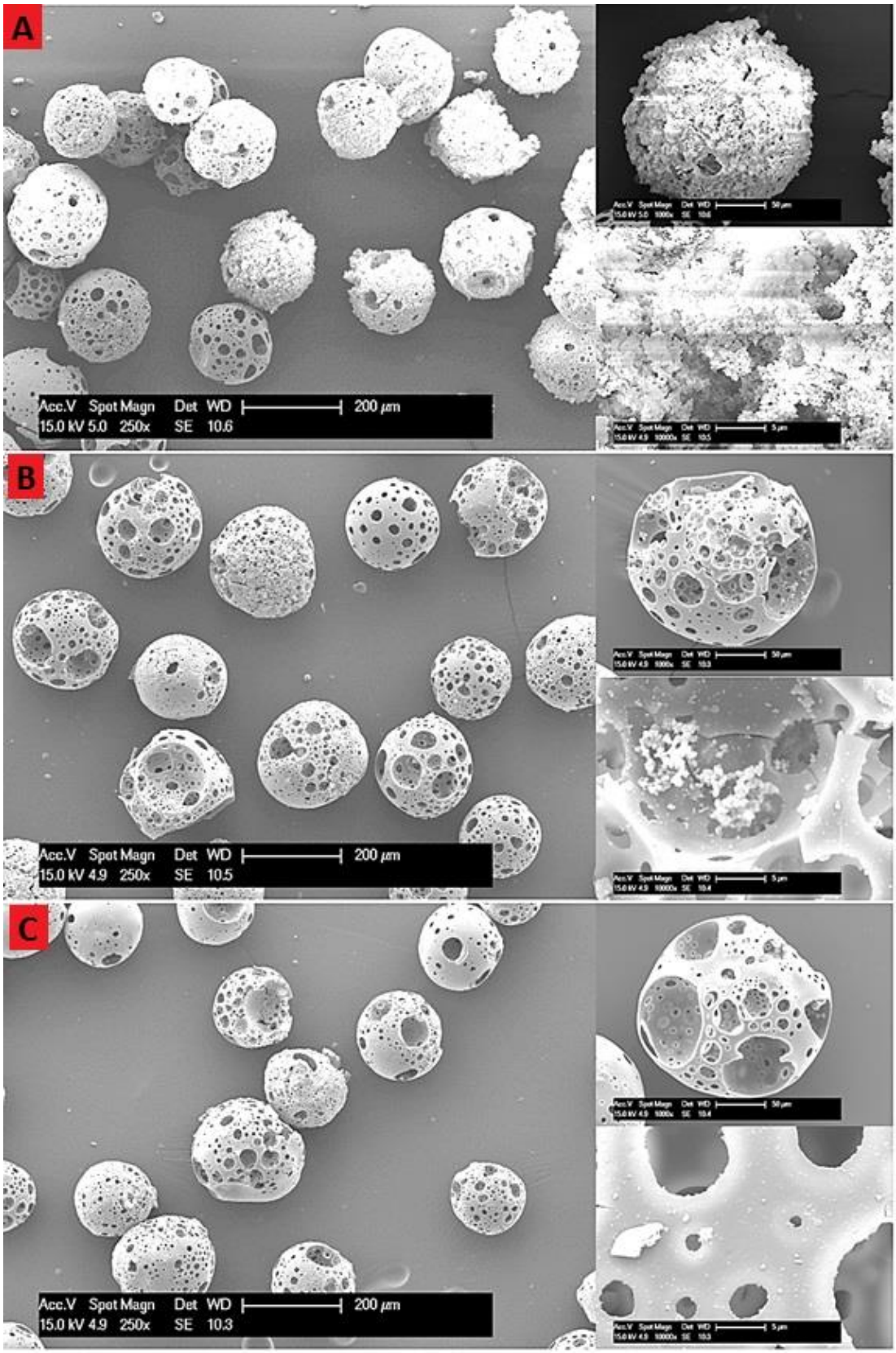


Figure 5.13: *SEM images of PGMS of A) M24T0, B) M8T0 and C) M2T1 glasses after 28 days of immersion in SBF.*

Table 5.4 shows the Ca/P atomic ratio of the SGMS and PGMS for the glass formulations investigated before and after 28 days of immersion in SBF. From **Table 5.4**, no significant changes of Ca/P for maximum SGMS were observed between day-0 and day-28 in SBF. However, significantly higher Ca/P ratio was found for some specific SGMS (highly degraded) after 28 days of immersion in SBF. For example, the Ca/P ratio increased from 0.2 to 0.70 for M24T0, 0.41 to 0.78 for M8T0 and 0.48 to 0.87 for M2T1. On the other hand, Ca/P ratio for PGMS of all glass formulations investigated increased after 28 days of immersion in SBF. Significant changes of Ca/P were found for PGMS of M24T0, where Ca/P ratio increased from 0.27 to 0.75 after 28 days immersion in SBF.

Table 5.4: *Ca/P (atomic ratio) of SGMS and PGMS for three glasses before and after 28 days of immersion in SBF.*

Day	SGMS			PGMS		
	M24T0	**M8T0**	**M2T1**	**M24T0**	**M8T0**	**M2T1**
Day-0	0.2 ± 0.01	0.41 ± 0.03	0.48 ± 0.02	0.27 ± 0.04	0.5 ± 0.05	0.62 ± 0.07
Day-28	**Overall average EDX values**					
	0.30 ± 0.02	0.47 ± 0.03	0.55 ± 0.02	0.75 ± 0.04	0.82 ± 0.06	0.92 ± 0.05
	Average EDX values for specific microspheres					
	0.70 ± 0.06	0.78 ± 0.08	0.87 ± 0.07	-	-	-

In addition, a relatively neutral pH value (at around 7.4) of the SBF containing the dissolution products was observed over the period of study for both solid and porous glass microspheres of all glass formulations investigated (see **Figure 5.14**).

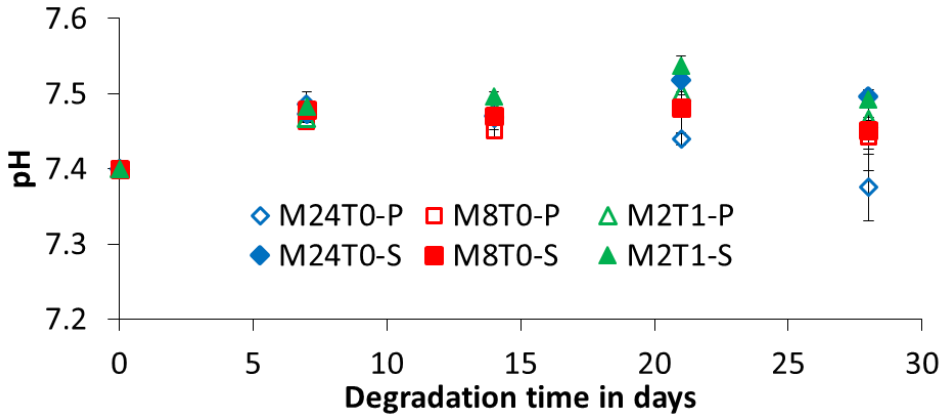


Figure 5.14: pH change as a function of immersion time (day) of the glass microspheres investigated in SBF at 37 °C over 28 day duration.

5.3 Discussion

The major objectives of this Chapter were to demonstrate the successful production of both solid and porous glass microspheres for three selective glass compositions based on degradation, ion release and *in vitro* bioactivity studies for a series of phosphate based glasses (reported in Chapter 4), via the flame spheroidisation method and to examine comparative studies between solid and porous glass microspheres on physical, thermal, degradation, ion release and *in vitro* bioactivity. This chapter also aimed to investigate whether different geometries of glass such as discs, solid and/or porous glass microspheres, having the same glass composition behaved similarly (especially with regards to degradation, ion release and *in vitro* bioactivity studies).

The results above confirmed successful manufacture of phosphate-based microspheres (both solid and porous) from three different PBG compositions via the flame spheroidisation method. **Figure 5.1** represents morphologies of the solid and porous glass microspheres produced. The glass particles were transformed into spheres due to surface tension forces during the cooling stage as the molten glass globules were ejected and exited the flame [270]. The manufacturing process of porous microspheres depends on various factors such as chemical and physical interaction of the porogen, glass viscosity, along with both being delivered within a suitable thermal processing window within a sufficient timeframe [265]. The yield of porous microspheres also depends on glass composition, which not only melts but also enables the material to achieve a suitable viscosity, sufficiently low enough to entrap and release gas bubbles from the porogen decomposition process within the molten globules. Previous studies within the research group also showed that both porogen quantity and size also effected pore size (and hence surface area). Therefore, specific size range (63–125 μm) of glass particle with 1:3 ratio of particle to porogen were used for these studies [265].

The cross-sectional SEM images of the porous microspheres (as shown in **Figure 5.2**) exposed the internal porosity, which clearly revealed that the pores were interconnected to each other for all the glass formulations explored.

After spheroidisation, SGMS remained fully amorphous, whereas only a single small peak (which correlated with $CaCO_3$ peak) was found for PGMS of each composition (see **Figures 5.3 A** and **B**) which was attributed to the use of the Ca-based porogen during spheroidisation for PGMS. The use of porogen in this process, increased the Ca content which consequently decreased P and other components for PGMS. Whereas, no significant variation in composition between BG and SGMS was observed (see **Figure 5.4**).

Thermal properties especially onset of crystallisation and crystallisation peaks for PGMS shifted to lower temperature in comparison to BG or SGMS of the same composition. This was attributed to the higher surface area: volume ratio [218] and due to potential remnants of the porogen used. The remnants could have been either the porogen itself or incorporation of CaO from the porogen decomposition stage (which also correlated with the EDX analysis). The surface area obtained via BET confirmed higher surface area for PGMS in comparison to SGMS. A similar result for the shifting of crystallisation peak to higher temperature with increasing particle size and consequently decreasing surface area: volume ratio of glass was observed by Al-noaman *et al.* for silicate glasses [218]. Similar findings were also observed in the previous experimental chapter (Chapter 4), where, the crystallisation peaks moved to higher temperature (from 587 ^{o}C to 643 ^{o}C) with increasing particle size ranges (from 45-100 μm to 350-500 μm) further highlighting the influence of particle sizes on thermal properties.

On the other hand, the onset of crystallisation and crystallisation peaks for the SGMS shifted to slightly higher temperatures in comparison to the BG of the same composition. This shift could be attributed to the same reason of differences in surface area due to i) the initial size distribution within the experimental particle size range (125-200 μm) and ii) potential of agglomerating molten particles, leading to larger particle sizes for SGMS. Comparatively, larger amounts of smaller particles within the size range of 125-200 μm may be present for BG compared to SGMS, which consequently increased the surface area of the BG:volume ratio [218]. However, for comparative analysis of surface area and particle size distribution between BG and

SGMS, BET surface area analysis for BG and particle size analysis comparing BG and SGMS will be further required.

The porous glass microspheres revealed 2 times higher porosity (~ 75%) (as measured via mercury porosimetry) in comparison to solid glass microspheres (~ 36%) (see **Table 5.3**). These results were attributed to the contribution of inter-particulate gaps for the measurement of the overall porosity for both the solid and porous glass microspheres. BET analysis confirmed the surface area of PGMS (~0.4 m^2g^{-1}) which showed increase many times over (94 %) as compared to SGMS (~0.02 m^2g^{-1}) although the values for the PGMS appeared to be quite low (i.e. less than 1 m^2g^{-1}). The main cause attributed to the low values obtained was due to the shell-like structure with fully interconnected pores for the PGMS produced. The introduction of porosity also caused an increase in mass loss during degradation (see **Figure 5.7 A**) and ion release rates (see **Figure 5.10 F**) in comparison to SGMS, which was expected due to the increased surface area achieved.

No significant variation in mass loss % was observed for the SGMS of all glass formulations. However, the mass loss % for SGMS was found to be ~ 8 % at day 28 which was more than 135 % higher than for glass discs (reported in the previous chapter 4) with the same composition due to significant increase in the surface area for SGMS in comparison to glass discs. On the other hand, the trend for mass loss % for PGMS was opposite to that observed for the glass discs. For example, M24T0 glass discs showed the lowest mass loss (2.3 %) (as shown in Chapter 4) whereas M24T0 PGMS showed highest mass loss (20 %) compared to other glass composition as observed in **Figure 5.7 A** and 770 % higher mass loss was observed for PGMS of M24T0 compared to glass discs. Moreover, among the PGMS, the lowest mass loss was observed for M2T1 (11.4 %) which was still 322 % higher in comparison to glass discs (2.7 %) of same composition. This observation of opposite mass loss trend of PGMS as compared to glass discs could be attributed to i) the differences in surface areas between the PGMS formulations tested, and ii) due to any structural changes that may have occurred for PGMS due to the addition of CaO during the porogen decomposition stage, as changes to the chemical composition (see **Figure 5.4**) post

flame spheroidisation were observed (i.e. an increase of CaO by 7 mol% for PGMS of M2T1 was observed). This extra CaO could have influenced crystallisation inside the PGMS during flame spheroidisation process, leading to more durable materials in comparison to amorphous glass structure. It has been observed from previous chapter 4 that the CaO content more than 32 mol% in the glass series of $40P_2O_5$-(24-x)MgO-(16+x)CaO-$20Na_2O$ showed a strong tendency towards crystallisation. Further analysis for confirmation via XRD was carried out for crushed versus starting porous microspheres and crystalline peaks of alpha-calcium pyrophosphate (α-$Ca_2P_2O_7$) apart from $CaCO_3$ peaks were observed for PGMS of M8T1 and M2T1 (see **Figure 5.15** below).

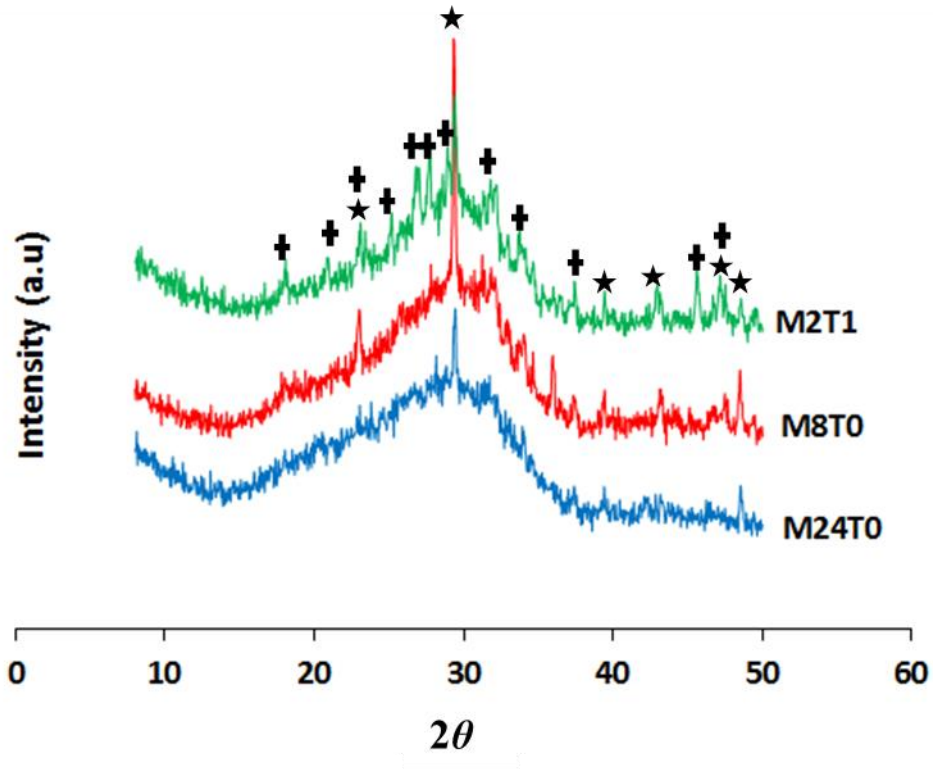


Figure 5.15: *XRD spectra of crushed starting porous glass microspheres. ★ represents for calcium carbonate ($CaCO_3$) peaks and ✚ represents for alpha-calcium pyrophosphate (α-$Ca_2P_2O_7$) peaks.*

Higher ion release rates (of Na, Ca, Mg, P and Ti) were observed for PGMS in comparison to SGMS (see insets of **Figure 5.10 A-E**) due to the higher surface area for

the PGMS. The total of both cations and anions released (highest 1090 ppm and lowest 777 ppm) was observed for M24T0-P and M2T1-P after 28 days of immersion in ultra-pure water, which correlated well with the mass loss profiles (See **Figure 5.7 A**). On the other hand, the lowest total ion release was observed for M24T0 glass discs with values found to be ~250 ppm (reported in previous Chapter 4). The ion release profiles from phosphate-based glasses could potentially be very useful for bone repair and regeneration. For example, Ca^{2+} ions is known to help stimulate proliferation and differentiation of osteoblasts as well as extracellular matrix mineralisation [333] whilst Mg^{2+} ions are useful for new bone formation [334]. In addition, PO_4^{3-} ions are required for calcium phosphate crystal deposition [335] and extracellular matrix mineralisation whilst Na^+ ions are mainly found in extracellular fluid [336].

The slight increase in pH values was observed at day-1 for porous glass microspheres which was attributed to the release of more cations than anions. For example, total cation (Na^+, Ca^{2+}, Mg^{2+}) release was found to be 47 ppm which was slightly higher than the anion (total P ion) release (45 ppm). The pH value then gradually decreased with increasing immersion time and slightly acidic pH around 6.5 was observed at day-28 due to the comparatively higher anion (total P ion) release than cations.

In vitro bioactivity tests conducted in this study suggested that apatite formation was not observed on solid and/or porous microspheres of any of the glass formulations tested even after 28 days of immersion in SBF (see **Figure 5.11**). However, nano-crystalline apatite (which could not be detected via XRD) may have formed on the surface of some specific SGMS (see **Figure 5.12**) and PGMS of M24T0 and M8T0 formulations (see **Figure 5.13**). On the other hand, the Ca/P ratios for solid (0.68-0.87) and porous (0.75-0.92) microspheres of all glass formulations fell within the range suggested for precipitated amorphous calcium phosphate (ACP) (0.67 to 1.5) [248,330]. It is noted that the true Ca/P ratios might be higher than the observed values as it was not possible to examine the compositional analysis only for a thin deposition layer on the surface of microspheres without doing the cross-section as the x-ray of EDX could penetrate through the thin layer and give an average compositional value. Moreover, it is quite difficult to do EDX for thin layer of surface of broken (degraded) or porous microspheres embedded in a cold set epoxy resin. However, the

precipitated ACP phase has been stated to be a precursor phase towards formation of hydroxyapatite [331].

5.4 Summary

In this chapter solid and porous glass microspheres for three selective compositions in $40P_2O_5$-(24-x)MgO-(16+x)CaO-(20-y)Na_2O-yTiO_2 (where $0 \leq x \leq 22$ and y=0 or 1) glass system were successfully prepared via flame spheroidisation technique.

Porous glass microspheres showed higher mass loss %, ion release rate and porosity in comparison to solid glass microspheres having same composition. This was attributed to the higher surface area for PGMS compared to SGMS. For the same reason PGMS showed lower onset crystallisation and crystallisation temperature in comparison to SGMS.

The trend for mass loss % for PGMS was opposite to that observed for the glass discs (in Ch 4) due to the internal crystallisation of M8T0 and M2T1 PGMS during flame spheroidisation, which consequently formed a more hydration resistant materials in comparison to the initial amorphous bulk glass structure.

PGMS showed higher Ca/P atomic ratio compared to SGMS of the same composition after 28 days of immersion in SBF. Moreover, due to the higher degradation and ion release rates for M24T0 PGMS, higher Ca/P atomic ratio (0.75) of this composition was found during the *in vitro* bioactivity study compared to the glass discs of same composition (0.42). No significant variation of Ca/P ratio for porous glass microspheres of M8T0 and M2T1 was found compared to glass discs of same composition. In addition, none of the solid or porous glass microspheres showed hydroxyapatite peaks even after 28 days of immersion in SBF. However, the Ca/P ratios for PGMS of all glass formulations (0.75 to 0.92) were observed within the range suggested for precipitated amorphous calcium phosphate (ACP) (0.67 to 1.5) which has been suggested to be a precursor phase for the formation of HA

CHAPTER 6

MANUFACTURE AND CHARACTERISATION OF SOLID AND POROUS BORATE GLASS MICROSPHERES FOR BIOMEDICAL APPLICATIONS

6.1 Introduction

The aim of this chapter was to prepare both SGMS and PGMS of three different types of borate glasses selected based on recent work in the literature (mainly from Prof. Delbert Day's group) i.e. 45B5, B53P4 and 1393B, which were derived based on their biosilicate equivalents 45S5, S53P4 and 1393, by replacing the SiO_2 with B_2O_3. Weight loss (%) and pH changes associated with the conversion were measured, and a variety of techniques (as detailed below) were used to characterise the structural and chemical changes. Moreover, a comparative analysis between SGMS and PGMS on physical, thermal, conversion of borate glass into HA in phosphate solution, ion release and *in vitro* bioactivity were carried out.

6.2 Results

6.2.1 Compositional analysis of starting borate glasses via ICP-MS

The relative concentration (mol%) of elements in each formulation were analysed via ICP-MS and the values are summarised in **Table 6.1**, where it can be seen that the respective oxide contents were within 1.5 mol% of their predicted values except P_2O_5 and CaO content in B53P4 where 2.5 mol% higher P_2O_5 and 2.3 mol% lower CaO were found from the expected values.

Table 6.1: *Expected and obtained chemical compositions from ICP-MS analysis of three different borate glass formulations investigated.*

Components	45B5		B53P4		1393B	
	Expected (mol%)	Actual (mol%)	Expected (mol%)	Actual (mol%)	Expected (mol%)	Actual (mol%)
B_2O_3	46.1	47.08 ± 0.19	53.85	54.36 ± 0.08	54.6	55.43 ± 0.22
P_2O_5	2.6	2.96 ± 0.01	1.72	4.22 ± 0.05	1.7	1.91 ± 0.01
CaO	26.9	26.33 ± 0.09	21.77	19.43 ± 0.02	22.1	21.61 ± 0.08
Na_2O	24.4	23.33 ± 0.05	22.66	21.81 ± 0.04	6	5.94 ± 0.12
MgO	-	-	-	-	7.7	7.35 ± 0.01
K_2O	-	-	-	-	7.9	7.77 ± 0.01

6.2.2 Manufacture of borate glass microspheres

SGMS of three different borate glasses investigated were prepared via flame spheroidisation processing route and SEM images are presented in **Figures 6.1 A-C**.

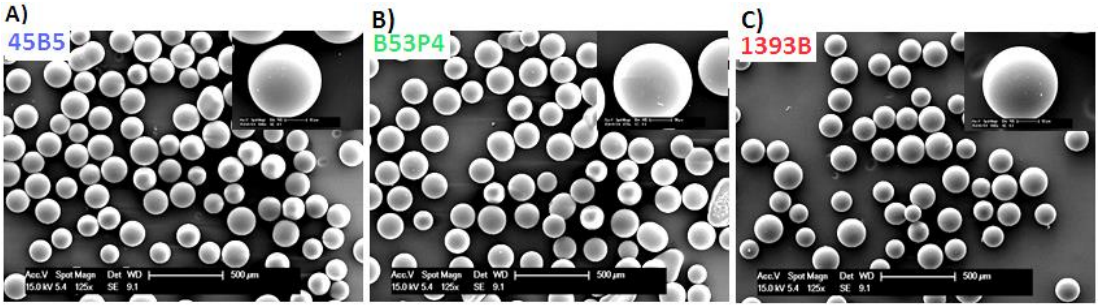


Figure 6.1: *SEM images for SGMS of A) 45B5, B) B53P4 and C) 1393B borate glass formulations investigated.*

PGMS were also successfully prepared via the flame spheroidisation processing route using the same parameters as used for making porous phosphate glass microspheres. However, different washing protocol was used for the removal of porogen from porous borate glass microspheres.

6.2.3 Post processing porous microspheres

Figures 6.2 A, B and **C** represent the SEM images of unwashed porous 45B5, B53P4 and 1393B borate glass microspheres, respectively after post-sieving using 63 micron sieve where residual porogen was observed with porous microspheres. It can be seen from **Figure 6.2**, pores of some of the microspheres (especially for 45B5) were not opened fully.

In order to expose/open the pores and remove the residual porogen from these porous microspheres (PGMS) post flame shperoidisation, a series of acid wash steps were explored where the PGMS were subjected to certain concentrations of acid for specific time points. This washing protocol was developed based on the findings of a previous research work where the porogen $CaCO_3$ was dissolved using acetic acid [337]. $CaCO_3$ can also be dissolved in strong acid (HCl), moderately strong acid (sulfamic) or other weak acids such as citric, sorbic, lactic and phosphoric acid. Initially, the same washing protocol (i.e. 5M acetic acid for 2 mins) that was developed for the PGMS of phosphate-based glasses was implemented for PGMS of borate glasses. However, all of the PGMS were completely dissolved along with the porogen. Therefore, the starting acid concentration was reduced significantly (to 0.5M acetic acid) for washing the PGMS of borate glasses.

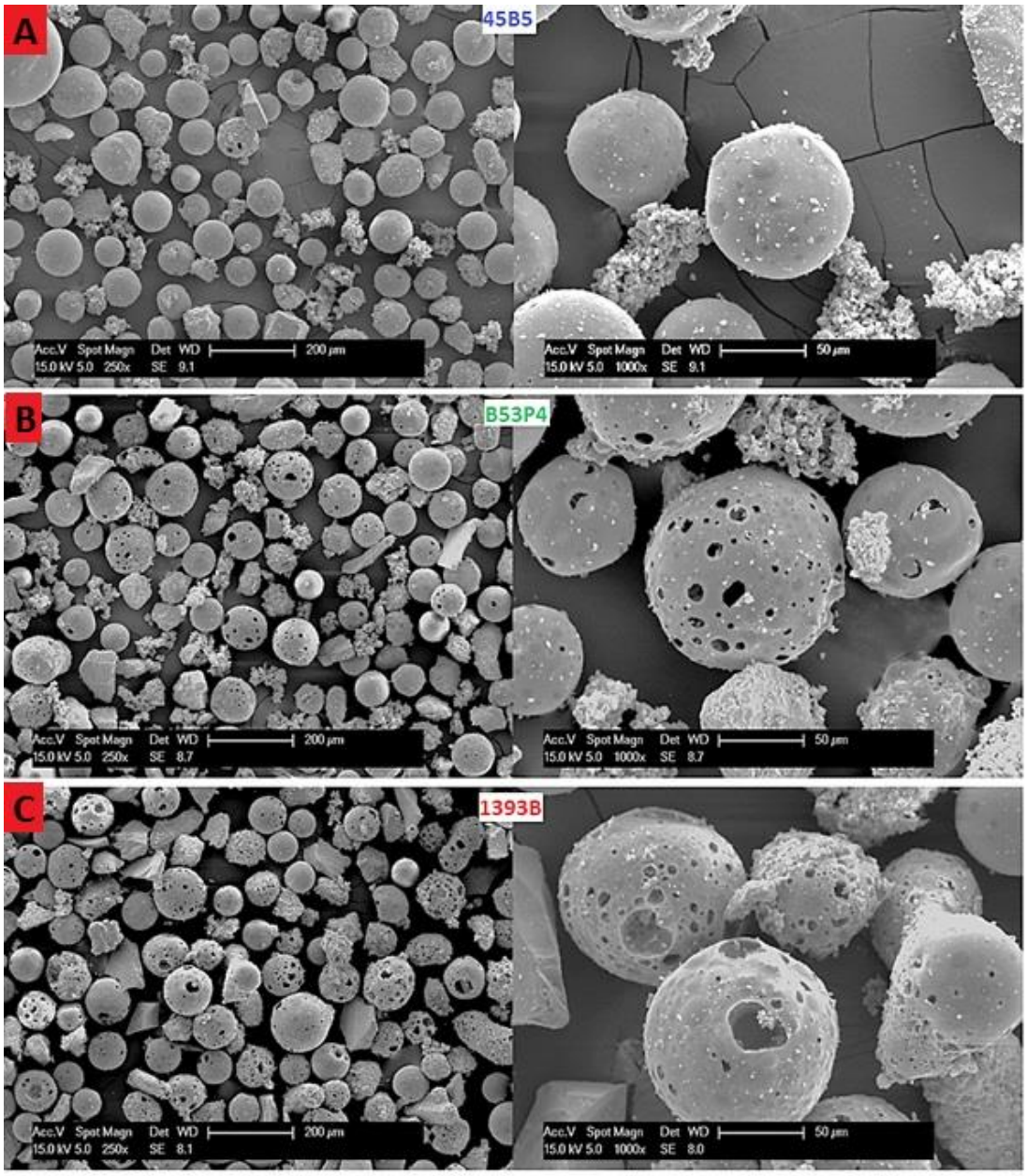
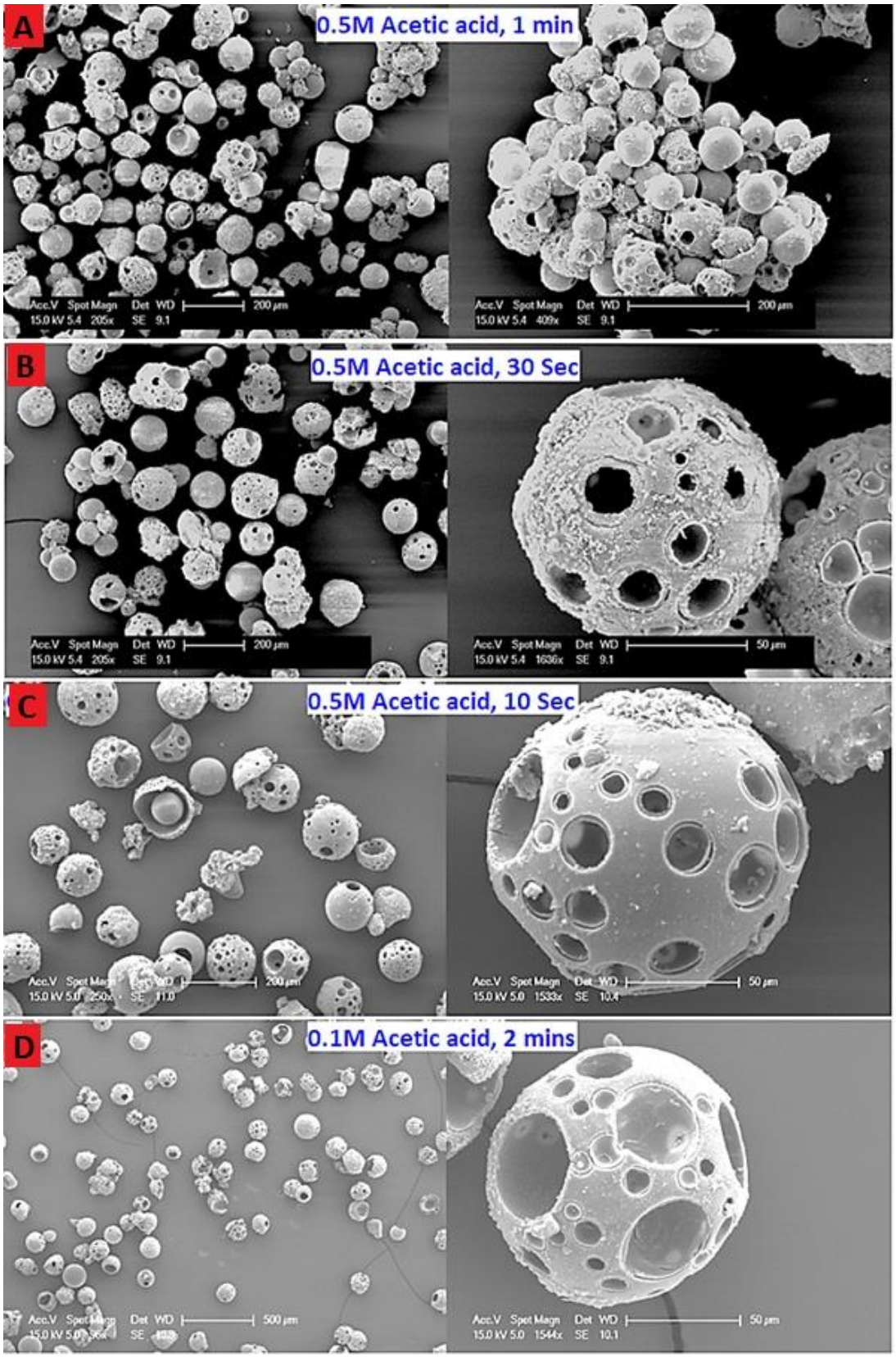


Figure 6.2: *SEM images of unwashed PGMS of A) 45B5, B) B53P4 and C) 1393B obtained via flame spheroidisation.*

Figures 6.3 A-G represent the effect of acid washing of the PGMS of 45B5 in different acetic acid concentrations for various time point. **Figure 6.3 A** shows the PGMS agglomerated together when the PGMS were washed with 0.5 M acetic acid for 1 min.


A
0.5M Acetic acid, 1 min
B
0.5M Acetic acid, 30 Sec
C
0.5M Acetic acid, 10 Sec
D
0.1M Acetic acid, 2 mins

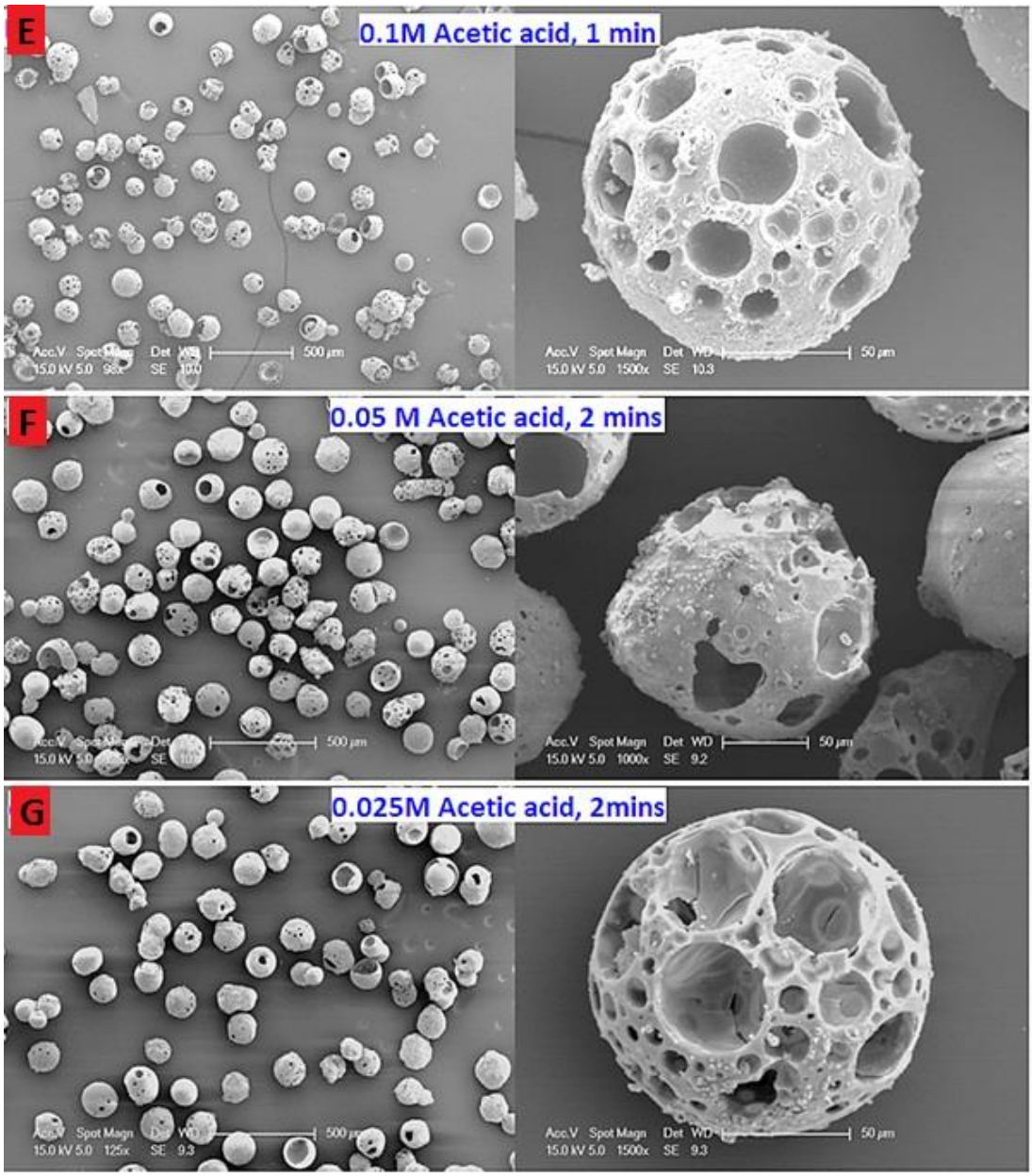


Figure 6.3: *SEM images from A-G displaying the effect of acid washing of the PGMS of 45B5 in different concentration of acetic acid for various time point.*

Agglomerations could be inhibited by further reducing the washing time at the same concentration of acid (see **Figures 6.3 B-C**). However, some reaction products might be formed on the surface of microspheres. Comparatively, better and cleaner surfaces of PGMS were found using 0.1M acetic acid for 2 mins (see **Figure 6.3 D**). Some of the porogen were found to still remain on the surface of PGMS when the microspheres were washed with further reduced concentration of acetic acid (see **Figures 6.3 F-G**) or shorter time (see **Figure 6.3 E**).

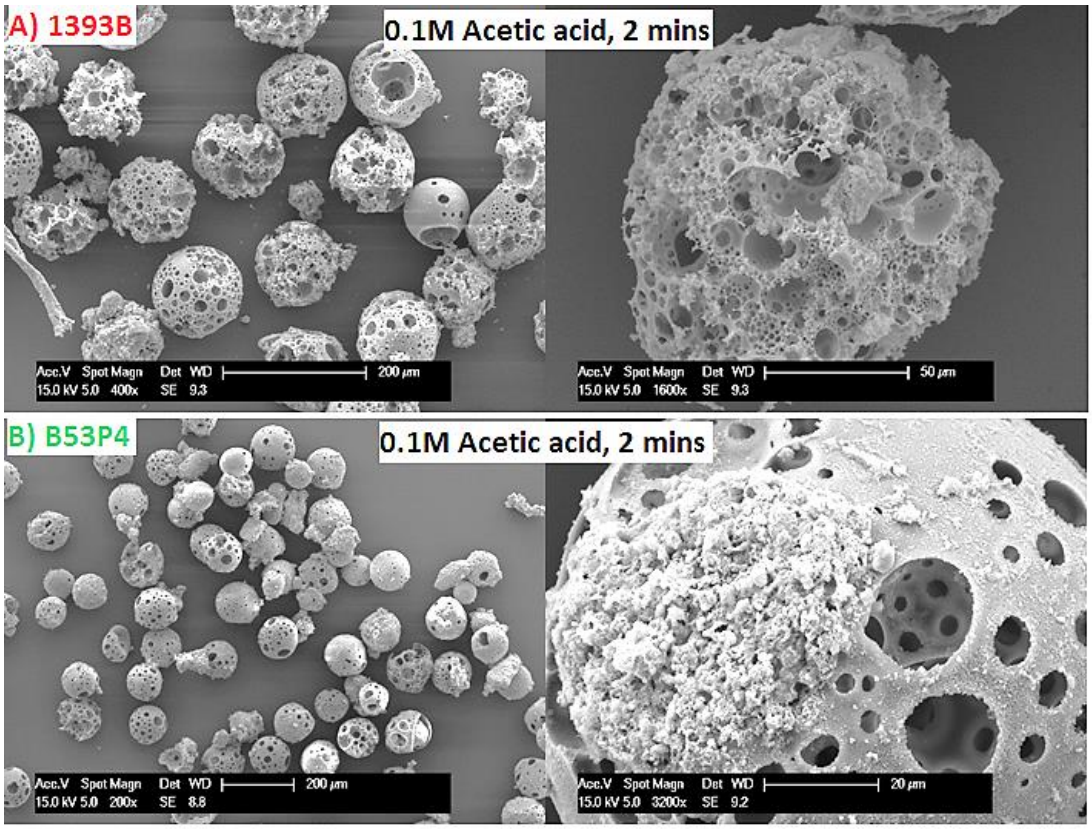


Figure 6.4: *SEM images displaying the effect of acid washing for the PGMS of A) 1393B and B) B53P4 in 0.1 M acetic acid for 2 mins.*

Figure 6.4 represents the SEM images of the PGMS of A) 1393B and B) B53P4 after washing using the protocol (0.1 M acetic acid for 2 mins) developed for the PGMS of 45B5. It can been seen from **Figure 6.4**, that the surface of PGMS of 13-93B were degraded and some reaction products had also formed on the surface of the B53P4 PGMS. Such damage and reaction products caused to the surface of these microspheres is undesirable since this is likely to cause a loss in mechanical properties and the reaction products could block the pores. The irregularity in morphology and the exposed pore struts would be deemed undesirable when trying to deliver these microspheres in a clinical setting as the free-flowing nature of spheres would be disrupted and the sharp exposed struts could have detrimental effects on cell viability. Therefore, further washing protocol was needed to develop the PGMS of these two glass compositions (1393B and B53P4). **Figures 6.5 A-D** represents SEM images of 1393B PGMS after washing in different media for 1 min. The surface of PGMS were also degraded when the microspheres were washed with very low concentrations such as 0.05M acetic acid or 0.05M citric acid. However, no

detrimental effects on the microspheres surface were observed via SEM when the microspheres were subjected to wash with 0.001M HCl acid or only water. Most of the loosely attached porogen was removed from the surface. Therefore, only water was used for washing the PGMS of 1393B and B53P4.

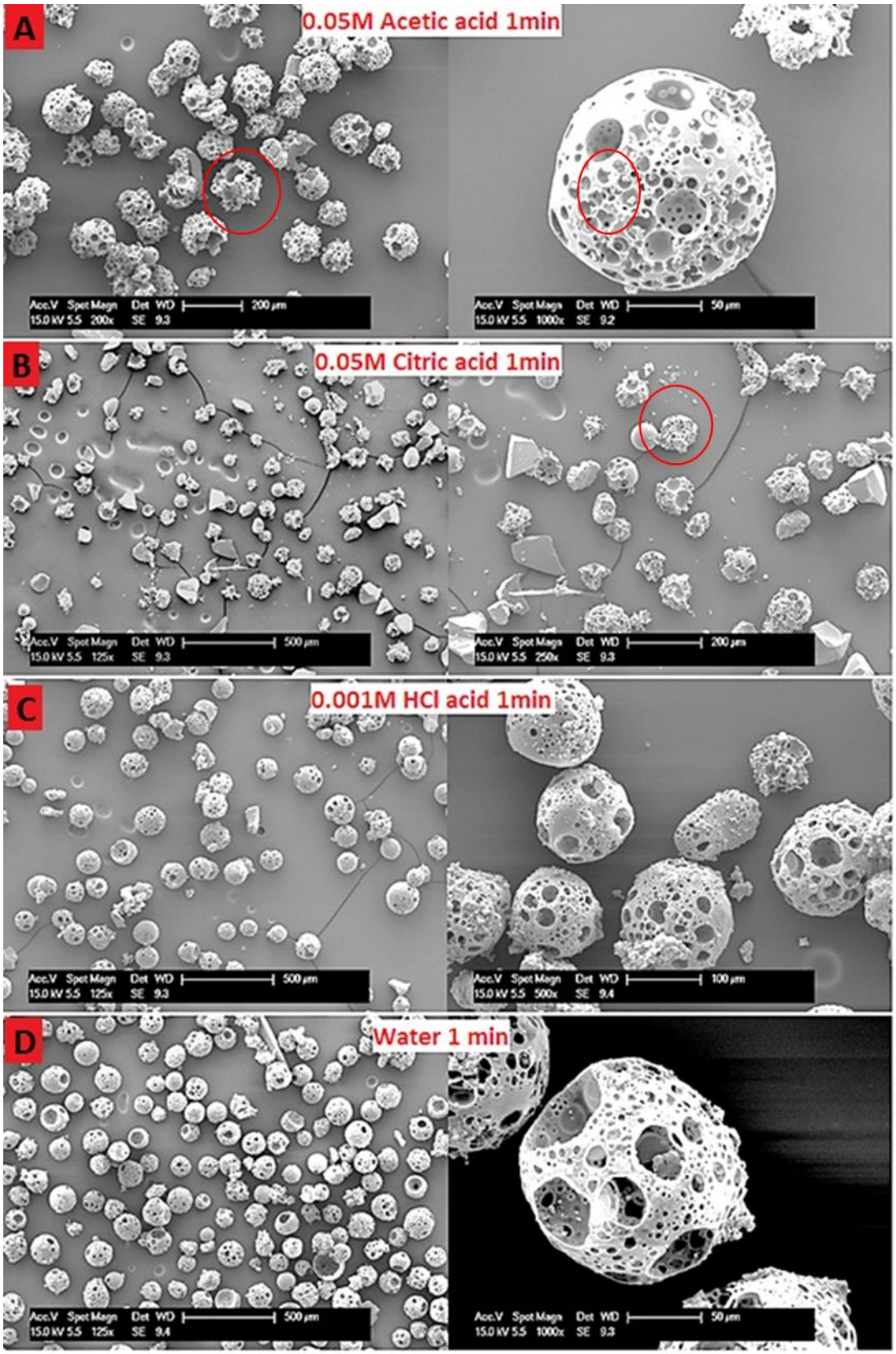


Figure 6.5: *SEM images from A-D displaying the effect of washing of the PGMS of 1393B in different media for 1 min. Microspheres degraded by acid wash shown in red circle.*

In order to examine the internal structure of the PGMS, cross-sections were imaged after embedding the microspheres in a cold setting epoxy resin and ground and polished using SiC paper and a diamond cloth. **Figure 6.6** shows the cross-sections of PGMS of the three different borate glasses.

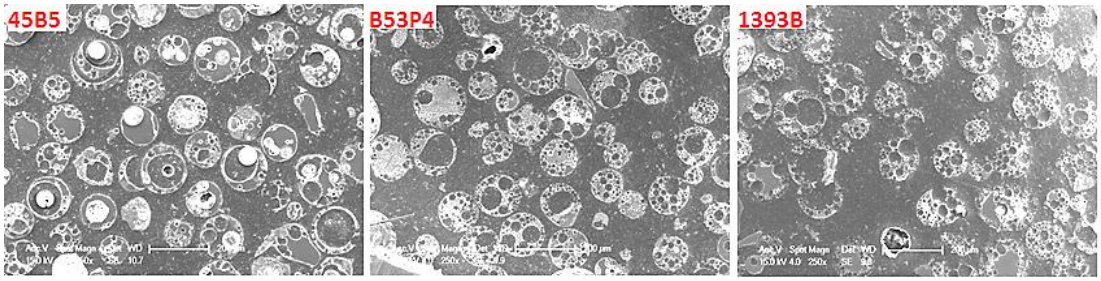


Figure 6.6: *Cross-section of PGMS for three different borate glass formulations investigated. (Scale bar represents 200 µm)*

Table 6.2 represents the chemical compositions obtained from ICP-MS analysis of the SGMS and PGMS for 45B5, B53P4 and 1393B glass formulations. As seen from **Table 6.1** and **Table 6.2**, no significant variation of chemical composition between starting bulk glass (BG) and SGMS was observed for all three glass formulations. However, in comparison significantly higher CaO content and lower B_2O_3 content was observed for PGMS. For example, around 5 mol% lower B_2O_3 and 8 mol% higher CaO was observed for PGMS of 45B5 as compared to the SGMS of the same glass formulation.

Table 6.2: *Compositional analysis of SGMS and PGMS of borate glasses via ICP-MS*

Components	45B5		B53P4		1393B	
	SGMS (mol%)	PGMS (mol%)	SGMS (mol%)	PGMS (mol%)	SGMS (mol%)	PGMS (mol%)
B_2O_3	47.70 ± 0.04	42.90 ± 0.04	54.54 ± 0.01	49.11 ± 0.26	55.40 ± 0.18	49.68 ± 0.20
P_2O_5	2.86 ± 0.02	2.97 ± 0.01	4.22 ± 0.01	3.85 ± 0.01	1.90 ± 0.01	1.77 ± 0.01
CaO	26.42 ± 0.09	34.12 ± 0.03	19.64 ± 0.01	27.56 ± 0.21	21.88 ± 0.18	29.77 ± 0.22
Na_2O	22.80 ± 0.02	19.74 ± 0.02	21.42 ± 0.02	19.26 ± 0.03	5.91 ± 0.01	5.27 ± 0.03
MgO	-	-	-	-	7.33 ± 0.01	6.68 ± 0.02
K_2O	-	-	-	-	7.58 ± 0.01	6.83 ± 0.02

6.2.4 X-ray diffraction analysis

XRD traces for the starting BG, SGMS and washed PGMS are presented in **Figures 6.7 A, B** and **C** respectively, where a single broad peak between 20° and 40° (2θ) was observed for BG and SGMS (except B53P4) of each composition. The absence of any sharp crystalline peaks for BG and SGMS (except B53P4) confirmed the amorphous nature of the glasses. However, three small sharp peaks were observed for SGMS of B53P4 and the peaks were correlated with the peaks of sodium calcium phosphate ($Na_3Ca_6(PO4)_5$) [00-011-0236(N)]. On the other hand, peaks were also observed for the PGMS of each composition. The peaks observed for PGMS correlated with the peaks for $CaCO_3$ as that was used as the porogen for making the glass microspheres porous.

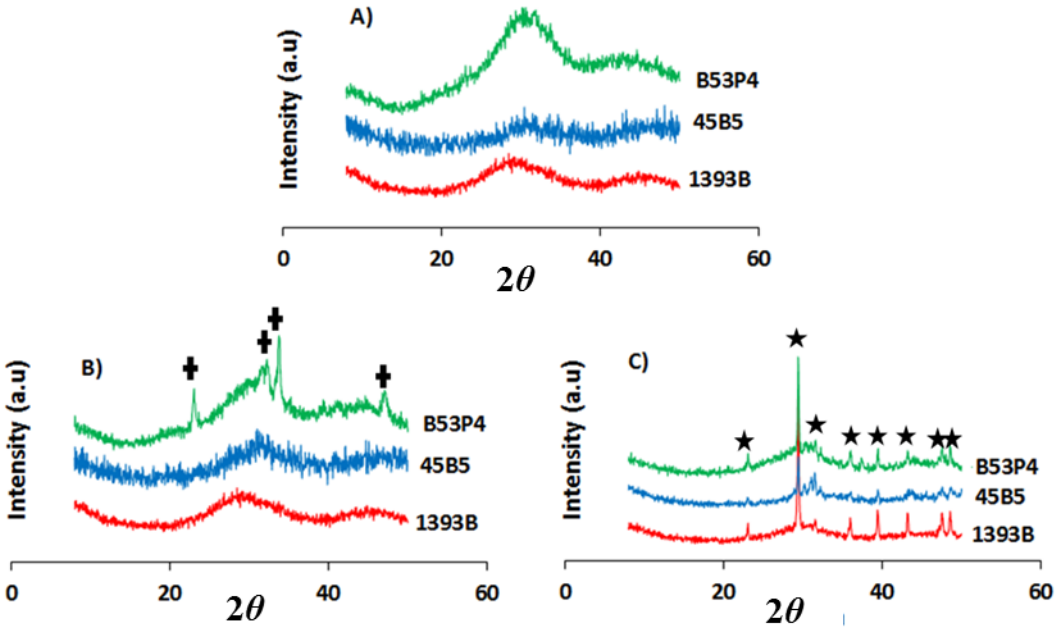


Figure 6.7: *X-ray diffraction pattern for A) BG, B) SGMS and C) washed PGMS of three borate glass formulations investigated. ★ represents for calcium carbonate ($CaCO_3$) peaks and ✚ represents for sodium calcium phosphate ($Na_3Ca_6(PO4)_5$) peaks.*

6.2.5 Thermal Analysis

Figure 6.8 shows the thermal traces of BG, SGMS and PGMS where the corresponding glass transition (T_g), onset of crystallisation (T_x), crystallisation peak (T_c) and melting (T_m) temperature have been labelled. The thermal data such as T_g, T_x, glass stability (ΔT), T_c and T_m for the three different morphologies (i.e. BG, SGMS and PGMS) of the three different borate glass formulations investigated are presented in **Table 6.3**. No significant changes of thermal properties (i.e. T_g, T_x, T_c, T_m) was observed between BG and SGMS of the same glass formulation (see **Table 6.3**). Moreover, no significant variation in T_g was observed between SGMS and PGMS however, significantly lower T_x and T_c were observed for the PGMS (depicted in broken lines) as compared to SGMS.

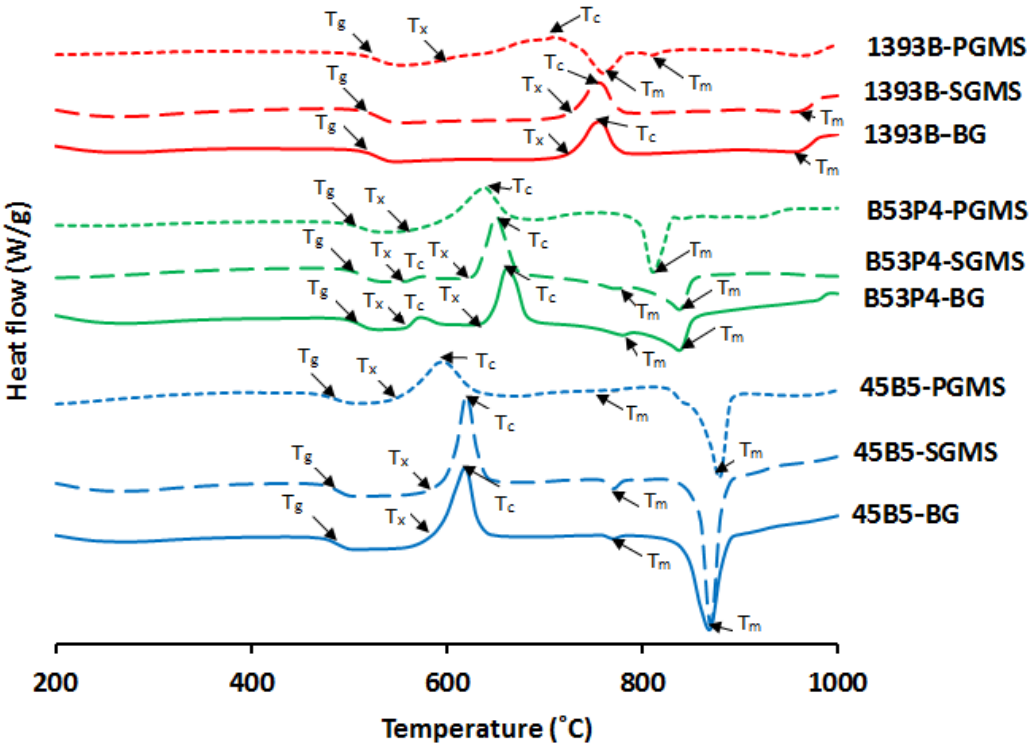


Figure 6.8: *DSC curves of the BG, SGMS and PGMS of three different borate glasses.*

Table 6.3: *Glass transition (T_g), onset of crystallisation (T_x), glass stability (ΔT), crystallisation peak (T_c) and melting temperature (T_m) for BG, SGMS and PGMS of different borate glass formulations, using a 20 $^oC\ min^{-1}$ heating rate.*

Glass Formulations	Glass transition T_g (^oC)	Onset crystallisation T_{x1}(^oC)/ T_{x2}(^oC)	Glass stability $\Delta T = (T_x - T_g)$ ^oC	Crystallisation Temperature T_{c1} (^oC)/ T_{c2} (^oC)	Melting Temperature T_{m1} (^oC)/ T_{m2} (^oC)
45B5-BG	484 ± 2	588 ± 3	104	620 ± 2/-	769 ± 2/873 ± 5
45B5-SGMS	485 ± 2	590 ± 3	105	623 ± 2/-	769 ± 3/869 ± 4
45B5-PGMS	484 ± 3	549 ± 2	65	596 ± 2/-	767 ± 3/877 ± 3
B53P4-BG	508 ± 3	559 ± 3/641 ± 2	52/133	573 ± 3/664 ± 2	779 ± 3/840 ± 4
B53P4-SGMS	510 ± 2	562 ± 2/628 ± 3	52/118	575 ± 2/652 ± 2	774 ± 2/840 ± 3
B53P4-PGMS	512 ± 2	560 ± 2	48	-/638 ± 3	813 ± 4/-
1393B-BG	526 ± 3	724 ± 3	198	756 ± 2/-	964 ± 5/-
1393B-SGMS	527 ± 3	726 ± 2	199	755 ± 2/-	966 ± 4/-
1393B-PGMS	526 ± 2	584 ± 2	58	711 ± 2/-	762 ± 3/809 ± 4

6.2.6 Density, tap density and porosity measurement

Table 6.4 shows the density (measured by He pycnometer and tap density) and porosity for SGMS and PGMS of 45B5, B53P4 and 1393B glass formulations. As seen from **Table 6.4**, the density and tap density reduced significantly for PGMS, however the porosity increased 2-3 folds for the PGMS for all of the glass compositions when compared to SGMS. For example, density and tap density for the SGMS were found to be around 2.4 and 1.7 g/cm^3, respectively. Whereas, density and tap density for the PGMS were found to be around 2.3 and 0.5-0.8 g/cm^3, respectively. On the other hand, porosity of SGMS and PGMS were found to be 27-31 and 65-75 %, respectively. Moreover, the theoretically calculated porosity (%) for PGMS was found to be quite similar values to the experimental data obtained via mercury porosimetry. The methodology for how these calculations (of porosity) were conducted is detailed in Chapter 3, section 3.3.13.

Table 6.4: *Density, tap density and porosity of SGMS and PGMS of three different borate glasses investigated.*

Formulation	Density	Tap density	% Porosity (Calculated)	% Porosity (Hg porosimetry)
45B5 PGMS	2.2859 ± 0.0035	0.82 ± 0.02	64.13	66
B53P4 PGMS	2.3613 ± 0.0053	0.65 ± 0.3	74.17	71
1393B PGMS	2.3021 ± 0.0060	0.50 ± 0.3	78.28	75
45B5 SGMS	2.4963 ± 0.0042	1.72 ± 0.03	31.10	-
B53P4 SGMS	2.4321 ± 0.0022	1.75 ± 0.02	28.05	-
1393B SGMS	2.4245 ± 0.0063	1.76 ± 0.02	27.82	-

6.2.7 Conversion of borate glasses into HA in dil. K_2HPO_4

6.2.7.1 Degradation studies in dil. K_2HPO_4

Figure 6.9 shows the mass loss (%) as a function of degradation time or reaction time in days for SGMS and PGMS of three different borate glass formulations during conversion to hydroxyapatite in 0.02 M K_2HPO_4 solution. For both SGMS and PGMS of each glass, mass loss (%) increased with time, eventually reaching a final limiting value. The attainment of limiting value was taken as an indication of the completion of reaction and the inverse of the time required to reach the limiting value was taken as a measure of the reaction rate. It can be seen from **Figure 6.9**, higher mass loss (%) was observed for PGMS compared to their respective SGMS of each glass compositions. Moreover, the data showed that the highest reaction rate was observed for B53P4 glass and the limiting value (around 52 % mass loss) was attained by 10 days for PGMS and the constant mass loss around 50 % was found for SGMS by 14 days. Whereas, the limiting value (around 40 % mass loss) for PGMS of 45B5 was achieved by 14 days and for SGMS of 45B5 was achieved by 21 days. On the other hand, the lowest mass loss % (19 % for PGMS and 14 % for SGMS) was observed for 1393B glass and no limiting value was found for both SGMS and PGMS of 1393B during 21 day duration of these studies.

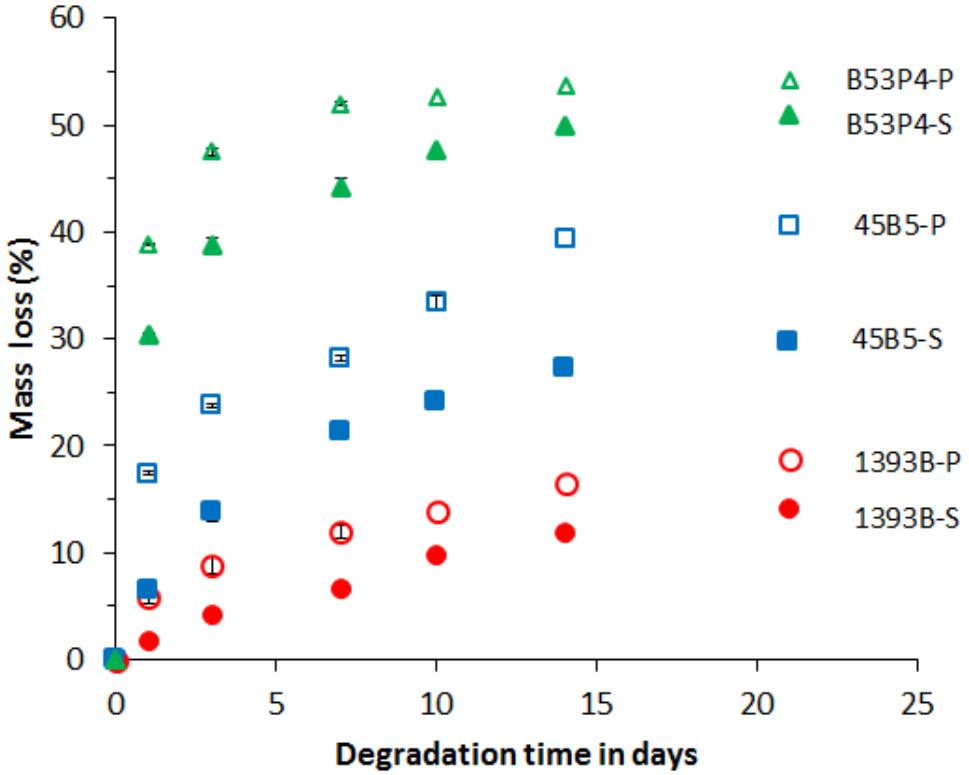


Figure 6.9: *Weight loss versus time in day during the conversion reaction of SGMS (represented as solid symbols) and PGMS (represented as open symbols) of three different borate glass in 0.02 M K_2HPO_4 solution at 37 ^oC.*

6.2.7.2 pH Measurement

Figure 6.10 represents the variation of pH of phosphate solution as a function of reaction time for both SGMS and PGMS of three different borate glasses. The starting pH value of the solution was 7.4 for all systems.

The pH for phosphate solution containing the dissolution products of PGMS increased from ~7.4 to ~10 for 45B5, 9.5 for B53P4 and 8.5 for 1393B at day-3 then gradually decreased with increasing degradation time as can be seen from **Figure 6.10**. The pH values at day-10 for the PGMS of B53P4 and 1393B were found to be 7.6 and 8, respectively and remained almost constant rest of the degradation time. Whereas, pH for PGMS of 45B5 gradually decreased with increasing time and the value was found to be 7.6 at day 21. On the other hand, the pH values for the solution containing dissolution products of SGMS also gradually increased from 7.4 to 9.8 for 45B5, 8.8

for B53P4 and 8.1 for 1393B at day-3 then gradually decreased to 8.3 by day-14 for 45B5 and 7.9 by day-10 for 1393B and remained relatively constant for the remainder of the study. On the other hand, pH value for SGMS of B53P4 was found to be 7.9 at day-10 and slightly higher pH value (8.5) was observed at day-14 and finally, pH value had decreased to 7.6 by day-21.

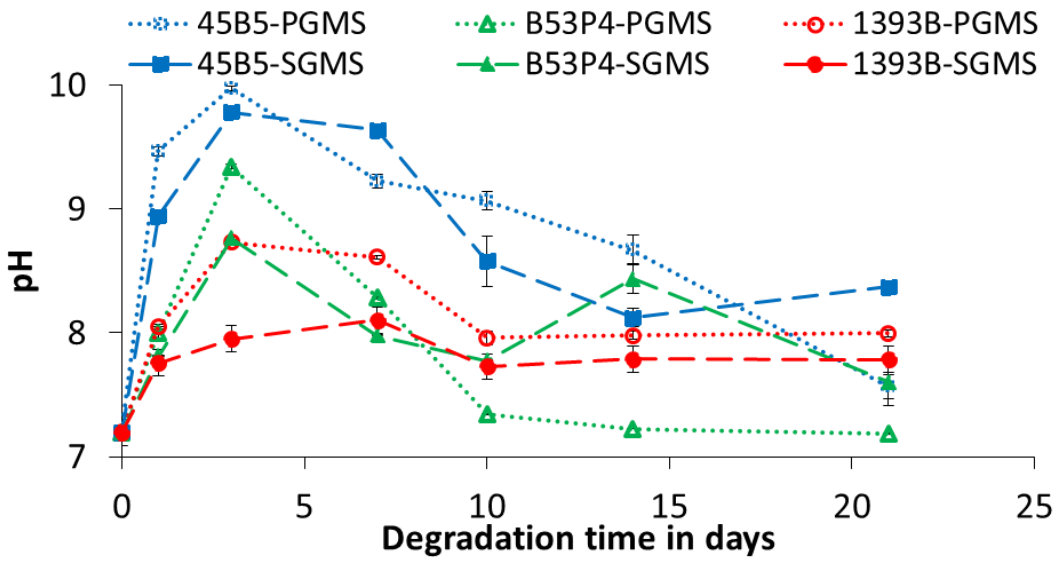


Figure 6.10: *pH change as a function of immersion time (day) of the SGMS (represented as solid symbols) and PGMS (represented as open symbols) investigated in 0.02 M K_2HPO_4 solution at 37 °C over 21 day duration.*

6.2.7.3 XRD

XRD spectra for both SGMS and PGMS of three different borate glasses, after reaction in the phosphate solution at various time points, are shown in **Figure 6.11**. The major peaks in the patterns corresponded to those of a standard HA, $Ca_{10}(PO_4)_6(OH)_2$ (JCPSD 72-1243), indicating the formation of HA during the reaction. A HA peak was observed at day-14 for SGMS, whereas the HA peak was found at an earlier time point (at day-10) for PGMS of 45B5 glass as seen from **Figure 6.11 A**. Moreover, peak intensity increased for both SGMS and PGMS with increasing reaction time and solely HA peak for PGMS was observed at day-21. From **Figure 6.11 B**, it can be seen that HA formed at day-14 for SGMS of B53P4 and other than HA no crystallisation peaks of sodium calcium phosphate ($Na_3Ca_6(PO4)_5$) [00-011-0236(N)] were observed which was

confirmed via XRD (see **Figures 6.7 B** and **C**) for starting SGMS prepared via flame spheroidisation route. Whereas, HA peak was observed at day-3 only for PGMS of B53P4. No crystallisation peaks other than HA were found at day-10 and HA peak intensity increased with increasing reaction time. On the other hand, no hydroxyapatite peak was observed for both SGMS and PGMS of 1393B even after reaction for 28 days. Only $CaCO_3$ peaks due to the presence of porogen residue in PGMS after washing were observed for PGMS of 1393B at each time point.

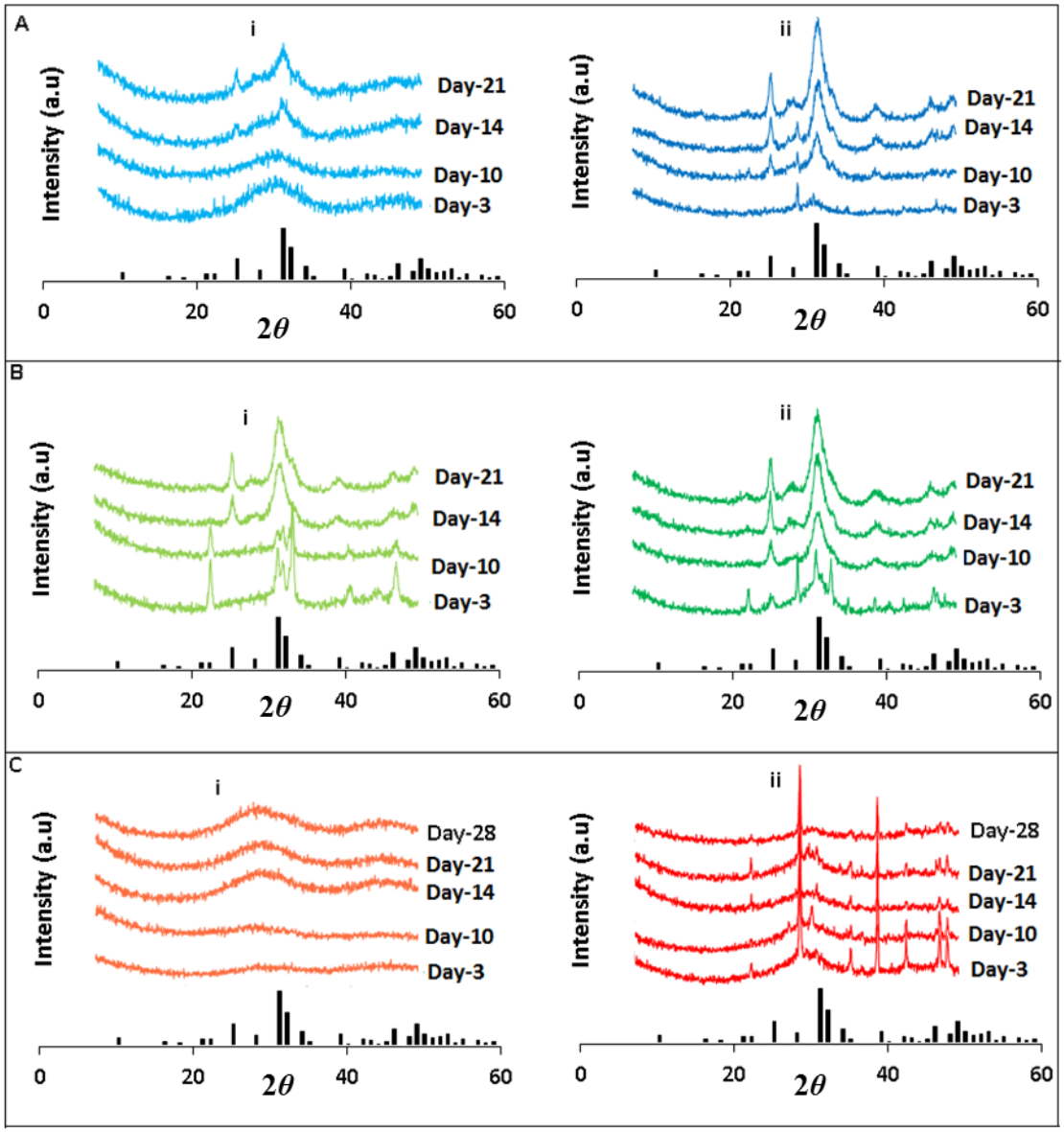


Figure 6.11: *X-ray diffraction pattern for both i) SGMS and ii) PGMS of three borate glass formulations A) 45B5, B) B53P4 and C) 1393B during the conversion reaction of microspheres in 0.02 M K_2HPO_4 solution at 37 °C at various time point. XRD spectra for HA shown in each Figure for comparison.*

6.2.7.4 SEM

Figure 6.12 and **Figure 6.13** represent the SEM images at different magnifications for SGMS and PGMS of borate glasses, respectively after 21 days of immersion in dil. K_2HPO_4 solution. It can be seen at higher magnification from both Figures that the HA formed on the surface of SGMS and both surface and inside of pores of PGMS of 45B5 and B53P4 (see **Figures 6.12 A-B** and **Figures 6.13 A-B**). However, no HA formation was observed on the surface of SGMS and PGMS of 1393B after 21 day of immersion in dil. K_2HPO_4 (see **Figure 6.12 C** and **Figure 6.13 C**).

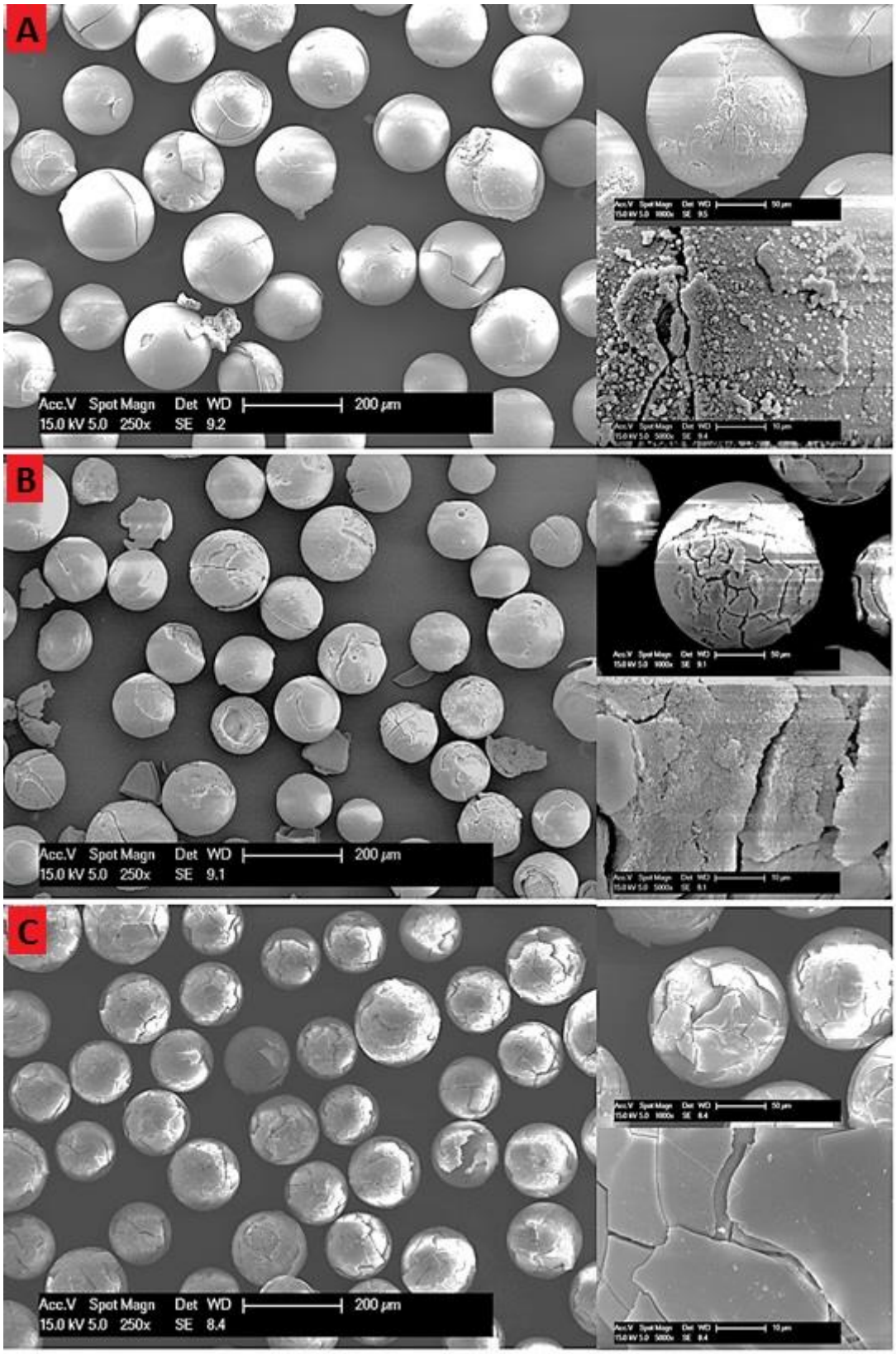


Figure 6.12: *SEM images of SGMS of three borate glass formulations A) 45B5, B) B53P4 and C) 1393B after conversion reaction of microspheres in 0.02 M K_2HPO_4 solution at 37 ^oC at day-21.*

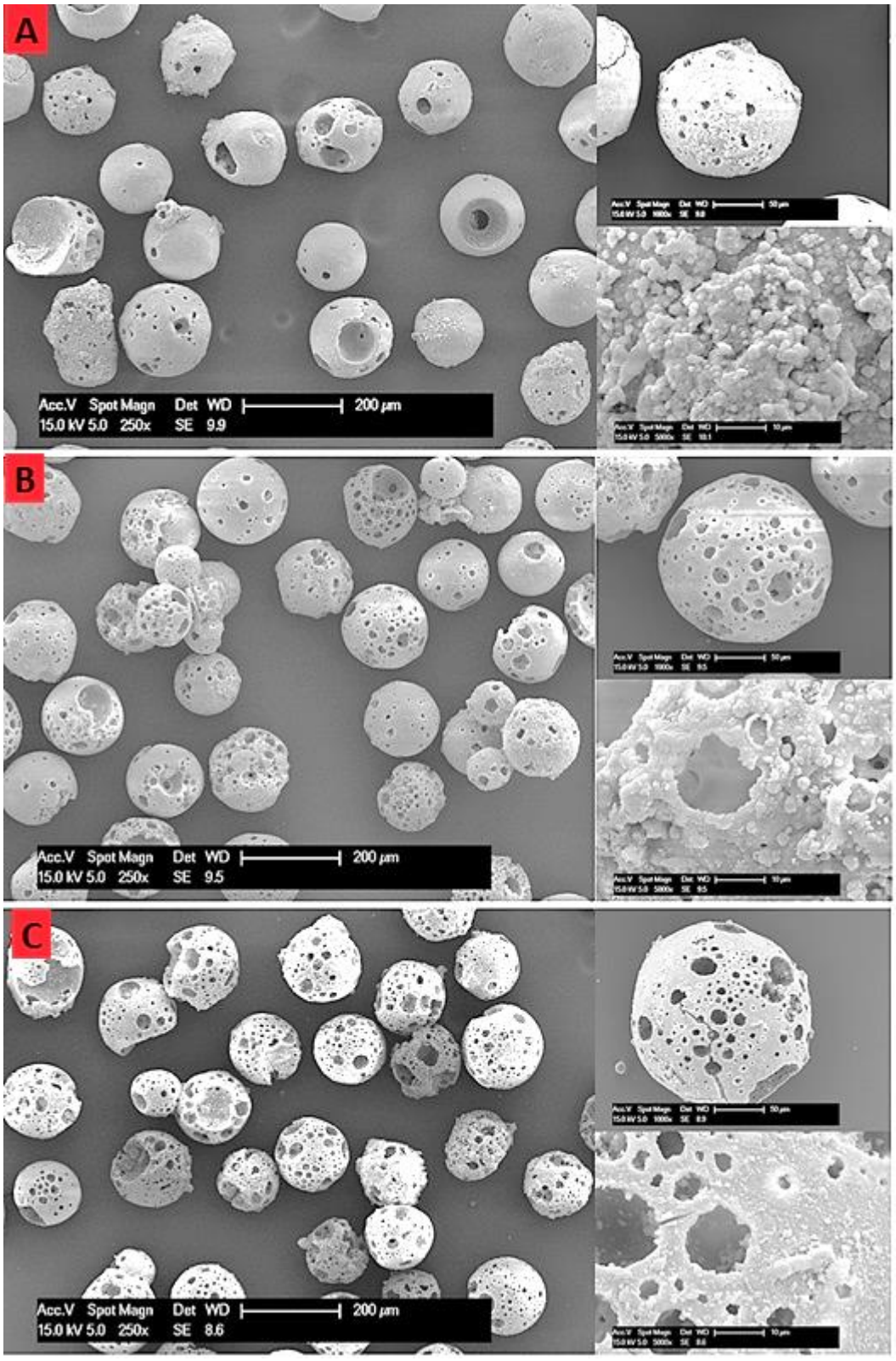


Figure 6.13: *SEM images of PGMS of three borate glass formulations A) 45B5, B) B53P4 and C) 1393B after conversion reaction of microspheres in 0.02 M K_2HPO_4 solution at 37 ^oC at day-21.*

Figures 6.14-6.19 represent the cross-section at different magnifications for SGMS and PGMS of three different borate glasses at A) day-0 (starting microspheres), B) day-10 and C) day-21 during the conversion reaction of microspheres in 0.02 M K_2HPO_4 solution at 37 ^oC and i and ii represent the EDX spectra for the outer (shell) and inner (core) point of microspheres, respectively. It can be noted that quantitative analysis or elemental mapping for boron containing compounds could not be measured accurately via EDX (Oxford Instruments INCA, UK) as boron is a very light element. However, boron can be detected via EDX. Therefore, the point spectra at several point for various microspheres was carried out to confirm the presence of boron before (at day-0) and after immersion (at day-10 and day-21) of the glass microspheres in dil. K_2HPO_4 solution. One of the spectrum for outer point and another one for core point are representative examples (see **Figures 6.14-6.19 A, B, C (i-ii)**).

The presence of boron inside and at the outer surface for starting SGMS and PGMS of all borate glasses (at day-0) was confirmed via EDX spectra (see **Figures 6.14-6.19 A (i-ii)**).

It can be seen that the conversion reaction for SGMS of 45B5 started from the outer surface (see **Figure 6.14 B**) and moved inward with increasing immersion time (see **Figure 6.14 C**) and multilayers of microspheres formed after 21 days of immersion in dil. K_2HPO_4 solution (see **Figure 6.14 C**). However, some plane areas between the cracks were observed at day 21. Boron was found for SGMS of 45B5 at the plane surface inside and outside of the microspheres even after 21 days of immersion in dil. K_2HPO_4 solution (see **Figures 6.14 C i-ii**). However, no boron was detected for the cracked surface (EDX spectra is not presented here) of the microspheres.

On the other hand, the PGMS could potentially have converted into HA from inside and outside of microspheres. It can be seen from **Figures 6.15 B i-ii**, the presence of boron was observed inside and outside for PGMS of 45B5 at day-10. However, no boron was found for PGMS of 45B5 after 21 days of immersion in dil. K_2HPO_4 solution (see **Figures 6.15 C i-ii**).

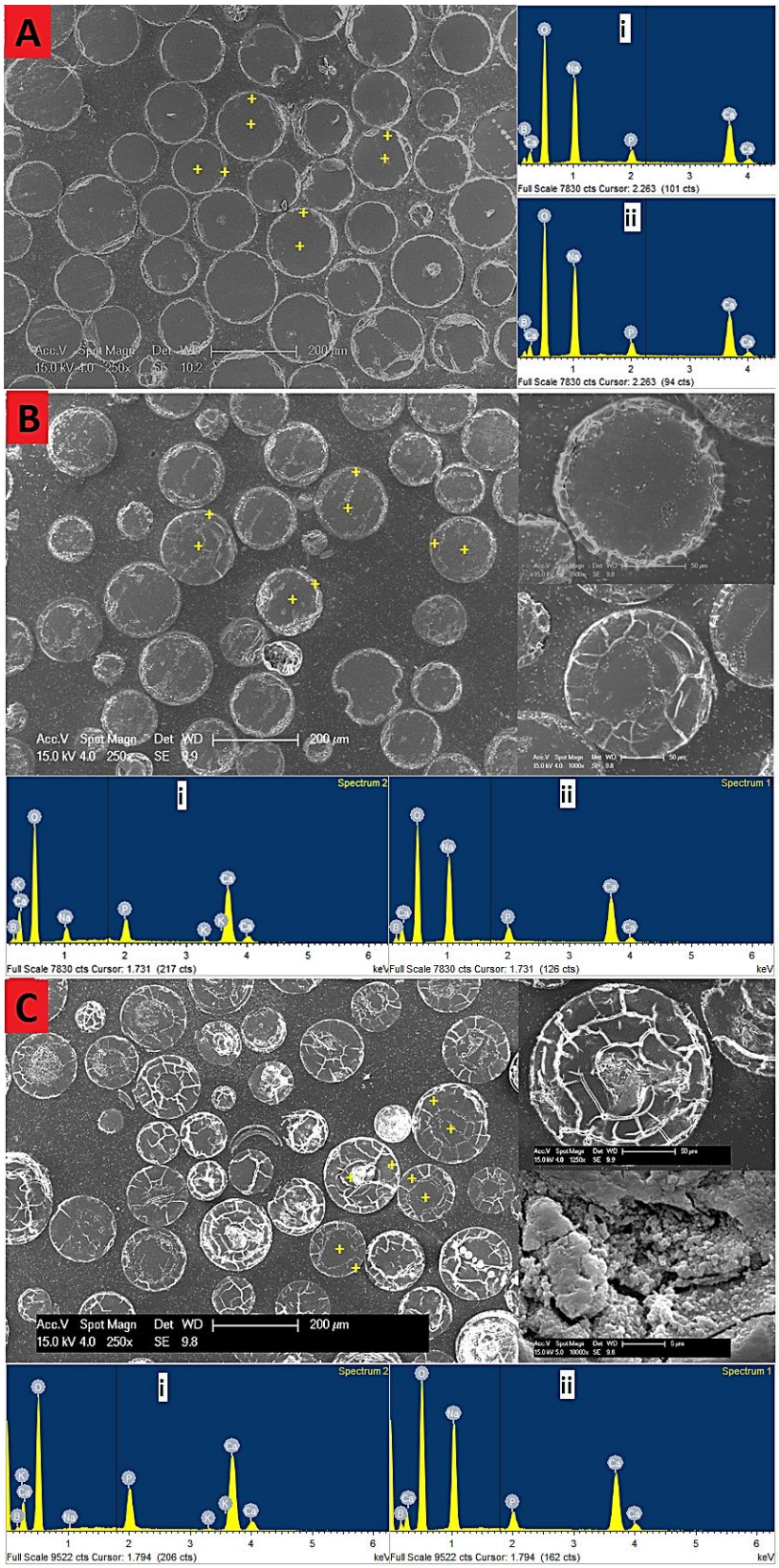


Figure 6.14: *Cross-section for SGMS of 45B5 borate glass at A) Day-0 (starting microspheres), B) Day-10 and C) Day-21 during the conversion reaction of microspheres in 0.02 M K_2HPO_4 solution at 37 ^oC and i and ii represent the EDX spectra for outer (shell) and inner (core) point of microspheres, respectively.*

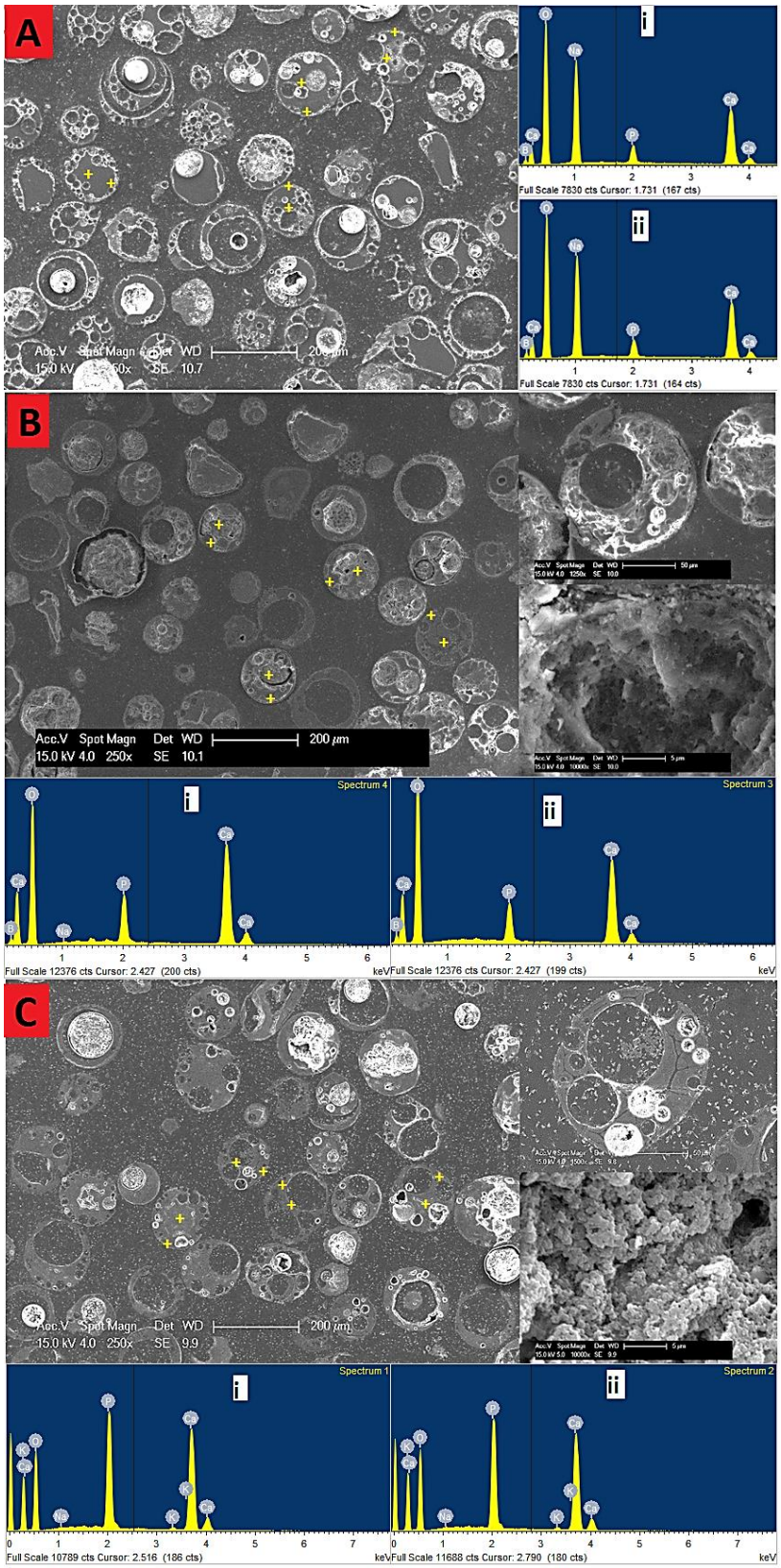


Figure 6.15: *Cross-section for PGMS of 45B5 borate glass at A) Day-0 (starting microspheres), B) Day-10 and C) Day-21 during the conversion reaction of microspheres in 0.02 M K_2HPO_4 solution at 37 ^oC and i and ii represent the EDX spectra for outer (shell) and inner (core) point of microspheres, respectively.*

It can be seen from **Figure 6.16** that the cross-section of the converted SGMS of B53P4 were quite different when compared to the cross-sections for converted SGMS of 45B5. Hollow microspheres for SGMS of B53P4 were observed at day-21 (see **Figure 6.16 C**). The presence of boron was observed only inside the SGMS of B53P4 at day-10. Whereas, no boron was found on the inner and outer surfaces of SGMS of B53P4 at day-21 (see **Figures 6.16 C i-ii**). On the other hand, no boron was detected on the inner and outer edges of the PGMS of B53P4 after 10 days of immersion in dil. K_2HPO_4 solution (see **Figures 6.17 B i-ii**).

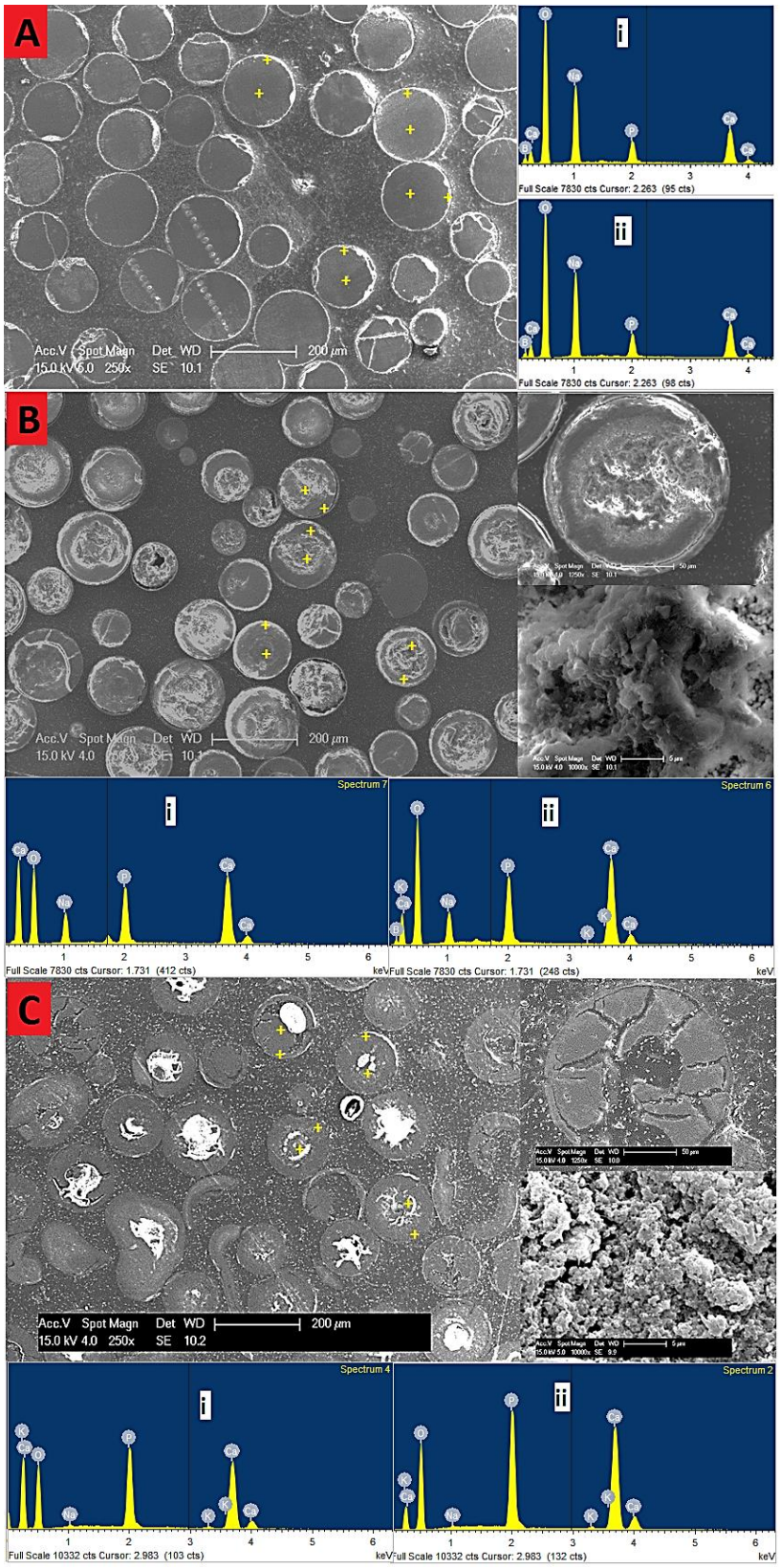


Figure 6.16: *Cross-section for SGMS of B53P4 borate glass at A) Day-0 (starting microspheres), B) Day-10 and C) Day-21 during the conversion reaction of microspheres in 0.02 M K_2HPO_4 solution at 37 ^oC and i and ii represent the EDX spectra for outer (shell) and inner (core) point of microspheres, respectively.*

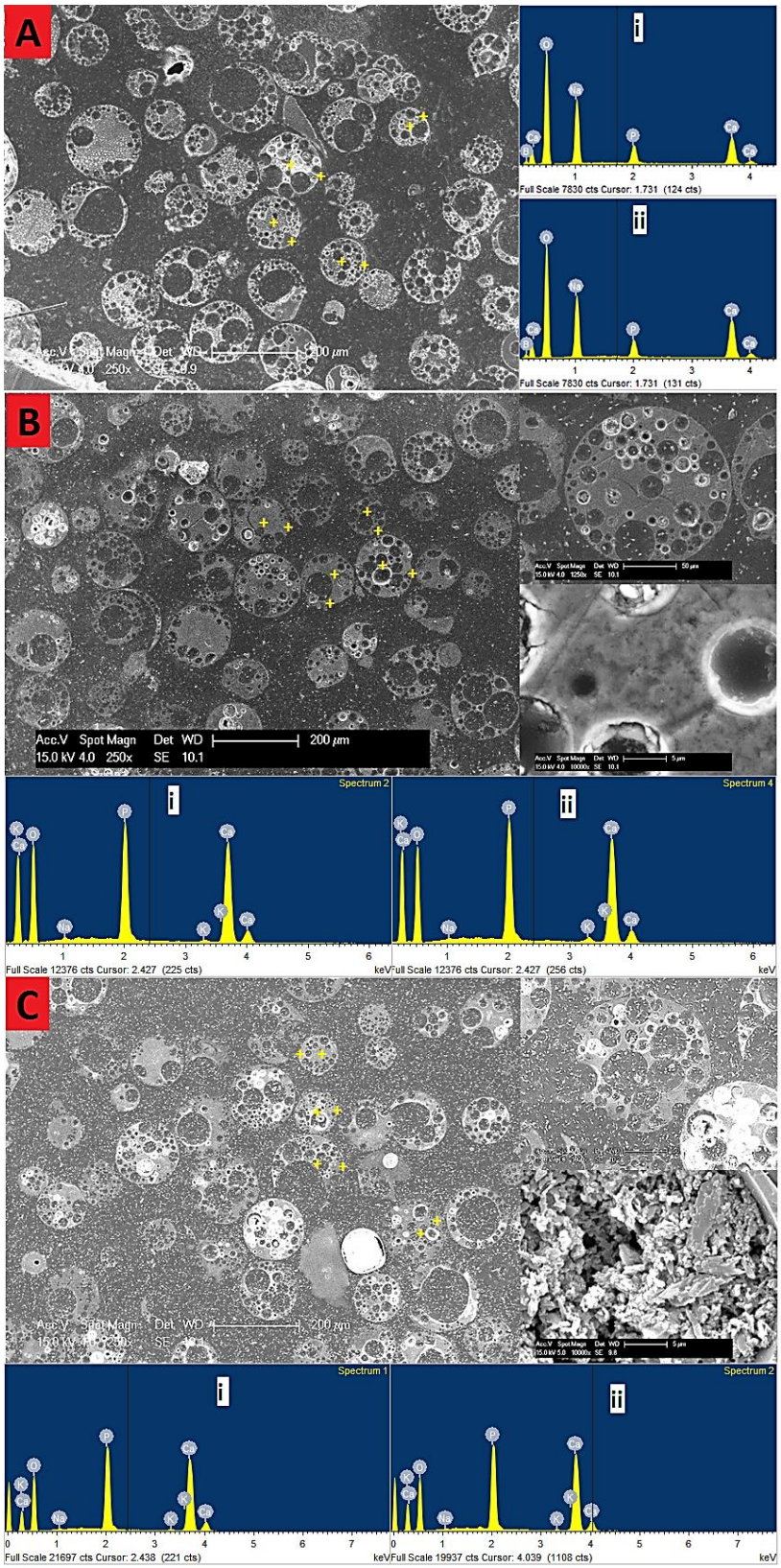


Figure 6.17: *Cross-section for PGMS of B53P4 borate glass at A) Day-0 (starting microspheres), B) Day-10 and C) Day-21 during the conversion reaction of microspheres in 0.02 M K_2HPO_4 solution at 37 ^oC and i and ii represent the EDX spectra for outer (shell) and inner (core) point of microspheres, respectively.*

SGMS of 1393B degraded quite differently when compared to both SGMS of 45B5 and B53P4 as can be seen from **Figure 6.18**. A large solid core and small degraded outer surfaces were observed for SGMS of 1393B even after 21 days of immersion in dil. K_2HPO_4 solution (see **Figure 6.18 C**). Boron was detected inside and outer surface for both SGMS and PGMS of 1393B at day-21 (see **Figures 6.18 C i-ii** and **Figures 6.19 C i-ii**).

Moreover, it can be seen from the EDX spectra for the cross-sections of microspheres, the lower peak intensity of Na was observed at higher degradation time point (day-10 or day-21) compared to the initial time point (day-0). In addition, the lower peak intensity of Na was observed at outer point (shell) compared to inner point (core) at the same time point for the degraded microspheres.

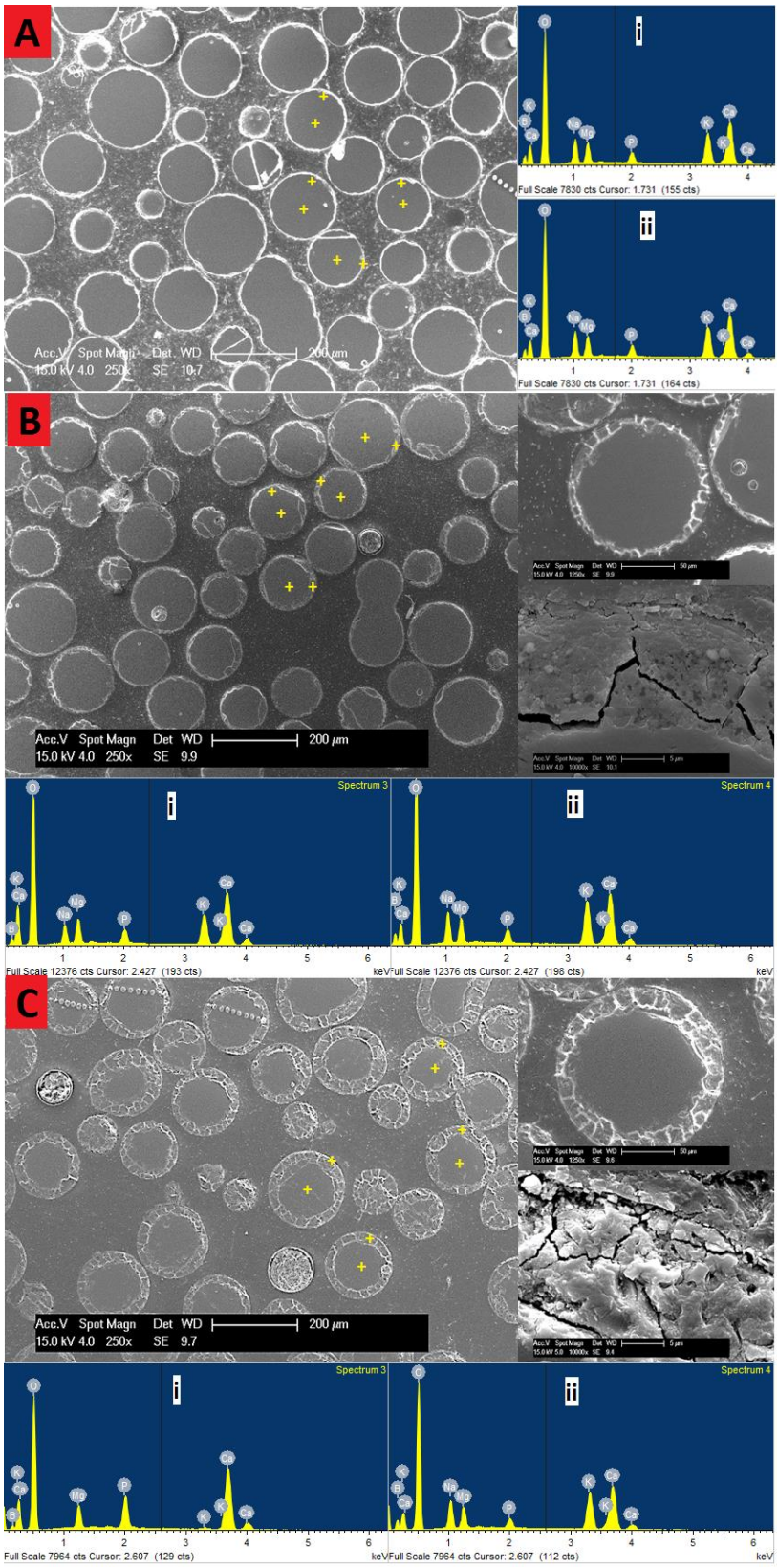


Figure 6.18: *Cross-section for SGMS of 1393B borate glass at A) Day-0 (before conversion), B) Day-10 and C) Day-21 during the conversion reaction of microspheres in 0.02 M K_2HPO_4 solution at 37 ^oC and i and ii represent the EDX spectra for outer (shell) and inner (core) point of microspheres, respectively.*

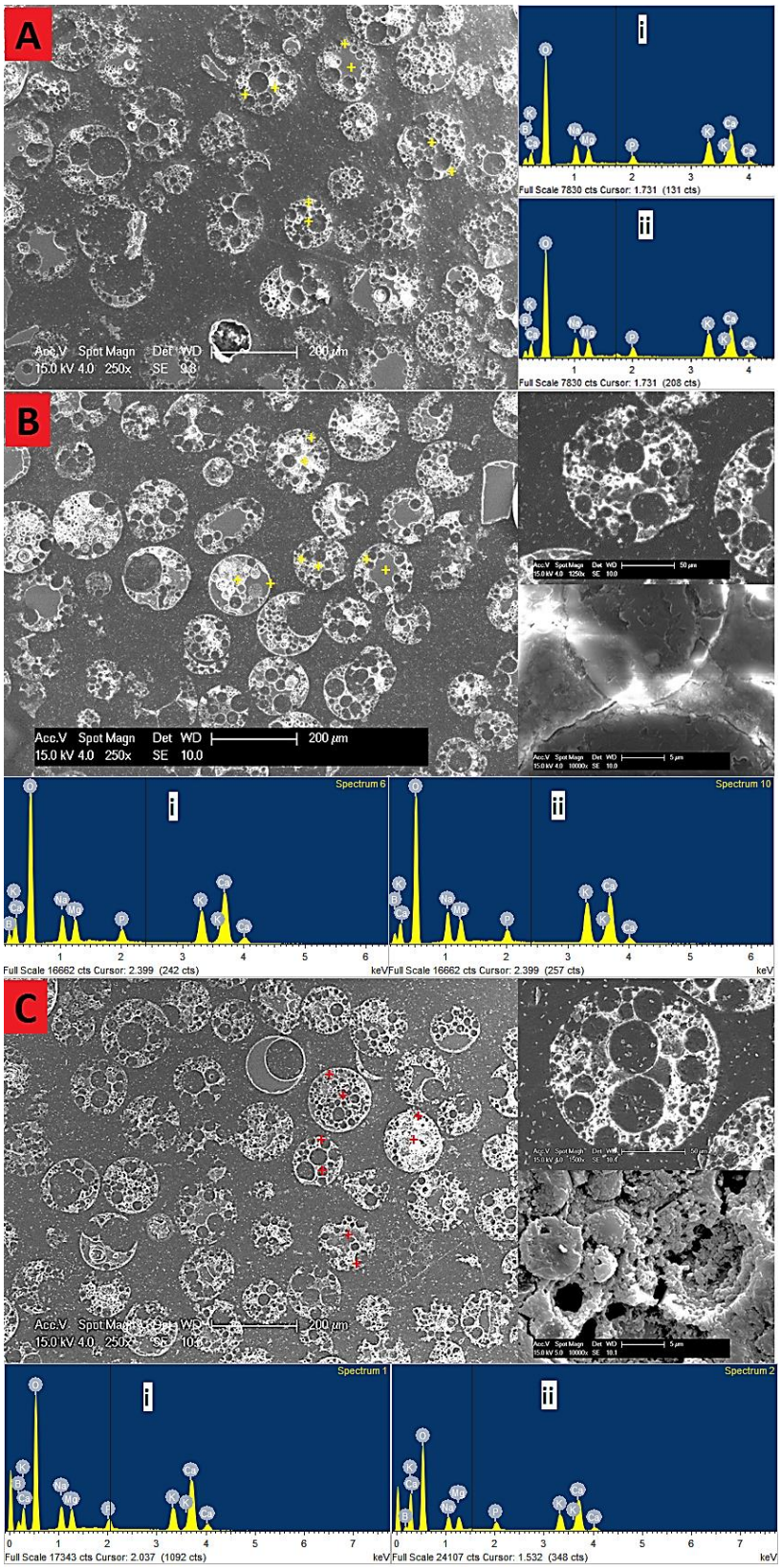


Figure 6.19: *Cross-section for PGMS of 1393B borate glass at A) Day-0 (before conversion), B) Day-10 and C) Day-21 during the conversion reaction of microspheres in 0.02 M K_2HPO_4 solution at 37 ^oC and i and ii represent the EDX spectra for outer (shell) and inner (core) point of microspheres, respectively.*

6.2.7.5 Ion release studies in dil. K_2HPO_4 solution

Ion release profiles for both SGMS and PGMS were investigated via ICP-MS, recording the release of B, P, Ca^{2+}, Na^{+}, K^{+} and Mg^{2+} ion in dil. K_2HPO_4 solution and the ion release profiles obtained are presented in **Figures 6.20 A-F**.

The maximum B ion release was observed at day-1 for all glass formulations (see **Figure 6.20 A**). Moreover, higher B ion release at day-1 was found for PGMS compared to their respective SGMS that was expected.

The highest B ion release at day-1 was observed for B53P4 (1108 ppm for PGMS and 1050 ppm for SGMS) then the ion release decreased with increasing immersion time. No B ion release was observed for PGMS of B53P4 at day-10 whereas, boron release was found to be zero for SGMS of B53P4 at day-21.

Boron release for PGMS of 45B5 was found to be 517 ppm at day-1 and then gradually decreased with increasing time and no boron was found at day-21. Whereas, boron release for SGMS of 45B5 was found to be 212 ppm at day-1 and remained constant up to day-7 then decreased to 85 ppm at day-10 and then remained almost constant up to day-21.

The lowest B ion release at day-1 was observed for 1393B formulation. Boron release for PGMS of 1393B was found to be 284 ppm at day-1 and then gradually decreased with increasing time and the value was found to be 82 ppm at day-10 and then the value was remained nearly constant up to day-21. On the other hand, boron release of 81 ppm was observed at day-1 for SGMS of 1393B and remained constant up to day-7 after which boron release decreased slightly to 71 ppm by day-10 and then remained constant again for the remainder period.

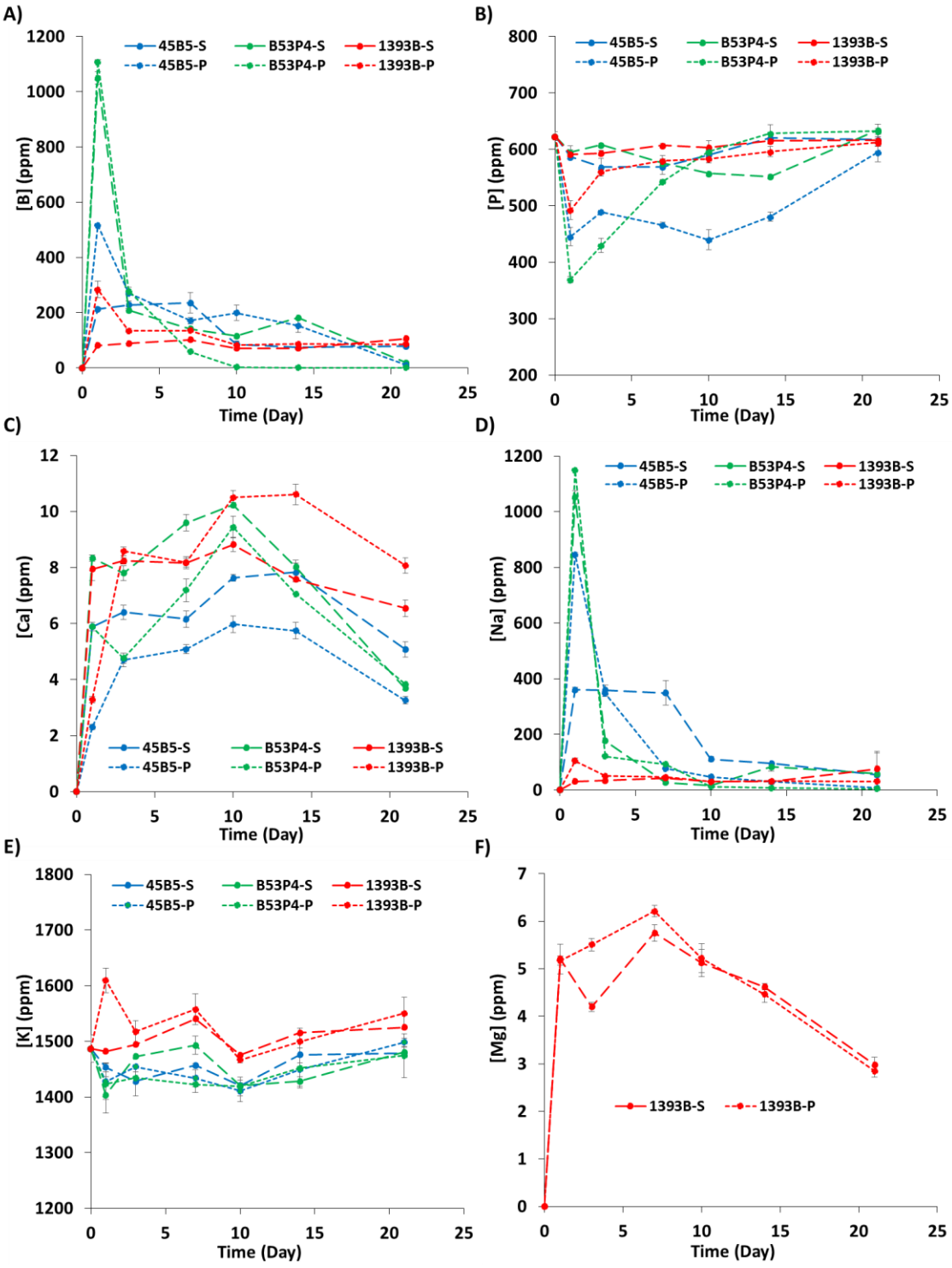


Figure 6.20: *Concentration of A) [B], B) [P], C) [Ca], D) [Na], E) [K] and F) [Mg] measured by ICP-MS for SGMS and PGMS of borate glasses investigated in dil. K_2HPO_4 during 21 days of immersion period. (Error bars are also included in the data above)*

From **Figure 6.20 B**, it can be seen that the highest P ion uptake from the solution was observed for PGMS of B53P4 at day-1 and the amount of ions uptake was found to be 253 ppm. P ion uptake from the solution was then gradually decreased with increasing time and the value was found to be 27 ppm only at day-10 and no P ion uptake was observed from the time point at day-14. P ion uptake was found to be 177 ppm at day-1 for PGMS of 45B5 then decreased to 133 ppm at day-3 and then increased to 183 ppm at day-10 after that it was gradually decreased with increasing time and the final value was found to be 28 ppm at day 21. The amount of P ion uptake was found to be 130 ppm at day-1 for PGMS of 1393B then decreased to 62 ppm at day-3 after that slowly decreased with increasing immersion time upto day-21 and the value was found to be 11 ppm at day-21.
On the other hand, lower P ion uptake was observed for SGMS compared to PGMS for the same glass compositions. The maximum P ion uptake was observed for SGMS of B53P4 and was found to be 71 ppm at day-14.

Both SGMS and PGMS followed nearly similar trend of Ca^{2+} ion release profiles for all borate glass formulations as can be seen from **Figure 6.20 C**. The Ca^{2+} ion release for SGMS was higher (except 1393B) in comparison to their respective PGMS. For 45B5, Ca^{2+} ion release increased with increasing time and the maximum value was found to be 7.8 ppm at day-14 for SGMS and 5.9 ppm at day-10 for PGMS and then gradually decreased with increasing time. Similarly, for B53P4, Ca^{2+} ion release increased to 10 ppm for SGMS and 9 ppm for PGMS at day-10 and then gradually decreased to 3 ppm at day-21 for both SGMS and PGMS. On the other hand, for 1393B, Ca^{2+} ion release increased to 8 ppm for SGMS and 10 ppm for PGMS at day-10 and then gradually decreased to 6 ppm for SGMS and 8 ppm for PGMS at day-21.

The trend for Na^{+} ion release profiles of all borate glass formulations were quite similar to the trend of B ion release as can be seen from **Figure 6.20 D**. The maximum Na^{+} ion release was observed at day-1 for all glass formulations (see **Figure 6.20 D**). In addition, higher Na^{+} ion release at day-1 was found for PGMS compared to their respective SGMS as expected. The maximum Na^{+} ion release at day-1 was observed for B53P4 (1148 ppm for PGMS and 1052 ppm for SGMS) then the ion release

decreased with increasing immersion time. Na^+ ion release of 4 ppm was observed for PGMS and 58 ppm for SGMS of B53P4 at day-21. Similarly, sodium ion release for PGMS of 45B5 was found to be 845 ppm at day-1 and then gradually decreased with increasing time and finally, the value was found to be 7 ppm at day-21. Whereas, sodium ion release for SGMS of 45B5 was found to be 360 ppm at day-1 and remained nearly constant up to day-7 then decreased to 111 ppm at day-10 and finally the value for Na^+ ion was 54 ppm at day-21. On the other hand, the lowest Na^+ ion release at day-1 was observed for the 1393B formulation. Sodium ion release for PGMS of 1393B was found to be 104 ppm at day-1 and then gradually decreased with increasing time to approx. 30 ppm at day-10 and then Na^+ ion release remained nearly constant up to day-21. Whereas, Na^+ ion release increased to 30 ppm only for SGMS of 1393B and remained constant up to day-14 and finally, Na^+ ion release was found to be 76 ppm at day-21.

The maximum K^+ ion release was found to be 123 ppm at day-1 for PGMS and 54 ppm at day-7 for SGMS of 1393B. Moreover, K^+ ion release of 64 ppm for PGMS and 39 ppm for SGMS of 1393B at day-21 was observed. However, small amount of K^+ ion uptake was observed at day-1 and day-10 for without potassium containing glass such as 45B5 and B53P4 as can be seen from **Figure 6.20 E**.

Mg^{2+} ion release for PGMS of 1393B increased to 6.2 ppm by day 7 and then gradually decreased to 2.8 ppm by day-21. Whereas, Mg^{2+} ion release for SGMS of 1393B increased to 5.2 by day-1 and then decrease to 4.1 ppm by day-3 and increased again to 5.7 at day-7 after that Mg^{2+} ion release gradually decreased to 2.9 ppm at day-21.

6.2.7.6 Compositional analysis

Table 6.5 represents the compositional analysis in mol% obtained via ICP-MS for SGMS and PGMS of three different borate glasses after conversion in dil. K_2HPO_4 at day 21. From analysis it can be seen that very negligible (less than 1 mol%) amount of B_2O_3 and Na_2O were found for both SGMS and PGMS of B53P4 and only for PGMS

of 45B5 and Ca/P (atomic %) ratio was found to be around 1.4 for all of them. Whereas, 35 mol% B_2O_3 remained in SGMS of 45B5 and Ca/P ratio was found to be 2.47 for SGMS of 45S5. On the other hand, B_2O_3 was found to be 50 mol% for SGMS and 35 mol% PGMS of 1393B glass and Ca/P ratio was found to be 3.23 and 2.6 for SGMS and PGMS of 1393B, respectively. Moreover, Na_2O was not dissolved completely from SGMS of 45B5 and from both SGMS and PGMS of 1393B. In addition, small amount of K_2O was found for all of the borate glass formulations.

Table 6.5: *Compositional analysis for SGMS and PGMS of borate glasses after conversion in dil. K_2HPO_4 at day 21.*

Components	**45B5**		**B53P4**		**1393B**	
	SGMS (mol%)	PGMS (mol%)	SGMS (mol%)	PGMS (mol%)	SGMS (mol%)	PGMS (mol%)
B_2O_3	35.96 ± 2.90	0.77 ± 0.09	0.84 ± 0.02	0.39 ± 0.04	50.74 ± 0.27	35.62 ± 1.23
P_2O_5	9.68 ± 1.47	25.88 ± 0.09	26.01 ± 0.09	26.42 ± 0.06	4.11 ± 0.12	8.16 ± 0.31
CaO	47.86 ± 3.63	71.68 ± 0.22	71.41 ± 0.14	71.59 ± 0.14	26.81 ± 0.11	42.48 ± 1.17
Na_2O	5.86 ± 2.22	0.30 ± 0.01	0.62 ± 0.01	0.34 ± 0.01	4.3 ± 0.01	2.05 ± 0.11
MgO	-	-	-	-	8.27 ± 0.08	8.78 ± 0.01
K_2O	0.34 ± 0.01	0.92 ± 0.01	0.83 ± 0.09	0.83 ± 0.02	5.78 ± 0.03	2.92 ± 0.14

6.2.7.7 Conversion reaction at different concentration and different type of phosphate solution

As B53P4 glass microspheres converted to HA in 0.02 M K_2HPO_4 solution at earlier time point (day-3 for PGMS) compared to other glasses, B53P4 microspheres were chosen for further investigation as to whether there were any effects for the formation of HA with the variation of K_2HPO_4 solution concentration.

Figure 6.21 shows X-ray diffraction pattern for both SGMS and PGMS of B53P4 and 1393B after immersion in 0.2 M K_2HPO_4 solution at 37 ^oC. HA formed after one day for PGMS of B53P4 when the microspheres were immersed in ten time's higher concentration of K_2HPO_4 solution (0.2 M) as can be seen from **Figure 6.21**. However, no HA peak was observed for SGMS of B53P4 in 0.2 M K_2HPO_4 solution at day-1.

On the other hand, no HA peak was observed for both SGMS and PGMS of 1393B even after 28 days of immersion in 0.2 M K_2HPO_4 solution. Therefore, an alternative phosphate solution (Na_2HPO_4) was explored and experiment was carried out only for PGMS of 1393B.

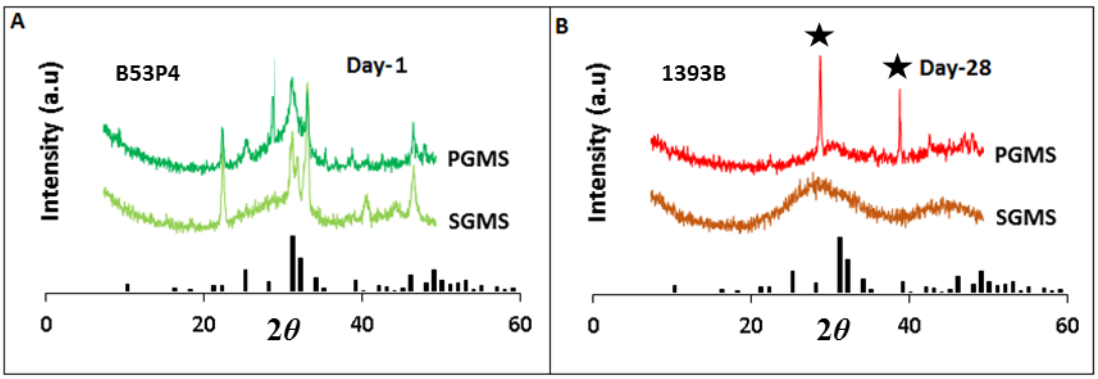


Figure 6.21*: X-ray diffraction pattern for both SGMS and PGMS of A) B53P4 at day-1 and B) 1393B at day-28 during the conversion reaction of microspheres in 0.2 M K_2HPO_4 solution at 37 ^oC. XRD spectra for HA shown in each Figure for comparison. ★ represents for calcium carbonate ($CaCO_3$) peaks.*

Figure 6.22 represents the mass loss % for PGMS of 1393B at two different concentrations of Na_2HPO_4 solution with the variation of degradation time in day. It can be seen from **Figure 6.22** that the mass loss % for PGMS of 1393B increased with increasing time up to day-14 and the mass loss % was found to be 40 % in 0.2 M Na_2HPO_4 solution which remained constant for the reminder time period. On the other hand, mass loss % was found to be only 28 % for the PGMS of 1393B after 28 days of immersion in 0.02 M Na_2HPO_4 solution. Moreover, no constant mass loss value was found within the 28 days period.

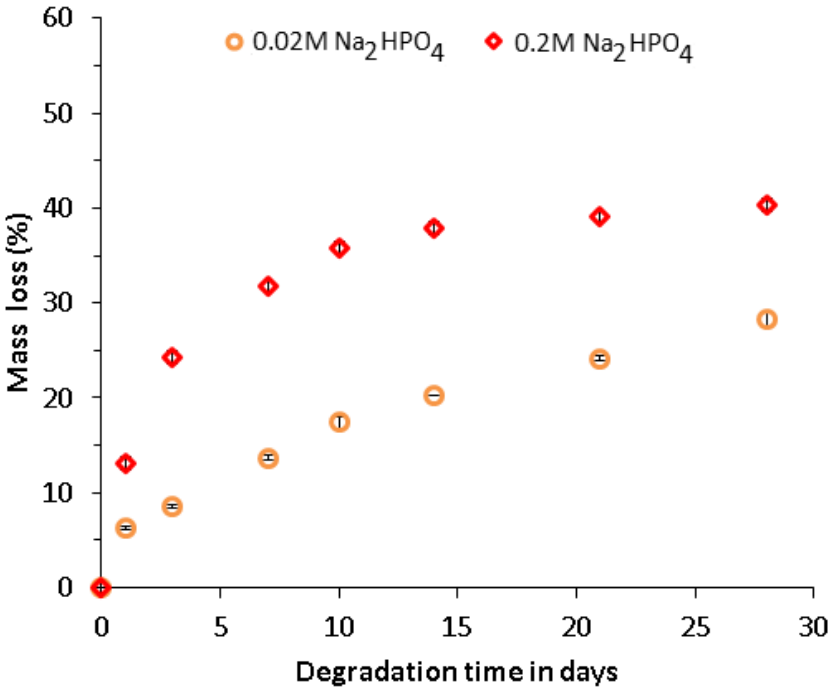


Figure 6.22: *Weight loss versus time in day during the conversion reaction for PGMS of 1393B at two different concentrations (0.02 and 0.2 M) of Na_2HPO_4 solution at 37 ^oC.*

Figure 6.23 represents the XRD spectra for PGMS of 1393B after 28 day of immersion in Na_2HPO_4 solution at two different concentrations. HA peak was observed for PGMS of 1393B after immersion in both concentrations (0.02 M and 0.2 M) of sodium phosphate solution. However, more intense and more crystalline peak of HA was found when the microspheres were immersed in 0.2 M Na_2HPO_4 compared to 0.02 M Na_2HPO_4 solution. In addition, $CaCO_3$ peaks were still present even after 28 days of immersion when 0.02 M Na_2HPO_4 solution was used for conversion reaction.

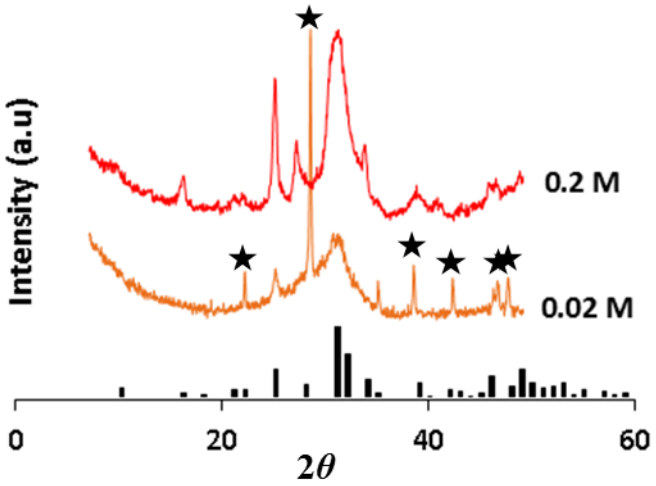


Figure 6.23: *X-ray diffraction pattern for PGMS of 1393B at day-28 during the conversion reaction of microspheres in 0.02 and 0.2 M Na_2HPO_4 solution at 37 °C. XRD spectra for HA shown for comparison. ★ represents for calcium carbonate ($CaCO_3$) peaks.*

Figures 6.24 A and **B** represent the SEM images at different magnifications for PGMS of 1393B after 28 days of immersion in 0.02 and 0.2 M Na_2HPO_4 solution at 37 °C, respectively. It can be seen from both Figures at higher magnification that HA formed on the surface and inside of pores of PGMS of 1393B in both concentrations using Na_2HPO_4 solution (and did not form any HA when using KH_2PO_4).

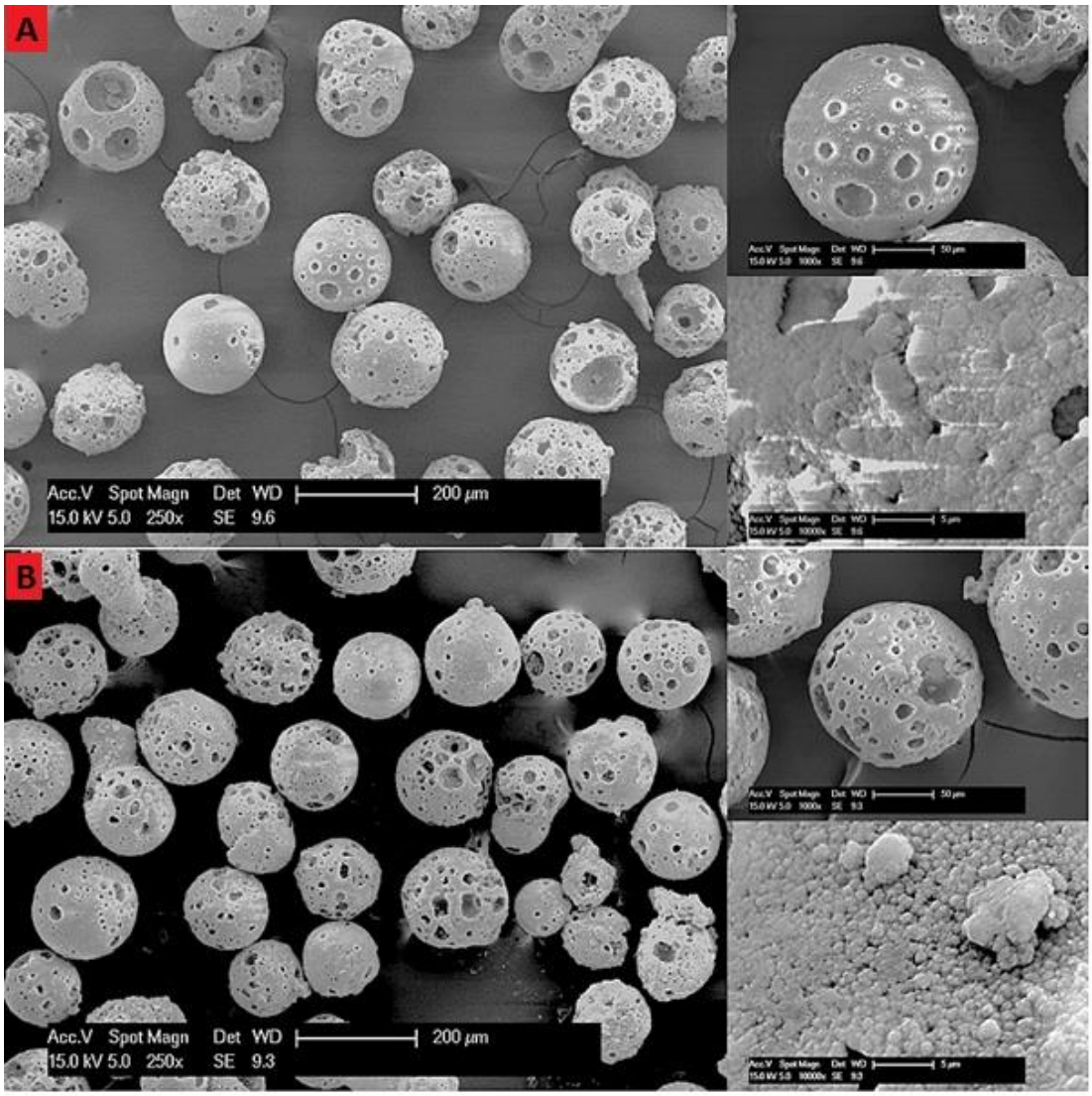


Figure 6.24: *SEM images for PGMS of 1393B glass formulations after conversion reaction of microspheres in A) 0.02 M Na_2HPO_4 and B) 0.2 M Na_2HPO_4 solution at 37 ^oC at day-28.*

6.2.8 *In vitro* bioactivity studies

6.2.8.1 XRD for bioactivity study

XRD profiles for both SGMS and PGMS of all borate glass formulations after immersion in SBF at 37 ^oC at various time points, are shown in **Figure 6.25**. The major peaks in the patterns corresponded to those of a standard HA, $Ca_{10}(PO_4)_6(OH)_2$ (JCPSD 72-1243), indicating the formation of HA during the reaction. HA peak was observed at day-7 for PGMS of all glass formulations and peak intensity increased with

increasing immersion time. Whereas, HA peak was found at later time point (at day-10) for SGMS of 45B5 and B53P4 and peak intensity increased with increasing time can be seen from **Figures 6.25 A** and **B**. On the other hand, HA peak was observed for SGMS of 1393B at day-14.

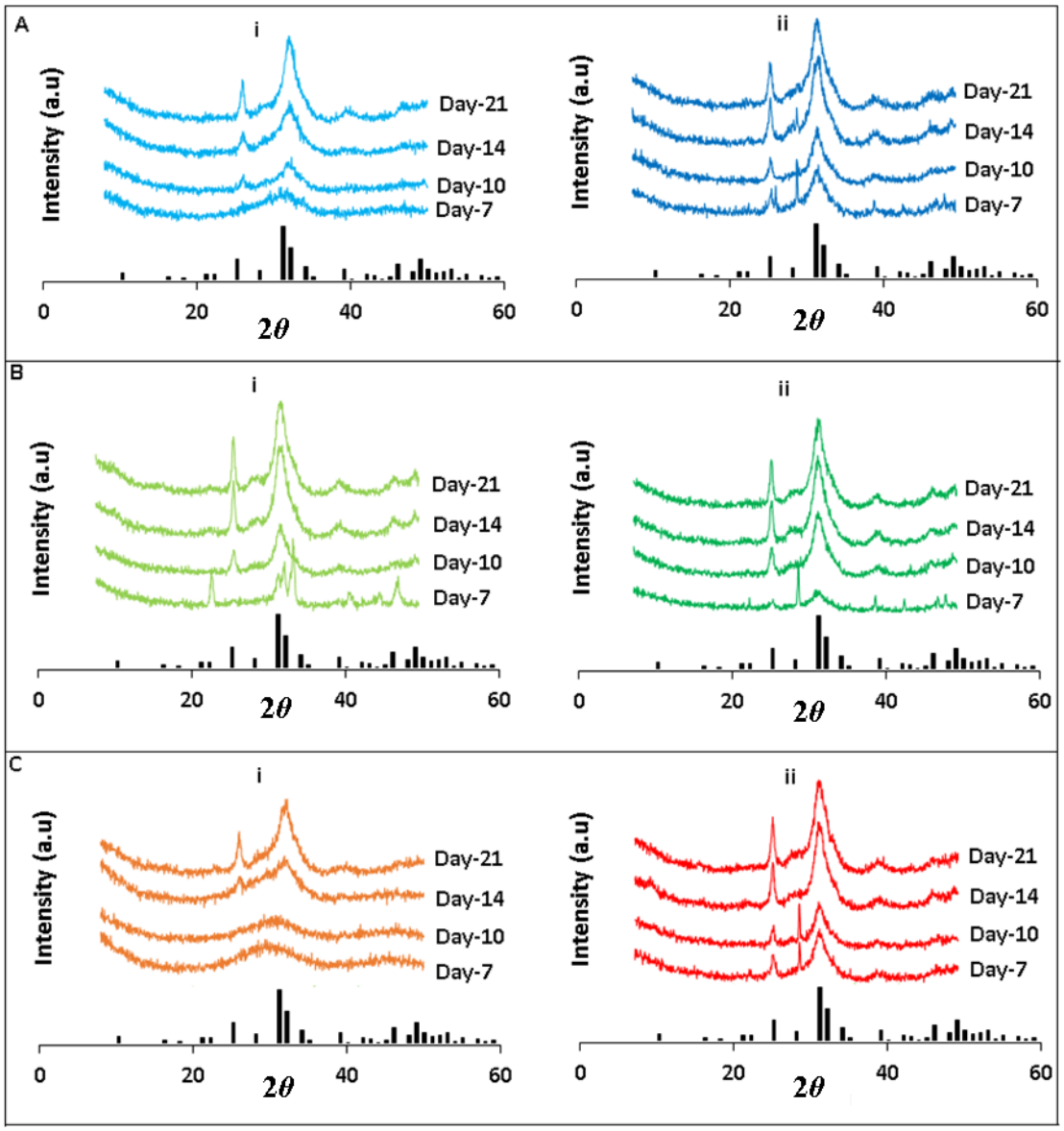


Figure 6.25: *X-ray diffraction patterns for both i) SGMS and ii) PGMS of three borate glass formulations A) 45B5, B)B53P4 and C) 1393B during the immersion of microspheres in SBF at 37 °C at various time point. XRD spectra for HA shown in each Figure for comparison.*

6.2.8.2 SEM for bioactivity study

Figure 6.26 and **Figure 6.27** represent the SEM images at different magnifications of SGMS and PGMS, respectively after 21 days of immersion in SBF. It can be seen at higher magnification that the HA formed on the surface of SGMS and both surface and inside of pores of PGMS of all borate glass formulations (see **Figures 6.26 A-C** and **Figures 6.27 A-C**).

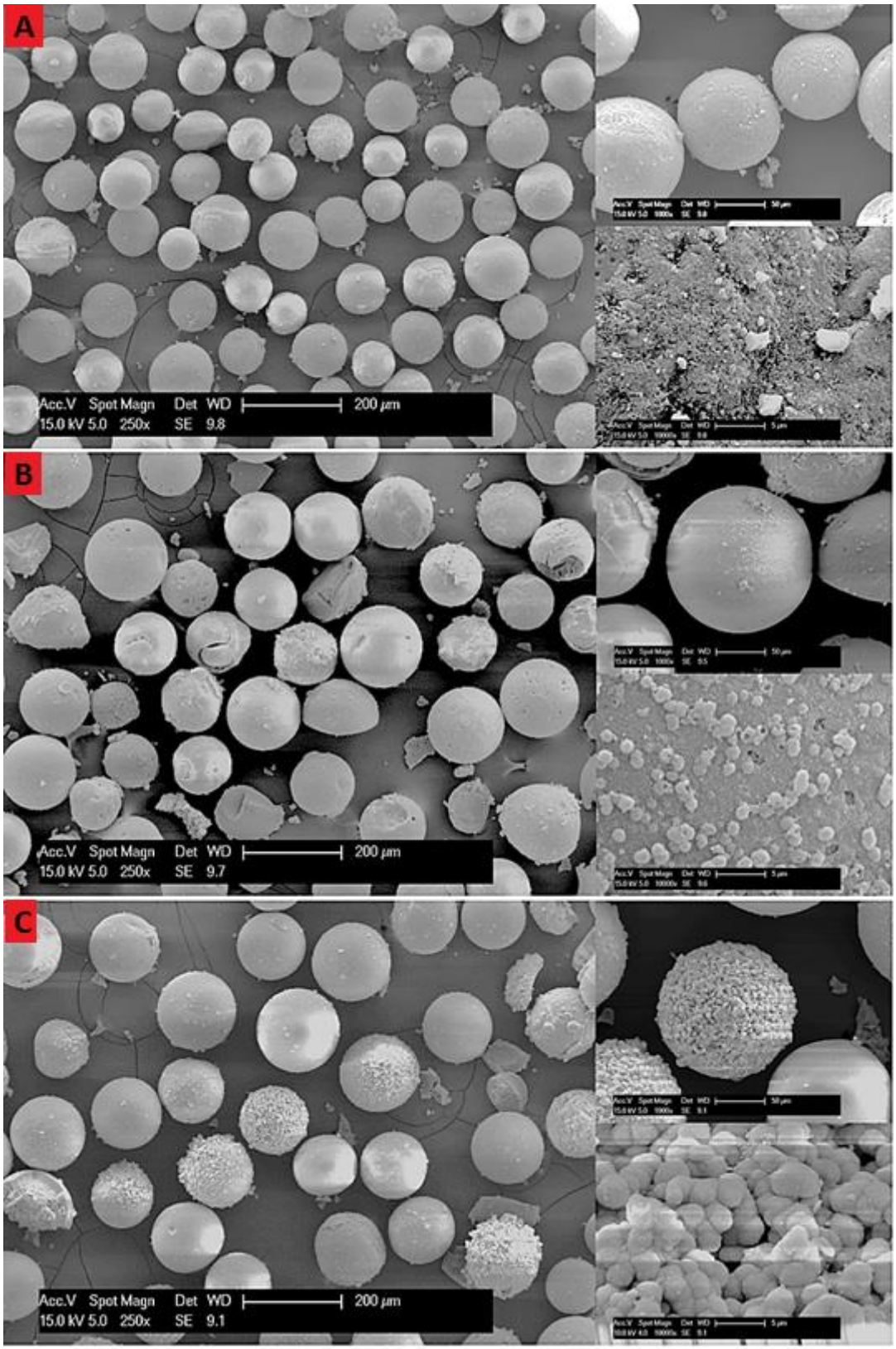


Figure 6.26: *SEM images for SGMS of three borate glass formulations A) 45B5, B) B53P4 and C) 1393B after immersion in SBF at 37 ^{o}C at day-21.*

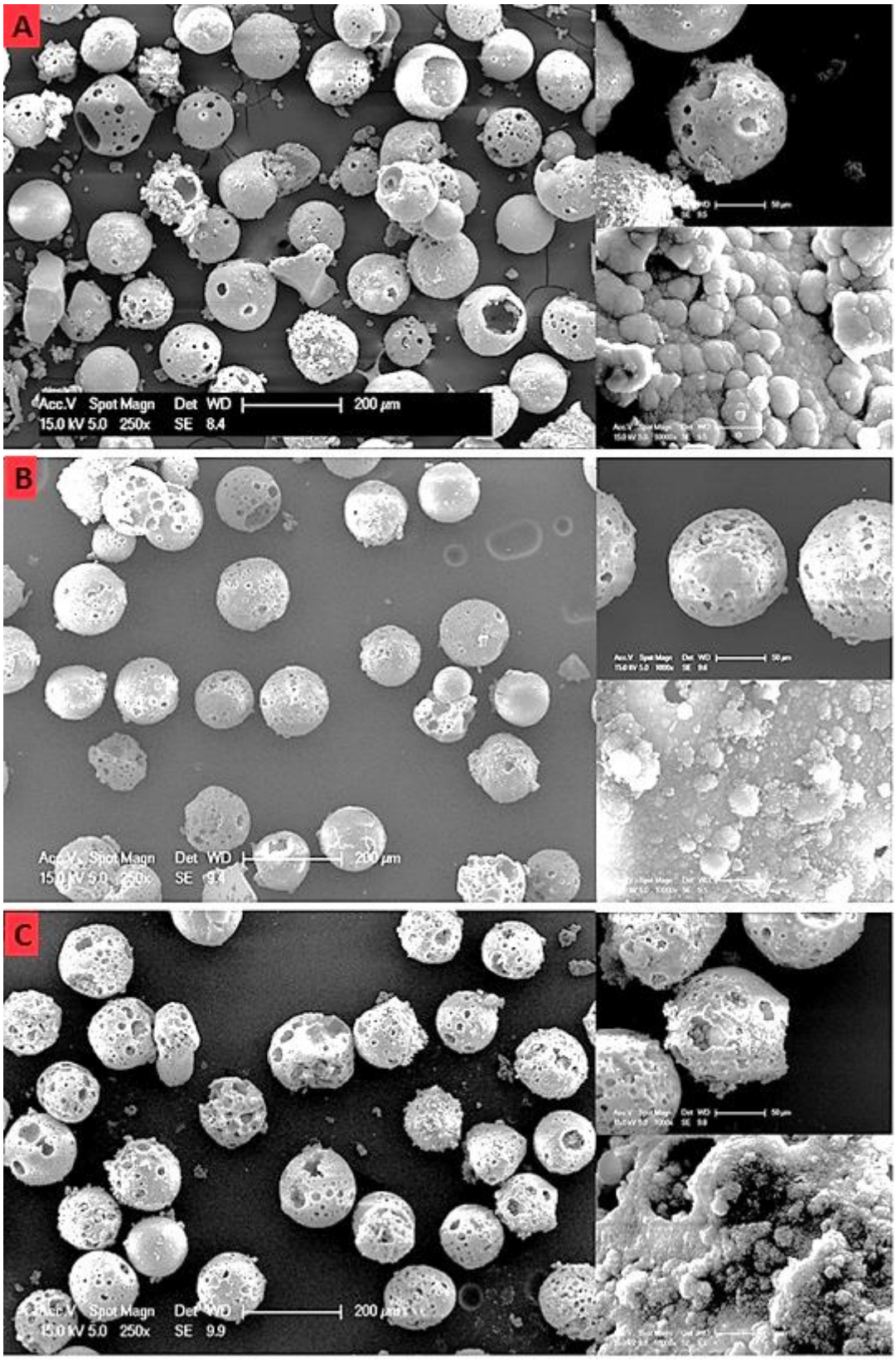


Figure 6.27: *SEM images for PGMS of three borate glass formulations A) 45B5, B) B53P4 and C) 1393B after immersion in SBF at 37 °C at day-21.*

6.2.8.3 Ion release studies in SBF

Ion release profiles for both SGMS and PGMS were investigated via ICP-MS, recording the release of B, P, Ca^{2+}, Na^{+}, K^{+} and Mg^{2+} ion in SBF and the ion release profiles obtained are presented in **Figures 6.28 A-F**.

SGMS and PGMS of each formulation followed a similar trend of B ion release profile and B ion release for PGMS was higher at earlier time point in comparison to their respective SGMS as can be seen in **Figure 6.28 A**. B ion release for B53P4 increased to 89 ppm for PGMS and 41 ppm for SGMS by day-1 and then decreased to 54 ppm for PGMS and 33 ppm for SGMS by day-3 and then increased again to 71 ppm for PGMS and 85 ppm for SGMS by day-7 and after that the boron ion release gradually decreased to nearly zero by 10 for PGMS and by 14 for SGMS.

Similarly, boron release of 44 ppm for PGMS and 37 ppm for SGMS of 45B5 was observed at day-1 and then decreased to 30 ppm for PGMS and 21 ppm for SGMS by day-3 and then increased again to 66 ppm for PGMS and 52 ppm for SGMS by day-7. No boron release was observed for PGMS of 45B5 at day-14. However, boron release of 41 ppm for SGMS of 45B5 was found even after 21 days of immersion in SBF.

On the other hand, B ion release for 1393B gradually increased to 85 ppm for both SGMS and PGMS by day-7. Boron release for PGMS of 1393B was found to be nearly 0 ppm at day-10 whereas, boron release of 54 ppm for SGMS of 1393B was observed at day-21.

From **Figure 6.28 B**, it can be seen that the maximum P ion uptake around 30 ppm from SBF was observed for PGMS of all glass compositions and SGMS of 45B5 at day-7. Whereas, the highest P ion uptake was found to be around 20 ppm for SGMS of B53P4 and 1393B at day-14 and day-21, respectively.

Initially, Ca^{2+} ion release into SBF solution was observed for both SGMS and PGMS of each glass formulations up to a certain time point and after that Ca^{2+} ion uptake from solution was observed (see **Figure 6.28 C**). For example, Ca^{2+} ion release for PGMS of 45B5 increased from 98 ppm to 141 ppm at day-7, after that decreased to 68 ppm (or 20 ppm Ca^{2+} ion uptake was found) at day-14 was observed. Moreover, Ca^{2+} ion uptake for PGMS of 45B5 was found to be 45 ppm at day-21.

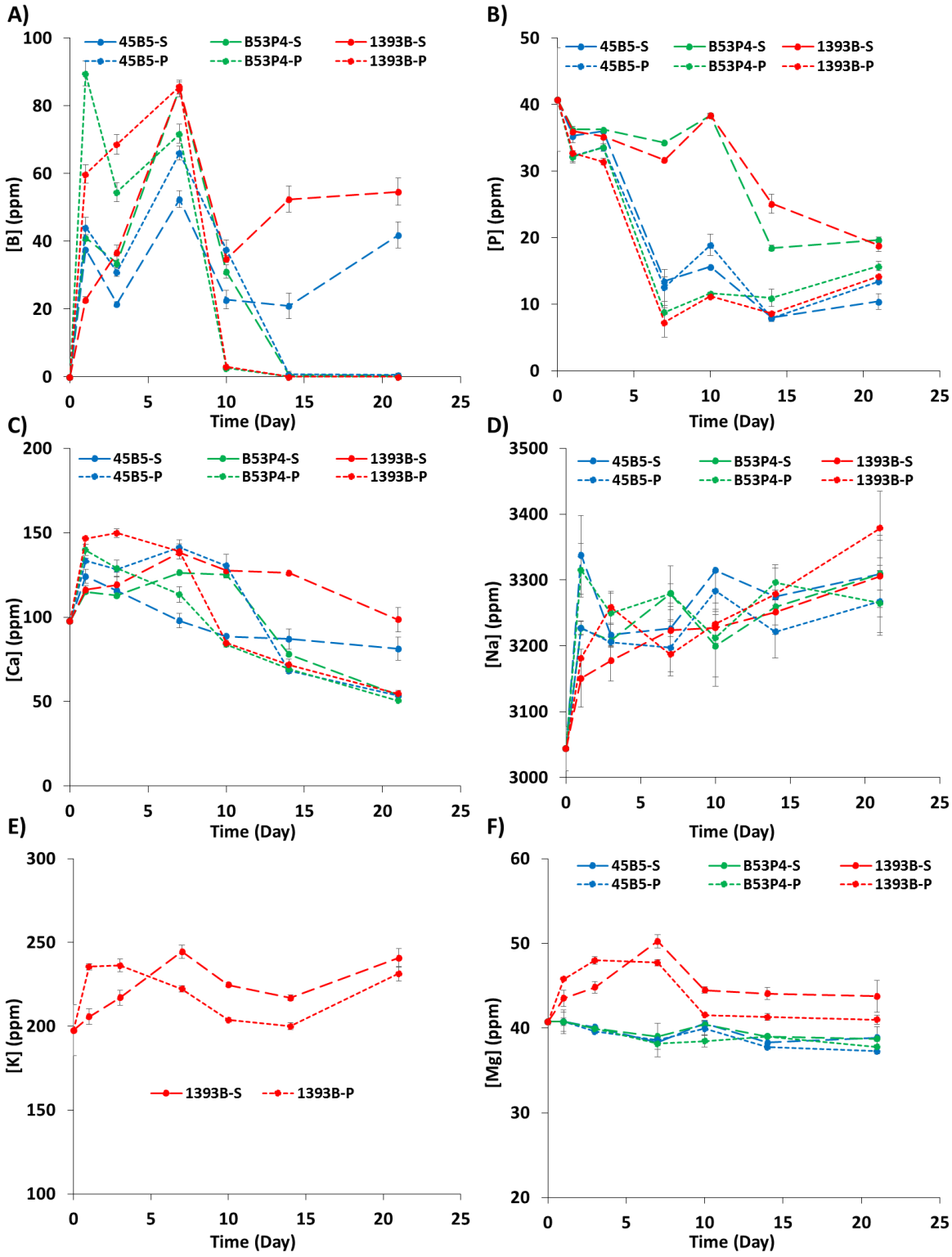


Figure 6.28: *Concentration of A) [B], B) [P], C) [Ca], D) [Na], E) [K] and F) [Mg] measured by ICP-MS for SGMS and PGMS of borate glasses investigated in SBF during 21 days of immersion period. (Error bars are also included in the data above)*

On the other hand, Ca^{2+} ion release for SGMS of 45B5 increased from 98 ppm to 124 ppm by day-1 and then gradually decreased to starting value (98 ppm) at day-7 after that Ca^{2+} ion uptake (10 ppm at day-10, 17 ppm at day-21) was observed. Similarly, Ca^{2+} ion release for B53P4 increased to 140 ppm for PGMS by day-1 and 126 ppm for SGMS by day-7 then Ca^{2+} ion release decreased with increasing immersion time for both SGMS and PGMS. Ca^{2+} ion uptake of 48 and 45 ppm at day-21 was observed for PGMS and SGMS of B53P4, respectively.

In addition, Ca^{2+} ion release of 51 ppm at day-3 for PGMS and 40 ppm at day-7 for SGMS of 1393B was observed then Ca^{2+} ion release decreased with increasing immersion time and Ca^{2+} ion uptake of 44 ppm was observed at day-21 for PGMS of 1393B.

Na^{+} ion release was found to be 200-300 ppm by day-1 for all of the glass formulations and then remained relatively constant for the remainder of the study as can be seen in **Figure 6.28 D**.

K^{+} ion release increased from 197 ppm to 244 ppm at day-7 for SGMS and from 197 to 236 ppm at day-3 for PGMS of 1393B and then gradually decreased to 216 ppm for SGMS and 200 ppm for PGMS at day-14. Moreover, 43 ppm (for SGMS of 1393B) and 34 ppm (for PGMS of 1393B) higher K^{+} ion release was observed at day-21 when compared to the initial (day-0) K^{+} ion in phosphate solution.

Mg^{2+} ion release increased from 40 to 50 ppm for SGMS and 47 ppm for PGMS of 1393B by day-7 and then decreased to 44 ppm for SGMS and 42 ppm for PGMS at day-10 and then remained relatively constant for the remainder of the study for both SGMS and PGMS as can be seen in **Figure 6.28 F**. However, small amount of Mg^{2+} ion uptake for both SGMS and PGMS of 45B5 and B53P4 was observed.

6.2.8.4 pH Measurements of SBF

Figure 6.29 represents the variation of pH change as a function of immersion time (day) of the SGMS and PGMS of three different borate glasses in SBF at 37 °C over 21 days duration. In general, the pH values in SBF slightly increased from 7.4 to 7.9 at day-3, then gradually decreased to 7.6 by day-10 and then remained relatively constant for the remainder of the study as can be seen in **Figure 6.29**.

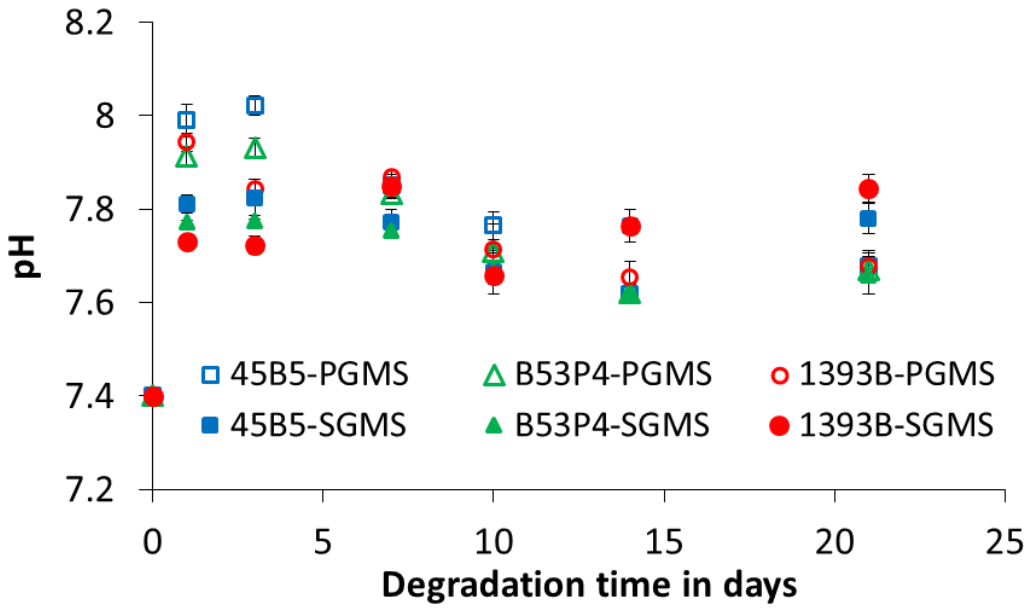


Figure 6.29: *pH change as a function of immersion time (day) for the SGMS (represented as solid symbols) and PGMS (represented as open symbols) of three different borate glasses investigated in SBF at 37 °C over 21 days duration.*

6.2.8.5 Compositional analysis via ICP-MS for bioactivity study

Table 6.6 represents the compositional analysis in mol% obtained via ICP-MS for SGMS and PGMS of three different borate glasses after immersion in SBF at day 21. From analysis it can be seen that very negligible (less than 0.3 mol%) amount of B_2O_3 was found for both SGMS and PGMS of B53P4 and only for PGMS of 45B5 and 1393B. However, B_2O_3 was found to be 1 and 4 mol% for SGMS of 45B5 and 1393B, respectively. Moreover, less than 1 mol% Na_2O was found for both SGMS and PGMS of each borate glass formulations. In addition, small amount of MgO (around 3 mol%)

was found for both SGMS and PGMS of without magnesium containing glasses such as 45B5 and B53P4. Moreover, 3 mol % MgO remained for both SGMS and PGMS of 1393B.

In addition, Ca/P (atomic ratio) was found to be around 1.5 for both SGMS and PGMS of each glass compositions after 21 days of immersion in SBF.

Table 6.6: *Compositional analysis for SGMS and PGMS of borate glasses after immersion in SBF at day 21.*

Components	45B5		B53P4		1393B	
	SGMS (mol%)	PGMS (mol%)	SGMS (mol%)	PGMS (mol%)	SGMS (mol%)	PGMS (mol%)
B_2O_3	1.05 ± 0.91	0.15 ± 0.03	0.23 ± 0.04	0.10 ± 0.01	4.27 ± 2.73	0.08 ± 0.01
P_2O_5	23.45 ± 0.45	24.37 ± 0.15	24.77 ± 0.26	24.26 ± 0.19	22.93 ± 2.37	24.45 ± 0.35
CaO	72.85 ± 1.01	71.56 ± 0.14	70.92 ± 0.46	71.72 ± 0.32	68.51 ± 3.45	71.69 ± 0.53
Na_2O	0.48 ± 0.23	0.73 ± 0.10	0.82 ± 0.02	0.76 ± 0.02	0.62 ± 0.25	0.70 ± 0.04
MgO	2.15 ± 1.1	3.17 ± 0.12	3.23 ± 0.22	3.13 ± 0.15	3.34 ± 0.02	3.05 ± 0.22
K_2O	-	-	-	-	0.33 ± 0.22	0.02 ± 0.01

6.3 Discussion

The major objectives of this Chapter were to demonstrate the successful production of both SGMS and PGMS of three different types of borate glasses such as 45B5, B53P4 and 1393B, which were derived based on 45S5, S53P4 and 1393 biosilicate glasses, respectively by fully replacing the SiO_2 with B_2O_3 and to examine comparative studies between SGMS and PGMS on physical, thermal, conversion of borate glass into HA in phosphate solution, ion release and *in vitro* bioactivity.

The results above exhibited successful manufacture of borate glass microspheres (both SGMS and PGMS) from three different borate glass compositions via flame spheroidisation process.

Figures 6.1 and **6.2** show the morphologies of the SGMS and PGMS produced. The glass particles were transformed into microspheres due to surface tension forces during the cooling stage as the molten glass globules were ejected and exited the flame as mentioned in Chapter 5 [270]. A similar method and similar parameters as mentioned in Chapter 5 were used for the manufacture of porous borate glass microspheres [265]. However, a new washing protocol had to establish for the PGMS of borate glasses as these glasses were highly degradable in acidic media. For the new washing protocol, 0.1 M acetic acid for 2 mins for 45B5 and only water for 1 min for B53P4 and 1393B PGMS were chosen based on SEM images of post processed PGMS. However, porogen were not removed or dissolved completely during washing from inside of porous microspheres (confirmed via XRD; see Figure 6.7 C) due to the use of very low concentration (0.1 M) acidic acid and water. However, the residual $CaCO_3$ present in the porous microspheres was not thought to have a cytotoxic effect on cells or hinder the biocompatibility of the material as has previously been found in studies involving Hela cells and porous spherical $CaCO_3$ microparticles [338].

The cross-sectional SEM images of the PGMS (as shown in **Figure 6.6**) revealed the internal porosity, which clearly showed that the pores were interconnected to each other for all the glass formulations investigated.

Borate glasses were prepared using splat quenching of molten glass for rapid cooling to avoid any crystallisation and amorphous nature of prepared glasses were

confirmed via XRD (see **Figure 6.7 A**). The SGMS of 45B5 and 1393B remained fully amorphous whereas SGMS of B53P4 crystallized. Small peaks of sodium calcium phosphate [$Na_3Ca_6(PO_4)_5$] for SGMS of B53P4 were observed after spheroidisation of the glass particles (see **Figure 6.7 B**). This crystallisation was attributed to the lower glass stability against crystallisation for this composition (see **Table 6.3**). In addition, the relatively higher content of P_2O_5 in B53P4 glass compared to expected value of P_2O_5 (confirmed via ICP-MS, see **Table 6.1**) could have aided the crystallisation process which resulted in the lower glass stability observed for B53P4. Literature reports show that phosphorus can influence the devitrification of glasses and is known as an important nucleating component [339]. A study on the influence of phosphorus speciation on the phase separation of Na_2O-B_2O_3- SiO_2 glasses was carried out by Muñoz *et al*. and reported that the larger ionic field strength of P^{5+} cations (2.1) compared to those of Si^{4+} (1.57) and B^{3+} (1.63 and 1.34, for three and four-fold coordinated boron atoms, respectively) increased the tendency of phosphorus to separate from the borosilicate network, thus causing the crystalline phase separation of the phosphate species [339]. On the other hand, $CaCO_3$ peaks were found for PGMS of each composition (see **Figure 6.7 C**) which was attributed to the use of Ca-based porogen utilised during spheroidisation for PGMS. For the PGMS of B53P4, apart from $CaCO_3$ peaks very short crystallisation peaks of sodium calcium phosphate [$Na_3Ca_6(PO_4)_5$] were observed which was also found for SGMS of the same compositions.

No significant variation in composition between SGMS and BG was observed as expected (see **Table 6.1** and **Table 6.2**). However, due to the addition of porogen in this process, increased the Ca content which consequently decreased B and other components for PGMS.

BG and SGMS of the same glass compositions showed similar thermal properties for same size range of glass particles and microspheres. On the other hand, the thermal properties especially T_x and T_c for PGMS of 45B5 and 1393B shifted to lower temperatures in comparison to BG or SGMS of the same glass composition. However, the first crystallisation peak was not found for PGMS of B53P4 where BG and SGMS of the same composition showed two crystallisation peaks. Moreover, onset of

crystallisation and crystallisation peaks for PGMS of B53P4 shifted to lower temperature when compared to the second onset and crystallisation temperature of BG and SGMS. This was attributed to the same reason of higher surface area: volume ratio [218] and due to potential remnants of the porogen used that was mentioned in Chapter 5 [218]. The remnants could have been either the porogen itself or incorporation of CaO from the porogen decomposition stage into the structure of the microspheres (which also correlated with the compositional analysis via ICP-MS). Similar finding was found for PGMS of phosphate-based glasses mentioned in Chapter 5.

The PGMS revealed 2 times higher porosity (~ 70%) compared to SGMS (~ 30%) (see **Table 6.4**). These results were attributed to the contribution of inter-particulate gaps for the measurement of the overall porosity for both the SGMS and PGMS as already highlighted in Chapter 5. The introduction of porosity also caused an increase in conversion rate for PGMS to porous HA microspheres in dil. K_2HPO_4 solution (see **Figure 6.9**) and ions release (see **Figure 6.20**) in comparison to SGMS, which was suggested to be due to the increased surface area achieved [265].

Theoretically material density should be the same for SGMS and PGMS. However, from the density analysis (using He pycnometer) lower density was observed for PGMS compared to SGMS. This may be due to the alteration of glass formulations, based on the addition of CaO via decomposition of the porogen during manufacture.

The higher mass loss % and the achievement of constant mass loss (%) (limiting value) at earlier time point was found for PGMS in comparison to SGMS of the same glass compositions (see **Figure 6.9**) again due to the higher surface area for PGMS [265]. Higher mass loss % was observed for B53P4 glass formulations which correlated with the higher initial B and Na^+ ion release (see **Figures 6.20 A** and **D**) and the limiting value (constant mass loss) was observed by 10 days for PGMS and by 14 days for SGMS. Obtaining the constant mass loss indicated the completion of conversion reaction for the microspheres of borate glasses in dil. K_2HPO_4 solution, where nearly complete release of B and Na^+ ion were observed (see **Figures 6.20 A** and **D**) and the uptake of P ion from solution which reacted with Ca^{2+} in the glass microspheres to form HA,

stopped after completing the conversion reaction (see **Figure 6.20 B**). This mass loss (%) also correlated well with XRD data where only HA peaks without any other peaks like $CaCO_3$ and initially observed peaks of sodium calcium phosphate [$Na_3Ca_6(PO_4)_5$] after flame spheroidisation were found at day-10 for PGMS and at day-14 for SGMS. Therefore, the conversion reaction/degradation was not affected by the crystallisation of sodium calcium phosphate [$Na_3Ca_6(PO_4)_5$] observed for starting SGMS and PGMS of B53P4 after flame spheroidisation. The conversion reaction was completed for PGMS of 45B5 by day-14 (see **Figure 6.9**) which was confirmed via XRD, although a small peak of $CaCO_3$ was also found at that time point. On the other hand, the lowest mass loss % was observed for 1393B glass formulation and no HA peak was observed (confirmed via XRD (see **Figure 6.11 C**) and SEM (see **Figure 6.12 C** and **Figure 6.13 C**) for both SGMS and PGMS even after 28 days of immersion in dil. K_2HPO_4 solution. This could be attributed to the presence of potassium in both glass microspheres and solution which could have inhibited the formation of HA. Mass loss % (constant mass loss was observed after certain time point, see **Figure 6.22**), XRD (see **Figure 6.23**) and SEM (see **Figure 6.24**) analysis of this study confirmed the conversion of PGMS of 1393B into HA in dil. Na_2HPO_4. Whether the microspheres were fully or partially converted after conversion reaction could be confirmed by the presence of boron in the microspheres. The PGMS had fully converted to HA at earlier time point that was also confirmed by the absence of boron via EDX spectra from the cross section of microspheres. For example, no boron was found from inside or outside for PGMS of 45B5, whereas, boron was found for SGMS of the same glass composition after 21 days of immersion is dil. K_2HPO_4 solution (see **Figures 6.14 C i-ii** and see **Figures 6.15 C i-ii**). These results correlated well with the compositional analysis obtained via ICP-MS (see **Table 6.5**). For B53P4, no boron was detected inside and outside the PGMS at day 10 (see **Figures 6.17 B i-ii**) and for SGMS at day-21 (see **Figures 6.16 C i-ii**). This results also correlated well with the mass loss % (conversion rate) and compositional analysis obtained via ICP-MS (see **Table 6.5**). However, the different morphologies for SGMS were observed after conversion into HA such as multi-layered structure was found for SGMS of 45B5 whereas, hollow microspheres were found for SGMS of B53P4. From cross sectional analysis of 1393B, it can be seen that the degradation occurred very slowly as the large solid core and small degraded

outer surface were observed for SGMS of 1393B after 21 days of immersion in dil. K_2HPO_4 solution (see **Figure 6.18 C**). Boron was also found on the inner and outer edges of the SGMS and PGMS of 1393B at day-21 (see **Figures 6.18 C i-ii** and **Figures 6.19 C i-ii**). These results also correlated with the degradation data and ICP-MS compositional analysis.

The SGMS and PGMS of borate glasses after conversion in dil. K_2HPO_4 at day 21, revealed that both SGMS and PGMS of B53P4 and only PGMS of 45B5 had fully converted into HA (where, Ca/P atomic ratios were ~1.4) as very negligible (less than 1 mol%) amount of B_2O_3 and Na_2O were found (see **Table 6.5**). Whereas, SGMS of 45B5 had been converted into HA (confirmed via XRD) partially as 35 mol% B_2O_3 still remained within the glass structure and consequently, higher Ca/P atomic ratio (2.47 was an average value obtained via ICP-MS from acid digested solution containing converted and unconverted portion of microspheres) was found for SGMS compared to PGMS of 45S5. On the other hand, no conversion reaction had occurred for both SGMS and PGMS of 1393B (confirmed via XRD-see **Figures 6.11 C i-ii**) because of the maximum B_2O_3 (50 mol% for SGMS and 35 mol% PGMS) remained within the glass structure of 1393B and the remainder of the B_2O_3 loss occurred due to the degradation of glass microspheres.

Small amount of K_2O (less than 1 mol %) was found for without potassium containing glass such as 45B5 and B53P4. This could be attributed to the facts that 1) the uptake of K^+ from potassium phosphate solution (see **Figure 6.20 E**), which correlated with the observation of K via EDX spectra for the cross-section of degraded microspheres (see **Figures 6.14-6.17, B-C, i-ii**), 2) possibility for contamination and 3) instrumental error.

The rapid increase of pH for phosphate solution was observed for both SGMS and PGMS at earlier time point and then gradually decreased to initial pH (~7.4) (except 1393B) with increasing degradation time or conversion of glass microspheres into HA as can be seen from **Figure 6.10**. The increase in pH results from the difference between the acidity and basicity of the ionic species involved in the solution precipitation reactions that occur during the conversion process [28]. Components in the glass such as Na_2O and B_2O_3 dissolved into the solution to form Na^+ and BO_4^{3-} ions,

whereas Ca^{2+} ions from the glass reacted with PO_4^{3-} from the solution to form HA. The strongly basic sodium hydroxide, NaOH overwhelmed the weak acidic tendency of boric acid, $B(OH)_3$, so the pH increased rapidly at the earlier time point due to the higher release of Na^+ ions [28].

It was noted that the boron leached out nearly completely from SGMS of 45B5 and 1393B in SBF where remaining boron was 36 mol % for 45B5 and 50 mol% for 1393B in K_2HPO_4 solution. This could be attributed to the presence of TRIS buffer in SBF which accelerated the dissolution of borate glass microspheres in comparison to phosphate solution [231]. The effect of TRIS buffer on degradation rate of 45S5 scaffolds was conducted by Rohanová et al. and reported that the scaffold material dissolved at double rate (0.2 wt.% h^{-1}) in the TRIS buffer compared to in dH_2O (0.1 wt.% h^{-1}) [231]. The significant reduction of material mass in the solutions containing TRIS buffer confirmed the accelerated dissolution of scaffolds, in comparison with solutions without TRIS buffer [231].

Both SGMS and PGMS of all of the borate glasses showed bioactivity in SBF which confirmed via XRD (see **Figure 6.25**), SEM images (see **Figure 6.26** and **Figure 6.27**) and compositional analysis via ICP-MS (see **Table 6.6**). However, PGMS showed bioactivity at earlier time point compared to SGMS which was again suggested to be due to the higher surface area for PGMS. Due to the same reason of high surface area, higher B ion release and P ion uptake (for conversion reaction) was observed for PGMS at earlier time point in comparison to their respective SGMS (see **Figures 6.28 A** and **B**). The slightly higher pH for SBF solution was observed for both SGMS and PGMS at earlier time point and then gradually decreased to initial pH (~7.4) with increasing immersion time (see **Figure 6.29**). This was attributed to the same reason of relatively higher release of Na^+ to ions as mentioned above for the pH change of phosphate solution [28]. Small amount of MgO (2-3 mol%) was detected for all of the glass compositions (both SGMS and PGMS) after 21 days of immersion in SBF (confirmed via ICP-MS; see **Table 6.6**). The presence of MgO for without MgO containing glasses such as 45B5 and B53P4 could be attributed to the absorption of Mg^{2+} from SBF (confirmed via ICP-MS; see **Figure 6.28 F**). Due to the presence of MgO (2-3 mol%) and trace amount of Na_2O (0.5-0.8 mol%), non-stoichiometric HA with

Ca/P atomic ratio ~1.5 was found for both SGMS and PGMS of each composition after 21 days of immersion in SBF. In literature, it is reported that calcium deficient HA (Ca/P atomic ratio <1.67) was found in natural bone, where the Ca deficiency was compensated by other elements such as sodium, magnesium, carbon, etc [340]. Therefore, the developed microspheres (both SGMS and PGMS) and converted HA microspheres in this chapter could potentially be useful for biomedical application especially for bone regeneration.

6.4 Summary

In this chapter solid and porous glass microspheres for three different types of borate glasses such as 45B5, B53P4 and 1393B, which were derived from 45S5, S53P4 and 1393 silicate glasses, respectively by fully replacing the SiO_2 with B_2O_3 were successfully prepared via flame spheroidisation technique.

Porous glass microspheres showed higher mass loss % and conversion rate to HA and porosity in comparison to solid glass microspheres having same composition. This was attributed to the higher surface area for PGMS compared to SGMS. For the same reason PGMS showed lower onset crystallisation and crystallisation temperature in comparison to SGMS.

PGMS of 45B5 and both SGMS and PGMS of B53P4 were fully converted into HA whereas, SGMS of 45B5 was partially converted into HA after 21 days and no conversion was observed for both SGMS and PGMS of 1393B even after 28 days of immersion in dil. K_2HPO_4 solution due to the presence of potassium in 1393B, which inhibited for conversion reaction. However, 1393B glass microspheres were converted into HA in dil. Na_2HPO_4 solution.

Borate glass microspheres (both SGMS and PGMS) of all glass compositions showed bioactivity in SBF and formation of HA was observed at earlier time point for PGMS compared to SGMS due to the higher surface area for PGMS. However, the calcium deficient HA (which found in natural bone, non-stoichiometric HA, Ca/P atomic ratio <1.67) formed, where Ca/P atomic % ratio was ~1.5, due to the presence of MgO (2-3 mol%) and trace amount of Na_2O (0.5-0.8 mol%) in HA. Therefore, the developed

borate glass microspheres (both SGMS and PGMS) and converted HA porous microspheres could potentially be useful for biomedical applications.

CHAPTER 7

MANUFACTURE AND CHARACTERISATION OF SOLID AND POROUS SILICATE GLASS MICROSPHERES FOR BIOMEDICAL APPLICATIONS

7.1 Introduction

Prof. Larry Hench [11] developed first silicate-based bioactive glass, 45S5 with a typical composition of 45% SiO_2, 24.5% Na_2O, 24.5% CaO, and 6% P_2O_5 (by weight) referred to as Bioglass, for bone repair applications [12,13]. Later other types of silicate-based bioactive glasses (i.e. S53P4, 1393) and glass-ceramics were developed which also had the ability to bond to bone tissue and enhance bone formation [12-21,341,342]. 45S5, S53P4 and 1393 bioactive glasses have been using for clinical applications. These glasses have shown to be bioactive in simulated body fluid (SBF) and have been successfully used as biomaterials for e.g. bioactive coatings or scaffolds for bone tissue engineering [280,284], however as irregular shaped particles.

Porous microspheres are more advantageous over solid microspheres and irregular shaped particles because they exhibit higher surface area, faster degradation rates and therapeutic ion release and lower mass density compared to solid glass microspheres [63].

The aim of this chapter was to investigate manufacture of both SGMS and PGMS of three different bio-silicate glasses (i.e. 45S5, S53P4 and 1393) via our flame spheroidisation process. A comparative analysis between SGMS and PGMS on thermal, degradation and *in vitro* bioactivity were also conducted.

7.2 Results

7.2.1 Preparation of solid bio-silicate glass microspheres (SGMS)

Solid (non-porous) glass microspheres of 45S5, S53P4 and 13-93 bio-silicate glasses are presented in **Figures 7.1 A-C**. SGMS of three bio-silicate glasses were prepared successfully via flame spheroidisation process as can be seen from **Figures 7.1 A-C**.

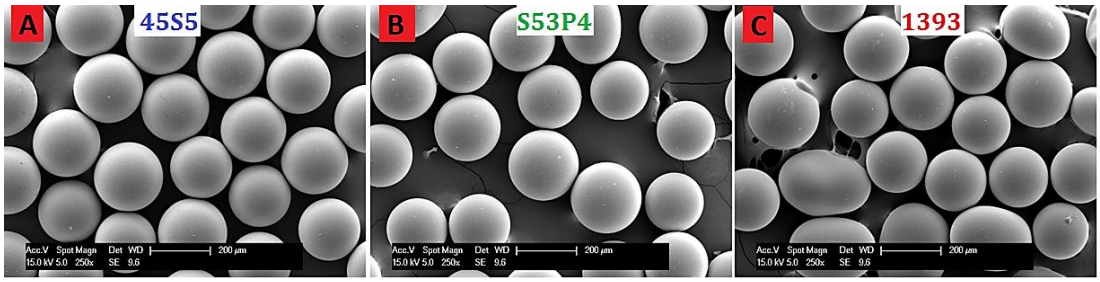


Figure 7.1: *SEM images for SGMS of A) 45S5, B) S53P4 and C) 1393 bio-silicate glass formulations investigated.*

7.2.2 Preparation of porous bio-silicate glass microspheres

7.2.2.1 Initial Trials using the 'Conventional Method'

Initial investigations to prepare porous bio-silicate glass microspheres were explored using similar parameters (i.e. particle to porogen ($CaCO_3$) ratio (1:3) and gas flow rate ratio (2.5:2.5) to those used for making porous phosphate and borate microspheres via flame spheroidisation process. The conventional method basically utilises the ground glass particles mixed with porogen directly and the outcomes are presented in **Figure 7.2 A)** 45S5 **B)** S53P4 and **C)** 1393. However, as can be seen the yield in terms of porous features and quantity of porous microspheres were very low.

Therefore, $SrCO_3$ was explored as a porogen as it has a higher decomposition temperature of 1100-1200 °C, which was closer to the melt profiles of the biosilicate glasses (1200-1250 °C), as compared to $CaCO_3$ (~800 °C).

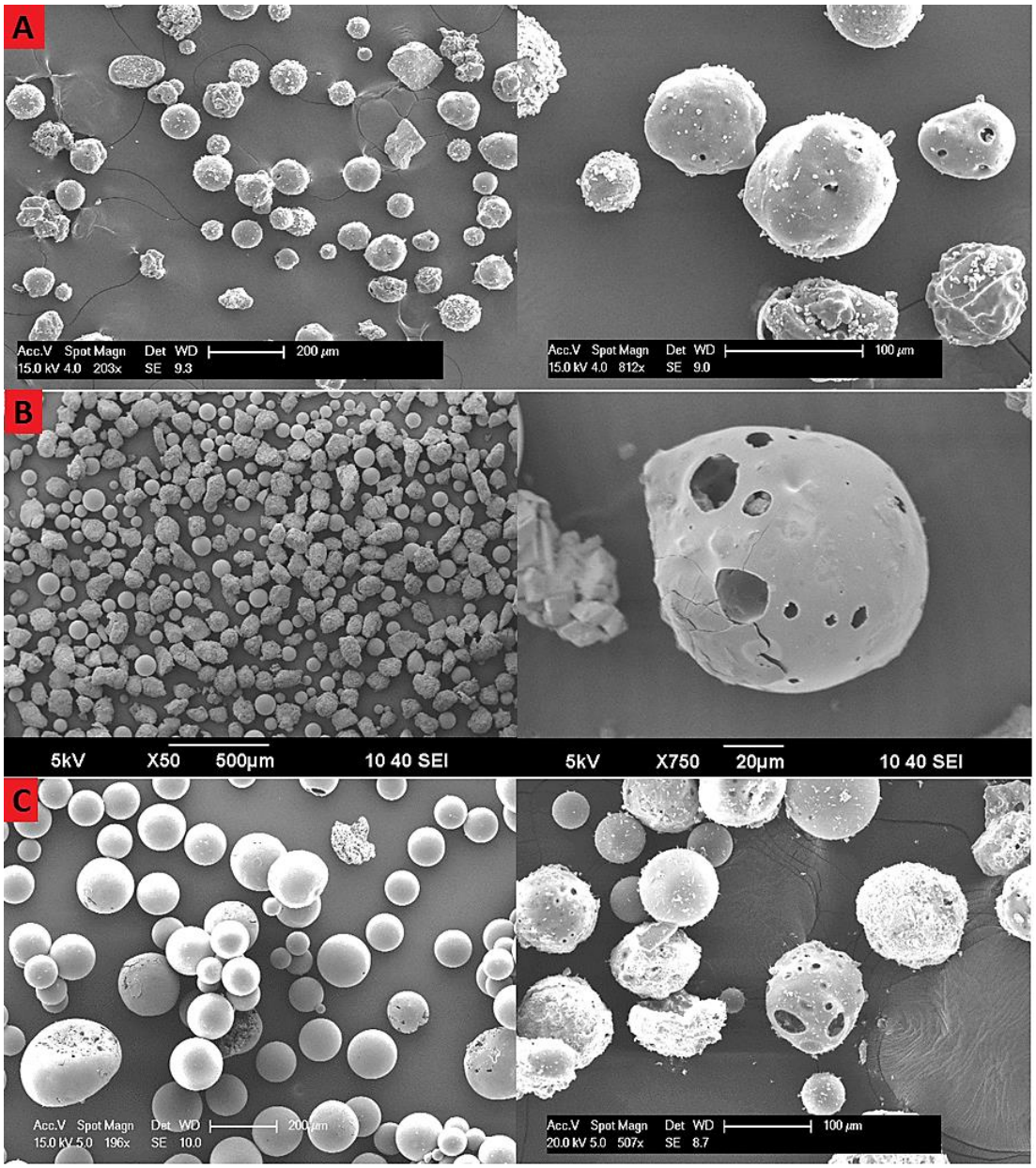


Figure 7.2: *Initial attempts to prepare porous A) 45S5, B) S53P4 and C) 1393 bio-silicate glass microspheres using $CaCO_3$ porogen via conventional method.*

For further improve the yield and porosity, 1393 bio-silicate glass was investigated further with different ratios (i.e. 1:3 and 1:5) of glass particles and porogen (i.e. $SrCO_3$ and $SrCO_3$ + $CaCO_3$) and with motor oil and without motor oil (with the aim to enhance attachment of porogen to the surface of the glass particles) as presented in **Figures 7.3 A-E**. However, no satisfactory results (in terms of porous features, quantity of porous microspheres, sphericity etc) were observed from these trials (see **Figure 7.3**).

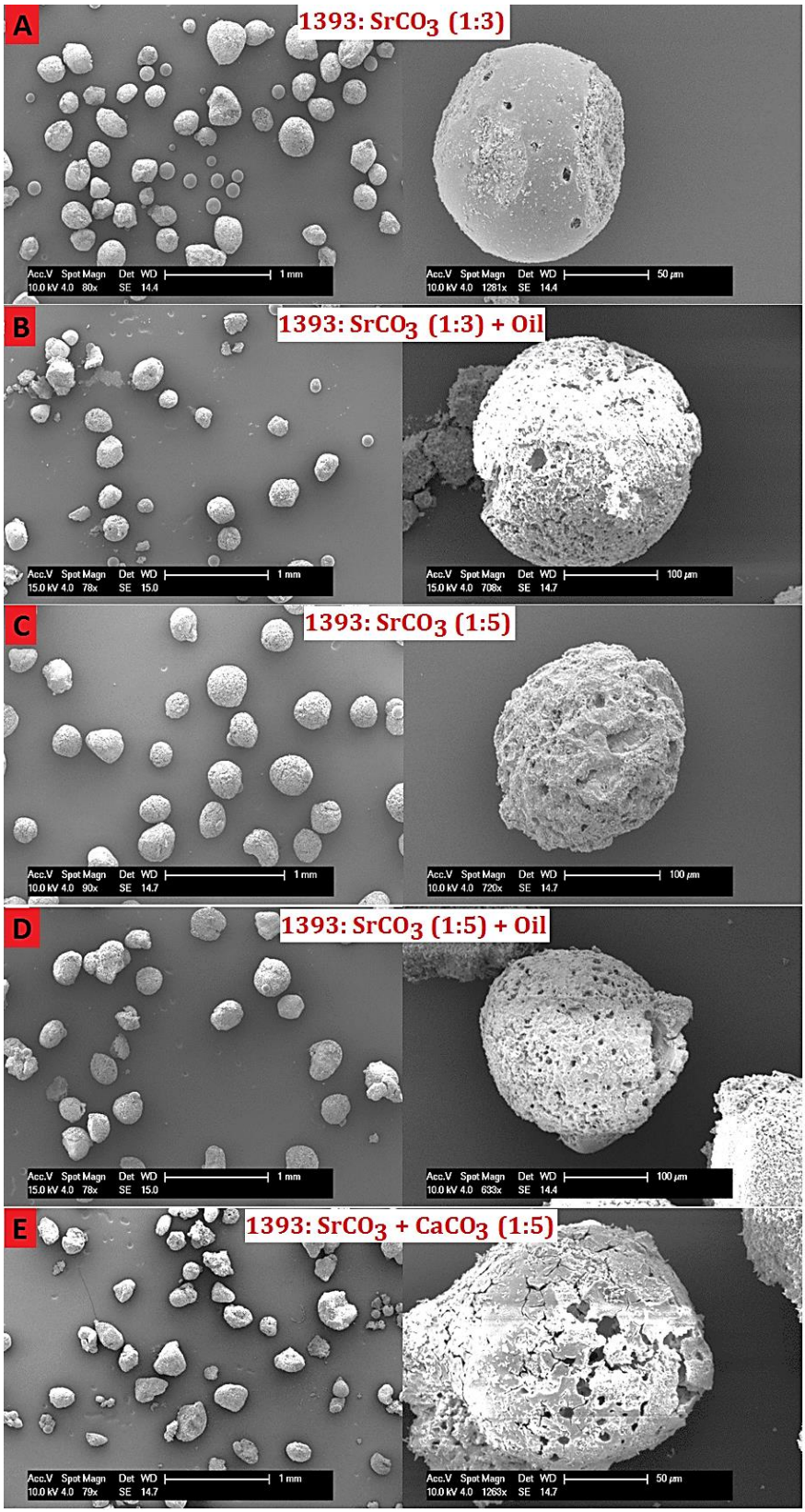


Figure 7.3: *Trials exploring A) particles: $SrCO_3$ (1:3), B) particles: $SrCO_3$ (1:3) + Motor oil, C) particles: $SrCO_3$ (1:5), D) particles: $SrCO_3$ (1:5) + Motor oil and E) particles: $SrCO_3$ + $CaCO_3$ (1:5) to improve the yield and porosity for 1393 bio-silicate glass microspheres.*

7.2.2.2 Revised particle preparation process named as 'Granular Method'

Two alternate methods were then explored to prepare porous bio-silicate microspheres by modifying the initial processing route of the above previous 'Conventional method'.

As bio-silicate glasses have high viscosity profiles and melt temperatures they were therefore relatively very difficult to process into porous microspheres compared to phosphate glass. As such, porogen/binary PBG and bio-silicate glass mixtures were made into 3D globules by preparing granulars by mixing porogen/binary PBG with the biosilicate glass particles before spheroidisation. The binary (P50 Na50) glass was utilised here, as this is a very fast resorbing glass (i.e. can degrade in minutes/hours). For **Method 1**, granular (200-350 μm) particles were prepared by mixing bio−silicate glass with binary phosphate glass particles using 2 % polyviniyl alcohol (PVA) solution. The glass particles (<45 μm) and P50Na50 (<45 μm) with the ratio of 1:0.5 were ground in ball mill at 500 rpm for 5 min. After flame spheroidisation, solid glass microspheres (SGMS) with the combination of bio-silicate glass and P50 Na50 glass were formed. Utilising this method, porous bio-silicate glass microspheres were formed after immersion in water for 24 hrs, based on the hypothesis that the P50Na50 glass being highly soluble would have leached out from the SGMS in the presence of water. **Figure 7.4** represents the schematic diagram of developed granular **Method 1** to prepare porous bio-silicate microspheres.

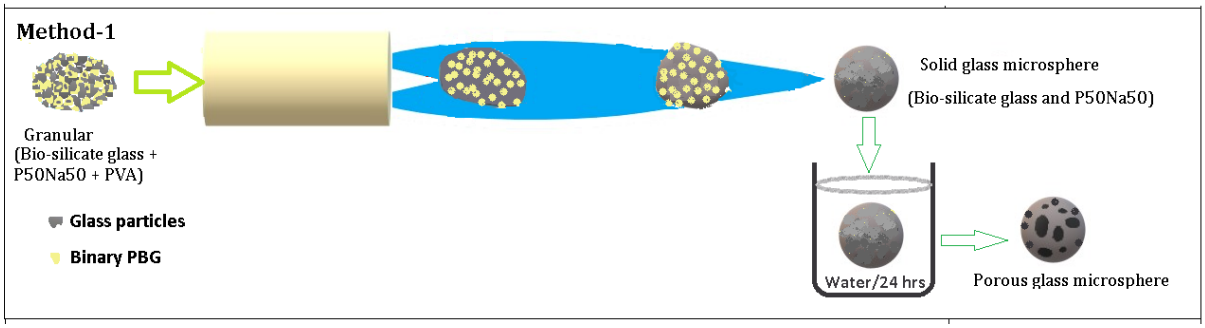


Figure 7.4: *Schematic diagram of developed granular **Method 1** to prepare porous bio-silicate microspheres.*

For **Method 2**, granular particles (200-350 μm) were also prepared by mixing bio-silicate glass particles (<45 μm) and porogen ($CaCO_3$ <5 μm) utilising PVA as above for Method 1 and following the same procedures of grinding. When the granulars were passed though the flame, the gas bubbles produced by decomposition of the porogen within the molten glass and porous microspheres formed after exiting the flame. **Figure 7.5** represents the schematic diagram of developed granular **Method 2** to prepare porous bio-silicate microspheres.

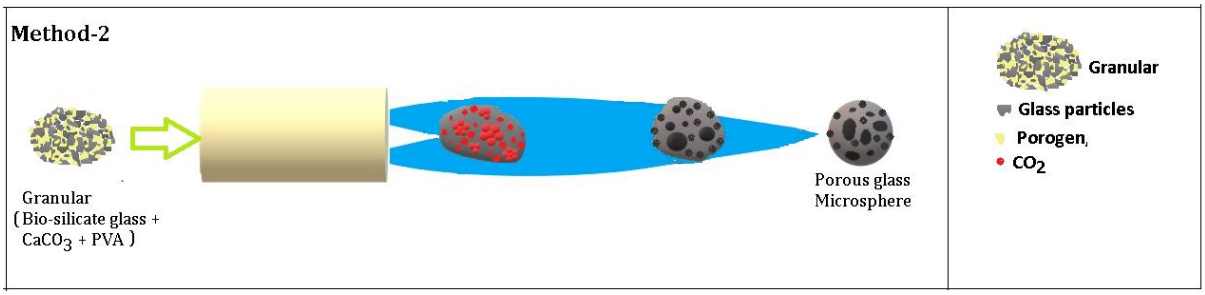


Figure 7.5: *Schematic diagram of developed granular **Method 2** to prepare porous bio-silicate microspheres.*

Figure 7.6 shows the SEM images for samples prepared from 13-93 bio-silicate glass with P50Na50 glass using **Method 1**. After leaching the binary phosphate glass (P50Na50 in water) from the solid microspheres produced, porous bio-silicate microspheres were formed (see **Figure 7.6 A**). Some of the microspheres were broken intentionally (depicted by the red line area, see **Figure 7.6 A**) using a sharp blade to investigate their internal porosity. **Figures 7.6 B-D** represent the cross-section of the microspheres prepared and a highly porous structure was observed inside the microspheres. However, this method was not used further as the surface pores were very small (which would not be useful for biological cell incorporation) and there was a possibility that the bio-glass chemical composition had been drastically altered.

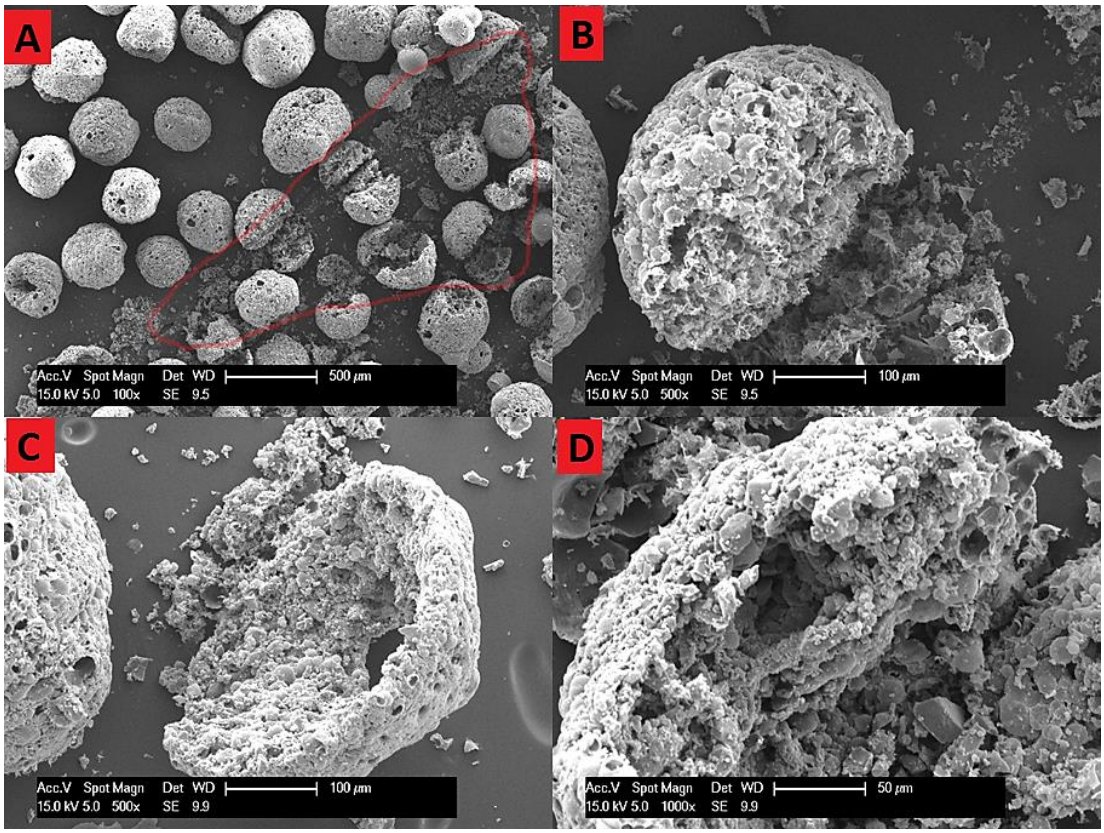


Figure 7.6: *Initial trial to prepare porous 1393 bio-silicate glass microspheres using granular* ***method 1*** *via flame spheroidisation process.*

Figure 7.7 shows the SEM images for the samples prepared from 1393 bio-silicate glass with $CaCO_3$ using **Method 2**. For the first trial, the granular size range of 200-350 µm was used. It can be seen that porous microspheres had formed (see **Figure 7.7 B**) although the pores were again very small and not fully opened (see **Figure 7.7 C**) as these were unwashed. Some of the microspheres were again broken intentionally (depicted by the red line areas, see **Figure 7.7 A**) using a sharp blade to investigate their internal porosity. **Figure 7.7 D** represents the cross-section of microspheres prepared and highly porous structure was again observed inside of the microspheres.

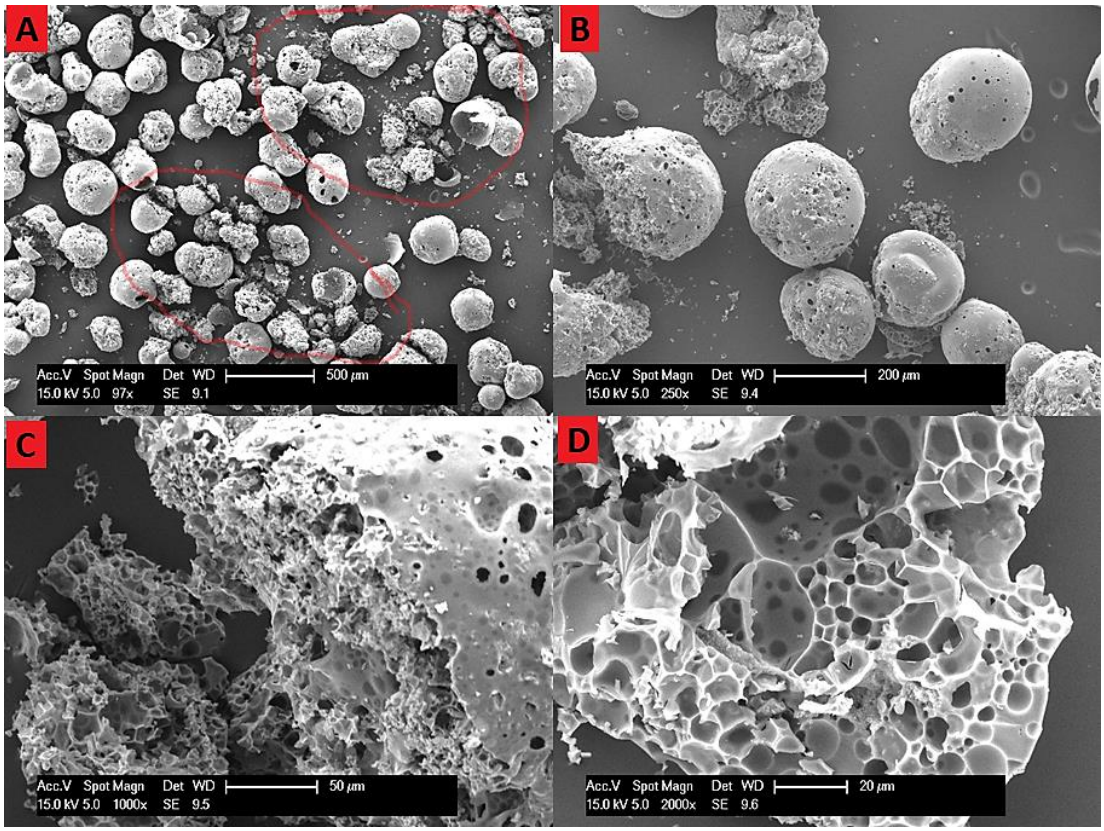


Figure 7.7: *Initial trial to prepare porous 1393 bio-silicate glass microspheres using granular* ***method 2*** *via flame spheroidisation process.*

A further trial was conducted to prepare porous 1393 bio-silicate glass microspheres using alternative **Method 2** to confirm the reproducibility and to improve the yield and porosity. Starting granular particle size range of 200-250 µm was used for spheroidisation and the output for this trial is presented in **Figure 7.8**. It can be seen that highly porous microspheres were observed after washing in 0.1 M acetic acid for 1 min (see **Figure 7.8**).

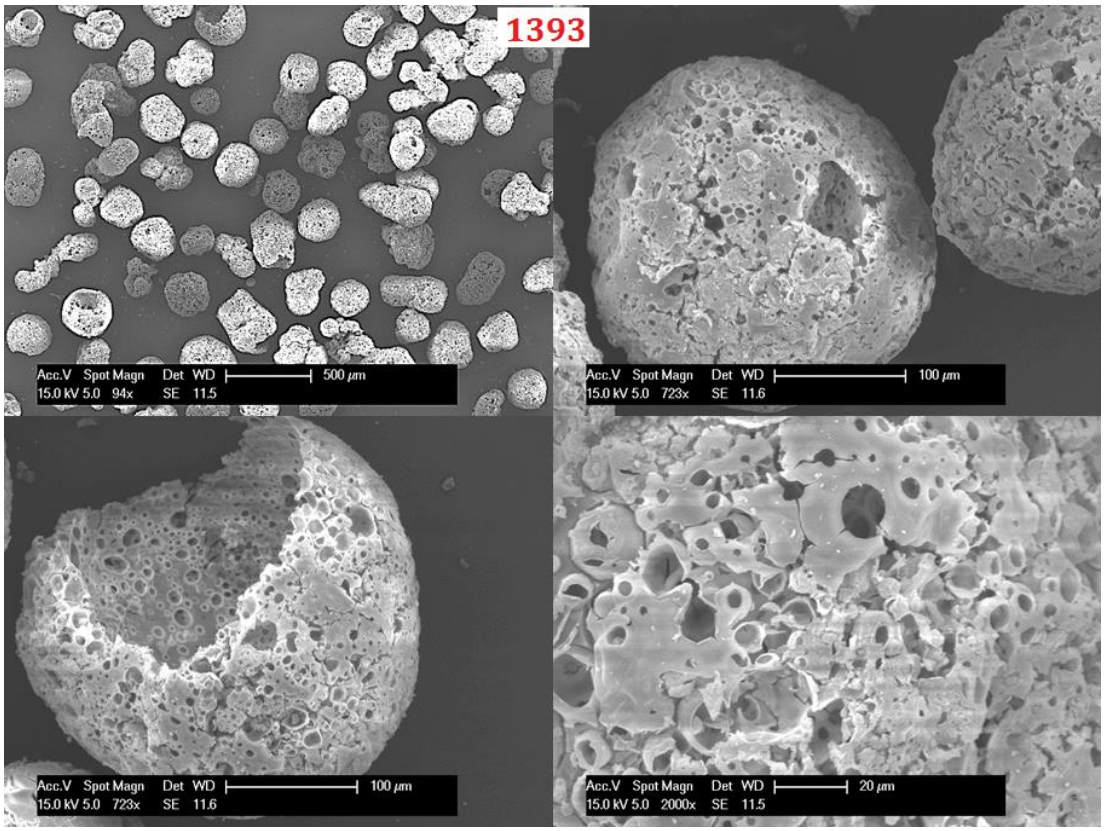


Figure 7.8: *Further trial to confirm the reproducibility and to improve the yield and porosity of porous 1393 bio-silicate glass microspheres using granular* ***method 2*** *via flame spheroidisation process.*

Porous S53P4 bio-silicate glass microspheres were also prepared using the same parameters of granular **Method 2**. **Figure 7.9** shows the SEM images of the unwashed S53P4 microspheres. The pores for some of the microspheres were not fully opened as can be seen from **Figure 7.9**.

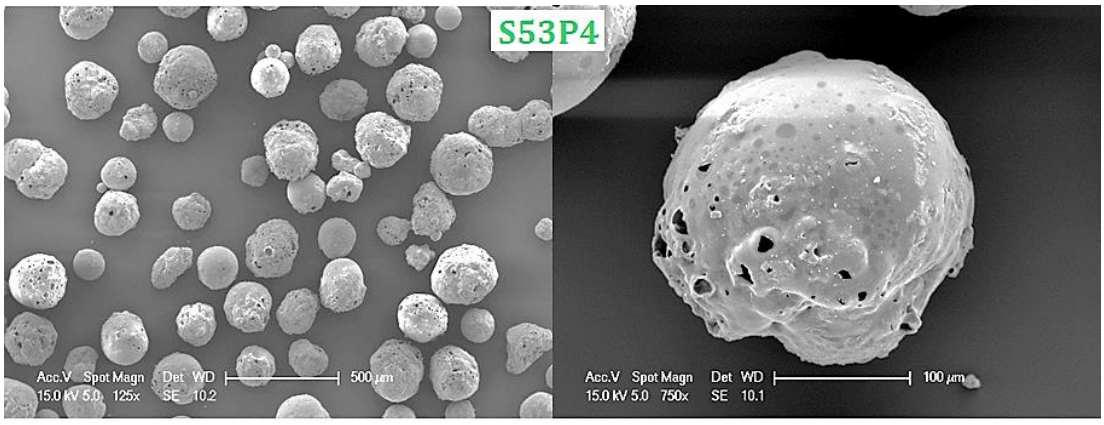


Figure 7.9: *SEM images for unwashed S53P4 bio-silicate glass microspheres.*

In order to expose/open the pores of the microspheres post flame shperoidisation, a series of acid wash steps were explored where the microspheres were subjected to certain concentrations of acid for specific time points (as presented in **Figures 7.10 A-C**). The washing protocol was developed based on previous findings where the porogen $CaCO_3$ was dissolved using acetic acid [337]. $CaCO_3$ can also be dissolved in strong acid (HCl), moderately strong acid (sulfamic) or other weak acids such as citric, sorbic, lactic and phosphoric acid [121]. Initially, the same washing protocol (i.e. 5M acetic acid for 2 mins) that was developed for the PGMS of phosphate-based glasses was implemented for bio-silicate glass. However, all of the PGMS revealed surface cracking morphology (not shown in **Figure 7.10**) when immersed in 5 M acetic acid. Therefore, the staring acid concentration was reduced significantly (to 1 M acetic acid) for the wash step protocol.

Figures 7.10 A-C represent the effect of acid washing of the PGMS of S53P4 in different acetic acid concentrations at various time points. It can be seen from **Figure 7.10 A** that the PGMS subjected to wash step using 1 M acetic acid for only 10 sec still exhibited a cracked surface morphology. Reduction of the surface cracking was further explored by significantly reducing the concentration of acid (See **Figure 7.10 B**). Comparatively, better and cleaner surface appearances for PGMS of S53P4 were observed using 0.1M acetic acid for 1 min (see **Figure 7.10 C**).

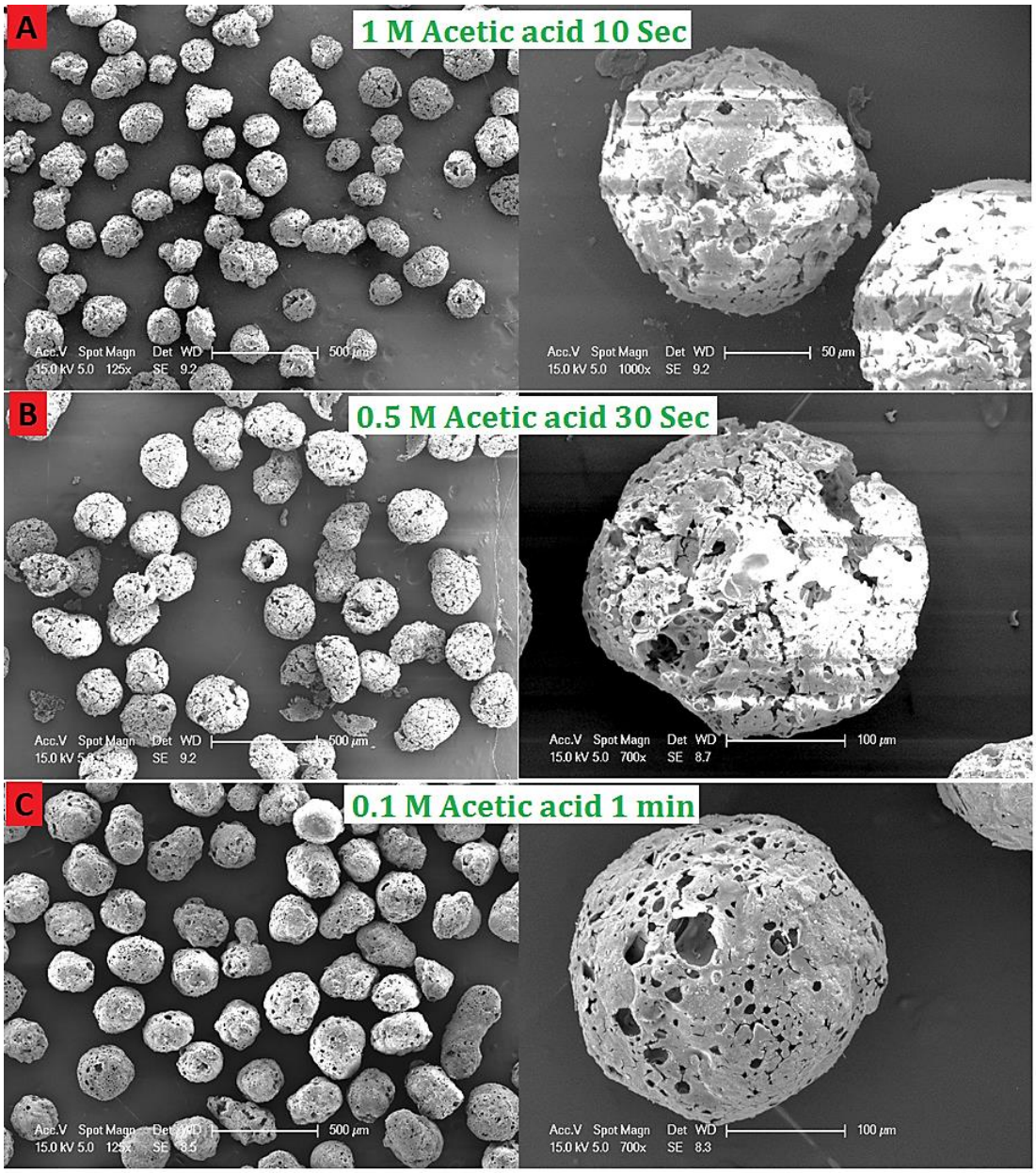


Figure 7.10: *SEM images from A-C displaying the effect of acid washing of the PGMS of S53P4 in different concentration of acetic acid for various time point A) 1M 10 sec, B) 0.5 M 30 secs and C) 0.1 M 1 min.*

Porous S53P4 bio-silicate glass microspheres were also prepared using the granular **method 2** with varying glass particle and $CaCO_3$ ratios (i.e. 1:0.5, 1:0.75 and 1:1) to increase the pore size on the surface. Porous microspheres formed (after washing) from all three different ratios are presented in **Figure 7.11**. It can be seen from **Figure 7.11** that the pore size increased with increasing $CaCO_3$ content. However, the glass

particles did not appear fused together for the 1:1 ratio samples and large cavities inside some of the microspheres were found (see **Figure 7.11 A**). The 1:0.75 ratio appeared to have achieved larger pores compared to 1:0.5 ratio. However, microspheres prepared using 1:0.5 ratio (glass particles: $CaCO_3$) were used for further analysis based on the results of distribution of pores and number of pores.

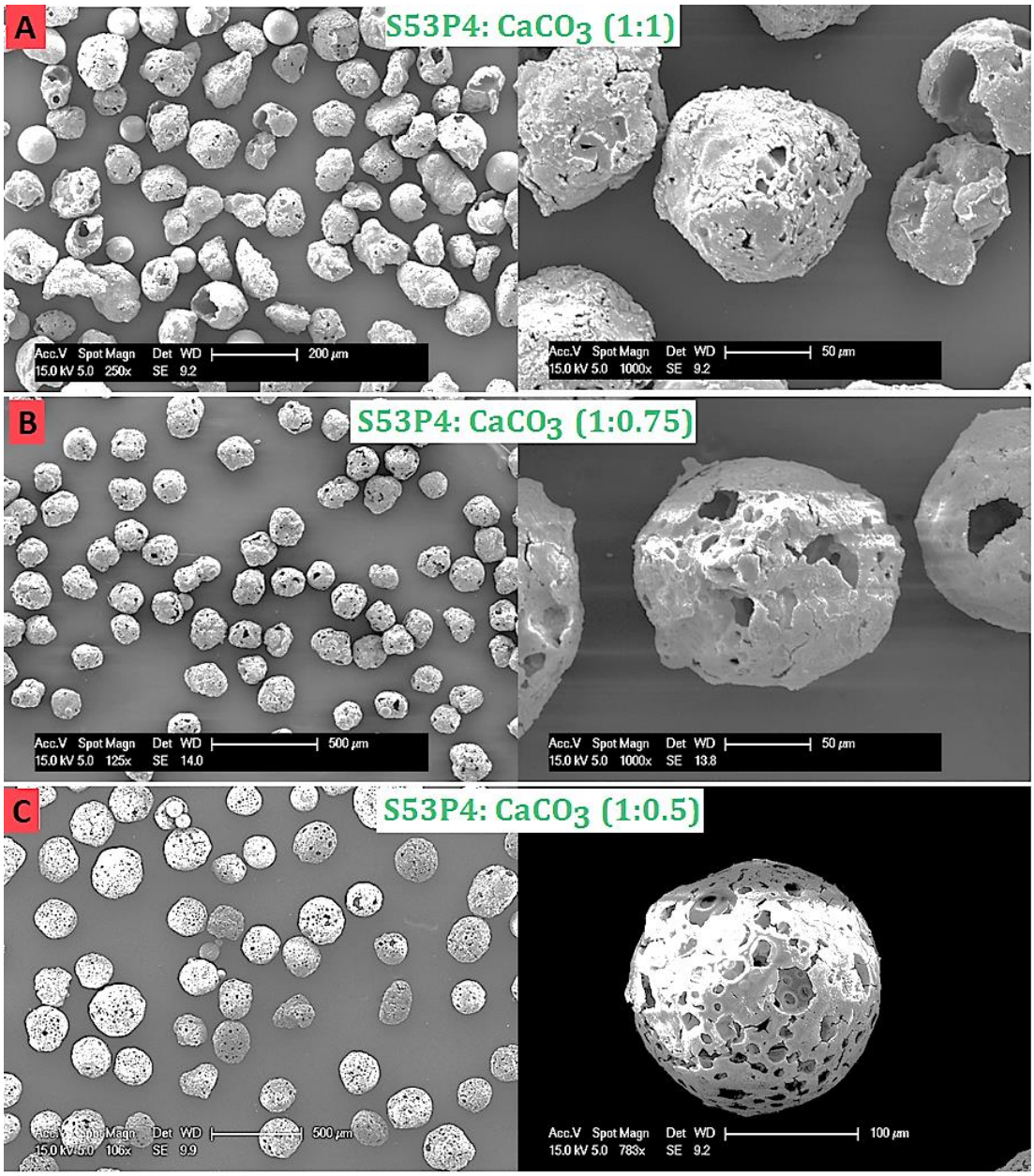


Figure 7.11: *Porous S53P4 bio-silicate glass microspheres using glass particles and porogen ratio of A) 1:1, B) 1:0.75 and C) 1:0.5 prepared via flame spheroidisation process.*

Porous 45S5 bio-silicate glass microspheres were also investigated using granular **method 2**. **Figure 7.12** shows the SEM images of washed 45S5 bio-silicate glass microspheres and porous microspheres formed.

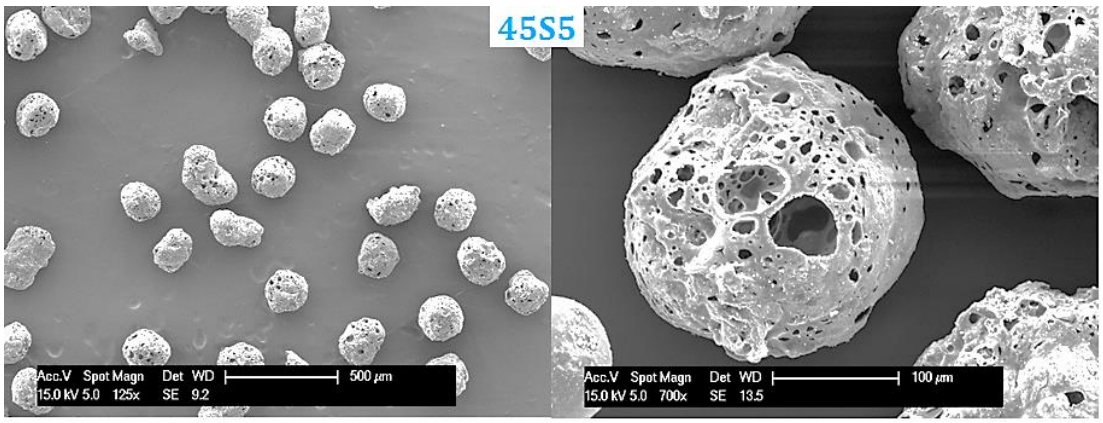


Figure 7.12: *SEM images of porous 45S5 bio-silicate glass microspheres using granular* ***method 2*** *via flame spheroidisation process.*

In order to examine the internal morphology of the PGMS's produced, cross-sections were imaged after embedding the microspheres in a cold setting epoxy resin and ground and polished using SiC paper and a diamond cloth. **Figure 7.13** shows the cross-sections for three different porous bio-silicate glass microspheres. Highly porous microspheres with interconnected pores were observed from the cross-sections of all three bio-silicate microspheres.

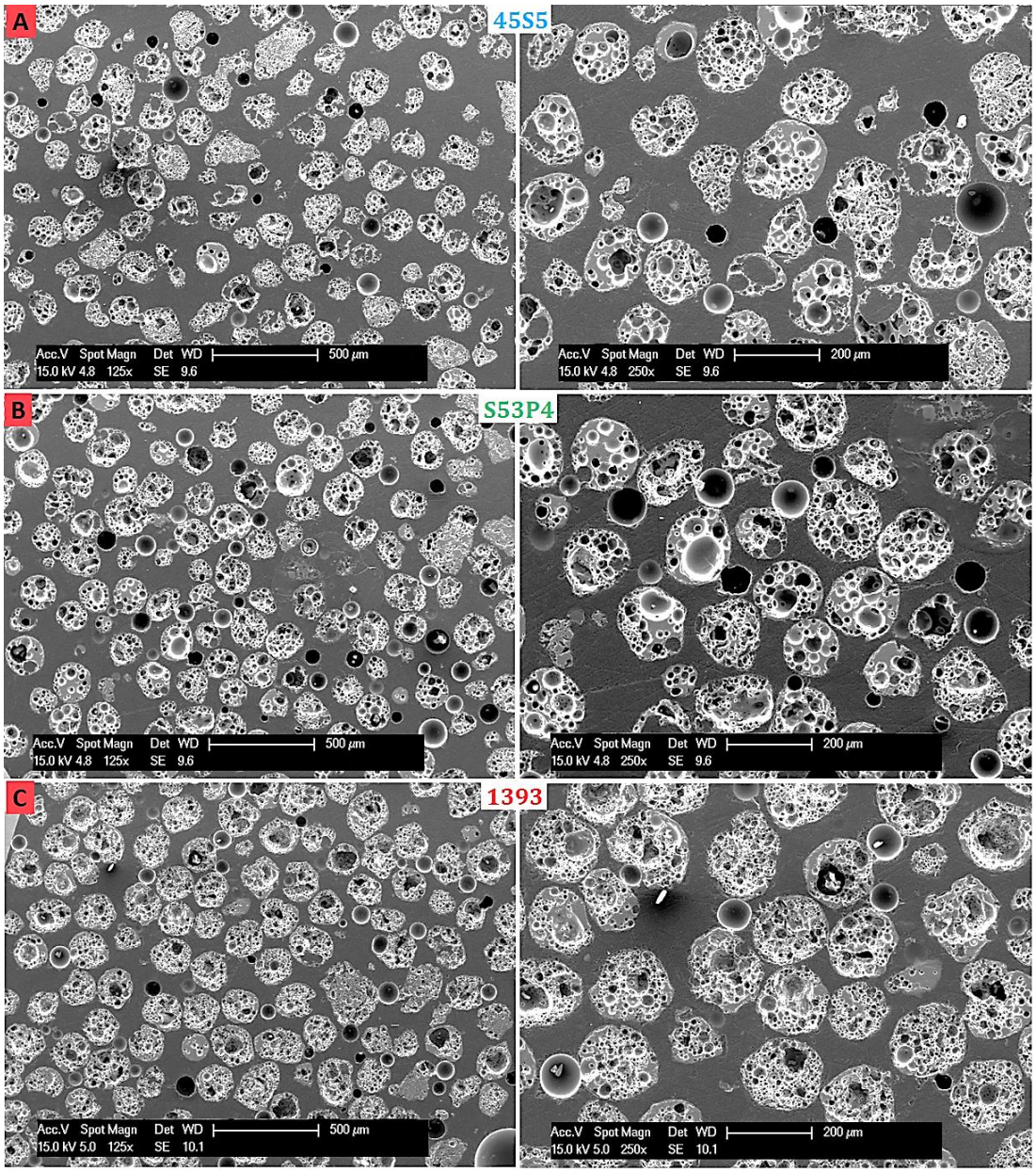


Figure 7.13: *Cross-section of porous A) 45S5, B) S53P4 and C) 1393 bio-silicate glass microspheres.*

7.2.3 Compositional analysis

The relative concentration (mol%) of elements in each formulation for bulk glass (BG), SGMS and PGMS were analysed via EDX and the values are summarised in **Table 7.1**. It can be seen that the respective oxide contents for BG were within 2 mol% of their predicted values. Moreover, no significant variation of chemical composition between starting BG and SGMS was observed for all three glass formulations.

However, in comparison significantly higher CaO content and lower SiO_2 content was observed for the PGMS. For example, around 10 mol% higher CaO and 8 mol% lower SiO_2 was observed for PGMS of 45S5 as compared to the SGMS of the same glass formulation.

Table 7.1: *Expected and actual chemical compositions obtained via EDX analysis for bulk glass (BG), SGMS and PGMS of three different bio-silicate glass formulations investigated.*

Formulations	SiO_2 (mol %)	P_2O_5 (mol %)	CaO (mol %)	Na_2O (mol %)	MgO (mol %)	K_2O (mol %)
45S5 Expected	46.1	2.6	26.9	24.4	-	-
45S5-BG	48.1 ± 0.2	2.3 ± 0.1	26.1 ± 0.7	23.6 ± 0.2	-	-
45S5-SGMS	49.3 ± 1.2	2.5 ± 0.1	24.9 ± 1.2	23.4 ± 0.5	-	-
45S5-PGMS	44.2 ± 4.8	2.1 ± 0.3	34.4 ± 5.7	19.3 ± 1.1	-	-
S53P4 Expected	53.85	1.72	21.77	22.66	-	-
S53P4-BG	53.3 ± 0.9	1.4 ± 0.3	22.2 ± 1.9	23.1 ± 2.5	-	-
S53P4-SGMS	54.6 ± 0.4	1.8 ± 0.7	20.7 ± 2.7	22.9 ± 1.8	-	-
S53P4-PGMS	51.7 ± 2.1	1.3 ± 0.3	28.2 ± 3.7	18.8 ± 1.9	-	-
1393 Expected	54.6	1.7	22.1	6	7.7	7.9
1393-BG	52.7 ± 0.3	1.7 ± 0.1	23.2 ± 0.9	5.2 ± 0.6	8.9 ± 0.8	8.3 ± 0.2
1393-SGMS	54.5 ± 0.7	1.7 ± 0.2	21.1 ± 0.7	5.7 ± 0.2	9.5 ± 0.2	7.6 ± 0.2
1393-PGMS	47.6 ± 7.4	1.5 ± 0.3	31.1 ± 8.2	4.1 ± 1.1	7.1 ± 2.0	8.5 ± 0.5

7.2.4 X-ray diffraction analysis

XRD traces for the starting BG, SGMS and PGMS are presented in **Figures 7.14 A, B** and **C** respectively, where a single broad peak between 20° and 40° (2θ) was observed for BG and SGMS of each composition. The absence of any sharp crystalline peaks for BG and SGMS highlighted the amorphous nature of the glasses. On the other hand, four small sharp peaks were observed for the PGMS of each composition and these

peaks were correlated with the peaks of nagelschmidtite ($7CaO\text{-}P_2O_5\text{-}2SiO_2$) [JCPSD 00-005-0646(D)].

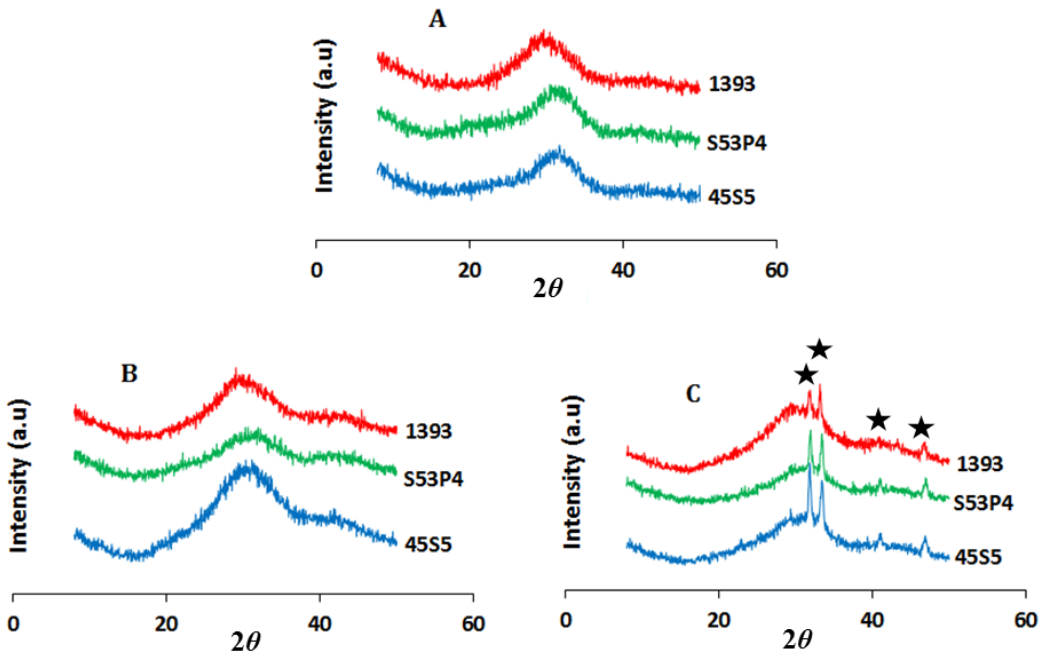


Figure 7.14*: X-ray diffraction pattern for A) BG, B) SGMS and C) PGMS (prepared via granular method) of three bio-silicate glass formulations investigated. ★ represents for nagelschmidtite ($7CaO\text{-}P_2O_5\text{-}2SiO_2$) peaks.*

7.2.5 Thermal Analysis

Figure 7.15 shows the thermal analysis profiles of BG, SGMS and PGMS where the corresponding glass transition (T_g), onset of crystallisation (T_x), crystallisation peak (T_c) and melting (T_m) temperature have been labelled. The thermal data such as T_g, T_x, glass stability (ΔT), T_c and T_m for three different morphologies (i.e. BG, SGMS and PGMS) of the three different bio-silicate glass formulations investigated are presented in **Table 7.2**. No significant changes of thermal properties (i.e. T_g, T_x, T_c, T_m) was observed between BG and SGMS of the same glass formulation (see **Table 7.2**). Moreover, no significant variation in T_g was observed between SGMS and PGMS however, significantly lower T_x and T_c were observed for the PGMS (depicted in small broken lines) as compared to SGMS.

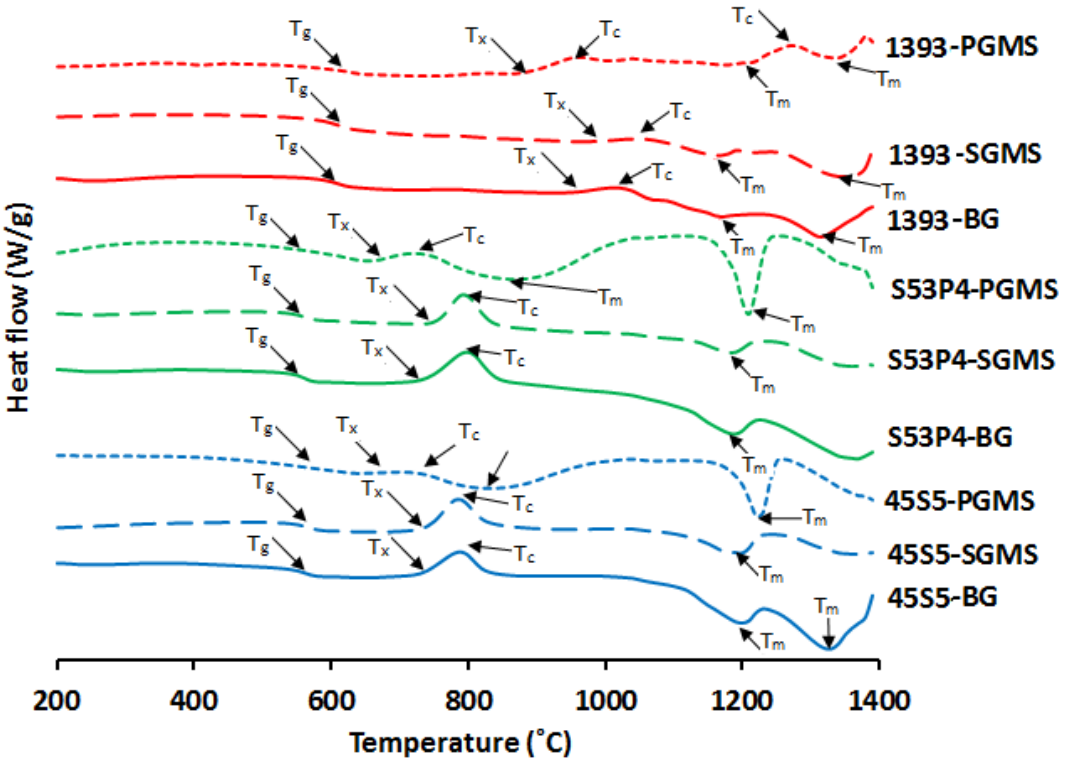


Figure 7.15: *DSC curves for BG (represented as solid line), SGMS (represented as large broken line) and PGMS (represented as small broken line) of three different bio-silicate glasses, presented with three different colours such as blue for 45S5, green for S53P4 and red for 1393.*

Table 7.2: *Glass transition (T_g), onset of crystallisation (T_x), glass stability (ΔT), crystallisation peak (T_c) and melting temperature (T_m) for BG, SGMS and PGMS of different bio-silicate glass formulations, using a 20 $^oC\ min^{-1}$ heating rate.*

Glass Formulations	Glass transition T_g (°C)	Onset crystallisation T_{x1}(°C)	Glass stability $\Delta T = (T_x - T_g)$ °C	Crystallisation Temperature T_{c1} (°C)	Melting Temperature T_{m1} (°C)/ T_{m2} (°C)
45S5-BG	552 ± 3	732 ± 3	180	788 ± 2	1202 ± 3/1332 ± 5
45S5-SGMS	549 ± 2	734 ± 3	185	785 ± 2	1197 ± 3/1389 ± 4
45S5-PGMS	547 ± 3	643 ± 5	96	717 ± 2	836 ± 3/1222 ± 3
S53P4-BG	549 ± 3	735 ± 3	186	798 ± 2	1188 ± 3/1370 ± 4
S53P4-SGMS	546 ± 3	745 ± 4	199	792 ± 2	1184 ± 3/-
S53P4-PGMS	540 ± 4	667 ± 4	127	723 ± 3	876 ± 4/1206 ± 4
1393-BG	593 ± 3	965 ± 3	362	1027 ± 3	1168 ± 5/1313 ± 4
1393-SGMS	592 ± 3	976 ± 5	389	1036 ± 3	1165 ± 4/1344 ± 3
1393-PGMS	590 ± 4	868 ± 4	278	962 ± 2	1173 ± 5/1137 ± 4

7.2.6 Density, tap density and porosity measurements

Table 7.3 shows the density (measured via He pycnometer and tap density) and porosity (calculated from true density and tap density data) for SGMS and PGMS of 45S5, S53P4 and 1393 glass formulations. As seen from **Table 7.3**, the true density and tap density reduced significantly for PGMS, however the porosity increased 2-3 folds for the PGMS for all of the glass compositions when compared to SGMS. For example, density and tap density for the SGMS were found to be around 2.6 and 1.8 g/cm^3, respectively. Whereas, density and tap density for the PGMS were found to be around 2.0 and 0.5 g/cm^3, respectively. On the other hand, porosity of SGMS and PGMS were found to be 25-30 and 70-80 %, respectively. The methodology for how these calculations were conducted is detailed in Chapter 3 Section 3.3.13.

Table 7.3: *Density, tap density and porosity of SGMS and PGMS of three different bio-silicate glasses investigated.*

Formulations	True density (g/cm^3)	Tap density (g/cm^3)	Porosity (%)
45S5 SGMS	2.53 ± 0.01	1.75 ± 0.02	30.71
45S5 PGMS	2.01 ± 0.01	0.43 ± 0.03	78.59
S53P4 SGMS	2.63 ± 0.01	1.95 ± 0.03	25.76
S53P4 PGMS	1.93 ± 0.01	0.45 ± 0.04	76.72
1393 SGMS	2.61 ± 0.01	1.87 ± 0.02	28.32
1393 PGMS	1.66 ± 0.01	0.49 ± 0.03	70.47

7.2.7 Degradation studies

The degradation profiles of the glass microspheres degraded in Milli-Q water at 37 °C over a period of 28 days are presented in **Figure 7.16**. An increase in mass loss was observed with increasing degradation time for all glass formulations (SGMS and PGMS). The PGMS showed higher mass loss compared to SGMS of the same glass composition (as expected). For example, PGMS of 45S5 showed 40 % higher mass loss at day-28 compared to their SGMS (see **Figure 7.16**). The mass loss % of porous glass microspheres were found to be 12.6, 11.9 and 10.2 % for 45S5, S53P4 and 1393, respectively after 28 days of immersion in Milli-Q water. Whereas, solid glass microspheres showed only 8.9 % for both 45S5 and S53P4 and 7.4 % mass loss for 1393 in Milli-Q water at day 28.

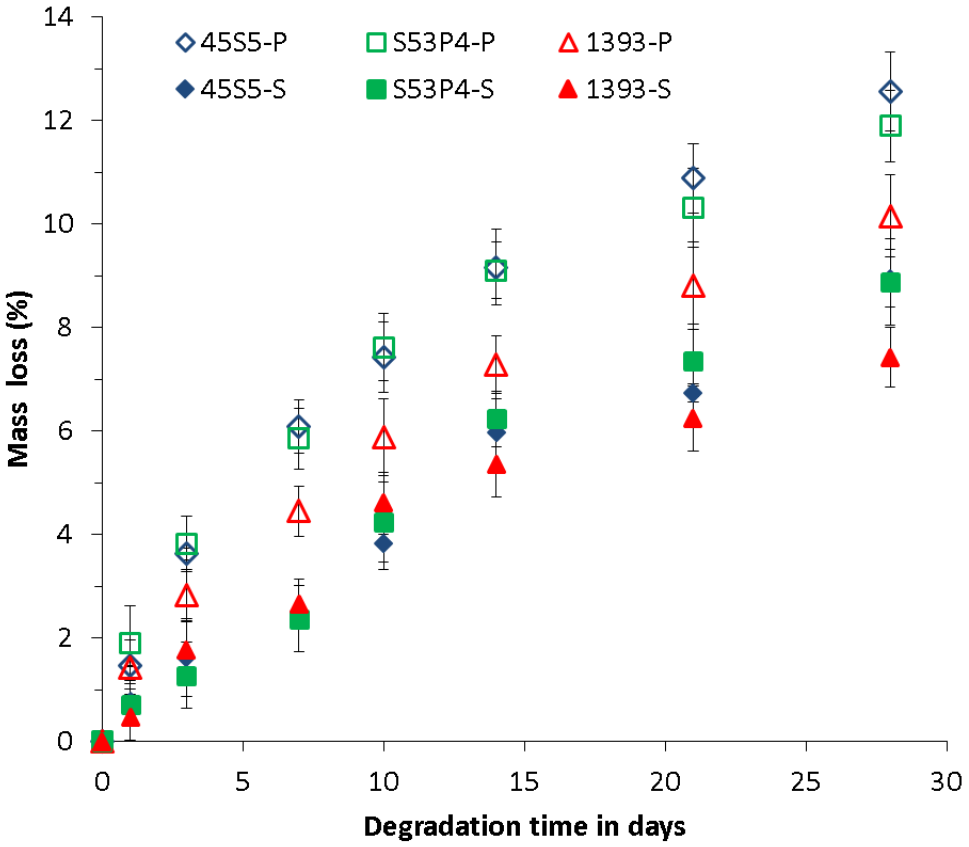


Figure 7.16: *Weight loss versus time in day during the degradation study of SGMS (represented as solid symbol) and PGMS (represented as open symbols) of three different bio-silicate glass in Milli-Q water at 37 °C.*

7.2.8 pH Measurement

Figure 7.17 represents the variation of pH of Milli-Q water as a function of degradation time for both SGMS and PGMS of three different bio-silicate glasses. The starting pH value of the solution was 7.8 for all systems.

The pH for the medium (Milli-Q water) used containing the dissolution products of porous microspheres rapidly increased from ~7.8 to ~11.9 at day-1 for all of the glass compositions then gradually decreased to ~11 by day-7 and remained almost constant for the reminder of the study as can be seen in **Figure 7.17**. On the other hand, the pH values for the solution containing dissolution products of solid

microspheres gradually increased from ~7.8 to ~10 by day-10 and remained almost constant for the remainder of the study.

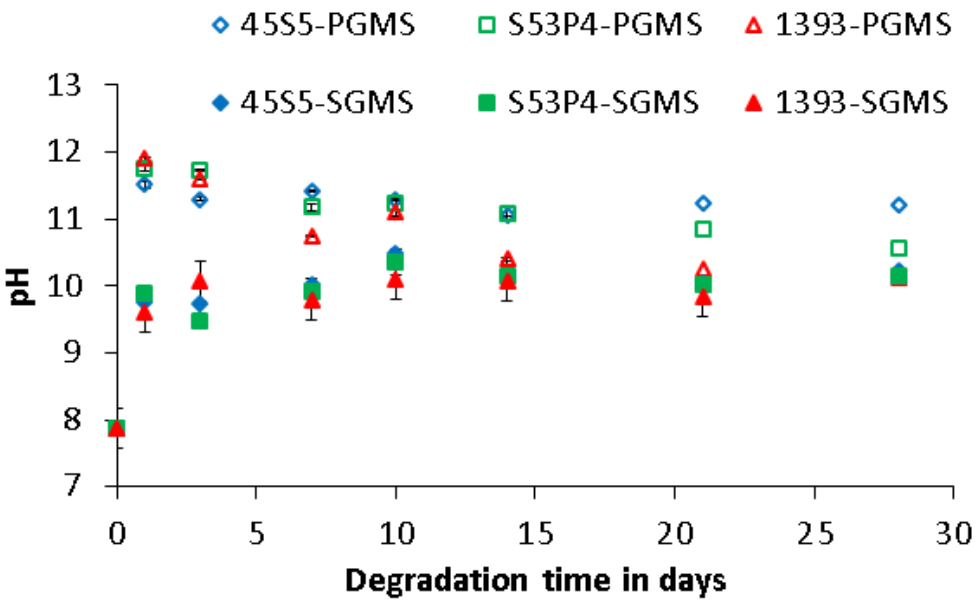


Figure 7.17: *pH change as a function of immersion time (day) of the SGMS (represented as solid symbol) and PGMS (represented as open symbol) of three different bio-silicate glass in Milli-Q water at 37 °C.*

7.2.9 *In vitro* bioactivity studies

7.2.9.1 XRD

XRD profiles for both SGMS and PGMS of all bio-silicate glass formulations after immersion in SBF (following ICG TCO4 method) at 37 °C up to 14 days, are shown in **Figure 7.18**. The major peaks in the patterns corresponded to those of a standard HA, $Ca_{10}(PO_4)_6(OH)_2$ (JCPSD 72-1243), indicating the formation of HA during the reaction. HA peak was observed at day-7 for SGMS except 1393 and PGMS of all glass formulations and peak intensity increased with increasing immersion time. Higher peak intensity was observed for PGMS compared to their respective SGMS. Peaks of Nagelschmidtite ($7CaO\text{-}P_2O_5\text{-}2SiO_2$) [JCPSD 00-005-0646(D)] for starting PGMS were not observed after 7 days of immersion in SBF, only HA peaks and a single $CaCO_3$ peak were observed. Furthermore, only HA peaks were observed for PGMS at day-14.

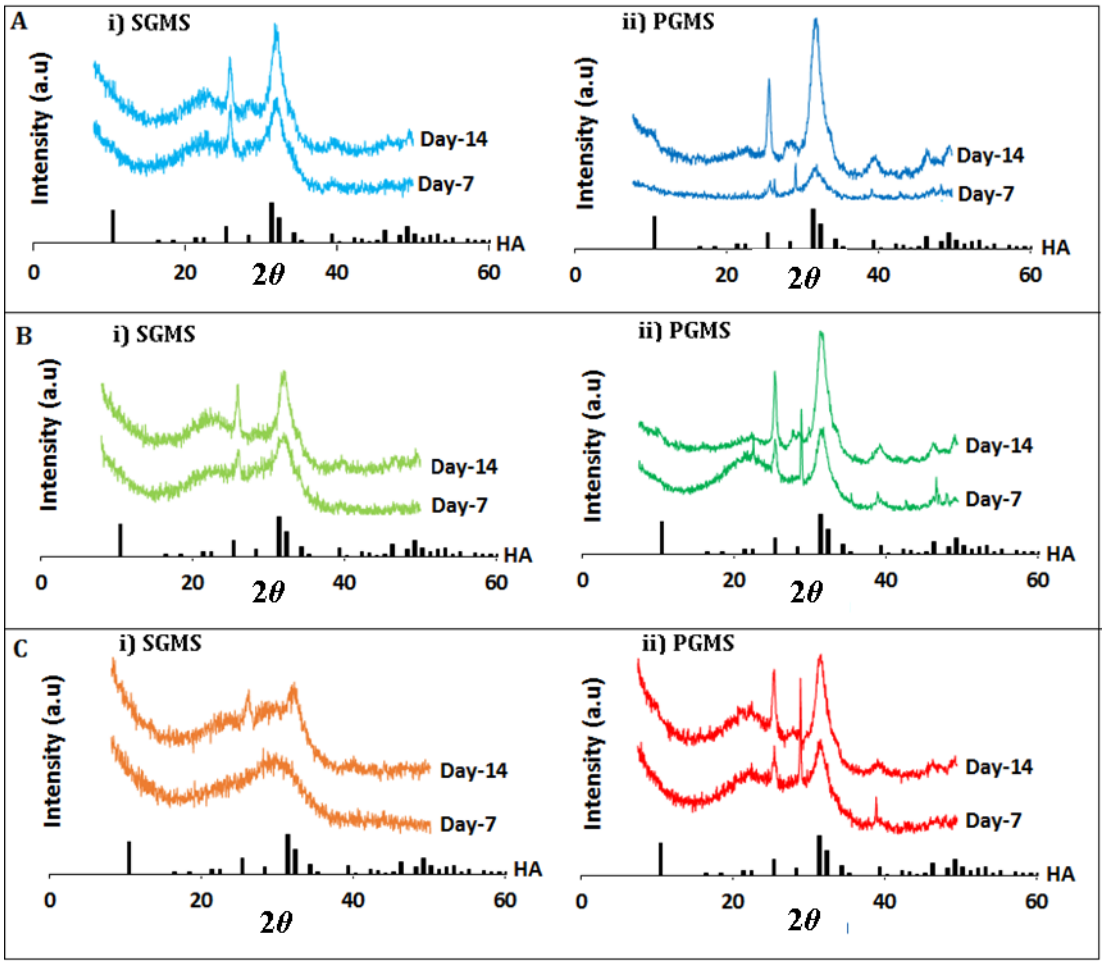


Figure 7.18: *X-ray diffraction pattern for both i) SGMS and ii) PGMS of three bio-silicate glass formulations A) 45S5, B) S53P4 and C) 1393 during the immersion of microspheres in SBF at 37 °C at various time points. XRD spectra for HA shown in each Figure for comparison.*

7.2.9.2 SEM for *in vitro* bioactivity study

Figure 7.19 and **Figure 7.20** represent the SEM images at different magnifications for SGMS and PGMS, respectively after 14 days of immersion in SBF. It can be seen at higher magnification that HA formed (as confirmed via XRD) on the surface of both SGMS and PGMS of all bio-silicate glass formulations (see **Figure 7.19** and **Figure 7.20**).

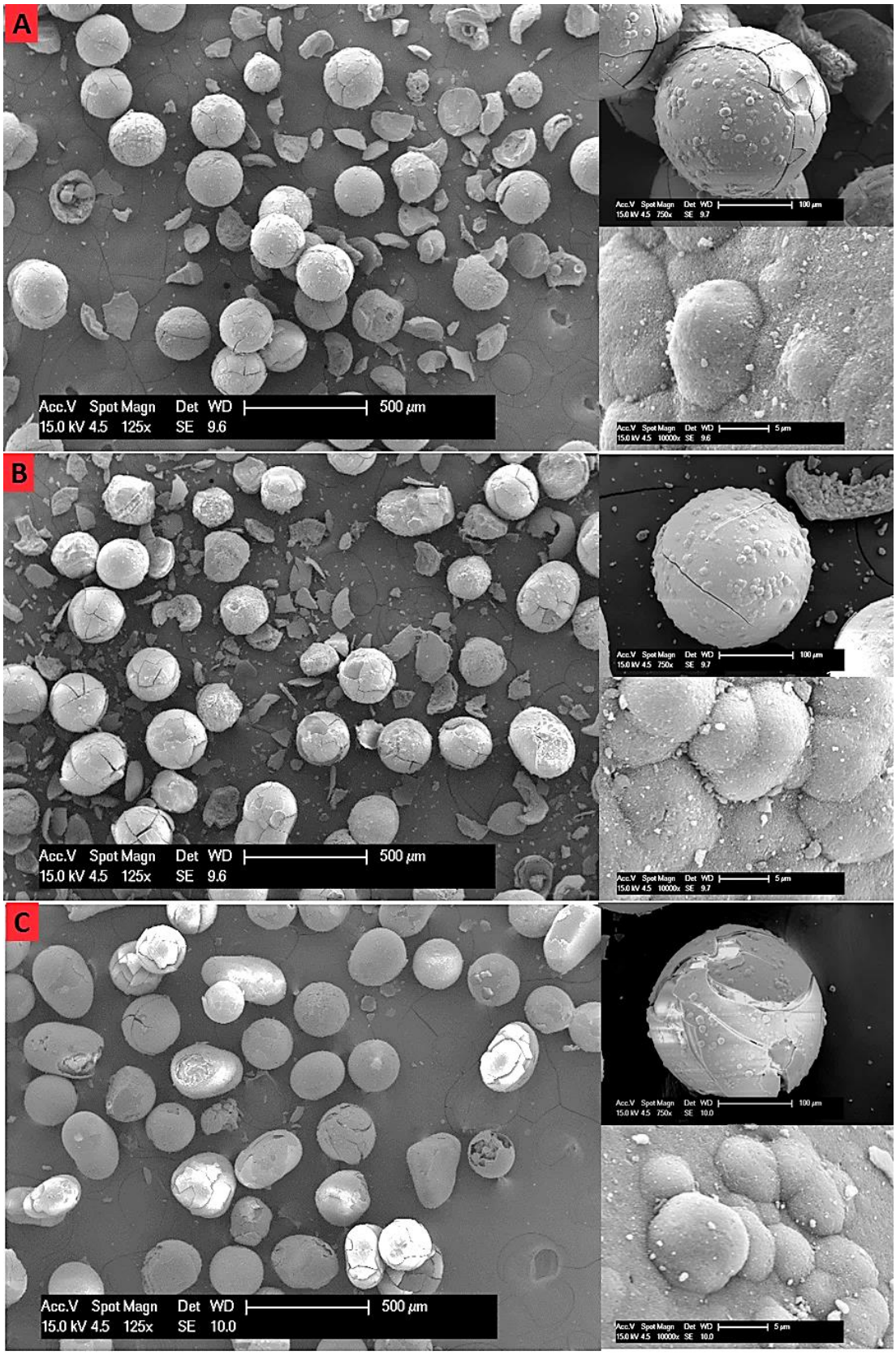


Figure 7.19: *SEM images for SGMS of three bio-silicate glass formulations A) 45S5, B) S53P4 and C) 1393 after immersion in SBF at 37 °C at day-14.*

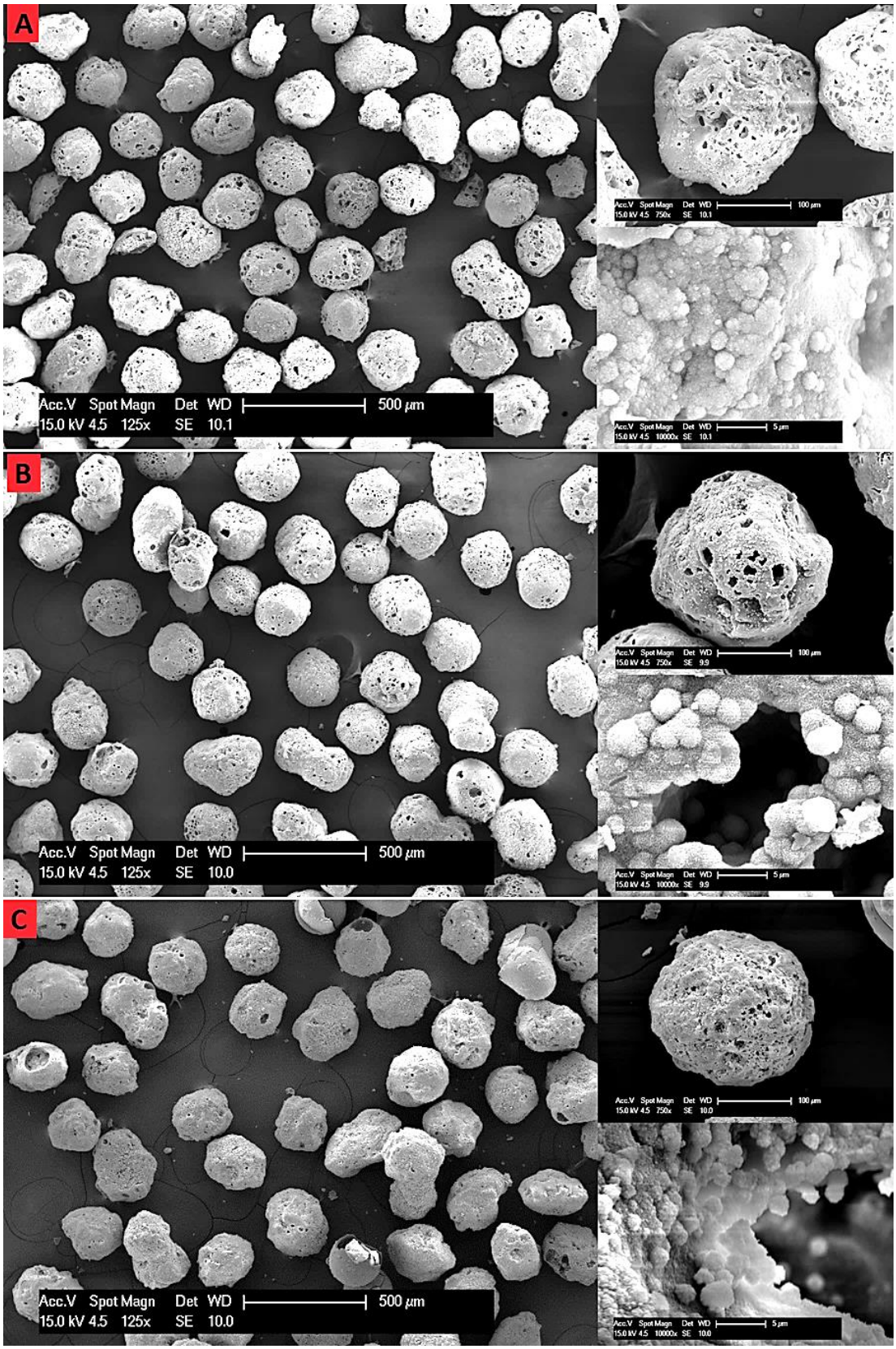


Figure 7.20: *SEM images for PGMS of three bio-silicate glass formulations A) 45S5, B) S53P4 and C) 1393 after immersion in SBF at 37 °C at day-14.*

7.2.9.3 pH Measurements of SBF

Figure 7.21 represents the variation of pH change as a function of immersion time (day) of the SGMS and PGMS of three different bio-silicate glasses in SBF at 37 °C over 14 days duration. In general, the pH values in SBF increased from 7.4 to 8 at day-7, then gradually decreased to 7.6 by day-10 and then remained relatively constant for the remainder of the study as can be seen in **Figure 7.21**.

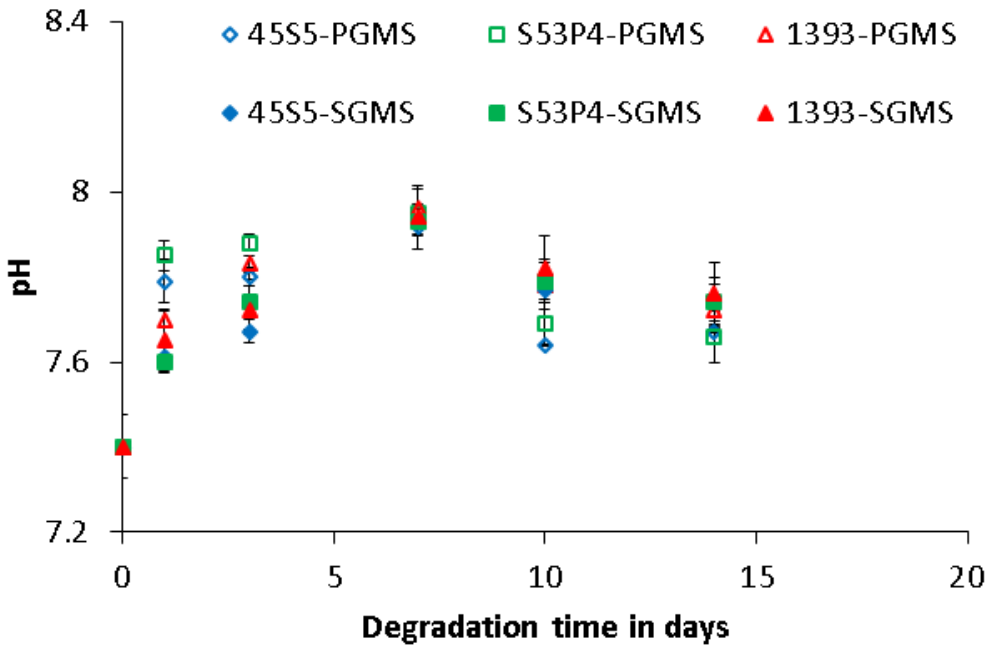


Figure 7.21: *pH change as a function of immersion time (day) for the SGMS and PGMS of three different bio-silicate glasses investigated in SBF at 37 °C over 14 days duration.*

7.2.9.4 Compositional analysis after *in vitro* bioactivity study

Table 7.4 represents the compositional analysis in mol % obtained via EDX for SGMS and PGMS of three different bio-silicate glasses after immersion in SBF at day 14. It can be seen that very small amounts of SiO_2 (2-4 mol %) and Na_2O (1-2 mol %) were observed along with CaO and P_2O_5 for both SGMS and PGMS of each bio-silicate glass formulations. In addition, small amount of MgO (around 3 mol %) was found for both SGMS and PGMS without magnesium containing glasses such as 45S5 and S53P4. Moreover, 4-5 mol % MgO was also found for both SGMS and PGMS of 1393.

In addition, Ca/P (atomic ratio) was found to be around 1.4 for the SGMS of each glass compositions and 1.5-1.66 for PGMS after 14 days of immersion in SBF.

Table 7.4: *Compositional analysis for SGMS and PGMS of three bio-silicate glasses after immersion in SBF at day 14.*

Components	45S5		S53P4		1393	
	SGMS (mol%)	PGMS (mol%)	SGMS (mol%)	PGMS (mol%)	SGMS (mol%)	PGMS (mol%)
SiO_2	1.78 ± 0.65	3.30 ± 0.43	1.05 ± 0.54	4.56 ± 0.51	1.12 ± 0.33	1.28 ± 0.52
P_2O_5	24.04 ± 0.45	21.56 ± 0.95	24.45 ± 0.46	22.73 ± 0.59	24.45 ± 1.07	23.30 ± 0.85
CaO	69.25 ± 1.01	71.78 ± 0.84	68.54 ± 0.86	68.64 ± 0.92	67.72 ± 1.45	70.14 ± 1.53
Na_2O	1.73 ± 0.25	0.78 ± 0.18	2.54 ± 0.32	1.02 ± 0.22	1.48 ± 0.35	1.10 ± 0.14
MgO	3.20 ± 0.88	2.58 ± 0.52	3.43 ± 0.67	3.05 ± 0.61	5.12 ± 0.53	4.18 ± 0.32
K_2O	-	-	-	-	0.11 ± 0.13	-

7.2.10 Improvement of sphericity

To improve the sphericity of the porous microspheres formed, further trials were carried out utilising the smaller starting granular particle size (ranging between 100-150 µm) for 1393 bio-silicate glass. **Figures 7.22 A** and **B** show the SEM images and cross-sections of porous 1393 microspheres for lower granular particle size range, respectively. It can be seen that spherical PGMS were formed, however the pore size and no. of pores on the surface of the microspheres had decreased (see **Figure 7.22 A**) although the internal morphology remained highly porous. (See **Figure 7.22 B**)

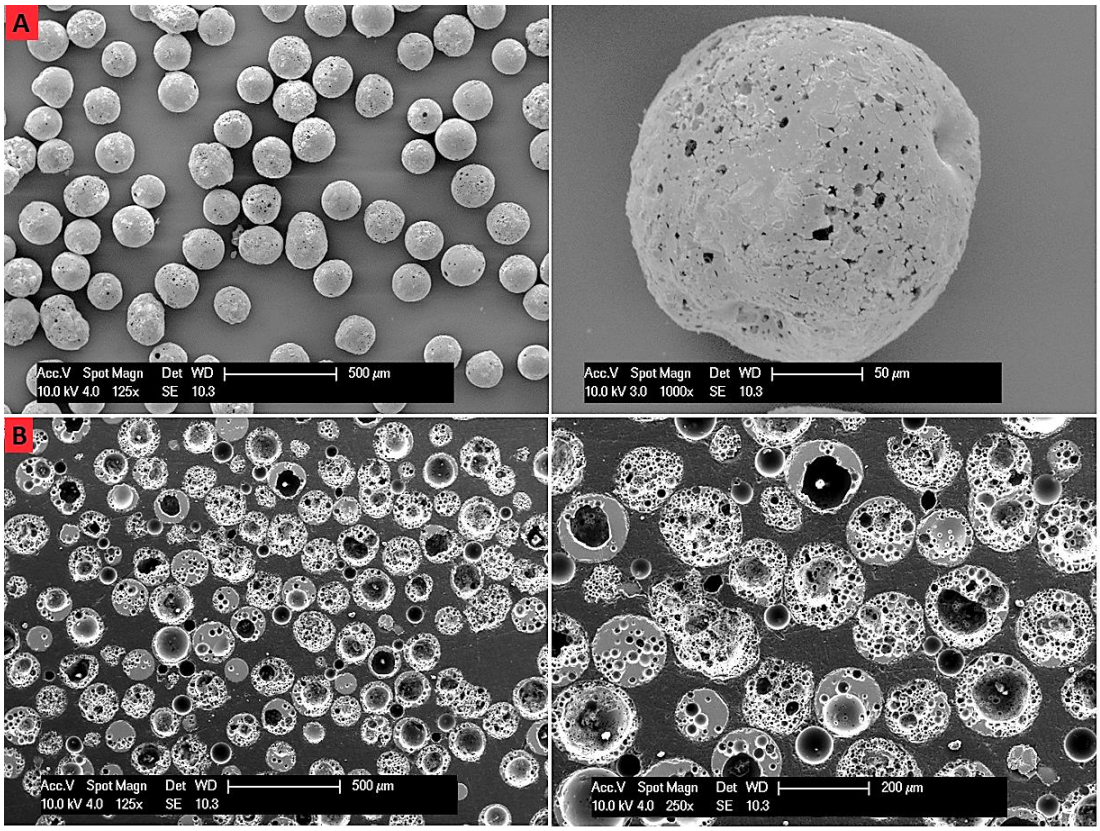


Figure 7.22: *A) SEM images and B) cross-sections of porous 1393 bio-silicate glass microspheres for smaller starting granular size range of 100-150 µm.*

7.2.11 Optimisation of the Initial 'Conventional Method'

Porous bio-silicate glass microspheres prepared via granular method showed following limitations:

1. They were not fully spherical
2. Pore size decreased with increasing sphericity
3. Porous microspheres were crystallised (four small sharp peaks of nagelschmidtite ($7CaO\text{-}P_2O_5\text{-}2SiO_2$) [JCPSD 00-005-0646(D) were observed) during processing.

Therefore, to minimise the limitations mentioned above and to reduce the processing steps (i.e. grinding and granular preparation) for porous bio-silicate glass microspheres, further optimisation of the conventional method was considered and trialled. This optimisation was based on the hypothesis that altering the viscosity profiles of the glasses would aid the porous microspheres manufacturing process.

Borax and V_2O_5 were added to 45S5 glass to significant alter its properties (focussing on mainly viscosity as these are known viscosity modifiers).

7.2.11.1 Compositional analysis of starting bulk glasses

Literature reports show that borax ($Na_2B_4O_7 \cdot 10H_2O$) and V_2O_5 act as viscosity modifiers and can reduce the melting temperature of glass [296,343]. Therefore, both 2 and 5 mol % borax and V_2O_5 doped 45S5 glass were prepared along with 45S5 glass for further analysis and trial. As highly porous microspheres were formed for phosphate glass via our conventional method (described in Chapter 5), the phosphate glass formulation M24T0/P40 was also included for comparative thermal (i.e. melting) and viscosity analysis with five bio-silicate glasses prepared (as shown highlighted in **Table 7.5**).

Table 7.5 also represents the compositional analysis for all six different glass formulations explored via Energy dispersive X-ray analysis (EDX). Experimental compositional analysis for 45S5 and V_2O_5 containing 45S5 glasses were found to be very similar to the value of expected composition. ICP-MS was conducted for accurate compositional analysis of borax containing glass. However, the compositional analysis for borax containing glasses was not conducted due to the unavailability of instrumental facility.

Table 7.5: *Compositional analysis for six different types of glass formulations via EDX analysis.*

Components (mol%)	Glass formulations					
	P40	45S5 Expected/ Actual	45S5 + 2 mol% Borax Expected/Actual	45S5 + 5 mol% Borax Expected/Actual	45S5 + 2 mol% V_2O_5 Expected/Actual	45S5 + 5 mol% V_2O_5 Expected/Actual
SiO_2	-	46.1/47.45	46.1/-	46.1/-	46.1/45.17	46.1/44.01
P_2O_5	40	2.6/3.11	2.6/-	2.6/-	2.6/2.56	2.6/2.67
MgO	24	-	-	-	-	-
CaO	16	26.9/26.48	26.9/-	26.9/-	26.9/27.45	26.9/27.28
Na_2O	20	24.4/22.96	22.4/-	19.4/-	22.4/23.09	19.4/20.97
Borax	-	-	2/-	5/-	-	-
V_2O_5	-	-	-	-	2/1.72	5/5.07

7.2.11.2 Thermal analysis

Figure 7.23 shows the thermal traces of the glasses, where the corresponding glass transition (T_g), onset of crystallisation (T_x), crystallisation peak (T_c) and melting (T_m) temperature have been labelled. It can be seen from **Figure 7.23** that the melting temperature for 45S5 (1213 °C) was 450 °C higher in comparison to P40 (766 °C). It was also observed that the thermal properties especially T_g and initial melting (T_m) temperatures for 45S5 glass decreased with increasing borax or V_2O_5 content in 45S5 (see **Table 7.6**). For example, the initial melting temperature (T_m) value was seen to decrease from 1213 °C (for 45S5) to 1033 °C (for 45S5 + 5 mol% borax) and 1017 °C (for 45S5 + 5 mol% V_2O_5) with increasing borax or V_2O_5 content from 0 to 5 mol%. In addition, three melting peaks were observed for 45S5 + 5 mol% V_2O_5 at 1017 °C, 1075 °C and 1140 °C.

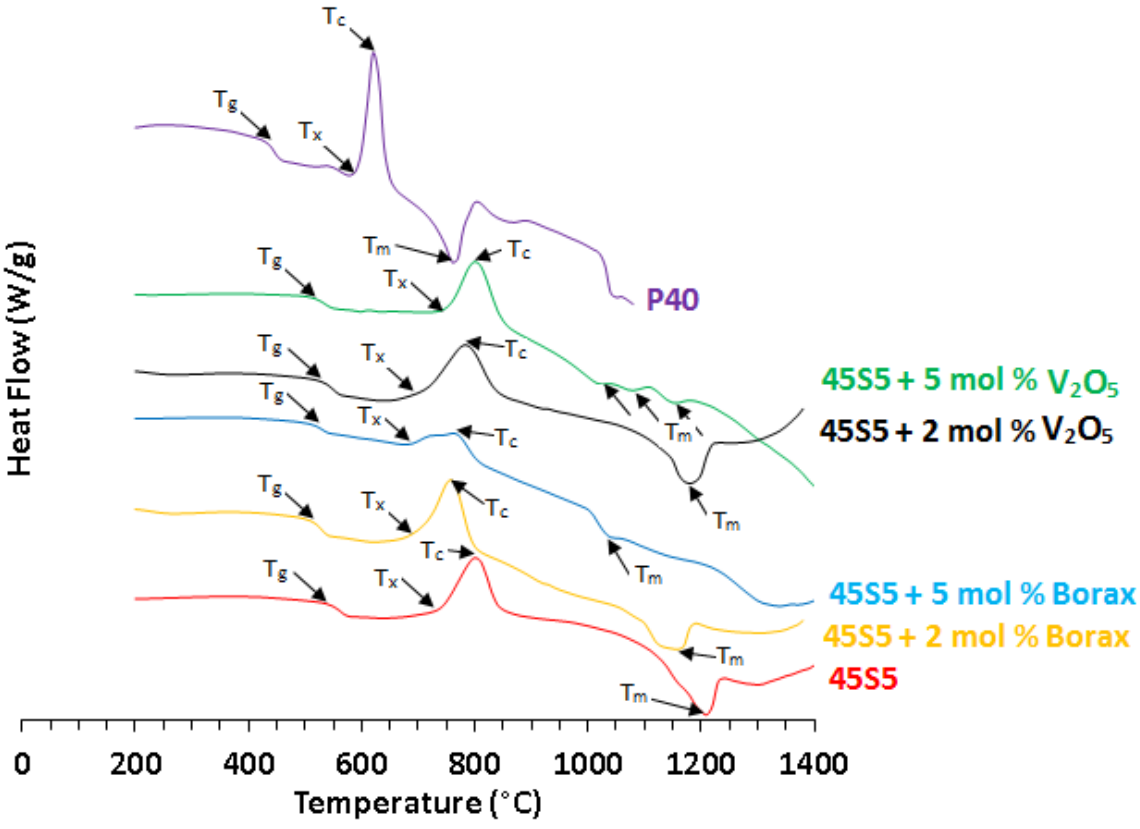


Figure 7.23: *DSC curves for six different glass formulations investigated at 20 °C min^{-1} heating rate.*

Table 7.6: *Glass transition (T_g), onset of crystallisation (T_x), glass stability (ΔT), crystallisation peak (T_c) and melting temperature (T_m) for six different glass formulations, using a 20 $^oC\ min^{-1}$ heating rate.*

Formulations	Glass transition $T_g \pm 3$ (°C)	Onset crystallisation $T_x \pm 3$ (°C)	Processing window $\Delta T = (T_x - T_g)$ (°C)	Crystallisation temperature $T_c \pm 3$ (°C)	Initial melting temperature $T_m \pm 5$ (°C)
45S5 (125-200 µm)	551	737	186	803	1213
45S5+2mol% Borax (125-200 µm)	526	697	171	756	1151
45S5+5mol% Borax (125-200 µm)	521	689	168	766	1033
45S5+2mol% V_2O_5 (125-200 µm)	547	714	167	785	1182
45S5+5mol% V_2O_5 (125-200 µm)	531	752	230	798	1017, 1075, 1140
P40 (125-200 µm)	436	588	152	623	766

7.2.11.3 Viscosity measurement

Viscosity of a material can be measured in various ways such as fibre elongation method, beam bending method, parallel plate viscometer, rotating cylinder and Hot Stage Microscopy (HSM). Among them, viscosity profiles for the glasses investigated were measured indirectly via HSM analysis and directly via rotating cylinder (High temperature viscometer). Hot Stage Microscopy (HSM) analysis provides information on the temperatures for various characteristic points such as first shrinkage, maximum shrinkage, sphere, hemisphere and flow point/melt temperature. The data obtained enables plots of the viscosity curves to be compared, including the temperature differences between sphere/hemisphere and flow points, which are all related to viscosity changes relative to temperature. The first two temperatures (i.e. first shrinkage, maximum shrinkage) were extracted from the sintering curve profiles

and the last three temperatures (i.e. sphere, hemisphere and flow) were determined based on height and width ratio and contact angle of materials from snapshot images, obtained by the software supplied with the heating microscope.

Figure 7.24 represents the snapshot images highlighting configurations for a sphere, hemisphere and flow based on height and width ratio and contact angle of materials obtained by the HSM software. These three characteristic points (i.e. sphere, hemisphere and flow) were also marked on sintering curves of each glass composition (see **Figure 7.25**).

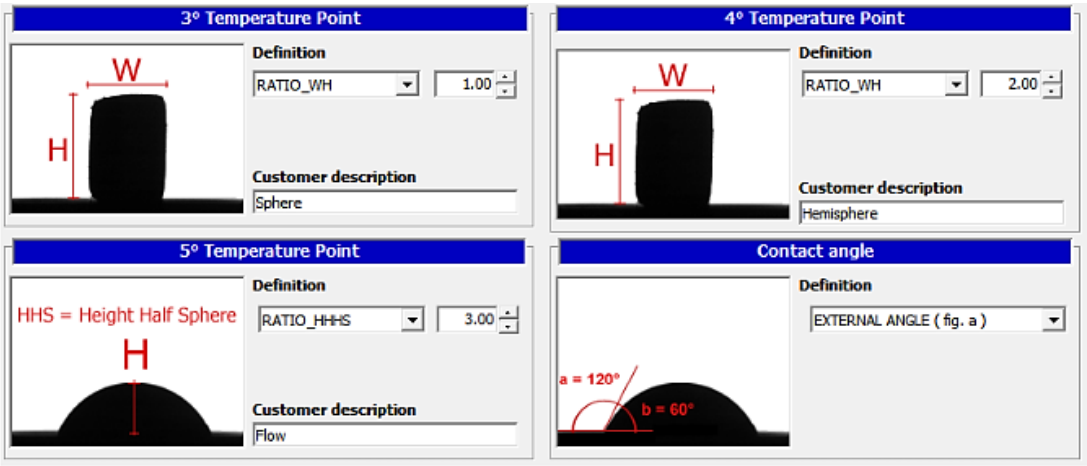


Figure 7.24: *An example of snapshot images for sphere, hemisphere and flow based on height and width ratio and contact angle of material obtained by the software of Hot Stage Microscopy (HSM).*

Figure 7.25 represents the sintering percentage for the glass compositions investigated against temperature obtained via HSM. From this analysis, it was clearly observed that the sintering profile for P40 glass had the lowest temperature compared with the 45S5 and borax or V_2O_5 containing 45S5 glass. Moreover, the sintering curves shifted to lower temperature (towards the P40 sintering curve) with increasing borax or V_2O_5 content in 45S5 glass. The highest shift for the sintering curve (among 45S5 glasses) towards lower temperature was observed for 5 mol % borax containing 45S5 glass (blue line) followed by the 5 mol % V_2O_5 (green line), 2 mol% borax (amber line) then 2 mol% V_2O_5 (black line) content 45S5 and finally 45S5 (red

line) glass alone. The sintering curve for P40 (purple line) was present at lowest temperature as can be seen from **Figure 7.25**.

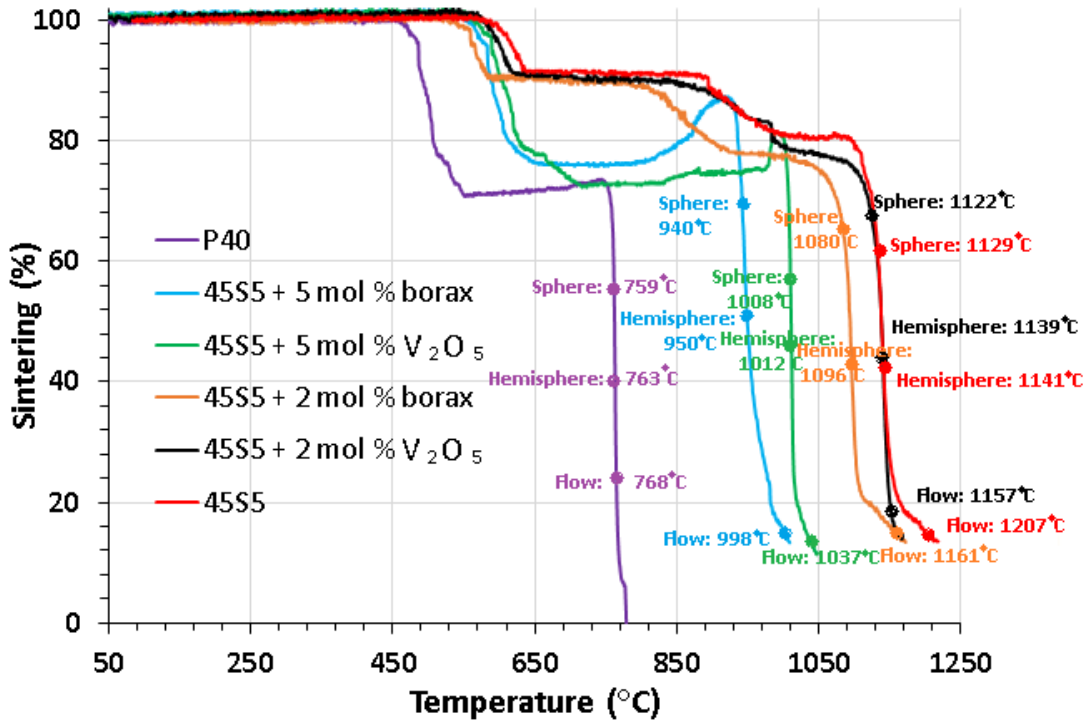


Figure 7.25: *Percentage of sintering as a function of temperature for six different glass formulations investigated via Hot Stage Microscopy (HSM).*

Figure 7.26 represents temperature for three different points such as flow, hemisphere and sphere for the six glass compositions investigated. The change from sphere or hemisphere to flow point happened very rapidly for the P40 phosphate glass compared to 45S5 glass as can be seen from **Figure 7.26**. Moreover, a smaller spread of these values was observed for the V_2O_5 containing 45S5 in comparison to borax containing 45S5. Therefore, the viscosity change relative to temperature (i.e. rate of viscosity change) could be another influential factor to achieve the desired porous microsphere morphologies. To calculate the rate of viscosity change, viscosity vs temperature curves were plotted using the fixed viscosity for the characteristics temperature points such as flow, hemisphere, sphere, maximum shrinkage, first shrinkage obtained via HSM analysis [344,345].

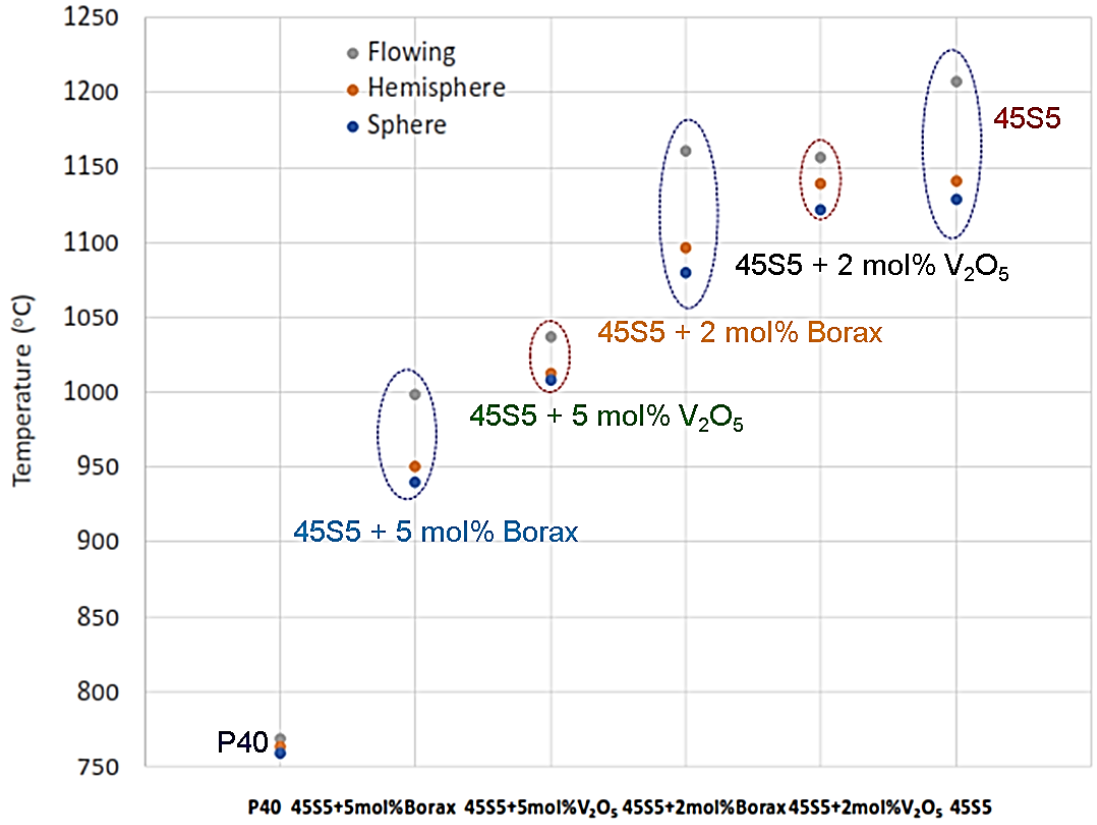


Figure 7.26: *Temperature difference among flow, hemisphere and sphere point for six different glass formulations investigated via Hot Stage Microscopy (HSM).*

The viscosity fitting curves using Vogel-Fulcher-Tammann (VFT) equation were plotted based on the characteristics temperature points obtained via HSM. Moreover, literature reported the fixed viscosity around $10^{12.3}$ Pa s for glass transition temperature [345]. Six fixed point viscosity such as flow, hemisphere, sphere, maximum shrinking, first shrinkage and glass transition temperature were used to fit the viscosity curves using VFT equation. **Figure 7.27** represents the viscosity fitting curves for six different glass formulations investigated using a fixed-point viscosity method via HSM (see **Figure 7.28** for this comparative study).

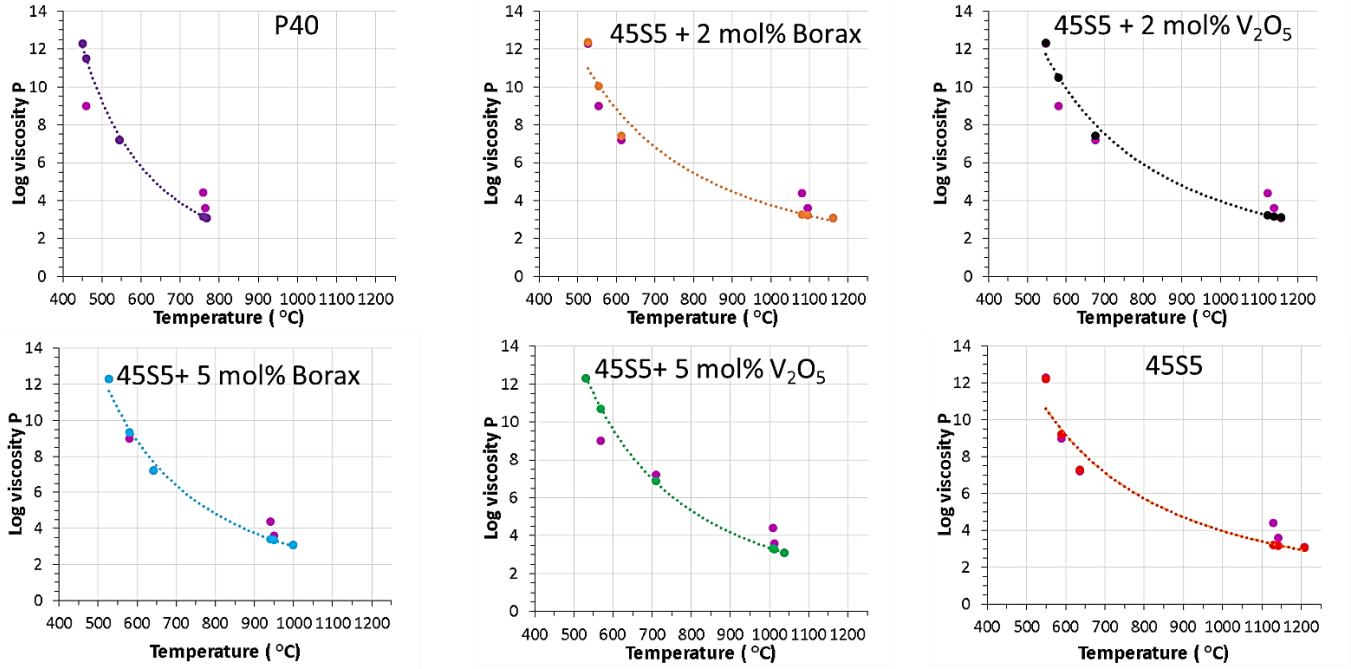


Figure 7.27: *Individual viscosity fitting curves for the six different glass formulations investigated using a fixed point viscosity method via Hot Stage Microscopy (HSM).*

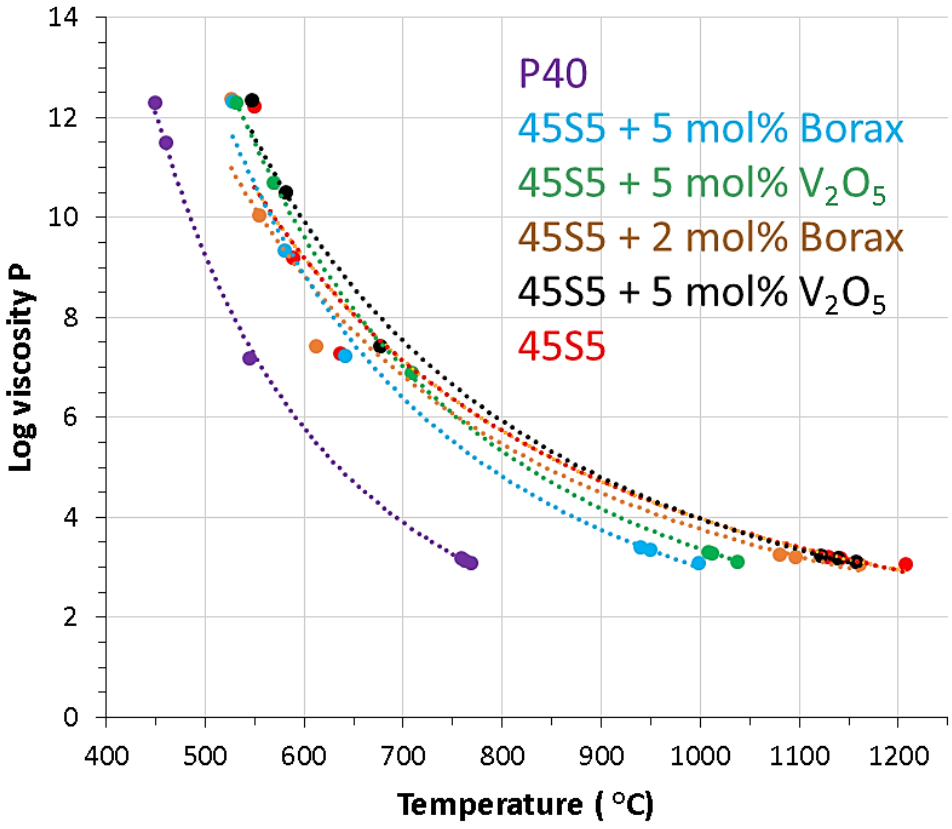


Figure 7.28: *Combined fixed point viscosity curves for all six different glass formulations investigated via Hot Stage Microscopy (HSM).*

It can be seen from **Figure 7.28** that the viscosity curves shifted to lower temperature with increasing borax or V_2O_5 content in 45S5 glass. A higher shift of viscosity curve for the 5 mol % borax containing 45S5 glass was observed in comparison to 5 mol % V_2O_5 content 45S5. Moreover, the viscosity curve for P40 glass had the lowest temperature compared with 45S5 and the borax or V_2O_5 containing 45S5 glasses. The rate of viscosity change (slope) between melt and hemisphere temperature and/or between melt and sphere temperature for all six glass formulations were calculated from viscosity curves as presented in **Table 7.7**. The rate of viscosity change (melt-sphere/melt-hemisphere) was 400 % higher for P40 compared to 45S5. The rate of viscosity change (melt-sphere/melt-hemisphere) for 45S5 increased with increasing borax or V_2O_5 content in 45S5. For examples, 250 % higher rate of viscosity change was observed for the 5 mol % V_2O_5 containing 45S5 glass compared to 45S5 alone. Moreover, higher rate of viscosity change (melt-sphere/melt-hemisphere) was observed for the V_2O_5 containing 45S5 compared to borax containing 45S5 (see **Table 7.7**).

Table 7.7: *Rate of viscosity change between two points (i.e. flow and sphere or flow and hemisphere) for six different types of glass formulations investigated*.

Formulations	Flow-Sphere (Slope negative) (log vis P/°C)	Flow-hemisphere (Slope negative) (log vis P/°C)
P40	0.01009	0.01001
45S5	0.00200	0.00196
45S5+2 mol% Borax	0.00228	0.00222
45S5+2 mol% V_2O_5	0.00379	0.00371
45S5+5 mol% Borax	0.00567	0.00557
45S5+5 mol% V_2O_5	0.00718	0.00714

Viscosity can also be measured directly via rotating viscometer, and these high temperature viscosity profiles were also measured for the six glass formulations investigated. **Figure 7.29** represents the viscosity fitting curves for the six glass formulations (using VFT equation) based on high temperature viscosity (HTV) data and the fixed viscosity for glass transition point (see **Figure 7.30** for this comparative study).

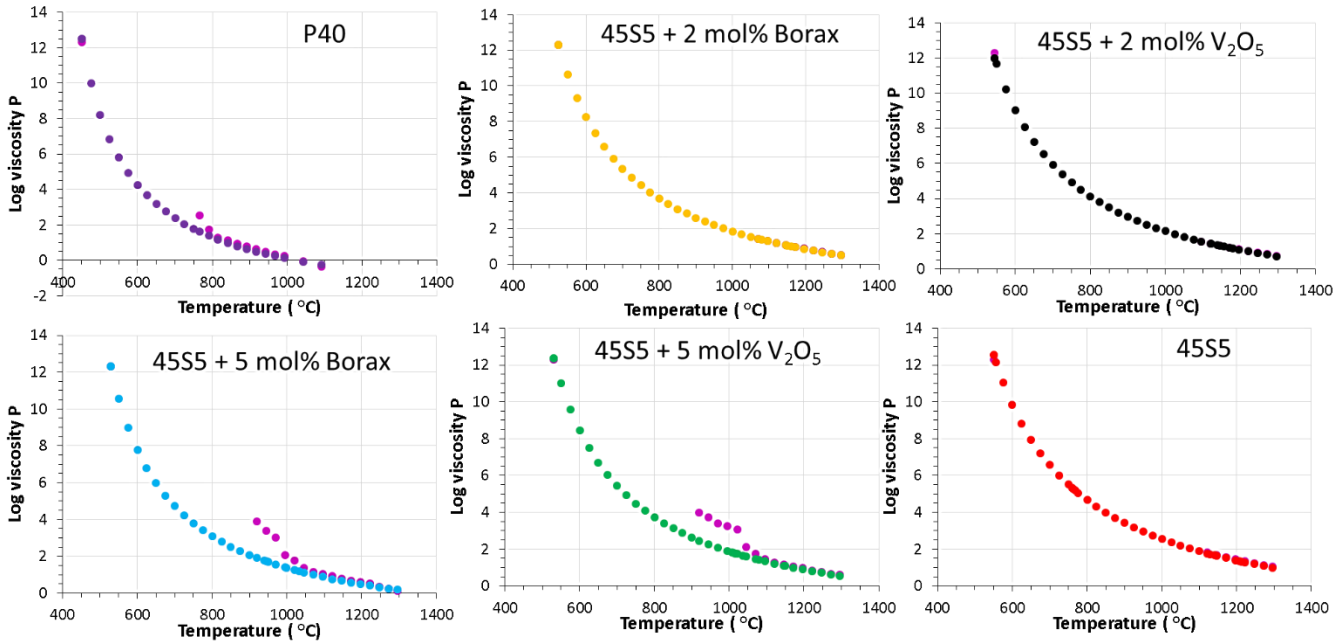


Figure 7.29: *Viscosity fitting curves for six different glass formulations investigated via high temperature viscometer.*

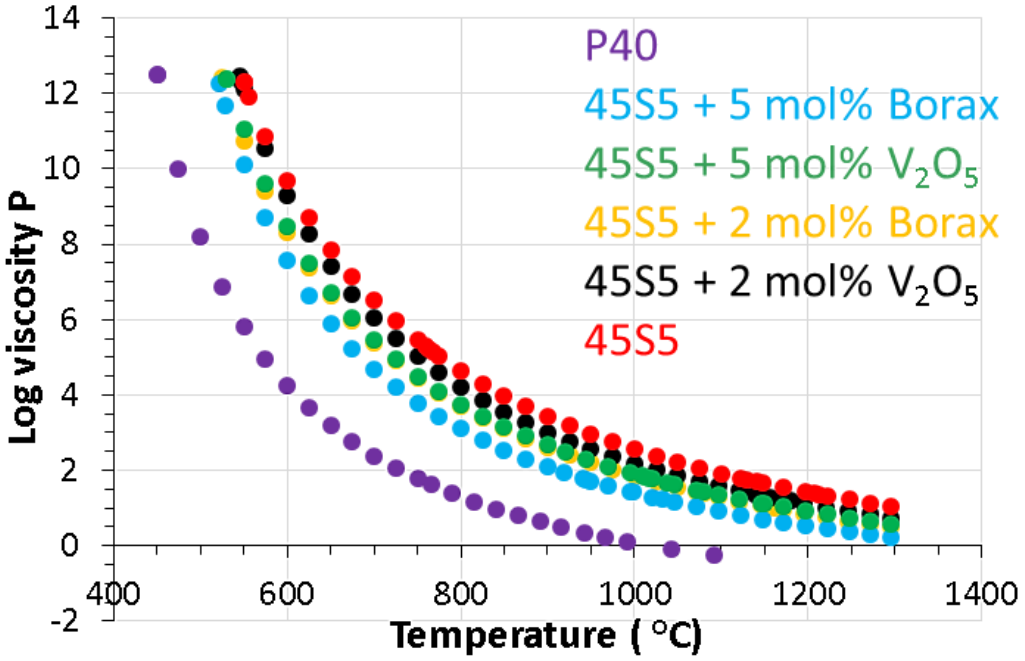


Figure 7.30: *Viscosity curves for six different glass formulations investigated via high temperature viscometer.*

The viscosity curves obtained via HTV followed similar trend to the viscosity curves obtained via HSM. It was seen from **Figure 7.30** that the viscosity curves shifted to

lower temperature with increasing borax or V_2O_5 content in 45S5 glass. The higher shift of viscosity curve for 5 mol % borax containing 45S5 glass to lower temperature was observed compared to 5 mol % V_2O_5 content in 45S5 glass. Viscosity curve for P40 glass had the lowest temperature compared with the 45S5 and borax or V_2O_5 containing 45S5 glass. The rate of viscosity change between melt and hemisphere temperature and/or between melt and sphere temperature for all six glass formulations were calculated from viscosity curves as presented in **Table 7.8**. The rate of viscosity change (melt-sphere/melt-hemisphere) was 125 % higher for P40 compared to 45S5. Moreover, 30 % and 45 % higher rate of viscosity change (melt-sphere/melt-hemisphere) was observed for the 5 mol % borax and 5 mol % V_2O_5 containing 45S5, respectively in comparison to 45S5. However, very similar rate of viscosity change (melt-sphere/melt-hemisphere) was observed for 45S5 and 2 mol % borax and V_2O_5 containing 45S5.

Table 7.8: *Rate of viscosity change between two points (i.e. flow and sphere or flow and hemisphere) for different types of glass formulations investigated.*

Formulations	Flow-Sphere (Slope negative) (log vis P/°C)	Flow-hemispheres (Slope negative) (log vis P/°C)
P40	0.01006	0.00997
45S5	0.00474	0.00467
45S5+2 mol% Borax	0.00473	0.00463
45S5+2 mol% V_2O_5	0.00480	0.00470
45S5+5 mol% Borax	0.00646	0.00635
45S5+5 mol% V_2O_5	0.00686	0.00672

The published viscosity data for P40 and for 45S5 and 1393 glass are presented in **Figure 7.31** and **Figure 7.32**, respectively to confirm the accuracy of the experimental viscosity curves obtained via HTV (as the viscosity curves were fitted using high temperature viscosity data and fixed viscosity for glass transition point rather than low temperature viscosity data) [346,347]. Similar values of slope in between flow and sphere points / in between flow and hemisphere points were observed for P40 experimental (-0.01006/-0.00997 log vis P/°C) and P40 literature (-0.00925/-0.00916

log vis P/°C) and for 45S5 experimental (-0.00474/-0.00467 log vis P/°C) and 45S5 literature (-0.00467/-0.00459 log vis P/°C).

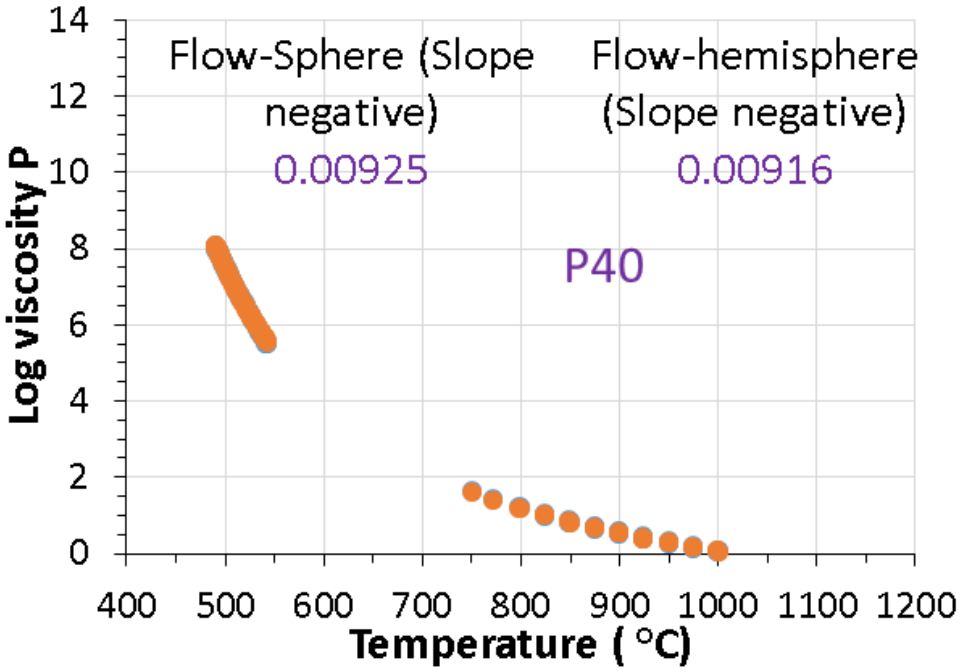


Figure 7.31: *Published viscosity curves for P40 glass* [346].

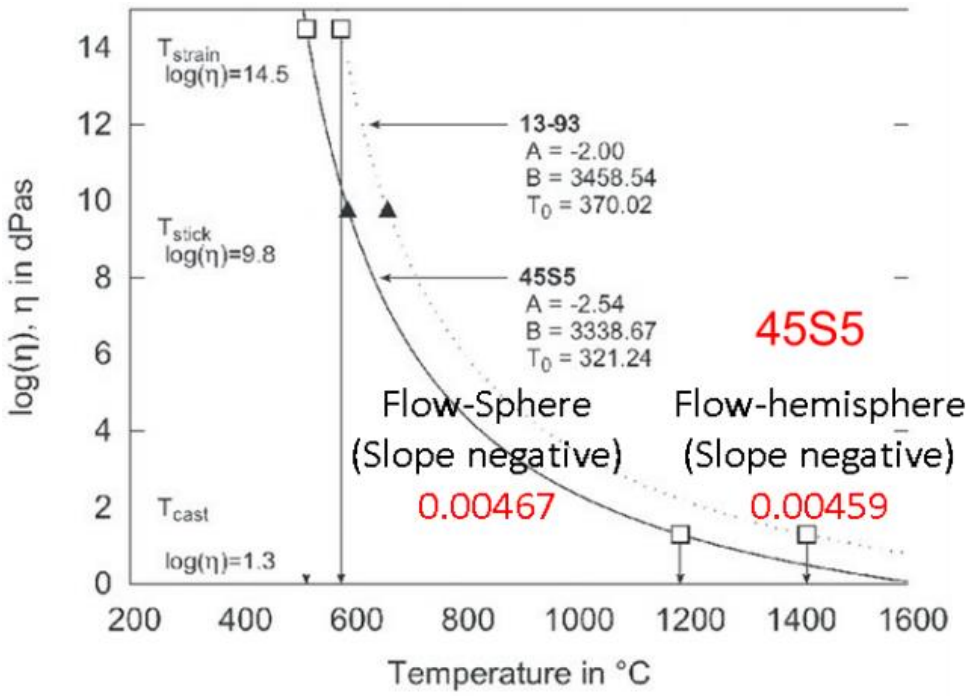


Figure 7.32: *Published viscosity curves for 45S5 and 1393 glass* [347].

7.2.11.4 Flame length measurement

It was noticed that the flame length changed with the variation of gas flow rate ratios. Therefore, the flame lengths utilised were measured to investigate their variation with gas flow ratio and are presented below in **Figure 7.33**. It can be seen that the flame length decreased from approximately 37 cm to 31 cm with increasing gas flow rate ratio from 2:2 to 3:3. Therefore, flame lengths and gas pressure also had an influence on the residence time of glass particles within the flame and thereby cooling rate.

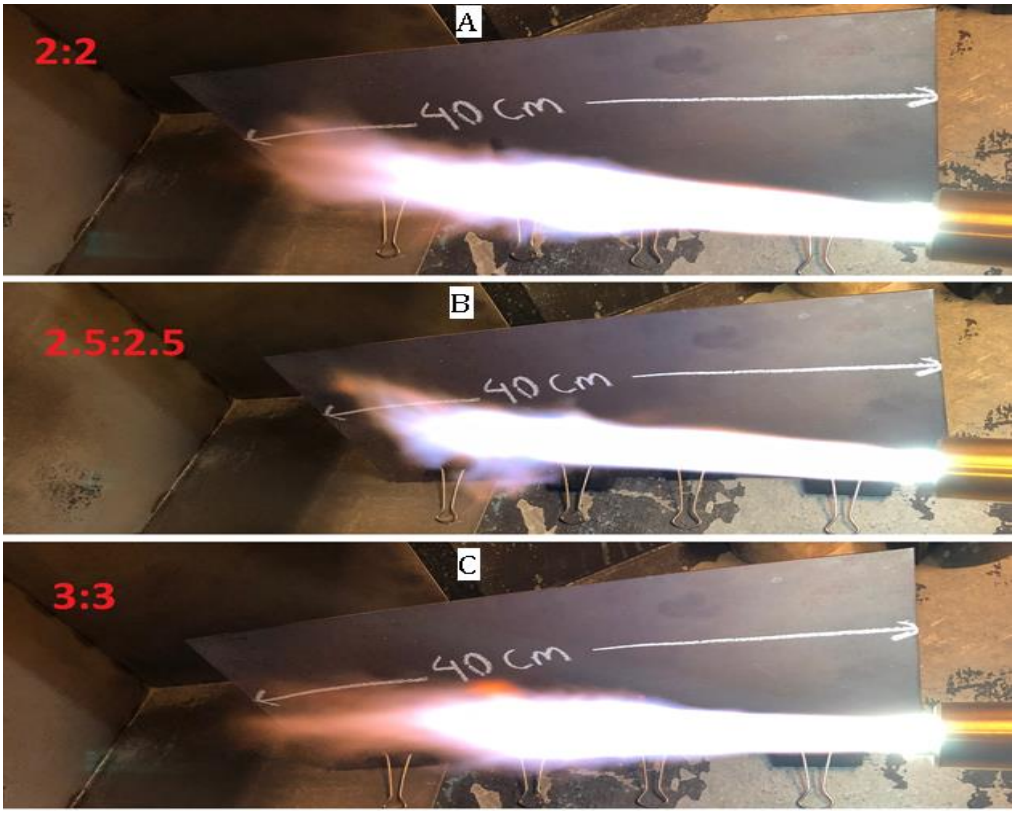


Figure 7.33: *Flame lengths for A) 2:2, B) 2.5:2.5 and C) 3:3 gas flow rate ratio.*

7.2.11.5 Trials of spheroidisation

As the melt temperature and viscosity for 45S5 glass decreased significantly by the addition of borax or V_2O_5, further trials of spheroidisation for both the 2 and 5 mol% borax and V_2O_5 content 45S5 and 45S5 alone were conducted using the same parameters as the initials trials (i.e. starting particle size range, particles to porogen ratio, porogen size range and so on) except for gas flow rate ratio. As P40 glass showed higher rate of viscosity change in between flow and hemisphere/sphere

point compared to 45S5, therefore, gas flow rate ratio of 3:3 instead of 2.5:2.5 (for initial trial) was used to increase cooling rate for molten micro particles.

7.2.11.5.1 Trials for borax content 45S5 glass

Figures 7.34 A-C show the SEM images of unwashed, washed (with 0.5 M acetic acid for 1 min) and cross-sections of **2 mol % borax** content 45S5 microspheres. It can be seen that very few pores were observed on some unwashed microspheres and the rest of them looked like solid microspheres (see **Figure 7.34 A**). However, porous microspheres were found after washing the microspheres with 0.5 M acetic acid for 1 min (see **Figure 7.34 B**). 70-80 % microspheres were fully porous and rest of them exhibited only surface pores with large solid core as can be seen from the cross-sections of microspheres (see **Figure 7.34 C**).

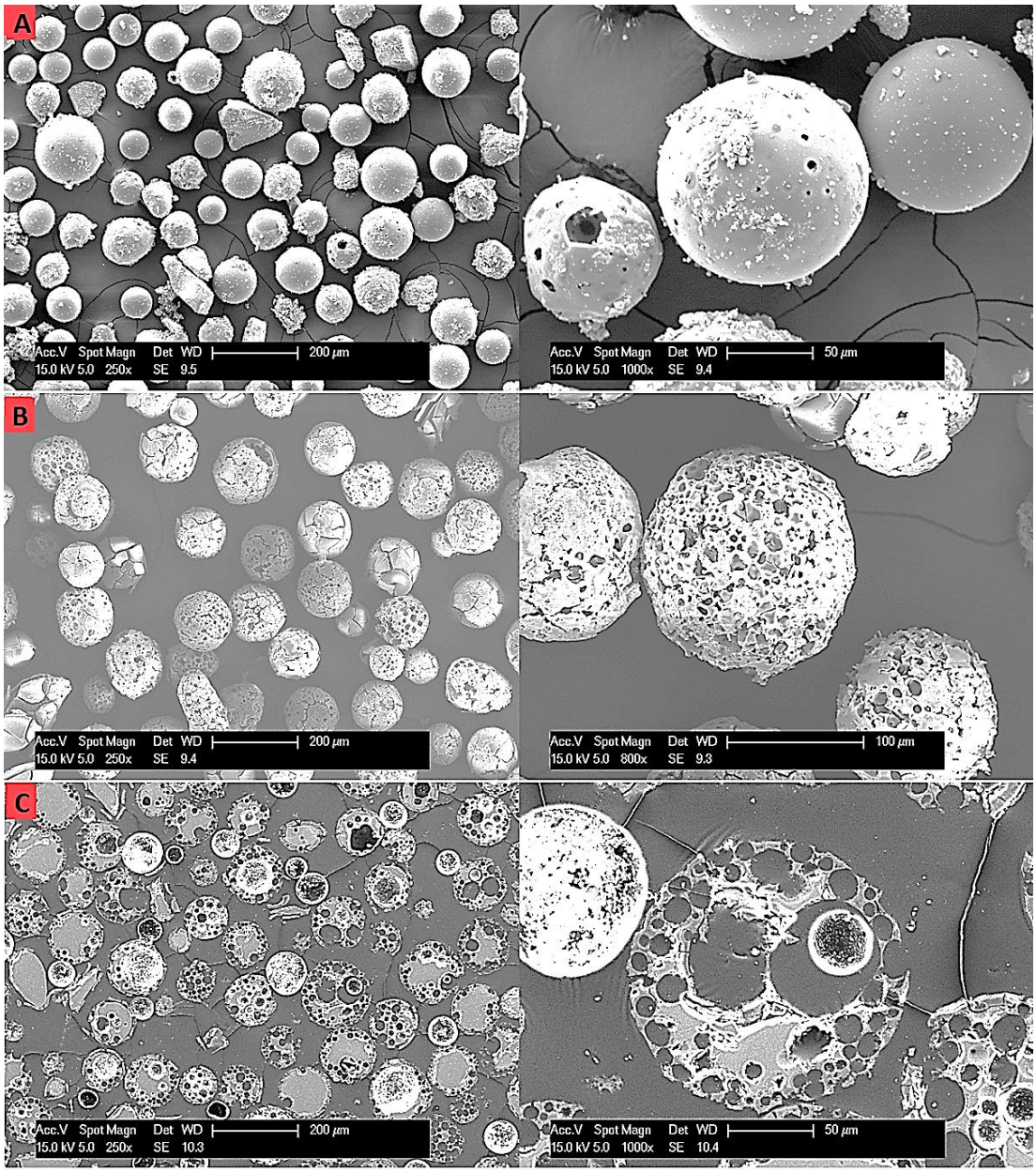


Figure 7.34: *SEM images of A) unwashed B) washed and C) cross-sections of 45S5 +* ***2 mol % borax*** *microspheres.*

Figures 7.35 A-C show the SEM images of unwashed, washed (with 0.5 M acetic acid for 1 min) and cross-sections for **5 mol % borax** content 45S5 microspheres. It was again observed that pores were present but were not fully opened for unwashed microspheres (see **Figure 7.35 A**). However, after washing the microspheres with 0.5 M acetic acid for 1 min, some of pores opened and the microspheres exhibited rough surface textures. Some microspheres had only surface pore with large solid core,

some had large cavities inside and some of the microspheres were fully porous as can be seen from the cross-sections of microspheres (see **Figure 7.35 C**).

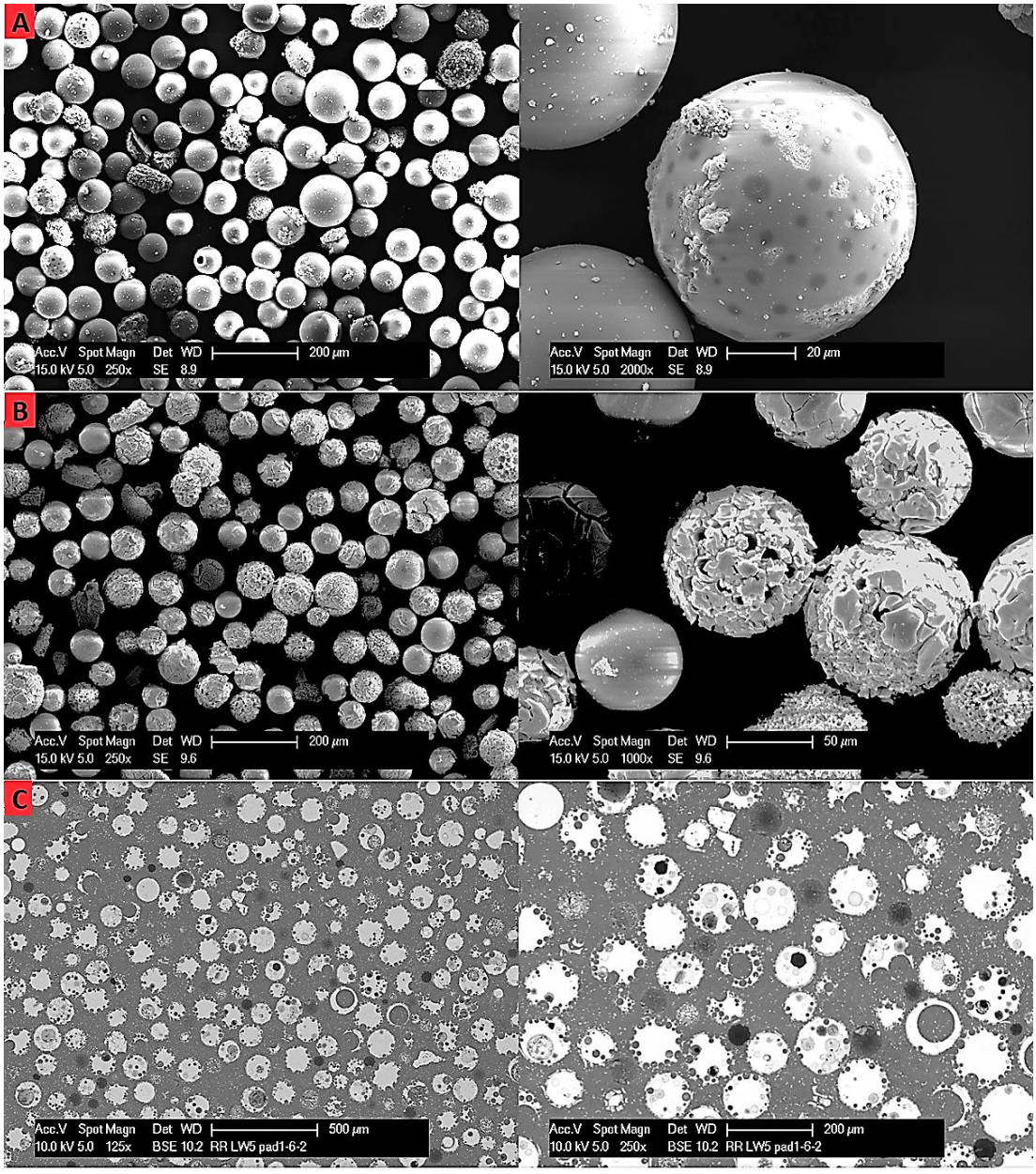


Figure 7.35: *SEM images of A) unwashed B) washed and C) cross-sections of 45S5 +* ***5 mol % Borax*** *microspheres.*

7.2.11.5.2 Trials for V_2O_5 content 45S5 glass

Figures 7.36 A-C show the SEM images of unwashed, washed (with 0.5 M acetic acid for 1 min) and cross-sections of **2 mol % V_2O_5** content 45S5 microspheres. It can be seen that pores were also not opened for unwashed microspheres (see **Figure 7.36**

A). However, porous microspheres with large pores were found after washing the microspheres with 0.5 M acetic acid for 1 min (see **Figure 7.36 B**). Larger pores were also observed for **2 mol% V_2O_5** containing 45S5 compared to 2/5 mol% borax containing 45S5. 70-80 % microspheres were fully porous and rest of them exhibited only surface pores with large solid core as can be seen from the cross-sections of microspheres (see **Figure 7.36 C**).

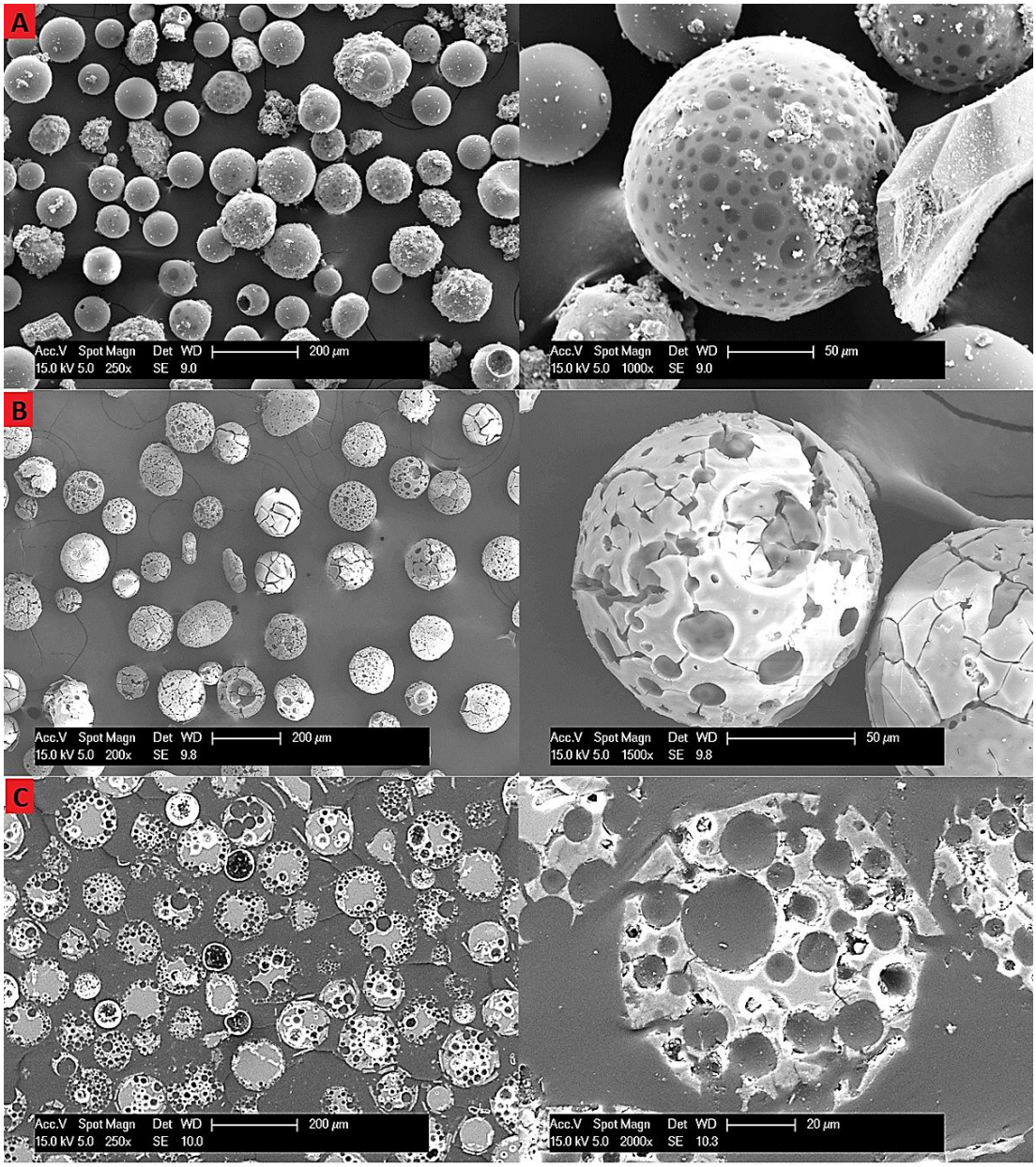


Figure 7.36: *SEM images of A) unwashed B) washed and C) cross-sections of 45S5 +* ***2 mol % V_2O_5*** *microspheres.*

Figures 7.37 A-C show the SEM images for unwashed, washed (with 0.5 M acetic acid for 1 min) and cross-sections of the **5 mol % V_2O_5** content 45S5 microspheres. It can be seen that pores were again not opened fully for some unwashed microspheres (see **Figure 7.37 A**) and relatively thin layer (or skin) of glass over the pores had formed for **5 mol % V_2O_5** compared to 5 mol % borax containing 45S5 microspheres. Highly porous microspheres were also observed after washing the microspheres with 0.5 M acetic acid for 1 min (see **Figure 7.37 B**). Moreover, fully porous microspheres formed as can be seen from the cross-sections of microspheres (see **Figure 7.37 C**).

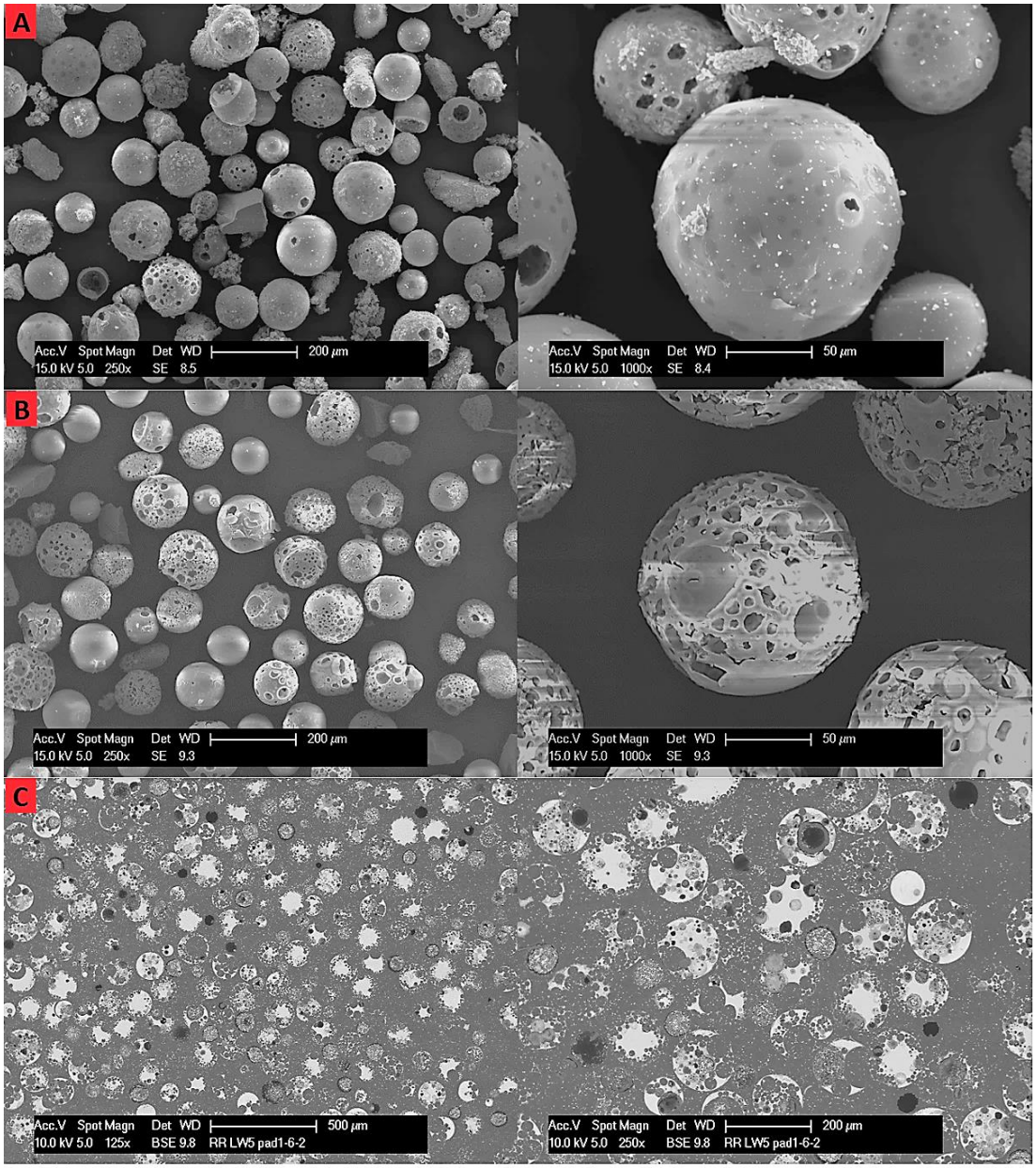


Figure 7.37: *SEM images of A) unwashed B) washed and C) cross-sections of 45S5 +* ***5 mol % V_2O_5*** *microspheres.*

7.2.11.5.3 Trials for 45S5 glass alone

Figures 7.38 A-C show the SEM images of unwashed, washed (with 0.5 M acetic acid for 1 min) and cross-sections of 45S5 microspheres alone. It can be seen that the pores were not open for unwashed microspheres (see **Figure 7.38 A**). However, after washing the microspheres with 0.5 M acetic acid for 1 min, a few porous microspheres with small pores were observed (see **Figure 7.38 B**). Some microspheres were solid (represented as red circle) and some microspheres only exhibited surface pores with a large solid core (represented as amber circle), whilst some had a large cavity inside the microspheres (represented as yellow circle) and only a few microspheres were fully porous which were relatively smaller size (represented as green circle) as can be seen from the cross-sections of microspheres (see **Figure 7.38 C**).

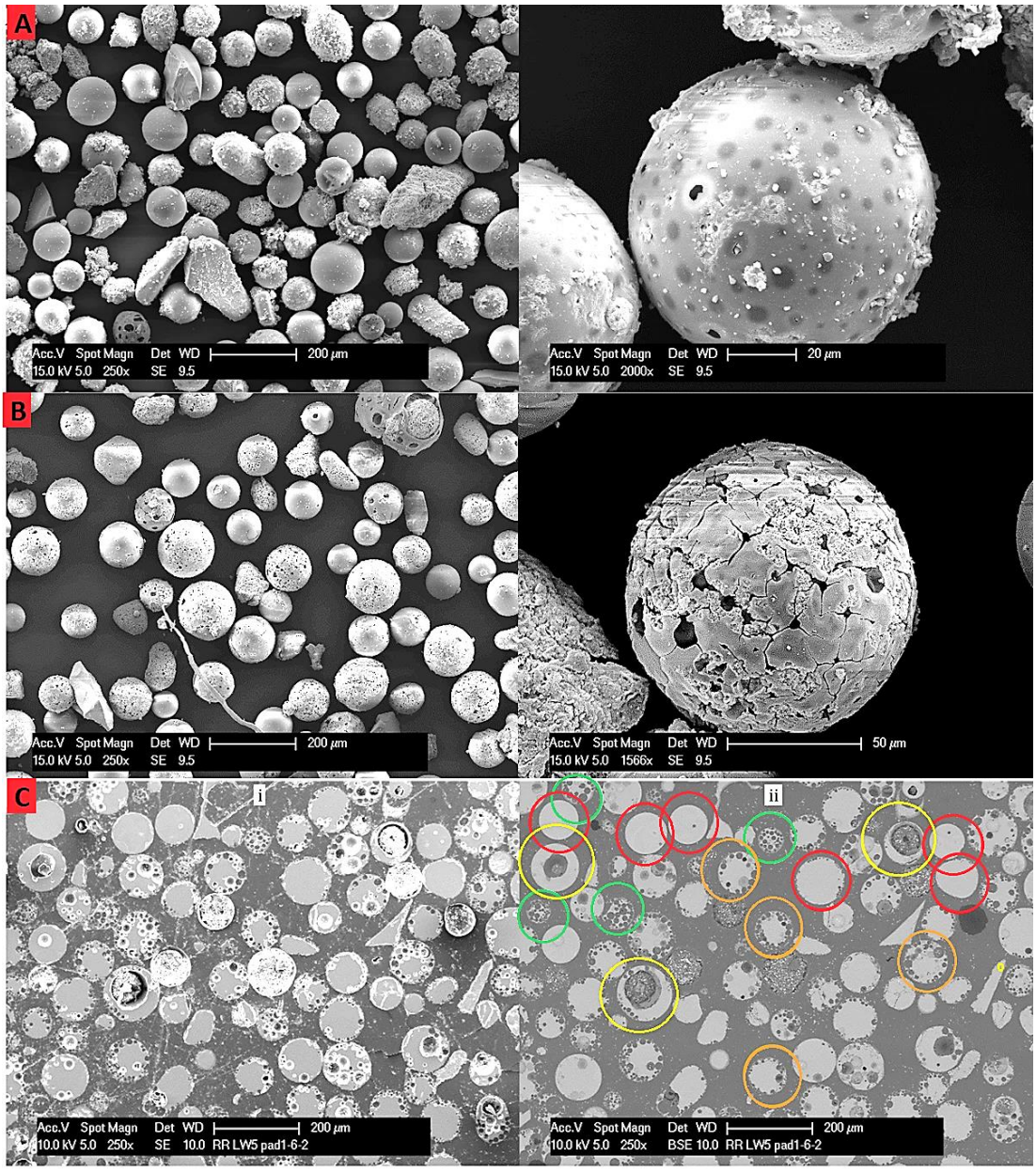


Figure 7.38: *SEM images of A) unwashed B) washed and C) cross-sections of 45S5 microspheres using 3:3 gas flow rate ratio for 63-125 µm starting glass particles.*

7.2.11.5.4 Further trials for 45S5 glass alone

Further trials for 45S5 glass alone were conducted using smaller starting particle size range (i.e. 63-71 µm) and with varying gas flow rate ratios (i.e. 3.5:3.5, 4:4, 4.5:4.5) to increase their cooling rate. The new parameters were chosen based on the output observed in the cross-sections for the previous trials of 45S5 alone, where the relatively smaller particles formed fully porous microspheres. **Figures 7.39 A-B** show the SEM images of washed (with 0.5 M acetic acid for 1 min) and cross-sections of

45S5 microspheres using 3:3 gas flow rate ratio and smaller starting glass particle size ranges of 63-71 µm rather than the larger variation 63-125 µm. Highly porous microspheres with large pores were formed as can be seen from **Figure 7.39 A**. Moreover, more than 95 % microspheres were fully porous as can be seen from the cross-sections of 45S5 microspheres (see **Figure 7.39 B**).

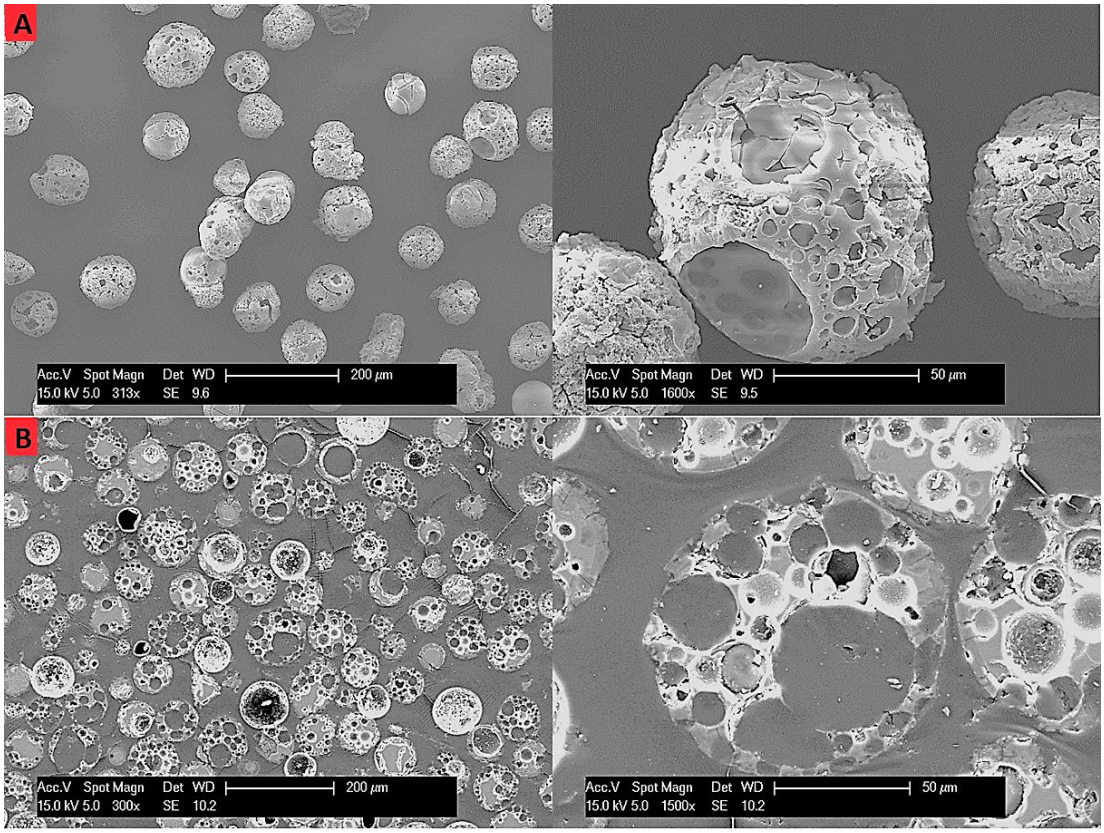


Figure 7.39: *SEM images of A) washed and B) cross-sections of porous 45S5 microspheres using 3:3 gas flow rate ratio for 63-71 µm starting glass particles.*

Figures 7.40 A-C show the SEM images for washed 45S5 microspheres for 3.5:3.5, 4:4 and 4.5:4.5 gas flow rate ratio for 63-125 µm starting glass particles, respectively. Highly porous microspheres were also observed for all of three gas flow rate ratios as can be seen from **Figure 7.40**.

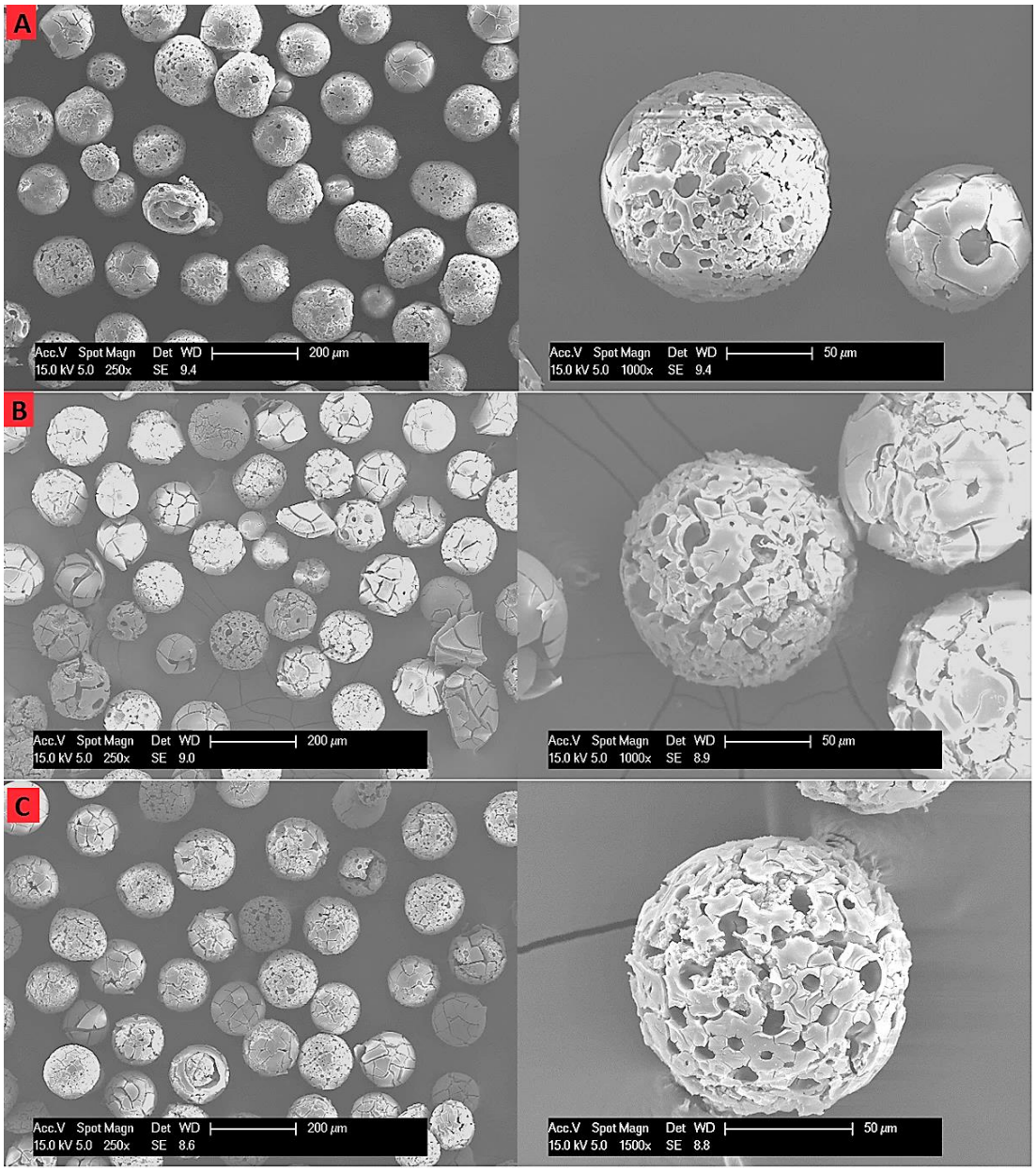


Figure 7.40: *SEM images for porous 45S5 microspheres (washed) using A) 3.5:3.5, B) 4:4 and C) 4.5:4.5 gas flow rate ratio for 63-125 µm starting glass particles.*

Figures 7.41 A-C show the cross-sections for washed porous 45S5 microspheres using 3.5:3.5, 4:4 and 4.5:4.5 gas flow rate ratio for 63-125 µm starting glass particles, respectively. The yield of fully porous microspheres was found to be more than 90 % as can be seen from the cross-sections of 45S5 microspheres (see **Figure 7.41 A-C**).

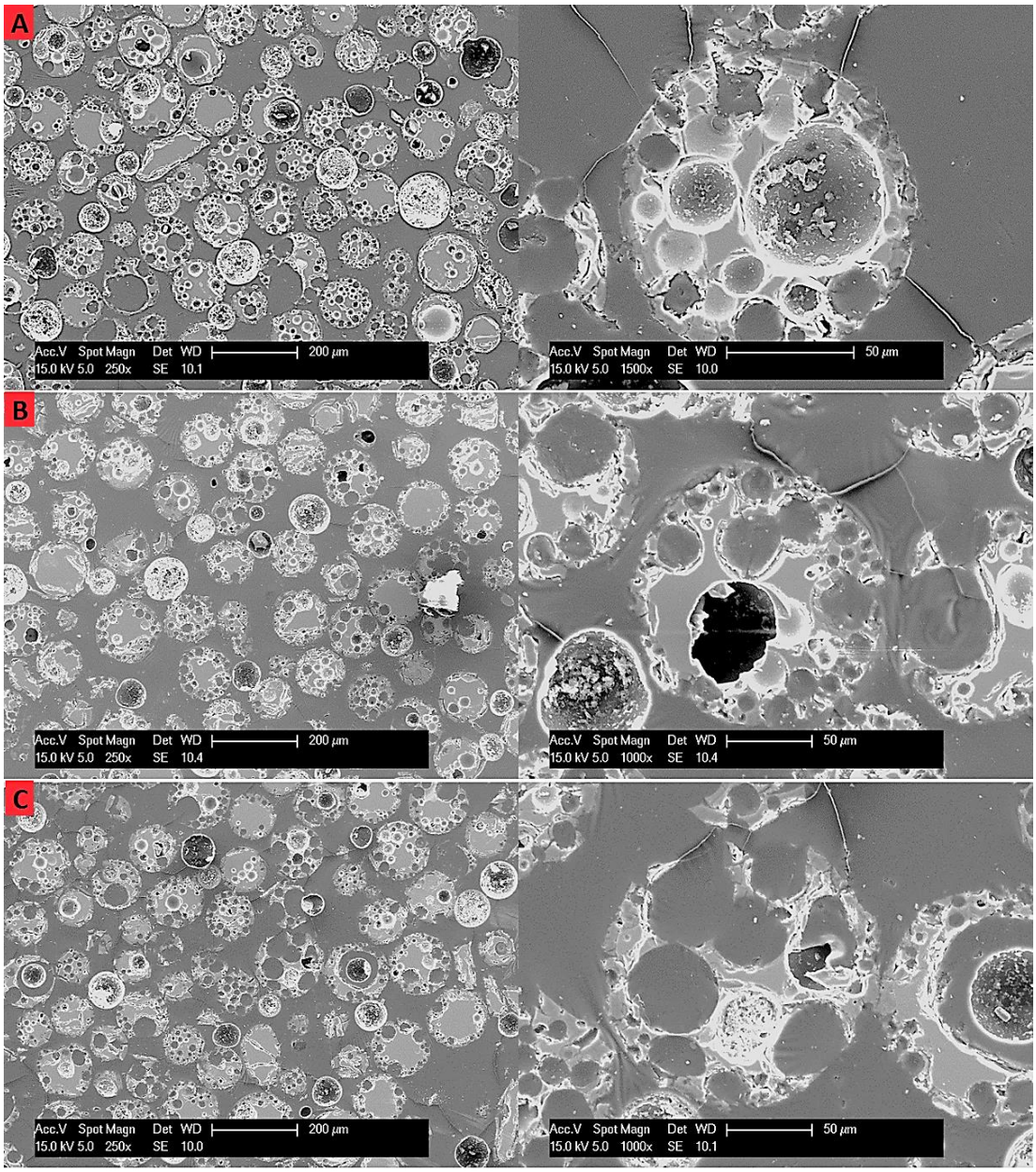


Figure 7.41: *Cross-sections for 45S5 PGMS using A) 3.5:3.5, B) 4:4 and C) 4.5:4.5 gas flow rate ratio for 63-125 µm starting glass particles.*

7.2.11.5.4.1 XRD of porous 45S5 glass microsphere

XRD profiles for porous 45S5 glass microspheres for different starting particle size (i.e. 63-71 µm and 63-125 µm) and different gas flow rate ratios (i.e. 3:3, 3.5:3.5, 4:4 and 4.5:4.5) are presented in **Figure 7.42**, where two broad peaks between 20^{o} and 40^{o} (2θ) was observed for all of the 45S5 PGMS. The absence of any sharp crystalline peaks for PGMS confirmed the amorphous nature of the glass microspheres.

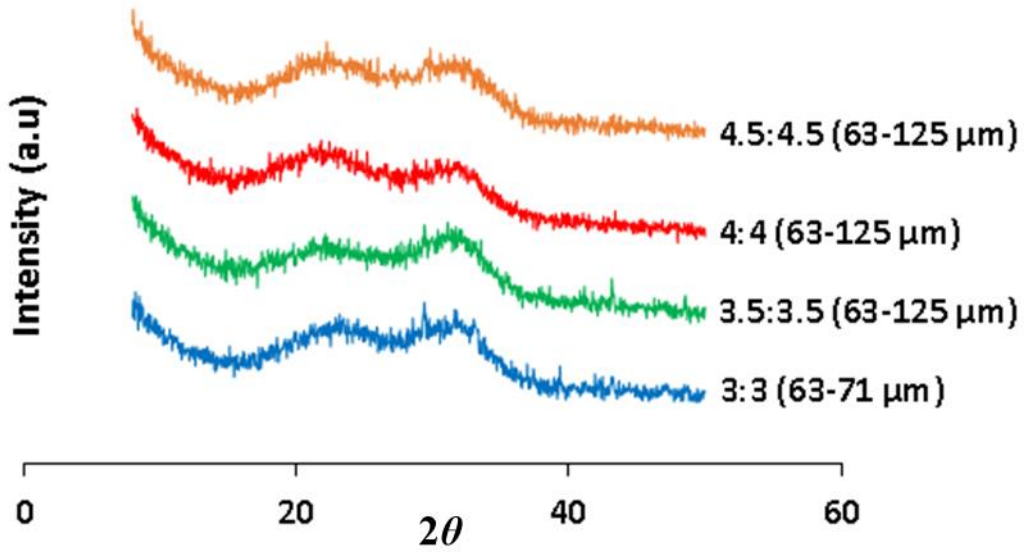


Figure 7.42: *X-ray diffraction pattern for porous 45S5 glass microspheres for different starting particle size (i.e. 63-71 µm and 63-125 µm) and different gas flow rate ratios (i.e. 3:3, 3.5:3.5, 4:4 and 4.5:4.5).*

7.2.11.5.4.2 Compositional analysis of porous 45S5 glass microsphere

Chemical compositions (mol %) for starting bulk glass (BG) and PGMS for different starting particle size (i.e. 63-71 µm and 63-125 µm) and different gas flow rate ratios (i.e. 3:3, 3.5:3.5, 4:4 and 4.5:4.5) obtained via EDX analysis and are presented in **Table 7.9**, where it can be seen that no significant variation of chemical composition between starting BG and PGMS were observed.

Table 7.9: *Chemical compositions for starting 45S5 bulk glass and 45S5 PGMS for different starting particle size (i.e. 63-71 µm and 63-125 µm) and different gas flow rate ratios (i.e. 3:3, 3.5:3.5, 4:4 and 4.5:4.5) obtained via EDX analysis.*

Formulations	SiO_2 (mol %)	P_2O_5 (mol %)	CaO (mol %)	Na_2O (mol %)
45S5-Starting bulk glass	47.5 ± 0.2	3.1 ± 0.1	26.5 ± 0.7	23.0 ± 0.2
45S5-PGMS (starting particles: 63-71 µm, gas flow rate ratio-3:3)	47.7 ± 1.5	2.6 ± 0.1	28.3 ± 0.6	21.4 ± 1.6
45S5-PGMS (starting particles: 63-125 µm, gas flow rate ratio-3.5:3.5)	46.6 ± 1.3	2.7 ± 0.2	28.9 ± 1.9	21.8 ± 0.8
45S5-PGMS (starting particles: 63-125 µm, gas flow rate ratio-4:4)	46.6 ± 1.3	2.7 ± 0.2	27.4 ± 0.4	23.3 ± 0.6
45S5-PGMS (starting particles: 63-125 µm, gas flow rate ratio-4.5:4.5)	46.8 ± 0.5	2.6 ± 0.1	27.7 ± 0.8	22.9 ± 0.5

7.3 Discussion

The objectives of this Chapter were to demonstrate the successful production of both SGMS and PGMS of three different bio-silicate glasses such as 45S5, S53P4 and 1393 via flame spheroidisation process and to examine the comparative differences between the SGMS and PGMS from each of these glasses on their processability, thermal, degradation and *in vitro* bioactivity.

The results revealed that successful manufacture of solid glass microspheres (SGMS) from the bio-silicate glasses was easily achieved. However, initial attempts to make porous bio-silicate glass microspheres using our 'Conventional method', following the same parameters such as glass particle to porogen ratio (1:3), gas flow rate ratio (2.5:2.5), used for making porous phosphate and borate glass microspheres had failed. The unsuccessful formation of porous bio-silicate glass microspheres was initially thought to be due to the large difference between glass melt temperatures (i.e. between 1200-1250 °C) and mis-match with the decomposition temperature of the $CaCO_3$ porogen (~800 °C). The hypothesis here was that if the porogen decomposed earlier than the glass particles had time to melt, then this could have caused the lack of pore formation. Therefore, $CaCO_3$ porogen was replaced with $SrCO_3$, which a much close decomposition temperature (1100-1200 °C) to the melt profiles of the biosilicate glasses. However, no satisfactory results (in terms of porous features, quantity of porous microspheres, sphericity etc) were again observed. This then led to considering the higher melt temperatures of these glasses alongside their viscosity profiles and comparing them to the phosphate and/or borate glasses, which easily formed highly porous microspheres via our conventional method [265]. Taking into consideration the higher melt temperature and viscosity profiles, an alternative granular method for processing bio-silicate glasses was developed where porogen/binary PBG glass mixtures were made into 3D globules by preparing granulars and mixing porogen/binary PBG with the biosilicate glass particles prior to spheroidisation. The binary (P50 Na50) glass had been utilised for granular Method 1, as this is a very fast resorbing glass (i.e. can degrade in minutes/hours), which could then be leached out in the presence of water. However, Method 1 was not used further as the surface pores of the microspheres were very small (which would not

be useful for biological cell incorporation [265]). On the other hand, the glass particles had fused together and formed porous microspheres by decomposition of the porogen (formation of CO_2 gas) inside the granulars during flame shperoidisation via Method 2. Highly porous microspheres (with 70-80 % porosity, see **Table 7.3**) with interconnected pores (see cross-sections, **Figure 7.13**) were formed via granular Method 2.

The SGMS of all three bio-silicate glasses remained fully amorphous, whereas PGMS of each composition crystallised partially as four small sharp peaks were observed from XRD analysis which correlated with the peaks of nagelschmidtite ($7CaO\text{-}P_2O_5\text{-}2SiO_2$) [JCPSD 00-005-0646(D)]. This crystallisation of porous bio-silicate glass microspheres was suggested to be due to the chemical reaction and interaction between $CaCO_3$ and bio-silicate glass during the grinding and subsequent spheroidisation process.

No significant variation in composition between SGMS and BG was observed as expected (see **Table 7.1**). However, the addition of porogen to produce PGMS, increased the Ca content significantly (~10 mol %) which consequently decreased Si and other components.

BG and SGMS of the same glass compositions also showed similar thermal properties for similar size range of glass particles and microspheres. On the other hand, the thermal properties especially T_x and T_c for PGMS of each composition shifted to lower temperatures in comparison to their respective BG or SGMS. This was attributed to the same reason of higher surface area: volume ratio [218] that was mentioned in previous Chapter 5. Similar findings were also found for PGMS of phosphate and borate glasses also as mentioned in the previous Chapters 5 and 6.

The PGMS revealed 2-3 times higher porosity (70-80 %) as compared to SGMS (25-30 %) (See **Table 7.3**). It was also noted that the theoretically calculated porosity (%) for PGMS of phosphate-based glasses and borate glasses were found to be quite similar values to the experimental data obtained via mercury porosimetry mentioned in the previous Chapters 5 and 6. These results were attributed to the contribution of inter-particulate gaps for the measurement of the overall porosity for both the SGMS and

PGMS. The introduction of porosity also caused an increase in degradation rate for the PGMS in comparison to SGMS, which was also suggested to be due to the increase in surface area for PGMS [265].

The higher mass loss (%) of PGMS correlated well with the rapid increase of pH of Milli-Q water for PGMS compared to SGMS at earlier time points. The rapid change of pH was attributed to rapid ion exchange reactions between the glass network modifiers (Na^+ and Ca^{2+}) and H^+ (or H_3O^+) ions from the solution, leading to hydrolysis of the silica groups and created silanol (Si–OH) groups on the glass surface: e.g.

$Si\text{-}O\text{-}Na^+ + H^+ \rightarrow Si\text{-}OH^+ + Na^+$ (aq)…….**Equation 7.1**

Therefore, the pH of the solution increased due to the consumption of H^+ ions [37].

Both SGMS and PGMS of all of the bio-silicate glasses showed bioactivity in SBF as confirmed via XRD (see **Figure 7.18**), SEM images (see **Figure 7.19** and **Figure 7.20**) and compositional analysis via EDX (see **Table 7.4**). However, the PGMS showed higher bioactivity (in terms of HA peak intensity) compared to SGMS which was again suggested to be due to the higher surface area for PGMS. Therefore, HA formation and degradation rate for PGMS had not been inhibited by the crystallisation observed for the PGMS of bio-silicate glasses. A slightly higher pH for SBF solution from 7.4 to 8 was observed for both SGMS and PGMS by day-7 which then gradually decreased to initial pH (~7.4) with increasing immersion time (see **Figure 7.21**). This was also attributed to the same reason for the consumption of H^+ ions from SBF solution as mentioned above for the pH change of Milli-Q water [37]. MgO had been found via EDX for all of the glass compositions (both SGMS and PGMS) after 14 days of immersion in SBF. The presence of MgO for without MgO containing glasses such as 45S5 and S53P4 was suggested to be due to the absorption of Mg^{2+} from SBF. Due to the presence of MgO (3-5 mol %) and trace amount of Na_2O (1-2 mol %), non-stoichiometric HA with Ca/P atomic ratio ~1.4 for SGMS and ~1.5 for PGMS formed after 14 days of immersion in SBF. Reports in the literature state that calcium deficient HA (Ca/P atomic ratio <1.67) was found in natural bone, where Ca deficiency was compensated by other elements such as sodium, magnesium, carbon,

etc [340]. Therefore, PGMS of bio-silicate glasses prepared via granular Method 2 could potentially be more useful compared to SGMS for biomedical application especially for bone regeneration.

However, PGMS microsphere obtained via granular Method 2 were not fully spherical. The characterisation (i.e. thermal, degradation and *in vitro* bio activity study) of these PGMS had been conducted without optimisation of sphericity due to the limited time frame for PhD. Spehericity for the PGMS had been increased later by reducing the starting granular particle size range, however the pore size and no. of pores on the surface of microspheres also decreased (see **Figure 7.22 A**) although the internal morphology remained highly porous (See **Figure 7.22 B**).

Therefore, further optimisation of our 'Conventional method' was considered and trialled to increase the sphericity and porosity and to reduce the crystallisation tendency and minimise compositional error as well as to reduce the processing steps (i.e. grinding and granular preparation) for production of PGMS of bio-silicate glass. As bio-silicate glass showed higher viscosity profiles and melt temperature (especially compared to phosphates and borates), 2 and 5 mol % viscosity modifiers (borax, V_2O_5) was added to 45S5 glass.

The melting (T_m) temperatures for 45S5 glass decreased by approximately 200 ^oC with the addition of 5 mol % borax or V_2O_5 in place of Na_2O in 45S5 (see **Table 7.6**). This was attributed to the lower melting temperature for borax (450-510 ^oC) and V_2O_5 (690 ^oC) compared to Na_2O (1132 ^oC). Wang *et.al.* studied the effect of B_2O_3 on melting temperature, viscosity and desulfurization capacity of CaO–based refining flux and reported that the low melting temperature of B_2O_3 (~450 °C), was favourable for decreasing the melting temperature of high melting temperature components such as CaO and Al_2O_3 [348]. Moreover, they reported that the viscosity for (CaO)(60%)–(Al_2O_3)(20%)–MgO(8%)–SiO_2(8%) systems decreased significantly with addition of 4 mass% B_2O_3 compared to the equal mass % of CaF_2 [348].

Viscosity is probably the most important property in glass making and depends on the chemical glass composition as well as temperature. It strongly influences the melting conditions in glass furnaces, which are correlated with the furnace energy consumption. The viscosity must be tightly controlled during glass forming processes

to maintain a high product quality. The temperatures throughout the glass cooling schedule are also dictated by the viscosity. Viscosity for the glasses was measured indirectly via Hot Stage Microscopy (HSM) and then directly via rotating cylinder (High temperature viscometer, HTV) method. The viscosity fitting curves for the six glass formulations were investigated using VFT equation (see **Figure 7.28** and **Figure 7.30**). The viscosity profiles for these glasses followed similar trends for both methods (HSM, HTV) where, viscosity curves shifted to lower temperature with the addition of viscosity modifiers (i.e. borax, V_2O_5) in 45S5 glass. This was attributed to higher oxidation state of B (+3) and V (+5, +4, +3, +2) which generally reduce the viscosity compared to oxidation state Na (+) [349]. The viscosity curve for P40 glass had the lowest temperature compared with 45S5 and the borax or V_2O_5 containing 45S5 glasses (see **Figure 7.28** and **Figure 7.30**).

The phosphate P40 glass formed very good quality porous microspheres (see Chapter 5, **Figure 5.1 B**) whereas, 45S5 didn't form (see **Figure 7.2 A**) via our 'Conventional method' utilising similar processing parameters. However, after addition of viscosity modifiers, both borax and V_2O_5 containing 45S5 glass formed porous microspheres though slightly higher gas flow rate ratio of 3:3 had been used instead of 2.5:2.5. However, the 5 mol % V_2O_5 containing 45S5 glass formed highly porous microspheres (see cross-section, **Figure 7.35** and **Figure 7.37**) compared with 5 mol % borax containing 45S5 glass, which was not expected as the borax formulation had significantly lower viscosity compared with the V_2O_5 formulation and both had very similar melt temperatures.

These results were then correlated with the HTM profiles to explore the temperature differences between flow and hemisphere/sphere point (see **Figure 7.26**), which was also related to viscosity change relative to temperature. Here a smaller gap in between flow and hemisphere/sphere point was found for the 5 mol% V_2O_5 containing 45S5 in comparison to 5 mol % borax containing 45S5. Moreover, the viscosity change relative to temperature between flow and sphere or hemisphere point also occurred rapidly for P40 compared to 45S5 glass (see from **Figure 7.26**). These results also supported the calculated rate of viscosity change between flow and hemisphere/sphere point from viscosity fitting curves obtained via HSM and HTM.

Therefore, in our process it appears that viscosity was not only the important factor to make desirable porous microspheres.

It had also been observed that the flame length decreased with increasing gas flow rate ratio which would also influence particle residence time in the flame as well as cooling rate of microspheres. According to reports in the literature, temperature for oxy-acetylene flame can range between 3100-3300 °C and the flame temperature would be same theoretically for each gas flow rate ratio [350,351]. However, the experimental flame temperature may vary with the variation of gas flow rate ratio, and the flame temperature at these ratios was not measured due to unavailability of appropriate thermal analysis camera (and therefore the flame temperature was not considered into the processing model).

A processing model was assembled taking into consideration all of the factors which could influence the porous microsphere manufacturing process and is presented in **Figure 7.43** below.

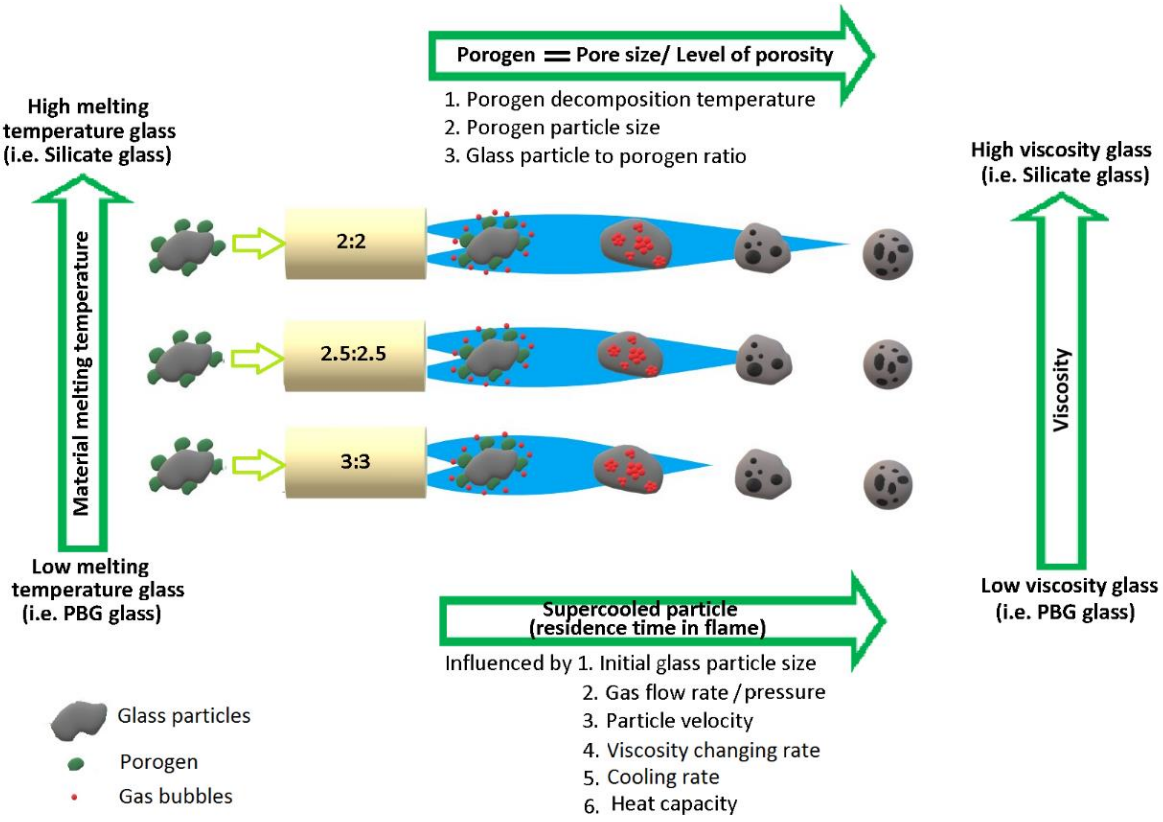


Figure 7.43: *Schematic diagram of proposed model including all of the parameters influencing to prepare porous bio-silicate microspheres.*

Although the processing time required for making porous microspheres from glass particles is less than 1 second (i.e. in milliseconds), a lot of parameters are involved to achieve the desired outcome of porous microspheres. All the influential parameters considered have been listed in **Table 7.10** (below) and the most important factors identified. Some parameters were instrument/experiment related (i.e. initial glass particle size, gas flow rate ratio) and could possibly be kept constant whilst other parameters were materials related (i.e. melt temperature, viscosity) and therefore were not constant.

Table 7.10: *Parameters involved to prepare porous bio-silicate glass microspheres.*

Parameters	Values	Constant/variable	Highly influential (√/×)	Comments
Initial glass particle size	63-125 µm	Constant	×	Not spherical >300 µm (Oxyacetylene flame) May vary with different flame torch
Feeder position	-	Constant	×	Particle residence time in the flame influenced by feeder position
Height of feeder from flame	-	Constant	×	Particle residence time in the flame influenced by height of feeder from flame
Gas flow rate ratio	3:3	Constant	×	Flame length varied with changing the gas flow rate ratio (Flame length decreased with increasing gas flow rate ratio)
Particle velocity	-	Constant	×	Particle velocity increases with increasing gas pressure (gas flow rates). Velocity also depends on glass particle size
Particle residence time	-	Constant	×	As glass particle size, gas flow rate ratio and particle velocity were constant, therefore, particle residence time in the flame assumed to be constant

Heat capacity	63-125 µm	Varies with mass of glass particles/size of particles	×	Large particle (i.e. 125 µm) should have higher heat capacity compared to small particle (i.e. 63 µm) of same material. As a fixed size range of particles were used, therfore, the heat capacity for the size range of 63-125 µm assumed to be constant.
Cooling rate of molten glass	63-125 µm/3:3	Constant	×	Depends on starting glass particle size, gas flow rate ratio and heat capacity
Glass particle to Porogen ratio	1:3	Constant	×	Level of porosity could be achieved by changing glass particles to porogen ratio.
Melting Temp. of glass		Varies with glass compositions	×	Glass with low melting temp. would be better for processing. However, this was not only the important factor. (i.e. 45S5 + 5 mol% Borax Vs 45S5 + 5 mol% V_2O_5)
Viscosity of glass		Varies with glass compositions	×	Glass with low viscosity would be better for processing. However, this was also not only important factor. (i.e. 45S5 + 5 mol % Borax Vs 45S5 + 5 mol % V_2O_5)
Viscosity at melting temp. (melt viscosity)		Constant (HSM)/Varies (HTV)	×	It was really difficult to select the value of viscosity when two or three melting temperatures were observed via DSC. (i.e. 45S5 + 5 mol% V_2O_5)
The rate of viscosity change (slope of viscosity curve)		Varies with glass compositions	√	Higher rate of viscosity changes would be favourable to retain the entrapped gas bubbles within the molten glass (i.e. P40 Vs 45S5)

The rate of viscosity change could be increased with increasing cooling rate as a result of increasing gas flow rate ratio and this result reflected on the trial for borax containg

45S5 and 45S5 glass alone using 3:3 gas flow rate ratio instead of 2.5:2.5 as was used for initial trial. Semi porous 45S5 microspheres had formed for 3:3 gas flow rate ratio, where some microspheres were solid (represented as red circles) and others only exhibited surface pores with a large solid core (represented as amber circle), whilst some had a large cavity inside the microspheres (represented as yellow circle) and only a few microspheres were fully porous (represented as green circle) (see cross-sections, **Figure 7.38 C**). For the microspheres with large cavity inside, two possibilities may be responsible; 1) Smaller gas bubbles may have coalesced together to form larger gas bubbles inside the microspheres, or 2) Larger porogen or large quantity of porogen had become entrapped inside the molten glass during spheroidisation and therefore formed larger voids within the microspheres. For the microspheres having surface pores with a large solid core, there might also be two possibilities; 1) Glass particles had not attained full melting condition and therefore, the porogen had penetrated only the surface of microsphere as 45S5 glass had higher melting temperature and viscosity. However this possibility had not been considered as 5 mol% V_2O_5 containing 45S5 formed better porous microspheres even though this glass had quite similar melting temperature and higher viscosity compared to 5 mol % borax containing 45S5 mentioned above (see **Table 7.6** and **Figure 7.28** and **Figure 7.30**). Or 2) Gas bubbles produced within the molten glass may have moved towards the surface as the rate of viscosity change for 45S5 or 5 mol % borax containing 45S5 glass was comparatively lower compared to P40 or 5 mol% V_2O_5 containing 45S5 (see **Table 7.7** and **Table 7.8**) and consequently, the bubbles had more time to move towards the surface. On the other hand, a few microspheres which had formed into fully porous microspheres were relatively smaller in size as compared to the others. Therefore, highly porous microspheres of 45S5 glass alone had successfully been achieved by choosing both smaller staring particle size ranges (as confirmed via SEM – see **Figure 7.39**) and increasing the gas flow rate ratio thereby increasing cooling rate for this rapid changing viscosity profile glass (see **Figure 7.40**). Moreover, the crystallisation and compositional change of PGMS had been minimised using the initial conventional method (confirmed via XRD and EDX, see **Figure 7.42** and **Table 7.9**). Therefore, the porous microspheres prepared via conventional method would possess enhanced bioactivity and bio-degradability in comparison to the PGMS

formed via granular Method 2. However, degradation and *in-vitro* bioactivity studies will be required for further confirmation. These porous bio-silicate glass microspheres could be regarded as the next evolution of Bioglass materials for biomedical applications.

7.4 Summary

In this chapter solid and porous glass microspheres (using both developed granular and conventional method) for three bio-silicate glasses, 45S5, S53P4 and 1393, were prepared via flame spheroidisation process.

Porous glass microspheres showed higher mass loss % in comparison to solid glass microspheres having same composition. This was attributed to the higher surface area for PGMS compared to SGMS. For the same reason PGMS showed lower onset crystallisation and crystallisation temperature in comparison to SGMS.

Bio-silicate glass microspheres (both SGMS and PGMS) of all glass compositions showed bioactivity in SBF and PGMS showed higher bioactivity compared to SGMS due to the higher surface area for PGMS. However, the calcium deficient HA (which found in natural bone, non-stoichiometric HA, Ca/P atomic ratio <1.67) formed, where Ca/P atomic ratio was ~1.5, due to the presence of MgO (3-5 mol%) and trace amount of Na_2O (1-3 mol%) in HA.

The viscosity change relative to the temperature (i.e. rate of viscosity change) was an important factor along with the materials melt temperature and viscosity to achieve the desirable porous microsphere structure via conventional method. Higher yield/highly porous bio-silicate microspheres were achieved by increasing rate of viscosity change/increasing cooling rate.

The developed PGMS of bio-silicate glasses could be considered for biomedical applications.

CHAPTER 8

CONCLUSIONS AND FUTURE WORK

8.1 Conclusions

The aim of the studies conducted was to develop novel phosphate-based glass formulations and to investigate manufacture of both solid and porous microspheres from phosphate, borate and bio-silicate based glasses, focussing on bone tissue repair applications.

The following conclusions can be made from the outcomes of this thesis:

- A series of phosphate-based glasses were developed focussing on the replacement of MgO by CaO in the glass system $40P_2O_5$-(24-x)MgO-(16+x)CaO-(20-y)Na_2O-yTiO_2 (in mol%; where $0 \leq x \leq 22$ and y=0 or 1) to enhance their bioactivity (as some literature studies reported that Mg inhibited bioactivity of glasses). It was found that glass formulations below 8 mol% MgO content showed a strong tendency towards crystallisation. Due to the replacement of higher field strength Mg^{2+} by lower field strength Ca^{2+}, the glass transition, onset crystallisation, crystallisation peak, initial melting temperature, density, oxygen density and activation energy of crystallisation, all decreased with decreasing MgO content.
- Addition of 1 mol% TiO_2 was found to be sufficient to suppress the crystallisation of lower MgO containing glasses (below 8 mol% MgO containing glasses) due to the replacement of lower field strength Na^+ by higher field strength Ti^{4+}.
- No significant change in Q^n species for the phosphate bulk glass formulations investigated was observed via NMR analyses. Moreover, titanium was found to be present as titanyl group (TiO_5), which was identified through Raman analysis, indicating that the low level of titanium incorporated acted as a network modifier.
- Replacing higher field strength Mg^{2+} by lower field strength Ca^{2+}, an increase of mass loss and total amount of ions (Na^+, Ca^{2+} and Mg^{2+}, P, Ti) released for

the glasses investigated, was seen to increase from 250 ppm to 363 ppm with decreasing MgO content from 24 to 8 mol%. However, addition of 1 mol% TiO_2 increased the resistance to hydrolysis.

- None of the bulk phosphate glasses formed hydroxyapatite (HA) during the *in vitro* bioactivity study. However, amorphous calcium phosphate (ACP; a precursor to HA) with the Ca/P ratio ranging from 0.79 to 1.07 was found on the surface of these glasses with reduced amounts of MgO (8 mol% and below).

Based on ACP deposition found on bulk phosphate glasses, M8T0 (8 mol% MgO with no TiO_2) and M2T1 (2 mol% MgO with 1 mol% TiO_2) were selected along with M24T0 (P40 glass; 24 mol% MgO with no TiO_2; as a control) to investigate manufacture of solid (SGMS) and porous glass microspheres (PGMS).

- Both SGMS and PGMS of selected PBG's were successfully prepared via the flame spheroidisation process.
- Due to the higher surface area, PGMS showed higher mass loss %, ion release rate and porosity in comparison to SGMS having same composition. However, the opposite trend of mass loss % for PGMS was observed than that of observed for bulk PBG's discs due to the crystallisation of M8T0 and M2T1 PGMS during flame spheroidisation, which consequently forming a more resistant materials to dissolution in comparison to the initial amorphous glass structure.
- SGMS and/or PGMS of all PBG's didn't form HA after 28 days of immersion in SBF. Only ACP which has been suggested to be a precursor phase for the formation of HA, deposited on PGMS of each glass formulations including M24T0 due to the higher degradation and ion release rates for M24T0 PGMS.

Three different types of borate glasses (i.e. 45B5, B53P4 and 1393B), which were derived based on their biosilicate equivalents 45S5, S53P4 and 1393, by replacing the SiO_2 with B_2O_3 were selected for investigation

- Both SGMS and PGMS were successfully prepared from these borate formulations via flame spheroidisation process.

- PGMS of borate glasses showed higher mass loss % and conversion rate to HA and porosity, due to their higher surface in comparison to SGMS.
- After 21 days of immersion in dil. K_2HPO_4 solution, only PGMS of 45B5 and both SGMS and PGMS of B53P4 had fully converted to HA. On the other hand, no conversion for both SGMS and PGMS was found for 1393B even after 28 days of immersion in dil. K_2HPO_4 solution due to the presence of potassium in 1393B, which inhibited the conversion reaction. However, 1393B glass microspheres instead converted into HA in dil. Na_2HPO_4 solution.
- Both SGMS and PGMS of each borate glass formulations showed bioactivity in SBF. Due to the higher surface area for PGMS compared to SGMS, HA formation was found at earlier time point for PGMS. In addition, due to the presence of MgO (2-3 mol%) and trace amount of Na_2O (0.5-0.8 mol%), non-stoichiometric HA (which found in natural bone, Ca/P atomic ratio <1.67) with Ca/P atomic ratio ~1.5 was found for both SGMS and PGMS of each composition after 21 days of immersion in SBF.

Due to the higher melt temperature and viscosity profiles for the bio-silicate glasses compared to phosphate or borates, an alternative granular method was developed for processing bio-silicate glasses where porogen and bio-silicate glass mixtures were made into 3D globules by preparing granulars prior to spheroidisation.

- Both SGMS and PGMS (using both developed granular and conventional method) for bio-silicate glasses (i.e. 45S5, S53P4 and 1393) were successfully prepared via flame spheroidisation process.
- The viscosity change relative to the temperature (i.e. rate of viscosity change) was found to be an important factor along with the materials melt temperature and viscosity to achieve the desirable porous microsphere structure via conventional method. Using the initial conventional method, higher yield/highly porous bio-silicate microspheres were achieved by increasing rate of viscosity change/increasing cooling rate.

- Similarly, higher surface area for PGMS in comparison to SGMS, for the bio-silicate glasses showed higher mass loss % and bioactivity at earlier time point.

8.2 Suggestions for future work

Based on the developments of this work, the following suggestions have been made for future studies:

- Due to the higher release of phosphate ion from P40 glass (which might inhibit HA formation as literature reported that the lower phosphate ion release helped for HA formation), an another series of phosphate glass (i.e. (40-x)P_2O_5-24MgO-(16+x)CaO-20Na_2O in mol%, where x=0-10)with decreasing phosphate content from 40 to 30 mol% can be considered for further studies to improve the bioactivity.
- As literature reported that orthophosphate formed HA and Ti helped for HA formation by the formation of Ti-OH gel and sodium helped for initial glass dissolution and formation of titania gel, therefore another alternative series of phosphate glass (i.e. 30P_2O_5-(24-x)MgO-16CaO-20Na_2O-xTiO_2, in mol%, where x=0-10) with TiO_2 with lower P_2O_5 content (30 mol%) can be considered for further studies to improve the bioactivity. Moreover, phosphate ion release would be decreased significantly by the addition of titanium as titanium makes the glass more stable.
- Phosphate glass microspheres could also be functionalised to improve their bioactivity.
- Biocompatibility and cytocompatibility study for phosphate, borate and bio-silicate glass microspheres prepared can be conducted prior to animal trial.
- B53P4 glass (which had 2.5 mol% higher P_2O_5 content compared to expected value (confirmed via ICP-MS)) showed comparatively higher crystallisation tendency in comparison to 45B5 and 1393B glass composition. Consequently, SGMS and PGMS of B53P4 crystallized and small peaks of sodium calcium phosphate [$Na_3Ca_6(PO_4)_5$] were observed after spheroidisation of glass particles. Therefore, further analysis for accurate composition of B53P4 glass

can be conducted to investigate whether the glass forming ability could be increased and /or crystallisation tendency for this glass composition during flame spheroidisation could be arrested.

- New washing protocol can be explored for porous borate glass microspheres as porogen were not removed completely using water or 0.1 M acetic acid.
- New washing protocol can be explored for porous bio-silicate glass microspheres for the removal of porogen completely without cracking the surface.

- To spheroidise and characterise porous microspheres of glass ceramic (i.e. apatite-wollastonite), very high viscosity glass (i.e. recycle glass), magnetite and TiO_2 using granular method for various applications such as biomedical, water treatment etc. Initial feasibility trials were carried out and SEM images for porous microspheres are shown in **Figure 8.1** as proof of concept.

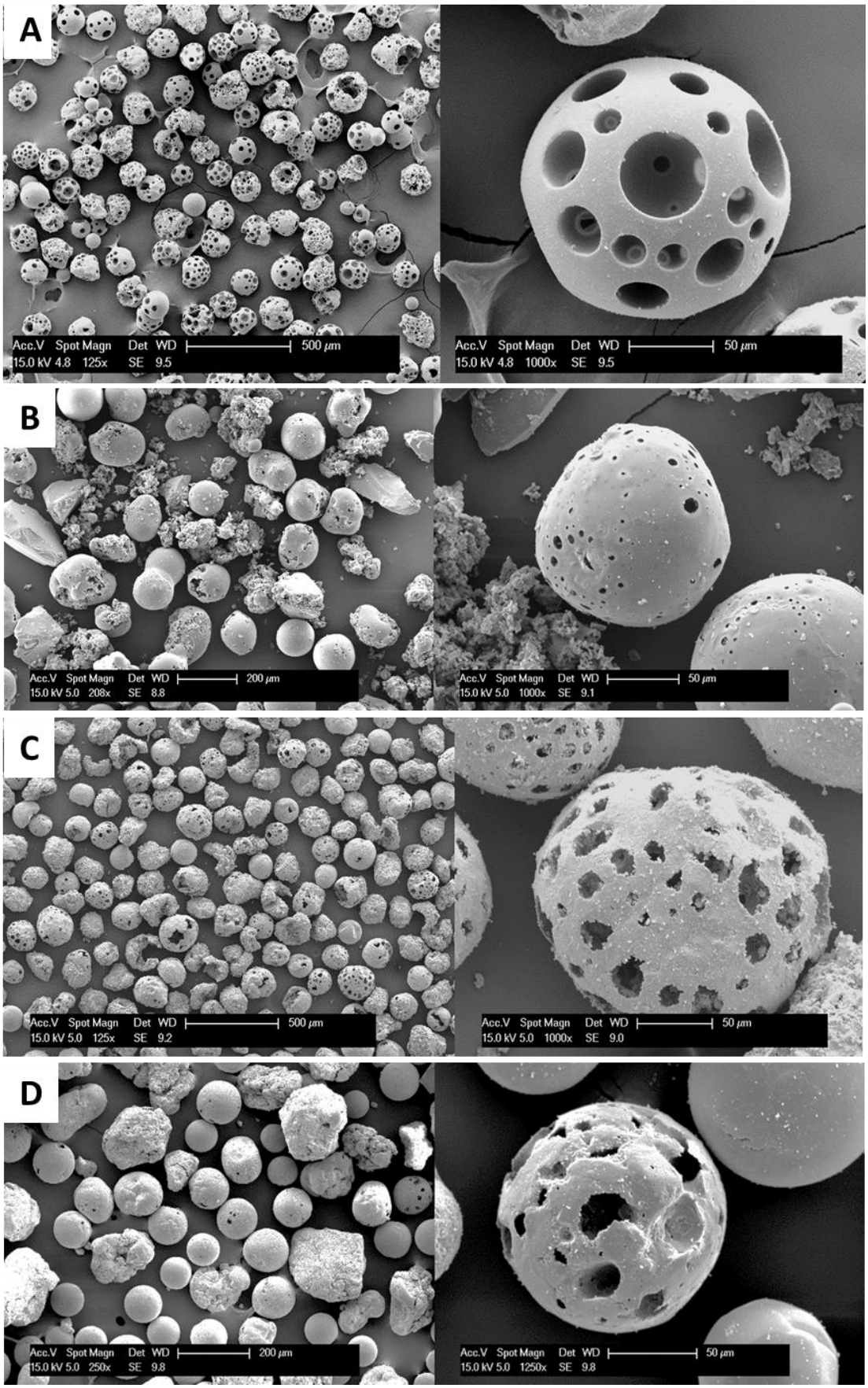


Figure 8.1: *SEM images of porous microspheres trialled with the A) Apatite-Wollastonite (AW), B) Recycle glass, C) Magnetite and D) TiO_2.*

REFERENCES

1. Zhu B, Lu Q, Yin J, Hu J, Wang Z. Alignment of osteoblast-like cells and cell-produced collagen matrix induced by nanogrooves. Tissue engineering 2005;11(5-6):825-34.
2. Riboldi SA, Sadr N, Pigini L, Neuenschwander P, Simonet M, Mognol P, Sampaolesi M, Cossu G, Mantero S. Skeletal myogenesis on highly orientated microfibrous polyesterurethane scaffolds. Journal of Biomedical Materials Research Part A 2008;84A(4):1094-1101.
3. Johnson WE, Wootton A, El Haj A, Eisenstein SM, Curtis AS, Roberts S. Topographical guidance of intervertebral disc cell growth in vitro: towards the development of tissue repair strategies for the anulus fibrosus. European Spine Journal 2006;15(3):389.
4. Her GJ, Wu HC, Chen MH, Chen MY, Chang SC, Wang TW. Control of three-dimensional substrate stiffness to manipulate mesenchymal stem cell fate toward neuronal or glial lineages. Acta Biomaterialia 2013;9(2):5170-5180.
5. Bryant SJ, Nicodemus GD, Villanueva I. Designing 3D Photopolymer Hydrogels to Regulate Biomechanical Cues and Tissue Growth for Cartilage Tissue Engineering. Pharmaceutical Research 2008;25(10):2379-2386.
6. Kokubo T, Takadama H. How useful is SBF in predicting in vivo bone bioactivity? Biomaterials 2006;27(15):2907-2915.
7. Fu Q, Rahaman MN, Bal BS, Kuroki K, Brown RF. In vivo evaluation of 13-93 bioactive glass scaffolds with trabecular and oriented microstructures in a subcutaneous rat implantation model. Journal of Biomedical Materials Research Part A 2010;95A(1):235-244.
8. Rahaman MN, Day DE, Sonny Bal B, Fu Q, Jung SB, Bonewald LF, Tomsia AP. Bioactive glass in tissue engineering. Acta Biomaterialia 2011;7(6):2355-2373.
9. Shah R, Sinanan ACM, Knowles JC, Hunt NP, Lewis MP. Craniofacial muscle engineering using a 3-dimensional phosphate glass fibre construct. Biomaterials 2005;26(13):1497-1505.

10. Moioli EK, Clark PA, Xin X, Lal S, Mao JJ. Matrices and scaffolds for drug delivery in dental, oral and craniofacial tissue engineering. Advanced Drug Delivery Reviews 2007;59(4):308-324.
11. Hench LL, Splinter RJ, Allen W, Greenlee T. Bonding mechanisms at the interface of ceramic prosthetic materials. Journal of biomedical materials research 1971;5(6):117-141.
12. Hench LL, Wilson J. Surface-active biomaterials. Science 1984;226(4675):630-636.
13. Hench LL. Bioceramics: from concept to clinic. Journal of the american ceramic society 1991;74(7):1487-1510.
14. Nakamura T, Yamamuro T, Higashi S, Kokubo T, Itoo S. A new glass-ceramic for bone replacement: Evaluation of its bonding to bone tissue. Journal of biomedical materials research 1985;19(6):685-698.
15. Gross U, Strunz V. The interface of various glasses and glass ceramics with a bony implantation bed. Journal of biomedical materials research 1985;19(3):251-271.
16. Höland W, Vogel W, Naumann K, Gummel J. Interface reactions between machinable bioactive glass-ceramics and bone. Journal of biomedical materials research 1985;19(3):303-312.
17. Kokubo T, Ito S, Sakka S, Yamamuro T. Formation of a high-strength bioactive glass-ceramic in the system MgO-CaO-SiO_2-P_2O_5. Journal of Materials Science 1986;21(2):536-540.
18. Yoshii S, Kakutani Y, Yamamuro T, Nakamura T, Kitsugi T, Oka M, Kokubo T, Takagi M. Strength of bonding between A-W glass-ceramic and the surface of bone cortex. Journal of biomedical materials research 1988;22(S14):327-338.
19. Kitsugi TO, Yamamuro T, Kokubo T. Bonding behavior of a glass-ceramic containing apatite and wollastonite in segmental replacement of the rabbit tibia under load-bearing conditions. The Journal of bone and joint surgery 1989;71(2):264-272.
20. Karlsson KH, Fröberg K, Ringbom T. A structural approach to bone adhering of bioactive glasses. Journal of Non-Crystalline Solids 1989;112(1-3):69-72.

21. Kokubo T, Kushitani H, Sakka S, Kitsugi T, Yamamuro T. Solutions able to reproduce in vivo surface-structure changes in bioactive glass-ceramic A-W3. Journal of biomedical materials research 1990;24(6):721-734.
22. Conzone SD, Brown RF, Day DE, Ehrhardt GJ. In vitro and in vivo dissolution behavior of a dysprosium lithium borate glass designed for the radiation synovectomy treatment of rheumatoid arthritis. Journal of Biomedical Materials Research: An Official Journal of The Society for Biomaterials, The Japanese Society for Biomaterials, and The Australian Society for Biomaterials and the Korean Society for Biomaterials 2002;60(2):260-268.
23. Day D, White J, Brown R, McMenamin K. Transformation of borate glasses into biologically useful materials. Glass Technology 2003;44(2):75-81.
24. Wang Q, Huang W, Wang D, Darvell BW, Day DE, Rahaman MN. Preparation of hollow hydroxyapatite microspheres. Journal of Materials Science: Materials in Medicine 2006;17(7):641-646.
25. Marion NW, Liang W, Liang W, Reilly GC, Day DE, Rahaman MN, Mao JJ. Borate Glass Supports the In Vitro Osteogenic Differentiation of Human Mesenchymal Stem Cells. Mechanics of Advanced Materials and Structures 2005;12(3):239-246.
26. Yang Q, Chen S, Shi H, Xiao H, Ma Y. In vitro study of improved wound-healing effect of bioactive borate-based glass nano-/micro-fibers. Materials Science and Engineering: C 2015;55:105-117.
27. Yao A, Wang D, Huang W, Fu Q, Rahaman MN, Day DE. In vitro bioactive characteristics of borate-based glasses with controllable degradation behavior. Journal of the American Ceramic Society 2007;90(1):303-306.
28. Huang W, Day DE, Kittiratanapiboon K, Rahaman MN. Kinetics and mechanisms of the conversion of silicate (45S5), borate, and borosilicate glasses to hydroxyapatite in dilute phosphate solutions. Journal of Materials Science: Materials in Medicine 2006;17(7):583-596.
29. Fu Q, Rahaman MN, Fu H, Liu X. Silicate, borosilicate, and borate bioactive glass scaffolds with controllable degradation rate for bone tissue engineering applications. I. Preparation and in vitro degradation. Journal of biomedical materials research Part A 2010;95(1):164-171.

30. Abdelghany A, ElBatal H, EzzElDin F. Bone bonding ability behavior of some ternary borate glasses by immersion in sodium phosphate solution. Ceramics International 2012;38(2):1105-1113.
31. Han X, Day DE. Reaction of sodium calcium borate glasses to form hydroxyapatite. Journal of Materials Science: Materials in Medicine 2007;18(9):1837-1847.
32. Modglin VC, Brown RF, Jung SB, Day DE. Cytotoxicity assessment of modified bioactive glasses with MLO-A5 osteogenic cells in vitro. Journal of Materials Science: Materials in Medicine 2013;24(5):1191-1199.
33. Wang H, Zhao S, Zhou J, Shen Y, Huang W, Zhang C, Rahaman MN, Wang D. Evaluation of borate bioactive glass scaffolds as a controlled delivery system for copper ions in stimulating osteogenesis and angiogenesis in bone healing. Journal of Materials Chemistry B 2014;2(48):8547-8557.
34. Deliormanlı AM, Liu X, Rahaman MN. Evaluation of borate bioactive glass scaffolds with different pore sizes in a rat subcutaneous implantation model. Journal of biomaterials applications 2014;28(5):643-653.
35. Bi L, Rahaman MN, Day DE, Brown Z, Samujh C, Liu X, Mohammadkhah A, Dusevich V, Eick JD, Bonewald LF. Effect of bioactive borate glass microstructure on bone regeneration, angiogenesis, and hydroxyapatite conversion in a rat calvarial defect model. Acta biomaterialia 2013;9(8):8015-8026.
36. Rey C, Combes C, Drouet C, Glimcher MJ. Bone mineral: update on chemical composition and structure. Osteoporosis International 2009;20(6):1013-1021.
37. Rahaman MN, Day DE, Bal BS, Fu Q, Jung SB, Bonewald LF, Tomsia AP. Bioactive glass in tissue engineering. Acta biomaterialia 2011;7(6):2355-2373.
38. Ahmed I, Lewis M, Olsen I, Knowles JC. Phosphate glasses for tissue engineering: Part 1. Processing and characterisation of a ternary-based P_2O_5–CaO–Na_2O glass system. Biomaterials 2004;25(3):491-499.
39. Neel EA, Ahmed I, Pratten J, Nazhat S, Knowles JC. Characterisation of antibacterial copper releasing degradable phosphate glass fibres. Biomaterials 2005;26(15):2247-2254.

40. Neel EA, O'Dell LA, Smith ME and Knowles JC. Processing, characterisation, and biocompatibility of zinc modified metaphosphate based glasses for biomedical applications. Journal of Materials Science: Materials in Medicine 2008;19 (4):1669-1679.
41. Ahmed I, Neel EA, Valappil SP, Nazhat S, Pickup DM, Carta D, Carroll DL, Newport RJ, Smith ME, Knowles JC. The structure and properties of silver-doped phosphate-based glasses. Journal of Materials Science 2007;42(23):9827-9835.
42. Ahmed I, Collins CA, Lewis MP, Olsen I, Knowles JC. Processing, characterisation and biocompatibility of iron-phosphate glass fibres for tissue engineering. Biomaterials 2004;25(16):3223-3232.
43. Neel EA, Chrzanowski W, Knowles JC. Effect of increasing titanium dioxide content on bulk and surface properties of phosphate-based glasses. Acta biomaterialia 2008;4(3):523-534.
44. Neel EA, Chrzanowski W, Pickup DM, O'Dell LA, Mordan NJ, Newport RJ, Smith ME, Knowles JC. Structure and properties of strontium-doped phosphate-based glasses. Journal of the Royal Society Interface 2008;6(34):435-446.
45. Islam MT, Felfel RM, Neel EA, Grant DM, Ahmed I, Hossain KM. Bioactive calcium phosphate–based glasses and ceramics and their biomedical applications: A review. Journal of tissue engineering 2017;8:2041731417719170.
46. Lankford K, Letourneau P. Evidence that calcium may control neurite outgrowth by regulating the stability of actin filaments. The Journal of cell biology 1989;109(3):1229-1243.
47. Ostomel TA, Shi Q, Tsung CK, Liang H, Stucky GD. Spherical bioactive glass with enhanced rates of hydroxyapatite deposition and hemostatic activity. Small 2006;2(11):1261-1265.
48. Kim CY, Clark AE, Hench LL. Early stages of calcium-phosphate layer formation in bioglasses. Journal of non-crystalline solids 1989;113(2-3):195-202.
49. Kokubo T, Kushitani H, Ohtsuki C, Sakka S, Yamamuro T. Effects of ions dissolved from bioactive glass-ceramic on surface apatite formation. Journal of Materials Science: Materials in Medicine 1993;4(1):1-4.

50. Sepulveda P, Jones JR, Hench LL. In vitro dissolution of melt-derived 45S5 and sol-gel derived 58S bioactive glasses. Journal of Biomedical Materials Research 2002;61(2):301-311.
51. Braun S, Rappoport S, Zusman R, Avnir D, Ottolenghi M. Biochemically active sol-gel glasses: The trapping of enzymes. Materials Letters 2007;61(14):2843-2846.
52. Jacques L, Thibaud C, Cécile R. Encapsulation of biomolecules in silica gels. Journal of Physics: Condensed Matter 2001;13(33):R673.
53. Blaker JJ, Nazhat SN, Boccaccini AR. Development and characterisation of silver-doped bioactive glass-coated sutures for tissue engineering and wound healing applications. Biomaterials 2004;25(7):1319-1329.
54. Neel EA, Ahmed I, Pratten J, Nazhat SN, Knowles JC. Characterisation of antibacterial copper releasing degradable phosphate glass fibres. Biomaterials 2005;26(15):2247-2254.
55. Gorustovich AA, Roether JA, Boccaccini AR. Effect of bioactive glasses on angiogenesis: a review of in vitro and in vivo evidences. Tissue Engineering Part B: Reviews 2009;16(2):199-207.
56. Day RM. Bioactive glass stimulates the secretion of angiogenic growth factors and angiogenesis in vitro. Tissue engineering 2005;11(5-6):768-77.
57. Fu Q, Saiz E, Tomsia AP. Bioinspired Strong and Highly Porous Glass Scaffolds. Advanced Functional Materials 2011;21(6):1058-1063.
58. Yan X, Yu C, Zhou X, Tang J, Zhao D. Highly Ordered Mesoporous Bioactive Glasses with Superior In Vitro Bone-Forming Bioactivities. Angewandte Chemie International Edition 2004;43(44):5980-5984.
59. Ghosh SK, Nandi SK, Kundu B, Datta S, De DK, Roy SK, Basu D. In vivo response of porous hydroxyapatite and β-tricalcium phosphate prepared by aqueous solution combustion method and comparison with bioglass scaffolds. Journal of Biomedical Materials Research Part B: Applied Biomaterials 2008;86B(1):217-227.
60. Zhang X, Zeng D, Li N, Wen J, Jiang X, Liu C, Li Y. Functionalized mesoporous bioactive glass scaffolds for enhanced bone tissue regeneration. Scientific Reports 2016;6:19361.

61. López-Noriega A, Arcos D, Vallet-Regí M. Functionalizing mesoporous bioglasses for long-term anti-osteoporotic drug delivery. Chemistry–A European Journal 2010;16(35):10879-10886.
62. Hossain KM, Patel U, Ahmed I. Development of microspheres for biomedical applications: a review. Progress in biomaterials 2015;4(1):1-19.
63. Cai Y, Chen Y, Hong X, Liu Z, Yuan W. Porous microsphere and its applications. International journal of nanomedicine 2013;8:1111.
64. Freiberg S, Zhu X. Polymer microspheres for controlled drug release. International journal of pharmaceutics 2004;282(1-2):1-18.
65. Li S, Nguyen L, Xiong H, Wang M, Hu TC, She JX, Serkiz SM, Wicks GG, Dynan WS. Porous-wall hollow glass microspheres as novel potential nanocarriers for biomedical applications. Nanomedicine: Nanotechnology, Biology and Medicine 2010;6(1):127-136.
66. Kokubo T, Kim HM, Kawashita M. Novel bioactive materials with different mechanical properties. Biomaterials 2003;24(13):2161-2175.
67. Cacaina D, Ylänen H, Simon S, Hupa M. The behaviour of selected yttrium containing bioactive glass microspheres in simulated body environments. Journal of Materials Science: Materials in Medicine 2008;19(3):1225-1233.
68. Sene FF, Martinelli JR, Okuno E. Synthesis and characterization of phosphate glass microspheres for radiotherapy applications. Journal of Non-Crystalline Solids 2008;354(42-44):4887-4893.
69. Martinelli JR, Sene FF, Kamikawachi CN, Partiti CD, Cornejo DR. Synthesis and characterization of glass–ceramic microspheres for thermotherapy. Journal of Non-Crystalline Solids 2010;356(44-49):2683-2688.
70. Wu C, Zhang Y, Ke X, Xie Y, Zhu H, Crawford R, Xiao Y. Bioactive mesopore-glass microspheres with controllable protein-delivery properties by biomimetic surface modification. Journal of Biomedical Materials Research Part A 2010;95(2):476-485.
71. Ho S, Lau W, Leung T, Johnson P. Internal radiation therapy for patients with primary or metastatic hepatic cancer: a review. Cancer: Interdisciplinary International Journal of the American Cancer Society 1998;83(9):1894-1907.

72. Kennedy AS, Nutting C, Coldwell D, Gaiser J, Drachenberg C. Pathologic response and microdosimetry of 90Y microspheres in man: review of four explanted whole livers. International Journal of Radiation Oncology* Biology* Physics 2004;60(5):1552-1563.

73. Salem R, Thurston KG. Radioembolization with 90Yttrium microspheres: a state-of-the-art brachytherapy treatment for primary and secondary liver malignancies: part 1: technical and methodologic considerations. Journal of vascular and interventional radiology 2006;17(8):1251-1278.

74. Ehrhardt GJ, Day DE. Therapeutic use of 90Y microspheres. International Journal of Radiation Applications and Instrumentation. Part B. Nuclear Medicine and Biology 1987;14(3):233-242.

75. Erbe EM, Day DE. Chemical durability of Y_2O_3-Al_2O_3-SiO_2 glasses for the in vivo delivery of beta radiation. Journal of biomedical materials research 1993;27(10):1301-1308.

76. White JE, Day DE. Rare earth aluminosilicate glasses for in vivo radiation delivery. Trans Tech Publications 1994;99:181-208.

77. Chen M, Wang X, Ye Z, Zhang Y, Zhou Y, Tan WS. A modular approach to the engineering of a centimeter-sized bone tissue construct with human amniotic mesenchymal stem cells-laden microcarriers. Biomaterials 2011;32(30):7532-7542.

78. Perez R, El-Fiqi A, Park JH, Kim TH, Kim JH, Kim HW. Therapeutic bioactive microcarriers: co-delivery of growth factors and stem cells for bone tissue engineering. Acta biomaterialia 2014;10(1):520-530.

79. Conti GN, Chiasera A, Ghisa L, Berneschi S, Brenci M, Dumeige Y, Pelli S, Sebastiani S, Feron P, Ferrari M, Ferrari M, Righini GC. Spectroscopic and lasing properties of Er^{3+}-doped glass microspheres. Journal of Non-Crystalline Solids 2006;352(23):2360-2363.

80. Lakhkar NJ, Park JH, Mordan NJ, Salih V, Wall IB, Kim HW, King SP, Hanna JV, Martin RA, Addison O, Mosselmans JF. Titanium phosphate glass microspheres for bone tissue engineering. Acta Biomaterialia 2012;8(11):4181-4190.

81. Dong CH, Xiao YF, Han ZF, Guo GC, Jiang X, Tong L, Gu C, Ming H. Low-Threshold Microlaser in Er:Yb Phosphate Glass Coated Microsphere. IEEE Photonics Technology Letters 2008;20(5):342-344.
82. Blaker JJ, Knowles JC, Day RM. Novel fabrication techniques to produce microspheres by thermally induced phase separation for tissue engineering and drug delivery. Acta Biomaterialia 2008;4(2):264-272.
83. Shelby JE. Introduction to glass science and technology: Royal Society of Chemistry; 2007.
84. Aguiar H, Serra J, González P, León B. Structural study of sol–gel silicate glasses by IR and Raman spectroscopies. Journal of Non-Crystalline Solids 2009;355(8):475-480.
85. Rao K. Structural chemistry of glasses: Elsevier; 2002.
86. Filho OP, La Torre GP, Hench LL. Effect of crystallization on apatite-layer formation of bioactive glass 45S5. Journal of Biomedical Materials Research 1996;30(4):509-514.
87. Hench LL, Andersson Ö. BIOACTIVE GLASSES. An Introduction to Bioceramics: WORLD SCIENTIFIC 1993:41-62.
88. Li R, Clark AE, Hench LL. Effects of structure and surface area on bioactive powders by sol-gel process. In Fifth Ultrastructure Processing Conference1991:627-633.
89. Hench LL, Andersson Ö. BIOACTIVE GLASSES. An Introduction to Bioceramics: WORLD SCIENTIFIC; 2011:41-62.
90. Haro Durand LA, Vargas GE, Romero NM, Vera-Mesones R, Porto-Lopez JM, Boccaccini AR, Zago MP, Baldi A, Gorustovich A. Angiogenic effects of ionic dissolution products released from a boron-doped 45S5 bioactive glass. Journal of Materials Chemistry B 2015;3(6):1142-1148.
91. Gorriti MF, López JM, Boccaccini AR, Audisio C, Gorustovich AA. In vitro Study of the Antibacterial Activity of Bioactive Glass-ceramic Scaffolds. Advanced Engineering Materials 2009;11(7):B67-B70.
92. Munukka E, Leppäranta O, Korkeamäki M, Vaahtio M, Peltola T, Zhang D, Hupa L, Ylänen H, Salonen JI, Viljanen MK, Eerola E. Bactericidal effects of

bioactive glasses on clinically important aerobic bacteria. Journal of Materials Science: Materials in Medicine 2008;19(1):27-32.

93. Salih V, Franks K, James M, Hastings GW, Knowles JC, Olsen I. Development of soluble glasses for biomedical use Part II: The biological response of human osteoblast cell lines to phosphate-based soluble glasses. Journal of Materials Science: Materials in Medicine 2000;11(10):615-620.
94. Karabulut M, Yuce B, Bozdogan O, Ertap H, Mammadov G. Effect of boron addition on the structure and properties of iron phosphate glasses. Journal of Non-Crystalline Solids 2011;357(5):1455-1462.
95. Donald I, Metcalfe B, Fong S, Gerrard L. The influence of Fe_2O_3 and B_2O_3 additions on the thermal properties, crystallization kinetics and durability of a sodium aluminum phosphate glass. Journal of non-crystalline solids 2006;352(28-29):2993-3001.
96. Gaune-Escard M. Molten salts: from fundamentals to applications: Springer Science & Business Media 2012: (52).
97. Yao A, Wang D, Huang W, Fu Q, Rahaman MN, Day DE. In Vitro Bioactive Characteristics of Borate-Based Glasses with Controllable Degradation Behavior. Journal of the American Ceramic Society 2007;90(1):303-306.
98. Toker H, Ozdemir H, Yuce HB, Goze F. The effect of boron on alveolar bone loss in osteoporotic rats. Journal of Dental Sciences 2016;11(3):331-337.
99. Liu X, Huang W, Fu H, Yao A, Wang D, Pan H, Lu WW. Bioactive borosilicate glass scaffolds: improvement on the strength of glass-based scaffolds for tissue engineering. Journal of Materials Science: Materials in Medicine 2008;20(1):365.
100. Fu Q, Rahaman MN, Bal BS, Bonewald LF, Kuroki K, Brown RF. Silicate, borosilicate, and borate bioactive glass scaffolds with controllable degradation rate for bone tissue engineering applications. II. In vitro and in vivo biological evaluation. Journal of Biomedical Materials Research Part A 2010;95A(1):172-179.
101. Liu X, Xie Z, Zhang C, Pan H, Rahaman MN, Zhang X, Fu Q, Huang W. Bioactive borate glass scaffolds: in vitro and in vivo evaluation for use as a drug delivery

system in the treatment of bone infection. Journal of Materials Science: Materials in Medicine 2010;21(2):575-582.

102. Brown RF, Rahaman MN, Dwilewicz AB, Huang W, Day DE, Li Y, Bal BS. Effect of borate glass composition on its conversion to hydroxyapatite and on the proliferation of MC3T3-E1 cells. Journal of Biomedical Materials Research Part A 2009;88A(2):392-400.
103. Neel EA, O'Dell LA, Smith ME, Knowles JC. Processing, characterisation, and biocompatibility of zinc modified metaphosphate based glasses for biomedical applications. Journal of Materials Science: Materials in Medicine 2008;19(4):1669-1679.
104. Ahmed I, Neel EA, Valappil SP, Nazhat SN, Pickup DM, Carta D, Carroll DL, Newport RJ, Smith ME, Knowles JC. The structure and properties of silver-doped phosphate-based glasses. Journal of Materials Science 2007;42(23):9827-9835.
105. Ahmed I, Collins CA, Lewis MP, Olsen I, Knowles JC. Processing, characterisation and biocompatibility of iron-phosphate glass fibres for tissue engineering. Biomaterials 2004;25(16):3223-3232.
106. Abou Neel EA, Chrzanowski W, Knowles JC. Effect of increasing titanium dioxide content on bulk and surface properties of phosphate-based glasses. Acta Biomaterialia 2008;4(3):523-534.
107. Lakhkar NJ, Neel EA, Salih V, Knowles JC. Strontium oxide doped quaternary glasses: effect on structure, degradation and cytocompatibility. Journal of Materials Science: Materials in Medicine 2009;20(6):1339.
108. Valappil SP, Pickup DM, Carroll DL, Hope CK, Pratten J, Newport RJ, Smith ME, Wilson M, Knowles JC. Effect of Silver Content on the Structure and Antibacterial Activity of Silver-Doped Phosphate-Based Glasses. Antimicrobial Agents and Chemotherapy 2007;51(12):4453-4461.
109. Neel EA, O'Dell LA, Chrzanowski W, Smith ME, Knowles JC. Control of surface free energy in titanium doped phosphate based glasses by co-doping with zinc. Journal of Biomedical Materials Research Part B: Applied Biomaterials 2009;89B(2):392-407.

110. Bitar M, Salih V, Knowles JC, Lewis MP. Iron-phosphate glass fiber scaffolds for the hard–soft interface regeneration: The effect of fiber diameter and flow culture condition on cell survival and differentiation. Journal of Biomedical Materials Research Part A 2008;87A(4):1017-1026.
111. Hoppe U. A structural model for phosphate glasses. Journal of Non-Crystalline Solids 1996;195(1):138-147.
112. Brow RK. Review: the structure of simple phosphate glasses. Journal of Non-Crystalline Solids 2000;263:1-28.
113. Moustafa Y, El-Egili K. Infrared spectra of sodium phosphate glasses. Journal of non-crystalline solids 1998;240(1):144-153.
114. Martin S. Review of the structures of phosphate glasses. ChemInform 1991;22(17).
115. Brauer DS. Phosphate glasses. Bio-Glasses: An Introduction 2012:45-64.
116. Becke-Goehring M. Phosphorus and its Compounds, Bd. 1: Chemistry, von JR Van Wazer. Interscience Publishers, New York-London 1958.
117. Martin S. Review of the structures of phosphate glasses. ChemInform 1991;22(17).
118. Bae BS, Weinberg MC. Oxidation–Reduction Equilibrium in Copper Phosphate Glass Melted in Air. Journal of the American Ceramic Society 1991;74(12):3039-3045.
119. Neel EA, Chrzanowski W, Valappil SP, O'Dell LA, Pickup DM, Smith ME, Newport RJ, Knowles JC. Doping of a high calcium oxide metaphosphate glass with titanium dioxide. Journal of Non-Crystalline Solids 2009;355(16–17):991-1000.
120. Neel EA, Knowles JC. Physical and biocompatibility studies of novel titanium dioxide doped phosphate-based glasses for bone tissue engineering applications. Journal of Materials Science: Materials in Medicine 2008;19(1):377-386.
121. Neel EA, Mizoguchi T, Ito M, Bitar M, Salih V, Knowles JC. In vitro bioactivity and gene expression by cells cultured on titanium dioxide doped phosphate-based glasses. Biomaterials 2007;28(19):2967-2977.

122. Neel EA, Young AM, Nazhat SN, Knowles JC. A Facile Synthesis Route to Prepare Microtubes from Phosphate Glass Fibres. Advanced Materials 2007;19(19):2856-2862.

123. Guedes JC, Park JH, Lakhkar NJ, Kim HW, Knowles JC, Wall IB. TiO_2-doped phosphate glass microcarriers: a stable bioactive substrate for expansion of adherent mammalian cells. Journal of biomaterials applications 2013;28(1):3-11.

124. Vitale-Brovarone C, Novajra G, Lousteau J, Milanese D, Raimondo S, Fornaro M. Phosphate glass fibres and their role in neuronal polarization and axonal growth direction. Acta Biomaterialia 2012;8(3):1125-1136.

125. Neel EA, Pickup DM, Valappil SP, Newport RJ, Knowles JC. Bioactive functional materials: a perspective on phosphate-based glasses. Journal of Materials Chemistry 2009;19(6):690-701.

126. Nazhat SN, Neel EA, Kidane A, Ahmed I, Hope C, Kershaw M, Lee PD, Stride E, Saffari N, Knowles JC. Controlled Microchannelling in Dense Collagen Scaffolds by Soluble Phosphate Glass Fibers. Biomacromolecules 2006;8(2):543-551.

127. Sene FF, Martinelli JR, Okuno E. Synthesis and characterization of phosphate glass microspheres for radiotherapy applications. Journal of Non-Crystalline Solids 2008;354(42–44):4887-4893.

128. Kretlow JD, Young S, Klouda L, Wong M, Mikos AG. Injectable Biomaterials for Regenerating Complex Craniofacial Tissues. Advanced Materials 2009;21(32-33):3368-3393.

129. Burguera EF, Xu HH, Sun L. Injectable calcium phosphate cement: Effects of powder-to-liquid ratio and needle size. Journal of Biomedical Materials Research Part B: Applied Biomaterials 2008;84B(2):493-502.

130. Vorndran E, Geffers M, Ewald A, Lemm M, Nies B, Gbureck U. Ready-to-use injectable calcium phosphate bone cement paste as drug carrier. Acta Biomaterialia 2013;9(12):9558-9567.

131. Turner TM, Urban RM, Singh K, Hall DJ, Renner SM, Lim TH, Tomlinson MJ, An HS. Vertebroplasty comparing injectable calcium phosphate cement

compared with polymethylmethacrylate in a unique canine vertebral body large defect model. The Spine Journal 2008;8(3):482-487.

132. Boccaccini AR, Chen Q, Lefebvre L, Gremillard L, Chevalier J. Sintering, crystallisation and biodegradation behaviour of Bioglass-derived glass-ceramics. Faraday Discuss 2007;136:27-44; discussion 107-23.
133. Zanotto ED. A bright future for glass-ceramics. American Ceramic Society Bulletin 2010;89(8):19-27.
134. Park J, Ozturk A. Bioactivity of Apatite-Wollastonite Glass-Ceramics Produced by Melting Casting. Surface Review and Letters 2013;20(01):1350010.
135. Thompson ID, Hench LL. Mechanical properties of bioactive glasses, glass-ceramics and composites. Proceedings of the Institution of Mechanical Engineers, Part H: Journal of Engineering in Medicine 1998;212(2):127-136.
136. Magallanes-Perdomo M, Luklinska ZB, De Aza AH, Carrodeguas RG, De Aza S, Pena P. Bone-like forming ability of apatite–wollastonite glass ceramic. Journal of the European Ceramic Society 2011;31(9):1549-1561.
137. Vitale-Brovarone C, Verné E, Robiglio L, Appendino P, Bassi F, Martinasso G, Muzio G, Canuto R. Development of glass–ceramic scaffolds for bone tissue engineering: Characterisation, proliferation of human osteoblasts and nodule formation. Acta Biomaterialia 2007;3(2):199-208.
138. Fujita H, Iida H, Ido K, Matsuda Y, Oka M, Nakamura T. Porous apatite-wollastonite glass-ceramic as an intramedullary plug. Journal of Bone and Joint Surgery 2000;82-B(4):614.
139. Long Q, Zhou DL, Zhang X, Zhou JB. Surface modification of apatite-wollastonite glass ceramic by synthetic coupling agent. Frontiers of Materials Science 2014;8(2):157-164.
140. Uhlmann DR. A kinetic treatment of glass formation. Journal of Non-Crystalline Solids 1972;7(4):337-348.
141. Joraid A. Limitation of the Johnson–Mehl–Avrami (JMA) formula for kinetic analysis of the crystallization of a chalcogenide glass. Thermochimica acta 2005;436(1):78-82.
142. Kissinger HE. Reaction kinetics in differential thermal analysis. Analytical chemistry 1957;29(11):1702-1706.

143. Augis J, Bennett J. Calculation of the Avrami parameters for heterogeneous solid state reactions using a modification of the Kissinger method. Journal of Thermal Analysis and Calorimetry 1978;13(2):283-292.
144. Marotta A, Buri A, Branda F. Surface and bulk crystallization in non-isothermal devitrification of glasses. Thermochimica Acta 1980;40(3):397-403.
145. Ray C, Day D. Identifying internal and surface crystallization by differential thermal analysis for the glass-to-crystal transformations. Thermochimica acta 1996;280:163-174.
146. Shelby JE. Introduction to glass science and technology: Royal Society of Chemistry; 2005.
147. Zhu P, Masuda Y, Koumoto K. The effect of surface charge on hydroxyapatite nucleation. Biomaterials 2004;25(17):3915-3921.
148. Kokubo T, Pattanayak DK, Yamaguchi S, Takadama H, Matsushita T, Kawai T, Takemoto M, Fujibayashi S, Nakamura T. Positively charged bioactive Ti metal prepared by simple chemical and heat treatments. Journal of The Royal Society Interface 2010;7(Suppl 5):S503-S513.
149. Huang W, Rahaman MN, Day DE, Li Y. Mechanisms for converting bioactive silicate, borate, and borosilicate glasses to hydroxyapatite in dilute phosphate solution. Physics and Chemistry of Glasses: European Journal of Glass Science and Technology Part B 2006;47(6):647-658.
150. Geng Z, Cui Z, Li Z, Zhu S, Liang Y, Lu WW, Yang X. Synthesis, characterization and the formation mechanism of magnesium- and strontium-substituted hydroxyapatite. Journal of Materials Chemistry B 2015;3(18):3738-3746.
151. Hench LL. The story of Bioglass®. Journal of Materials Science: Materials in Medicine 2006;17(11):967-978.
152. Hench LL, Wilson J. Surface-active biomaterials. Science 1984;226(4675):630.
153. Fujibayashi S, Neo M, Kim HM, Kokubo T, Nakamura T. A comparative study between in vivo bone ingrowth and in vitro apatite formation on Na_2O–CaO–SiO_2 glasses. Biomaterials 2003;24(8):1349-1356.
154. Clark AE, Pantano CG, Hench LL. Auger Spectroscopic Analysis of Bioglass Corrosion Films. Journal of the American Ceramic Society 1976;59(1-2):37-39.

155. Gunawidjaja PN, Mathew R, Lo AY, Izquierdo-Barba I, García A, Arcos D, Vallet-Regí M, Edén M. Local structures of mesoporous bioactive glasses and their surface alterations in vitro: inferences from solid-state nuclear magnetic resonance. Philosophical Transactions of the Royal Society A: Mathematical, Physical and Engineering Sciences 2012;370(1963):1376-1399.

156. Chen Q, Miyaji F, Kokubo T, Nakamura T. Apatite formation on PDMS-modified $CaO–SiO_2–TiO_2$ hybrids prepared by sol–gel process. Biomaterials 1999;20(12):1127-1132.

157. Liang W, Rüssel C, Day DE, Völksch G. Bioactive comparison of a borate, phosphate and silicate glass. Journal of materials research 2006;21(01):125-131.

158. De Aza P, Guitian F, De Aza S. Bioactivity of wollastonite ceramics: in vitro evaluation. Scripta metallurgica et materialia 1994;31(8):1001-1005.

159. AZA P, Luklinska Z, Anseau M, Guitian F, AZA S. Morphological studies of pseudowollastonite for biomedical application. Journal of microscopy 1996;182(1):24-31.

160. De Aza PN, Guitian F, De Aza S. Bioeutectic: a new ceramic material for human bone replacement. Biomaterials 1997;18(19):1285-1291.

161. De Aza PN, Luklinska ZB, Anseau MR, Hector M, Guitian F, De Aza S. Reactivity of a wollastonite–tricalcium phosphate Bioeutectic® ceramic in human parotid saliva. Biomaterials 2000;21(17):1735-1741.

162. Liu X, Ding C, Chu PK. Mechanism of apatite formation on wollastonite coatings in simulated body fluids. Biomaterials 2004;25(10):1755-1761.

163. Xin R, Leng Y, Chen J, Zhang Q. A comparative study of calcium phosphate formation on bioceramics in vitro and in vivo. Biomaterials 2005;26(33):6477-6486.

164. Dorozhkina EI, Dorozhkin SV. Surface mineralisation of hydroxyapatite in modified simulated body fluid (mSBF) with higher amounts of hydrogencarbonate ions. Colloids and Surfaces A: Physicochemical and Engineering Aspects 2002;210(1):41-48.

165. Pattanayak DK, Yamaguchi S, Matsushita T, Nakamura T, Kokubo T. Apatite-forming ability of titanium in terms of pH of the exposed solution. Journal of The Royal Society Interface 2012;9(74):2145-2155.

166. Kokubo T, Miyaji F, Kim HM, Nakamura T. Spontaneous Formation of Bonelike Apatite Layer on Chemically Treated Titanium Metals. Journal of the American Ceramic Society 1996;79(4):1127-1129.

167. Kim HM, Miyaji F, Kokubo T, Nakamura T. Preparation of bioactive Ti and its alloys via simple chemical surface treatment. Journal of Biomedical Materials Research 1996;32(3):409-417.

168. Kim HM, Miyaji F, Kokubo T, Nishiguchi S, Nakamura T. Graded surface structure of bioactive titanium prepared by chemical treatment. Journal of Biomedical Materials Research Part A 1999;45(2):100-107.

169. Kokubo T, Miyaji F, Kim HM, Nakamura T. Spontaneous formation of bonelike apatite layer on chemically treated titanium metals. Journal of the American Ceramic Society 1996;79(4):1127-1129.

170. Kim HM, Miyaji F, Kokubo T, Nakamura T. Preparation of bioactive Ti and its alloys via simple chemical surface treatment. Journal of biomedical materials research 1996;32(3):409-417.

171. Wei M, Kim HM, Kokubo T, Evans J. Optimising the bioactivity of alkaline-treated titanium alloy. Materials Science and Engineering: C 2002;20(1):125-134.

172. Jonášová L, Müller FA, Helebrant A, Strnad J, Greil P. Biomimetic apatite formation on chemically treated titanium. Biomaterials 2004;25(7):1187-1194.

173. Yousefpour M, Afshar A, Chen J, Zhang X. Bioactive layer formation on alkaline-acid treated titanium in simulated body fluid. Materials & design 2007;28(7):2154-2159.

174. Kasuga T, Kondo H, Nogami M. Apatite formation on TiO_2 in simulated body fluid. Journal of Crystal Growth 2002;235(1):235-240.

175. Textor M, Sittig C, Frauchiger V, Tosatti S, Brunette DM. Properties and Biological Significance of Natural Oxide Films on Titanium and Its Alloys. Titanium in Medicine: Material Science, Surface Science, Engineering,

Biological Responses and Medical Applications. Springer, Berlin Heidelberg 2001: 171-230.

176. Kasuga T, Hattori T, Niinomi M. Phosphate glasses and glass-ceramics for biomedical applications. Phosphorus Research Bulletin 2012;26(0):8-15.
177. Rajkumar G, Rajendran V, Aravindan S. Role of MgO on the HAp forming ability in phosphate based glasses. Ceramics International 2012;38(5):3781-3790.
178. Kasuga T, Hosoi Y, Nogami M, Niinomi M. Apatite formation on calcium phosphate invert glasses in simulated body fluid. Journal of the American Ceramic Society 2001;84(2):450-452.
179. Rajendran V, Rajkumar G, Aravindan S, Saravanakumar B. Analysis of Physical Properties and Hydroxyapatite Precipitation In Vitro of TiO_2-Containing Phosphate-Based Glass Systems. Journal of the American Ceramic Society 2010;93(12):4053-4060.
180. Nan Y, Lee WE, James PF. Crystallization behavior of $CaO–P_2O_5$ glass with TiO_2, SiO_2, and Al_2O_3 additions. Journal of the American Ceramic Society 1992;75(6):1641-1647.
181. Tanaka K, Mukai T, Ishihara T, Hirao K, Soga N, Sogo S, Ashida M, Kato R. Preparation and Optical Properties of Transparent Glass-Ceramics Containing Cobalt (ll) Ions. Journal of the American Ceramic Society 1993;76(11):2839-2845.
182. KASUGA T, HOSOI Y, NOGAMI M, NIINOMI M. Biomimetic apatite formation on calcium phosphate invert glasses. Phosphorus Research Bulletin 2001;12(0):39-44.
183. Gerhardt LC, Boccaccini AR. Bioactive Glass and Glass-Ceramic Scaffolds for Bone Tissue Engineering. Materials 2010;3(7):3867-3910.
184. Drouet C. Apatite formation: why it may not work as planned, and how to conclusively identify apatite compounds. BioMed research international 2013;2013.
185. Elliott JC. Structure and chemistry of the apatites and other calcium orthophosphates: Elsevier; 2013.
186. Videau JJ, Portier J, Piriou B. Raman spectroscopic studies of fluorophosphate glasses. Journal of Non-Crystalline Solids 1982;48(2):385-392.

187. Hartwig A. Role of magnesium in genomic stability. Mutation Research/Fundamental and Molecular Mechanisms of Mutagenesis 2001;475(1):113-121.

188. Xynos ID, Edgar AJ, Buttery LD, Hench LL, Polak JM. Ionic products of bioactive glass dissolution increase proliferation of human osteoblasts and induce insulin-like growth factor II mRNA expression and protein synthesis. Biochemical and biophysical research communications 2000;276(2):461-465.

189. Zreiqat H, Howlett C, Zannettino A, Evans P, Schulze-Tanzil G, Knabe C, Shakibaei M. Mechanisms of magnesium-stimulated adhesion of osteoblastic cells to commonly used orthopaedic implants. Journal of Biomedical Materials Research Part A 2002;62(2):175-184.

190. Hoppe A, Güldal NS, Boccaccini AR. A review of the biological response to ionic dissolution products from bioactive glasses and glass-ceramics. Biomaterials 2011;32(11):2757-2774.

191. Yamasaki Y, Yoshida Y, Okazaki M, Shimazu A, Uchida T, Kubo T, Akagawa Y, Hamada Y, Takahashi J, Matsuura N. Synthesis of functionally graded $MgCO_3$ apatite accelerating osteoblast adhesion. Journal of Biomedical Materials Research Part A 2002;62(1):99-105.

192. Erol M, Özyuguran A, Çelebican Ö. Synthesis, characterization, and in vitro bioactivity of sol-gel-derived Zn, Mg, and Zn-Mg Co-doped bioactive glasses. Chemical Engineering & Technology 2010;33(7):1066-1074.

193. Saboori A, Sheikhi M, Moztarzadeh F, Rabiee M, Hesaraki S, Tahriri M, Nezafati N. Sol-gel preparation, characterisation and in vitro bioactivity of Mg containing bioactive glass. Advances in Applied Ceramics: Structural, Functional and Bioceramics 2009;108(3):155.

194. Oliveira J, Correia R, Fernandes M. Effects of Si speciation on the in vitro bioactivity of glasses. Biomaterials 2002;23(2):371-379.

195. Oliveira J, Correia R, Fernandes M. Surface modifications of a glass and a glass-ceramic of the MgO-3CaO· P_2O_5-SiO_2 system in a simulated body fluid. Biomaterials 1995;16(11):849-854.

196. Salinas A, Roman J, Vallet-Regi M, Oliveira J, Correia R, Fernandes M. In vitro bioactivity of glass and glass-ceramics of the $3CaO\cdot P_2O_5$–$CaO\cdot SiO_2$–$CaO\cdot MgO\cdot 2SiO_2$ system. Biomaterials 2000;21(3):251-257.

197. Kasuga T, Nakagawa K, Yoshida M, Miyade E. Compositional dependence of formation of an apatite layer on glass-ceramics in simulated physiological solution. Journal of materials science 1987;22(10):3721-3724.

198. Ebisawa Y, Kokubo T, Ohura K, Yamamuro T. Bioactivity of $CaO\cdot SiO_2$-based glasses: in vitro evaluation. Journal of Materials Science: Materials in Medicine 1990;1(4):239-244.

199. Vallet-Regi M, Salinas A, Roman J, Gil M. Effect of magnesium content on the in vitro bioactivity of CaO-MgO-SiO_2-P_2O_5 sol-gel glasses. Journal of Materials Chemistry 1999;9(2):515-518.

200. Zhao J, Liu Y, Sun WB, Zhang H. Amorphous calcium phosphate and its application in dentistry. Chemistry Central Journal 2011;5:40-40.

201. Shaim A, Et-Tabirou M. Role of titanium in sodium titanophosphate glasses and a model of structural units. Materials chemistry and physics 2003;80(1):63-67.

202. Kishioka A, Haba M, Amagasa M. Glass formation in multicomponent phosphate systems containing TiO_2. Bulletin of the Chemical Society of Japan 1974;47(10):2493-2496.

203. Neel EA, Knowles JC. Physical and biocompatibility studies of novel titanium dioxide doped phosphate-based glasses for bone tissue engineering applications. Journal of Materials Science: Materials in Medicine 2008;19(1):377-386.

204. Brauer DS, Rüssel C, Li W, Habelitz S. Effect of degradation rates of resorbable phosphate invert glasses on in vitro osteoblast proliferation. Journal of Biomedical Materials Research Part A 2006;77(2):213-219.

205. Navarro M, Ginebra MP, Planell JA. Cellular response to calcium phosphate glasses with controlled solubility. Journal of Biomedical Materials Research Part A 2003;67(3):1009-1015.

206. Dias A, Lopes M, Trigo Cabral A, Santos J, Fernandes M. In vitro studies of calcium phosphate glass ceramics with different solubility with the use of

human bone marrow cells. Journal of Biomedical Materials Research Part A 2005;74(3):347-355.

207. Nocuń M. Structural studies of phosphate glasses with high ionic conductivity. Journal of non-crystalline solids 2004;333(1):90-94.

208. Fernandes HR, Tulyaganov DU, Ferreira JM. The role of P_2O_5, TiO_2 and ZrO_2 as nucleating agents on microstructure and crystallization behaviour of lithium disilicate-based glass. Journal of materials science 2013;48(2):765-773.

209. Kržmanc MM, Došler U, Suvorov D. Effect of a TiO_2 nucleating agent on the nucleation and crystallization behavior of $MgO–B_2O_3–SiO_2$ glass. Journal of the American Ceramic Society 2012;95(6):1920-1926.

210. Danewalia SS, Singh K. Intriguing role of TiO_2 in glass-ceramics: Bioactive and magneto-structural properties. Journal of the American Ceramic Society 2018;101(7):2819-2830.

211. Arya S, Kaur B, Kaur G, Singh K. Optical and thermal properties of $(70– x) SiO_2–xNa_2O–15CaO–10Al_2O_3–5TiO_2$ $(10\leq x\leq 25)$ glasses. Journal of Thermal Analysis and Calorimetry 2015;120(2):1163-1171.

212. Helebrant A, Jonasova L, Sanda L. The influence of simulated body fluid composition on carbonated hydroxyapatite formation. Ceramics 2002;46(1):9-14.

213. Varila L, Fagerlund S, Lehtonen T, Tuominen J, Hupa L. Surface reactions of bioactive glasses in buffered solutions. Journal of the European Ceramic Society 2012;32(11):2757-2763.

214. Abo-Naf SM, Khalil ES, El-Sayed ES, Zayed HA, Youness RA. In vitro bioactivity evaluation, mechanical properties and microstructural characterization of $Na_2O–CaO–B_2O_3–P_2O_5$ glasses. Spectrochimica Acta Part A: Molecular and Biomolecular Spectroscopy 2015;144:88-98.

215. Turdean-Ionescu C, Stevensson B, Grins J, Izquierdo-Barba I, García A, Arcos D, Vallet-Regí M, Edén M. Composition-dependent in vitro apatite formation at mesoporous bioactive glass-surfaces quantified by solid-state NMR and powder XRD. RSC Advances 2015;5(105):86061-86071.

216. Bui X, Nguyen V, Le T, Do Q. 'In vitro'apatite formation on the surface of bioactive glass. Glass Physics & Chemistry 2013;39(1).

217. Lööf J, Svahn F, Jarmar T, Engqvist H, Pameijer CH. A comparative study of the bioactivity of three materials for dental applications. dental materials 2008;24(5):653-659.

218. Al-Noaman A, Rawlinson SC, Hill RG. The role of MgO on thermal properties, structure and bioactivity of bioactive glass coating for dental implants. Journal of Non-Crystalline Solids 2012;358(22):3019-3027.

219. Kim HM, Himeno T, Kokubo T, Nakamura T. Process and kinetics of bonelike apatite formation on sintered hydroxyapatite in a simulated body fluid. Biomaterials 2005;26(21):4366-4373.

220. Kokubo T, Ito S, Huang Z, Hayashi T, Sakka S, Kitsugi T, Yamamuro T. Ca, P-rich layer formed on high-strength bioactive glass-ceramic A-W. Journal of Biomedical Materials Research Part A 1990;24(3):331-343.

221. Ohtsuki C, Kushitani H, Kokubo T, Kotani S, Yamamuro T. Apatite formation on the surface of ceravital-type glass-ceramic in the body. Journal of biomedical materials research 1991;25(11):1363-1370.

222. Lepry WC, Nazhat SN. Highly Bioactive Sol-Gel-Derived Borate Glasses. Chemistry of Materials 2015;27(13):4821-4831.

223. Liang W, Rahaman MN, Day DE, Marion NW, Riley GC, Mao JJ. Bioactive borate glass scaffold for bone tissue engineering. Journal of Non-Crystalline Solids 2008;354(15):1690-1696.

224. Theodorou G, Goudouri O, Kontonasaki E, Chatzistavrou X, Papadopoulou L, Kantiranis N, Paraskevopoulos K. Comparative bioactivity study of 45S5 and 58S bioglasses in organic and inorganic environment. Bioceramics Development and Applications 2011;1:1-4.

225. Faure J, Balamurugan A, Benhayoune H, Torres P, Balossier G, Ferreira J. Morphological and chemical characterisation of biomimetic bone like apatite formation on alkali treated Ti6Al4V titanium alloy. Materials Science and Engineering: C 2009;29(4):1252-1257.

226. Implants for surgery: in vitro evaluation for apatite-forming ability of implant materials. ISO ISO/DIS 23317, International Organization for Standardization. Geneva, Switzerland; 2014.

227. Maçon AL, Kim TB, Valliant EM, Goetschius K, Brow RK, Day DE, Hoppe A, Boccaccini AR, Kim IY, Ohtsuki C. A unified in vitro evaluation for apatite-forming ability of bioactive glasses and their variants. Journal of Materials Science: Materials in Medicine 2015;26(2):1-10.

228. Mei J, Shelton R, Marquis P. Changes in the elemental composition of Bioglass during its surface development in the presence or absence of proteins. Journal of Materials Science: Materials in Medicine 1995;6(12):703-707.

229. Radin S, Ducheyne P, Rothman B, Conti A. The effect of in vitro modeling conditions on the surface reactions of bioactive glass. Journal of biomedical materials research 1997;37(3):363-375.

230. Fagerlund S, Hupa L, Hupa M. Comparison of reactions of bioactive glasses in different aqueous solutions. Advances in bioceramics and biotechnologies: ceramic transactions 2010;218:101.

231. Rohanová D, Boccaccini AR, Yunos DM, Horkavcová D, Březovská I, Helebrant A. TRIS buffer in simulated body fluid distorts the assessment of glass–ceramic scaffold bioactivity. Acta biomaterialia 2011;7(6):2623-2630.

232. Hlavac J, Rohanová D, Helebrant A. The effect of tris-buffer on the leaching behaviour of bioactive glass-ceramics. Ceramics 1994;38(3-4):119-122.

233. Ogino M, Hench LL. Formation of calcium phosphate films on silicate glasses. Journal of Non-Crystalline Solids 1980;38:673-678.

234. Fujiu T, Ogino M. Difference of bond bonding behavior among surface active glasses and sintered apatite. Journal of Biomedical Materials Research Part A 1984;18(7):845-859.

235. Pan H, Zhao X, Darvell BW, Lu WW. Apatite-formation ability–predictor of "bioactivity"? Acta biomaterialia 2010;6(11):4181-4188.

236. Oyane A, Kim HM, Furuya T, Kokubo T, Miyazaki T, Nakamura T. Preparation and assessment of revised simulated body fluids. Journal of Biomedical Materials Research Part A 2003;65A(2):188-195.

237. Kim HM, Miyazaki T, Kokubo T, Nakamura T. Revised simulated body fluid. Key Engineering Materials 2001;1:47-50.

238. Rohanová D, Boccaccini AR, Horkavcová D, Bozděchová P, Bezdička P, Častorálová M. Is non-buffered DMEM solution a suitable medium for in vitro bioactivity tests? Journal of Materials Chemistry B 2014;2(31):5068-5076.

239. Popa A, Stan G, Husanu M, Mercioniu I, Santos L, Fernandes H, Ferreira J. Bioglass implant-coating interactions in synthetic physiological fluids with varying degrees of biomimicry. International Journal of Nanomedicine 2017;12:683.

240. Zhou Z, Yi Q, Liu X, Liu L, Liu Q. In vitro degradation behaviors of poly-L-lactide/bioactive glass composite materials in phosphate-buffered solution. Polymer bulletin 2009;63(4):575-586.

241. Li H, Chang J. pH-compensation effect of bioactive inorganic fillers on the degradation of PLGA. Composites science and technology 2005;65(14):2226-2232.

242. Brown RF, Rahaman MN, Dwilewicz AB, Huang W, Day DE, Li Y, Bal BS. Effect of borate glass composition on its conversion to hydroxyapatite and on the proliferation of MC3T3-E1 cells. Journal of Biomedical Materials Research Part A 2009;88(2):392-400.

243. Ning J, Yao A, Wang D, Huang W, Fu H, Liu X, Jiang X, Zhang X. Synthesis and in vitro bioactivity of a borate-based bioglass. Materials letters 2007;61(30):5223-5226.

244. Rámila A, Vallet-Regı M. Static and dynamic in vitro study of a sol–gel glass bioactivity. Biomaterials 2001;22(16):2301-2306.

245. Zhang D, Hupa M, Aro HT, Hupa L. Influence of fluid circulation on in vitro reactivity of bioactive glass particles. Materials Chemistry and Physics 2008;111(2):497-502.

246. Siriphannon P, Kameshima Y, Yasumori A, Okada K, Hayashi S. Comparitive study of the formation of hydroxyapatite in simulated body fluid under static and flowing systems. Journal of biomedical materials research 2002;60(1):175-185.

247. Strnad J, Protivínský J, Mazur D, Veltruská K, Strnad Z, Helebrant A, Šesták J. Interaction of acid and alkali treated titanium with dynamic simulated body environment. Journal of thermal analysis and calorimetry 2004;76(1):17-31.

248. Habraken W, Habibovic P, Epple M, Bohner M. Calcium phosphates in biomedical applications: materials for the future? Materials Today 2016;19(2):69-87.

249. Zhao J, Liu Y, Sun WB, Zhang H. Amorphous calcium phosphate and its application in dentistry. Chemistry Central Journal 2011;5(1):40.

250. Combes C, Rey C. Amorphous calcium phosphates: Synthesis, properties and uses in biomaterials. Acta Biomaterialia 2010;6(9):3362-3378.

251. Dorozhkin SV, Epple M. Biological and Medical Significance of Calcium Phosphates. Angewandte Chemie International Edition 2002;41(17):3130-3146.

252. Dorozhkin SV. Calcium orthophosphates in dentistry. Journal of Materials Science: Materials in Medicine 2013;24(6):1335-1363.

253. Gupta R, Prakash V. CPP-ACP complex as a new adjunctive agent for remineralisation: a review. Oral health & preventive dentistry 2011;9(2).

254. Iijima Y, Cai F, Shen P, Walker G, Reynolds C, Reynolds E. Acid resistance of enamel subsurface lesions remineralized by a sugar-free chewing gum containing casein phosphopeptide-amorphous calcium phosphate. Caries Research 2004;38(6):551-556.

255. Jones JR, Brauer DS, Hupa L, Greenspan DC. Bioglass and bioactive glasses and their impact on healthcare. International Journal of Applied Glass Science 2016;7(4):423-434.

256. Butscher A, Bohner M, Doebelin N, Hofmann S, Müller R. New depowdering-friendly designs for three-dimensional printing of calcium phosphate bone substitutes. Acta Biomaterialia 2013;9(11):9149-9158.

257. Bahraminasab M, Sahari B, Edwards K, Farahmand F, Arumugam M. Aseptic loosening of femoral components–Materials engineering and design considerations. Materials & Design 2013;44:155-163.

258. Yang Y, Kim KH, Ong JL. A review on calcium phosphate coatings produced using a sputtering process—an alternative to plasma spraying. Biomaterials 2005;26(3):327-337.

259. Gross KA, Berndt CC. Biomedical Application of Apatites. Reviews in Mineralogy and Geochemistry 2002;48(1):631-672.

260. Sezer N, Evis Z, Kayhan SM, Tahmasebifar A, Koç M. Review of magnesium-based biomaterials and their applications. Journal of magnesium and alloys 2018;6(1):23-43.

261. Dorozhkin SV. Calcium orthophosphate coatings on magnesium and its biodegradable alloys. Acta Biomaterialia 2014;10(7):2919-2934.

262. Chernousova S, Klesing J, Soklakova N, Epple M. A genetically active nano-calcium phosphate paste for bone substitution, encoding the formation of BMP-7 and VEGF-A. RSC Advances 2013;3(28):11155-11161.

263. Sokolova V, Knuschke T, Kovtun A, Buer J, Epple M, Westendorf AM. The use of calcium phosphate nanoparticles encapsulating Toll-like receptor ligands and the antigen hemagglutinin to induce dendritic cell maturation and T cell activation. Biomaterials 2010;31(21):5627-5633.

264. Lin ST, Krebs SL, Kadiyala S, Leong KW, LaCourse WC, Kumar B. Development of bioabsorbable glass fibres. Biomaterials 1994;15(13):1057-1061.

265. Hossain KM, Patel U, Kennedy AR, Macri-Pellizzeri L, Sottile V, Grant DM, Scammell BE, Ahmed I. Porous calcium phosphate glass microspheres for orthobiologic applications. Acta biomaterialia 2018;72:396-406.

266. Choi SW, Zhang Y, Yeh YC, Wooten AL, Xia Y. Biodegradable porous beads and their potential applications in regenerative medicine. Journal of Materials Chemistry 2012;22(23):11442-11451.

267. Rouquerol J, Avnir D, Fairbridge C, Everett D, Haynes J, Pernicone N, Ramsay J, Sing K, Unger K. Recommendations for the characterization of porous solids (Technical Report). Pure and Applied Chemistry 1994;66(8):1739-1758.

268. Simão L, Caldato R, Innocentini M, Montedo O. Permeability of porous ceramic based on calcium carbonate as pore generating agent. Ceramics International 2015;41(3):4782-4788.

269. Wu C, Zreiqat H. Porous bioactive diopside ($CaMgSi_2O_6$) ceramic microspheres for drug delivery. Acta biomaterialia 2010;6(3):820-829.

270. Lakhkar NJ, Park JH, Mordan NJ, Salih V, Wall IB, Kim HW, King SP, Hanna JV, Martin RA, Addison O. Titanium phosphate glass microspheres for bone tissue engineering. Acta biomaterialia 2012;8(11):4181-4190.

271. Bohner M, Tadier S, van Garderen N, de Gasparo A, Döbelin N, Baroud G. Synthesis of spherical calcium phosphate particles for dental and orthopedic applications. Biomatter 2013;3(2):25103.

272. Kim KK, Pack DW. Microspheres for drug delivery. BioMEMS and biomedical nanotechnology: Springer; 2006:19-50.

273. Fu H, Rahaman MN, Day DE. Effect of process variables on the microstructure of hollow hydroxyapatite microspheres prepared by a glass conversion method. Journal of the American Ceramic Society 2010;93(10):3116-3123.

274. Lakhkar NJ, M Day R, Kim HW, Ludka K, Mordan NJ, Salih V, Knowles JC. Titanium phosphate glass microcarriers induce enhanced osteogenic cell proliferation and human mesenchymal stem cell protein expression. Journal of tissue engineering 2015;6:2041731415617741.

275. McLaren JS, Macri-Pellizzeri L, Hossain KMZ, Patel U, Grant DM, Scammell BE, Ahmed I, Sottile V. Porous Phosphate-Based Glass Microspheres Show Biocompatibility, Tissue Infiltration, and Osteogenic Onset in an Ovine Bone Defect Model. ACS applied materials & interfaces 2019.

276. Conzone SD, Day DE. Preparation and properties of porous microspheres made from borate glass. Journal of Biomedical Materials Research Part A 2009;88(2):531-542.

277. Chen AM, Gu P, Ni ZM. 3D flower-like magnesium borate microspheres assembled by nanosheets synthesized via PVP-assisted method. Materials Letters 2012;68:187-189.

278. Conzone SD, Hall MM, Day DE, Brown RF. Biodegradable radiation delivery system utilizing glass microspheres and ethylenediaminetetraacetate chelation therapy. Journal of Biomedical Materials Research Part A 2004;70(2):256-264.

279. Huang W, Rahaman MN, Day DE, Miller BA. Strength of hollow hydroxyapatite microspheres prepared by a glass conversion process. Journal of Materials Science: Materials in Medicine 2009;20(1):123.

280. Hench LL. The story of Bioglass. J Matter Sci: Matter Med. Springer Science; 2006.

281. Jones JR. Review of bioactive glass: from Hench to hybrids. Acta biomaterialia 2013;9(1):4457-4486.

282. Fu H, Rahaman MN, Day DE, Huang W. Long-term conversion of 45S5 bioactive glass–ceramic microspheres in aqueous phosphate solution. Journal of Materials Science: Materials in Medicine 2012;23(5):1181-1191.

283. Bortot M, Prastalo S, Prado M. Production and characterization of glass microspheres for hepatic cancer treatment. Procedia Materials Science 2012;1:351-358.

284. Hong W, Guo F, Hu L, Wang X, Xing C, Tan Y, Zhao X, Xiao P. A hierarchically porous bioactive glass-ceramic microsphere with enhanced bioactivity for bone tissue engineering. Ceramics International 2019.

285. Kraxner J, Michalek M, Romero AR, Elsayed H, Bernardo E, Boccaccini AR, Galusek D. Porous bioactive glass microspheres prepared by flame synthesis process. Materials Letters 2019;256:126625.

286. Kim TK, Yoon JJ, Lee DS, Park TG. Gas foamed open porous biodegradable polymeric microspheres. Biomaterials 2006;27(2):152-159.

287. Karageorgiou V, Kaplan D. Porosity of 3D biomaterial scaffolds and osteogenesis. Biomaterials 2005;26(27):5474-5491.

288. Chang BS, Hong KS, Youn HJ, Ryu HS, Chung SS, Park KW. Osteoconduction at porous hydroxyapatite with various pore configurations. Biomaterials 2000;21(12):1291-1298.

289. Gauthier O, Bouler JM, Aguado E, Pilet P, Daculsi G. Macroporous biphasic calcium phosphate ceramics: influence of macropore diameter and macroporosity percentage on bone ingrowth. Biomaterials 1998;19(1-3):133-139.

290. Diao J, OuYang J, Deng T, Liu X, Feng Y, Zhao N, Mao C, Wang Y. 3D-Plotted Beta-Tricalcium Phosphate Scaffolds with Smaller Pore Sizes Improve In Vivo Bone Regeneration and Biomechanical Properties in a Critical-Sized Calvarial Defect Rat Model. Advanced healthcare materials 2018;7(17):1800441.

291. Ray N. Composition—property relationships in inorganic oxide glasses. Journal of Non-Crystalline Solids 1974;15(3):423-434.

292. Fredholm YC, Karpukhina N, Law RV, Hill RG. Strontium containing bioactive glasses: glass structure and physical properties. Journal of Non-Crystalline Solids 2010;356(44):2546-2551.

293. Sharmin N, Hasan MS, Rudd CD, Boyd D, Werner-Zwanziger U, Ahmed I, Parsons AJ. Effect of boron oxide addition on the viscosity-temperature behaviour and structure of phosphate-based glasses. Journal of Biomedical Materials Research Part B: Applied Biomaterials 2017;105(4):764-777.

294. Barrera Betanzos F. Development of innovative techniques for the manufacture of bioresorbable composites intended as fracture fixation devices: University of Nottingham; 2018.

295. AWARE WT, DOCUMENTATION TP. Implants for surgery—In vitro evaluation for apatite-forming ability of implant materials. 2007.

296. Fluegel A. Glass viscosity calculation based on a global statistical modelling approach. Glass Technology-European Journal of Glass Science and Technology Part A 2007;48(1):13-30.

297. Koudelka L, Mošner P. Study of the structure and properties of Pb–Zn borophosphate glasses. Journal of non-crystalline solids 2001;293:635-641.

298. Kiani A, Hanna JV, King SP, Rees GJ, Smith ME, Roohpour N, Salih V, Knowles JC. Structural characterization and physical properties of P_2O_5–CaO–Na_2O–TiO_2 glasses by Fourier transform infrared, Raman and solid-state magic angle spinning nuclear magnetic resonance spectroscopies. Acta biomaterialia 2012;8(1):333-340.

299. Carta D, Pickup DM, Knowles JC, Ahmed I, Smith ME, Newport RJ. A structural study of sol–gel and melt-quenched phosphate-based glasses. Journal of non-crystalline solids 2007;353(18):1759-1765.

300. Valappil SP, Ready D, Neel EA, Pickup DM, Chrzanowski W, O'Dell LA, Newport RJ, Smith ME, Wilson M, Knowles JC. Antimicrobial gallium-doped phosphate-based glasses. Advanced functional materials 2008;18(5):732-741.

301. Tiwari B, Dixit A, Kothiyal G, Pandey M, Deb S. Preparation and characterization of phosphate glasses containing titanium. Barc Newsletter 2007;285:167.

302. Brauer DS, Karpukhina N, Law RV, Hill RG. Effect of TiO_2 addition on structure, solubility and crystallisation of phosphate invert glasses for biomedical applications. Journal of Non-Crystalline Solids 2010;356(44-49):2626-2633.

303. Massera J, Fagerlund S, Hupa L, Hupa M. Crystallization mechanism of the bioactive glasses, 45S5 and S53P4. Journal of the American Ceramic Society 2012;95(2):607-613.

304. Massera J, Mayran M, Rocherullé J, Hupa L. Crystallization behavior of phosphate glasses and its impact on the glasses' bioactivity. Journal of Materials Science 2015;50(8):3091-3102.

305. Massera J, Hupa L, Hupa M. Influence of the partial substitution of CaO with MgO on the thermal properties and in vitro reactivity of the bioactive glass S53P4. Journal of Non-Crystalline Solids 2012;358(18):2701-2707.

306. David R. Lide e. CRC Handbook of Chemistry and Physics: CRC Press, Boca Raton, FL, 2005; Internet Version 2005, <http://www.hbcpnetbase.com>.

307. Shih P, Chin T. Preparation of lead-free phosphate glasses with low Tg and excellent chemical durability. Journal of materials science letters 2001;20(19):1811-1813.

308. Carta D, Qiu D, Guerry P, Ahmed I, Neel EA, Knowles JC, Smith ME, Newport RJ. The effect of composition on the structure of sodium borophosphate glasses. Journal of Non-Crystalline Solids 2008;354(31):3671-3677.

309. Qiu D, Guerry P, Ahmed I, Pickup DM, Carta D, Knowles JC, Smith ME, Newport RJ. A high-energy X-ray diffraction, ^{31}P and ^{11}B solid-state NMR study of the structure of aged sodium borophosphate glasses. Materials Chemistry and Physics 2008;111(2):455-462.

310. Navarro JM. El vidrio: Consejo Superior de Investigaciones Científicas; 1991.

311. Morikawa H, Lee S, Kasuga T, Brauer DS. Effects of magnesium for calcium substitution in P_2O_5–CaO–TiO_2 glasses. Journal of Non-Crystalline Solids 2013;380:53-59.

312. Parsons A, Ahmed I, Rudd C, Cuello G, Pellegrini E, Richard D, Johnson M. Neutron scattering and ab initio molecular dynamics study of cross-linking in biomedical phosphate glasses. Journal of Physics: Condensed Matter 2010;22(48):485403.

313. Brauer DS, Karpukhina N, Law RV, Hill RG. Effect of TiO_2 addition on structure, solubility and crystallisation of phosphate invert glasses for biomedical applications. Journal of Non-Crystalline Solids 2010;356(44):2626-2633.

314. Rajendran V, Devi AG, Azooz M, El-Batal F. Physicochemical studies of phosphate based P_2O_5–Na_2O–CaO–TiO_2 glasses for biomedical applications. Journal of non-crystalline solids 2007;353(1):77-84.

315. VOGEL J, Wange P, Knoche S, RÜSSEL C. Chemical solubility of phosphate glasses in the system Na_2O-CaO-MgO-P_2O_5-Al_2O_3-TiO_2 in aqueous solutions of different pH values. Glass science and technology 2004;77(2):82-87.

316. Wange P, VOGEL J, Knoche S, RÜSSEL C. Crystallization and viscosity of phosphate melts in the system Na_2O-CaO-MgO-P_2O_5-Al_2O_3-TiO_2. Glass science and technology 2004;77(4):172-176.

317. Dietzel A. Strukturchemie des Glases. Die Naturwissenschaften: Springer; 1941:537-547.

318. Karakassides M, Saranti A, Koutselas I. Preparation and structural study of binary phosphate glasses with high calcium and/or magnesium content. Journal of Non-Crystalline Solids 2004;347(1):69-79.

319. Vogel J, Wange P, Hartmann P. Effect of composition changes on the structure and properties of phosphate glasses in the pyrophosphate region. Glass science and technology 1997;70(1):23-27.

320. Clupper D, Hench L. Crystallization kinetics of tape cast bioactive glass 45S5. Journal of non-crystalline solids 2003;318(1):43-48.

321. Bretcanu O, Chatzistavrou X, Paraskevopoulos K, Conradt R, Thompson I, Boccaccini AR. Sintering and crystallisation of 45S5 Bioglass® powder. Journal of the European Ceramic Society 2009;29(16):3299-3306.

322. Li W, Mitchell BS. Nucleation and crystallization in calcium aluminate glasses. Journal of non-crystalline solids 1999;255(2):199-207.

323. Çelikbilek M, Ersundu AE, Aydın S. Crystallization kinetics of amorphous materials: INTECH Open Access Publisher; 2012.

324. Shih PY, Shiu HM. Properties and structural investigations of UV-transmitting vitreous strontium zinc metaphosphate. Materials Chemistry and Physics 2007;106(2):222-226.

325. Shih P. Properties and FTIR spectra of lead phosphate glasses for nuclear waste immobilization. Materials chemistry and physics 2003;80(1):299-304.

326. Pickup DM, Ahmed I, Guerry P, Knowles JC, Smith ME, Newport RJ. The structure of phosphate glass biomaterials from neutron diffraction and ^{31}P nuclear magnetic resonance data. Journal of Physics: Condensed Matter 2007;19(41):415116.

327. Koo J, Bae BS, Na HK. Raman spectroscopy of copper phosphate glasses. Journal of non-crystalline solids 1997;212(2-3):173-179.

328. Byun JO, Kim BH, Hong KS, Jung HJ, Lee SW, Izyneev A. Properties and structure of RO-Na_2O-Al_2O_3-P_2O_5 (R= Mg, Ca, Sr, Ba) glasses. Journal of non-crystalline solids 1995;190(3):288-295.

329. Patel U. Manufacture and Structural Characterisation of Novel Resorbable Phosphate-Glass Microspheres for Bone Repair Applications. University of Nottingham 2017.

330. Bohner M. Design of ceramic-based cements and putties for bone graft substitution. Eur Cell Mater 2010;20(1):3-10.

331. Eanes ED. Amorphous calcium phosphate: thermodynamic and kinetic considerations. Calcium phosphates in biological and industrial systems: Springer; 1998:21-39.

332. Giesche H. Mercury porosimetry: a general (practical) overview. Particle & particle systems characterization 2006;23(1):9-19.

333. Maeno S, Niki Y, Matsumoto H, Morioka H, Yatabe T, Funayama A, Toyama Y, Taguchi T, Tanaka J. The effect of calcium ion concentration on osteoblast viability, proliferation and differentiation in monolayer and 3D culture. Biomaterials 2005;26(23):4847-4855.

334. Yoshizawa S, Brown A, Barchowsky A, Sfeir C. Role of magnesium ions on osteogenic response in bone marrow stromal cells. Connective tissue research 2014;55(sup1):155-159.

335. Julien M, Khoshniat S, Lacreusette A, Gatius M, Bozec A, Wagner EF, Wittrant Y, Masson M, Weiss P, Beck L. Phosphate-dependent regulation of MGP in osteoblasts: Role of ERK1/2 and Fra-1. Journal of Bone and Mineral Research 2009;24(11):1856-1868.

336. Hamasaki D. The effect of sodium ion concentration on the electroretinogram of the isolated retina of the frog. The Journal of physiology 1963;167(1):156-168.

337. Blinkova E, Eliseev E. Dissolution of calcium carbonate in aqueous solutions of acetic acid. Russian journal of applied chemistry 2005;78(7):1064-1066.

338. Zhang Y, Ma P, Wang Y, Du J, Zhou Q, Zhu Z, Yang X, Yuan J. Biocompatibility of porous spherical calcium carbonate microparticles on Hela cells. World Journal of Nano Science and Engineering 2012;2(01):25.

339. Muñoz F, Montagne L, Delevoye L. Influence of phosphorus speciation on the phase separation of Na_2O–B_2O_3–SiO_2 glasses. Physics and Chemistry of Glasses-European Journal of Glass Science and Technology Part B 2008;49(6):339-345.

340. Rivera-Muñoz EM. Hydroxyapatite-based materials: synthesis and characterization. Biomedical Engineering-Frontiers and Challenges: InTech; 2011.

341. Lindfors N, Hyvönen P, Nyyssönen M, Kirjavainen M, Kankare J, Gullichsen E, Salo J. Bioactive glass S53P4 as bone graft substitute in treatment of osteomyelitis. Bone 2010;47(2):212-218.

342. Fu Q, Rahaman MN, Bal BS, Brown RF, Day DE. Mechanical and in vitro performance of 13–93 bioactive glass scaffolds prepared by a polymer foam replication technique. Acta biomaterialia 2008;4(6):1854-1864.

343. Tooley FV. The handbook of glass manufacture: a book of reference for the plant executive, technologist, and engineer: Ogden Publishing Company, New York; 1953.

344. Montanari F, Miselli P, Leonelli C, Boschetti C, Henderson J, Baraldi P. Calibration and use of the heating microscope for indirect evaluation of the viscosity and meltability of archeological glasses. International Journal of Applied Glass Science 2014;5(2):161-177.

345. Garcia-Valles M, Hafez H, Cruz-Matias I, Verges E, Aly M, Nogués J, Ayala D, Martinez S. Calculation of viscosity–temperature curves for glass obtained from four wastewater treatment plants in Egypt. Journal of thermal analysis and calorimetry 2013;111(1):107-114.

346. Sharmin N, Hasan MS, Rudd CD, Boyd D, Werner-Zwanziger U, Ahmed I, Parsons AJ. Effect of boron oxide addition on the viscosity-temperature behaviour and structure of phosphate-based glasses. Journal of Biomedical Materials Research Part B: Applied Biomaterials 2017;105(4):764-777.

347. Vedel E, Arstila H, Ylänen H, Hupa L, Hupa M. Predicting physical and chemical properties of bioactive glasses from chemical composition. Part 1: Viscosity characteristics. Glass Technology-European Journal of Glass Science and Technology Part A 2008;49(6):251-259.

348. Wang H, Zhang T, Zhu H, Li G, Yan Y, Wang J. Effect of B_2O_3 on melting temperature, viscosity and desulfurization capacity of CaO–based refining flux. ISIJ international 2011;51(5):702-706.

349. Hewlett PC. Lea's Chemistry of Cement and Concrete. Elsevier 2003.

350. Brown TL. Chemistry: the central science: Pearson Education; 2009.

351. Lua'y AZ, Morrison PW. Optimizing diamond growth for an atmospheric oxyacetylene torch. Journal of materials research 1997;12(5):1237-1252.